UNIVERSITÀ
DEGLI STUDI
FIRENZE

DOTTORATO DI RICERCA IN
SCIENZE DELLA TERRA

CICLO XXIX

COORDINATORE Prof. LORENZO ROOK

Petrogeochemical and geochronological framework of element mobilities during magmatic-metasomatic processes (Campiglia Marittima, Tuscany)

(Settore Scientifico Disciplinare GEO/07)

Dottorando
Dott. Paoli Gabriele

Tutore
Prof. Rocchi Sergio

Co-Tutore:
Dr. Andrea Dini

Coordinatore
Prof. Lorenzo Rook

a.a. 2013/2016

Table of contents

General Outlook of the thesis

Project target

This PhD thesis is part of a larger project on the magmatic-hydrothermal system of Campiglia Marittima that involves the collaboration between CNR and University of Pisa, as well as the University of Geneva (UNIGE). The research aim is to investigate the processes resulting from the emplacement of the Campiglia Marittima magmatic bodies in its carbonatic host. Indeed, at Campiglia it is possible to observe a complex magmatic-hydrothermal system generated by multiple magmatic events, likely last several 100s ka. These magmatic processes began with the emplacement of the Botro ai Marmi monzogranitic pluton (ca. 5.4 Ma), which was followed by mafic and later felsic porphyritic bodies (ca. 4.4. Ma) crosscutting the contact aureole generated by the monzogranite intrusion in the host rock. The final event is represented by an early Pliocene rhyolitic extrusive complex (4.38±0.04 Ma), which occurred to the west of the carbonate horst. The hydrothermal activity generated distal mineralised skarn bodies, exploited for base metals (Cu, Pb, Zn) and Ag for over twenty-seven centuries, from Etruscan times to 1979, when mining activity in the area definitely ceased. Moreover, this skarn system is considered in literature as a classic example of contact exoskarn generated by the interaction between a magmatic rock and a marble host rock.

In this context, the aims of this PhD thesis are (i) to characterise the complex metasomatic rocks at the pluton-host carbonate contact, which resulted from prolonged fluids-rock interaction, (ii) to identify the metasomatic processes that generate alteration and consequent replacement of the original granite and host carbonate, (iii) to recognise the litho-geochemical vectors responsible for the pronounced element mobilisation, especially also the local mobilisation of usually poorly mobile elements such as HFSE and REE. Thus, I carried out detailed textural and geochemical investigations of the monzogranite, the host carbonate, and the products of their hydrothermal-metasomatic alteration, in the field, under the microscope, and by QEMSCAN, EPMA and (LA)-ICP-MS.

The obtained results allowed to discriminate between metasomatic processes occurring at varying temperatures, fluid compositions and acidities, as well as to recognise preferential pathway for fluid circulation (e.g. fracture in the granite, folds in the host rock). Moreover, the reconstruction of a mineral paragenetic sequence coupled with precise chemical analysis allow to model the sequence of these metasomatic events. To define the chronological framework of the multiple igneous episodes occurring in the Campiglia Marittima area and to constrain the multiple hydrothermal episodes, precise CA-ID-TIMS U-Pb dating has been carried out, at the University of Geneva, on carefully selected zircon grains from the Botro ai Marmi monzogranite, the San Vincenzo rhyolite and the Temperino porphyry crosscutting the metasomatic aureole.

Thesis structure and main contents

The thesis is made up of introductory chapters (chapters 1-3), and a detailed description of the analytical methodologies (chapter 4). Chapter 5 to 7 are organised as papers to be submitted to scientific journal(s) as independent works. Each chapter is provided of an introduction, the geological background, a summary of the analytical methodologies, the results, a discussion and the main conclusions.

Chapter 1 and 2 illustrate a general introduction and regional geology.

Chapter 3 resumes the main knowledge about metasomatic processes occurring in magmatic-hydrothermal systems related to a granite intrusion hosted in a carbonatic sequence.

Chapter 4 describes in detail the most significant analytical procedures performed during this work. Methods are briefly recalled in each chapter.

Chapter 5 presents a detailed petrographic, mineralogical and bulk-rock data of the Botro ai Marmi monzogranite, the metasomatic rocks and the host carbonate, as well as petrographic and bulk-rock description of a borehole crosscutting

the entire sequence. This chapter introduces the possible metasomatic processes responsible for fluid-rock interaction and element mobility in the system, comparing bulk-rock data of selected samples with the unaltered granite, in order to identify a specific element exchange process. In closing it has been shown a possible paragenetic sequence for the different lithologies observed in the mine and in the borehole, important to reconstruct a timeline of the metasomatic processes.

Chapter 6 investigates in detail the minerals texture and geochemistry, with major and trace element data obtained by EMP and LA-ICP-MS analysis. The study describes the concentration and multiple remobilisation process of major elements, HFSE and REE. Ca-F-rich fluid(s) are responsible for the increasing elements mobilisation. These features are pointed out by the prominent occurrence of REE-rich minerals (e.g., allanite, thorite, uraninite, ekanite) and by the unusual enrichment of REE-Y (±Zr, F) in several hydrothermal minerals (e.g., vesuvianite, titanite, epidote). The composition of these minerals, usually characterised by a prominent chemical zoning, allows to define a final model, showing the timing of mineral growth and fluids evolution with respect to contact metamorphism and metasomatic events.

Chapter 7 points out how magmas released by the melting of continental crust commonly draw little attention in the studies concerning timing of magmatic processes in magma chambers and eruptive environment. CA-ID-TIMS U–Pb data on zircon grains from the Botro ai Marmi granite, the Temperino porphyry and the San Vincenzo rhyolite allow to identify complex zircon age populations discerning between *in-situ* crystallization versus crystallization at a deeper level. Moreover, the comparison of new U-Pb data with Ar-Ar ages obtained in a previous PhD thesis (same igneous and metasomatic bodies) allows to reconstruct the timing of crystallization for different minerals (zircon, biotite, and phlogopite) in the different sub-units (granite and skarn). In this chapter, the Botro ai Marmi pluton dataset has been compared to other well-documented examples (Monte Capanne pluton, Fisch Canyon Tuff, Torres del Paine complex). The distribution of zircon ages is at odds with what can be expected for the crystallization interval of an igneous body. Indeed, that interval is short for the Botro ai Marmi pluton (~100 ka), intermediate for the subvolcanic mafic Temperino porphyry (~650 ka), and long for the volcanic San Vincenzo rhyolite (~1000 ka).

Thus, geochronological data for the Campiglia igneous system lend support to a scenario in which a bimodal deep reservoir remains in a magmatic condition (melt-present) for ~1 Ma. The magma extraction from a crustal felsic reservoir fed a pluton and its hydrothermal system during a short time interval at 5.4 Ma. At ~4.9 Ma the extraction of magma from a mafic reservoir supplied the Temperino mafic porphyry. Finally, the late extraction of magma from the felsic reservoir (probably the same of the Botro ai Marmi granite) fed the San Vincenzo rhyolites, where early-crystallised zircons were transported/recycled within portions of melts extracted from the reservoir.

Chapter 8 concludes with the most significant results of this project, opening a discussion and giving suggestions for further improvements of the presented research.

Abstract

Processes of post-magmatic element mobilisation have been reported for a number of magmatic-hydrothermal systems occurring in diverse geodynamic contexts. To constrain the processes that control these types of systems is a challenging task because the effects of hydrothermal/metasomatic processes on element distribution are poorly known, also the relationships of alteration types to mineralisation stages have not been well documented. This study presents the results of a detailed petrogeochemical and geochronological investigation, involving mineral and bulk-rock analysis as well as a precise CA-ID-TIMS U-Pb zircon dating. Based on these data, a model has been developed to explain the role of metasomatic processes in mobilising elements in a granitic system and to define the timing of igneous events controlling the mobility of fluids observed at Campiglia Marittima magmatic-hydrothermal system.

At Campiglia the occurrence of multiple magmatic events over about 1 Ma generated an intense metasomatic fluid circulation. These magmatic processes began with the emplacement of the Botro ai Marmi monzogranitic pluton (~5.4 Ma), that was followed by mafic and later felsic porphyritic bodies (from 4.9 to 4.5 Ma) crosscutting the contact aureole generated by the monzogranite intrusion in the carbonate host rock. The closing event is represented by the early Pliocene (~4.4 Ma) rhyolitic extrusive complex of San Vincenzo. The hydrothermal metasomatic activity related to the whole igneous cycle generated proximal endo- and exoskarn as well as distal mineralised skarn bodies, exploited for Cu-Pb-Zn-Ag for over twenty-seven centuries and which are considered as a classic example of contact exoskarn generated by the interaction between a magmatic body and a marble host rock.

This study focuses on (i) the characterisation of the different metasomatic lithofacies occurring at the pluton-host carbonate contact, resulting from prolonged fluids-rock interaction, (ii) the identification of the metasomatic processes that generated chemical transformation and a consequent replacement of the original granite and host carbonate, (iii) the identification of the geochemical processes responsible for the significant element mobilisation, regarding also the local mobilisation of usually poorly mobile elements, such as HFSE and REE. Thus, this study carried out detailed textural and geochemical investigations of the monzogranite, the host carbonate, and the products of their hydrothermal-metasomatic alteration, in the field, under the optical and electron microscope, and by QEMSCAN, EPMA and (LA)-ICP-MS. The obtained results allowed to discriminate between metasomatic processes occurred at variable temperature, fluid composition and pH, as well as to recognise preferential pathways for fluid circulation. Moreover, the reconstruction of the mineral paragenetic sequence coupled with chemical analysis allows to reconstruct the sequence of these metasomatic events. To define the chronological framework of the multiple igneous episodes occurring in the Campiglia Marittima area and to constrain the multiple hydrothermal episodes, a precise CA-ID-TIMS U-Pb dating has been carried out at the University of Geneva, on carefully selected zircon grains from the Botro ai Marmi monzogranite, the San Vincenzo rhyolite and the Temperino mafic porphyry crosscutting the metasomatic aureole.

The Campiglia system offers exposures of the full range of emplacement types for magmas and related fluids, thus represents a prime case study to investigate the timescales of mechanism of magma deep storage, extraction, transfer, and shallow emplacement/eruption. New U-Pb CA-ID-TIMS geochronology from the Campiglia igneous system allows to reconstruct the evolution of crustal-derived and mantle-derived magmas that fed plutonic, subvolcanic and volcanic units over 1000 ka. Distribution of zircon ages is at odds with what can be expected for the crystallization interval of an igneous body. Indeed, that interval is short for the Botro ai Marmi pluton (100 ka), intermediate for the subvolcanic mafic Temperino porphyry (450 ka), and long for the volcanic San Vincenzo rhyolite (700 ka). The youngest zircons from the Botro ai Marmi granite have ages identical to ^{40}Ar-^{39}Ar ages of biotite from the granite and metasomatic phlogopite from skarn crosscutting the granite. The Temperino mafic porphyry and the San Vincenzo rhyolite show younger sanidine ages (emplacement/eruption age). The youngest zircon age from the pluton is therefore assumed to approximate the age of emplacement and final crystallization of the melt, whereas the zircons from the

Temperino mafic porphyry and the San Vincenzo rhyolite are considered antecrystic, derived from re-mobilised earlier magma extracted from a deeper reservoir at the emplacement age.

The new documentation of an extended period of crystallization for the Campiglia igneous system (about 1000 ka) matches with observations for the long-lived magmatic systems of Larderello and Elba Island. These data support the existence of multiple crustal reservoirs far larger than the outcropping igneous products. The observed mantle signature of metasomatic fluids suggests the presence of hidden mantle-derived reservoir able to activate episodically crustal melting and magma transfer to shallow levels. This sequential magmatic activity (both from mantle and crust) could be controlled by multiple, small batches of mafic magma, that did not lead to the formation of a single, homogeneous, hybrid pluton at the emplacement level.

1. Introduction

Natural resources are a key issue for the society and their availability has been called into question (e.g., Moss et al., 2011). Indeed, recent advances in high-technology industries created a large increase in demand for the base and critical metals and a need to develop robust models of ore genesis to facilitate their successful exploration. In this context, metasomatic rocks are one of the world's major source of these elements. Metasomatism, which is defined as the process in which rocks change their composition while remaining effectively solid, is self-evidently important in the evolution of a wide range of rock types, but it remains quite poorly understood.

Any crustal fluid can give rise to metasomatism when it migrates from one rock type to another. Metasomatism is usually related to existing pathway for fluid flow, such as fractures, faults, shear zones, or lithological variability (i.e. lithologies more permeable than those around them). The comparison of a wide range of crustal fluids shows that they share many systematic characteristics. Fluid compositions can be buffered by local host rocks, they can reflect the temperature at which they have interacted with the host rocks, their salinity, and their origin. Thus, they provide a basis for interpreting some of the common chemical changes seen in metasomatic rocks (e.g., Pirajno, 2009; Harlov and Austrheim, 2013).

Metasomatic processes produce the mobilisation of major elements (Fe, Ti, Si, Al, P) and trace elements (e.g. Th, Nb, Zr, HFSE, and REE), possibly generating changes in the bulk composition of the metasomatised rocks. Thus, understanding the anatomy of magmatic-hydrothermal systems provides crucial knowledge on generation, segregation, and transfer of magmatic-hydrothermal fluids, fundamental processes that involve transfer of elements, mass and heat within the upper crust.

In this way, the significance of this work is to provide the timing of element mobility between granite, fluids and metasomatic bodies for a shallow crustal magmatic-hydrothermal systems. In this context, the reconstruction of metasomatic processes, generating progressive elements mobilisation, asserts the importance of petrographic and geochemical characterisation of bulk-rock as well as major and accessory metasomatic minerals, to evaluate the potentiality for the occurrence of ore-minerals. Outline geometries and spatial relationship of the main geological bodies, mineralogical paragenesis and mineral zoning of a magmatic-hydrothermal system are important to reconstruct the timing of fluid-rock interaction and element mobility. Multiple metasomatic effects can overlap through time, resulting in complex mineral associations, as well as a continuously renewed magmatic-hydrothermal system, with evolving fluid circuits, could produce several hydrothermal paragenesis. Understanding the temporal relationships existing between metasomatic processes, mineral paragenesis, and element mobility, using textural, geochemical and accessory minerals dating technique, could provide a fundamental piece of information in order to identify potentially productive mineral deposits.

In this context, the Campiglia Marittima magmatic-hydrothermal system, located in southern Tuscany (Italy), is an example of a magmatic-hydrothermal system associated to a small size mineralized deposit (ca. 50 kt of base metals), with modest residual economic interest. Despite this, its geological characters make it an ideal site to study the metasomatic and fluid-rock interaction processes. Indeed, the Campiglia carbonate horst of Campiglia was intruded by the Botro ai Marmi monzogranite pluton (~5.4-5.5 Ma; this work), that generates a wide metamorphic aureole (~6-7 km^2), crosscut by slightly younger mafic (~5.1-5.3 Ma; this work) and felsic porphyritic dikes (~4.3 Ma; Borsi et al., 1967). The early Pliocene (~4.4 Ma; Feldstein et al., 1994) rhyolitic extrusive complex of San Vincenzo covers the early sedimentary sequence exposed to the west of the carbonate horst. The results of the thermal metamorphism were metasomatic bodies in close spatial relation with the pluton, occurring as: (i) massive exoskarn bodies occurring at the pluton-host carbonate contact, (ii)

calc-silicate endoskarn veins, that follow brittle fractures in the granite pluton, (iii) low- grade veins and disseminations Sn-W-As-Bi ore and (iv) the main Campiglia Fe-Cu-Zn-Pb(-Ag) skarn deposit (Vezzoni et al., 2016), consisting of several bodies and veins that crop out discontinuously. The primary assemblage of the monzogranite changes from magmatic quartz, K-feldspar, plagioclase and biotite (±apatite, zircon, and late magmatic turmaline) to secondary, hydrothermal K-feldspar, phlogopite, titanite, diopside (±apatite, zircon) and REE-bearing minerals (e.g. allanite, uraninite, thorite). A pervasive hydrothermal alteration, due to late-magmatic hydrothermal fluids, results in the mobilisation of major and trace elements, with the almost complete replacement of biotite.

The Campiglia Marittima area offers a suitable scenario to study the duration of processes at different levels of the plumbing system and the connection existing between felsic and mafic sources at such a shallow anatectic level. Here, uplift and erosional processes have exposed plutonic, subvolcanic, and volcanic rocks (both from mantle and crust), as well as hydrothermal products. Detailed textural and geochemical investigations on the products of the hydrothermal activity have been carried out in the field, under the optical microscope and by QEMSCAN, EPMA and (LA)-ICP-MS. High-precision U-Pb thermal ionization mass spectrometry (TIMS) geochronology on zircons from all these igneous units provides the opportunity to resolve time-transgressive crystallization of crustal igneous processes. To set these data in a larger framework, the obtained ages are compared with other well-documented examples of time-transgressive construction of volcanic and plutonic magmatic systems.

Thus, this thesis examines in detail a system linking plutonic, subvolcanic, volcanic and hydrothermal realms aiming to determine (i) the link between igneous and hydrothermal deposits, (ii) the mechanisms controlling the element mobility between granite-fluid(s)-host rock, (iii) the timescale of processes at different levels of the plumbing system and the genetic relationships between exposed rocks and their hidden sources, both of melt and metasomatic fluid(s).

2. Geological setting

The present-day geological framework of the the Peri-Mediterranean regions is mainly the result of the collision between the African and European plates, active since late Cretaceous-late Eocene. The continental collision led to the formation of important orogenic belts all around the Mediterranean area (Platt, 2007; Fig. 2.1), including the Apennine belt. The NW-SE directed Northern Apennine thrust-and-fold belt consists of strongly deformed superimposed tectonic units. During the convergence between Africa and Adria a series of kinematic processes affected the Appennine chain, such as subduction, back-arc basin opening, strike-slip faulting, and lateral extrusion of lithospheric blocks. Tuscany is located in the inner part of the chain and consists of several tectonic units stacked during the Apennine orogenesis, then dissected by Miocene-Pliocene extensional normal faults that generated extensional basins filled with Neogene sediments (e.g., Carmignani et al., 2001, Dini et al., 2005; Peccerillo, 2005). The Tuscan tectonostratigraphic units mainly consist of (i) a Paleozoic basement that underwent two Alpine tectono-metamorphic deformation phases (Franceschelli et al., 2004) overlain by (ii) Permian to early Miocene sedimentary units, such as the metasedimentary sequence of the Verrucano Formation, and the late Triassic evaporite sequence of the Burano Formation and an extended carbonatic succession (e.g., Decandia et al., 2001; Brogi and Cerboneschi, 2007). Tectonically superimposed on the Tuscan units one can observe (i) the Ligurian domain, consisting of middle-late Jurassic oceanic rocks and their sedimentary cover, (ii) the Oligo-Miocene Sub-Ligurian domain (clastic marine sediments) and (v) the Umbria-Marche domain, made of Miocene to Pleistocene sediments infilling extensional post-orogenic depressions (e.g. Decandia et al., 2001).

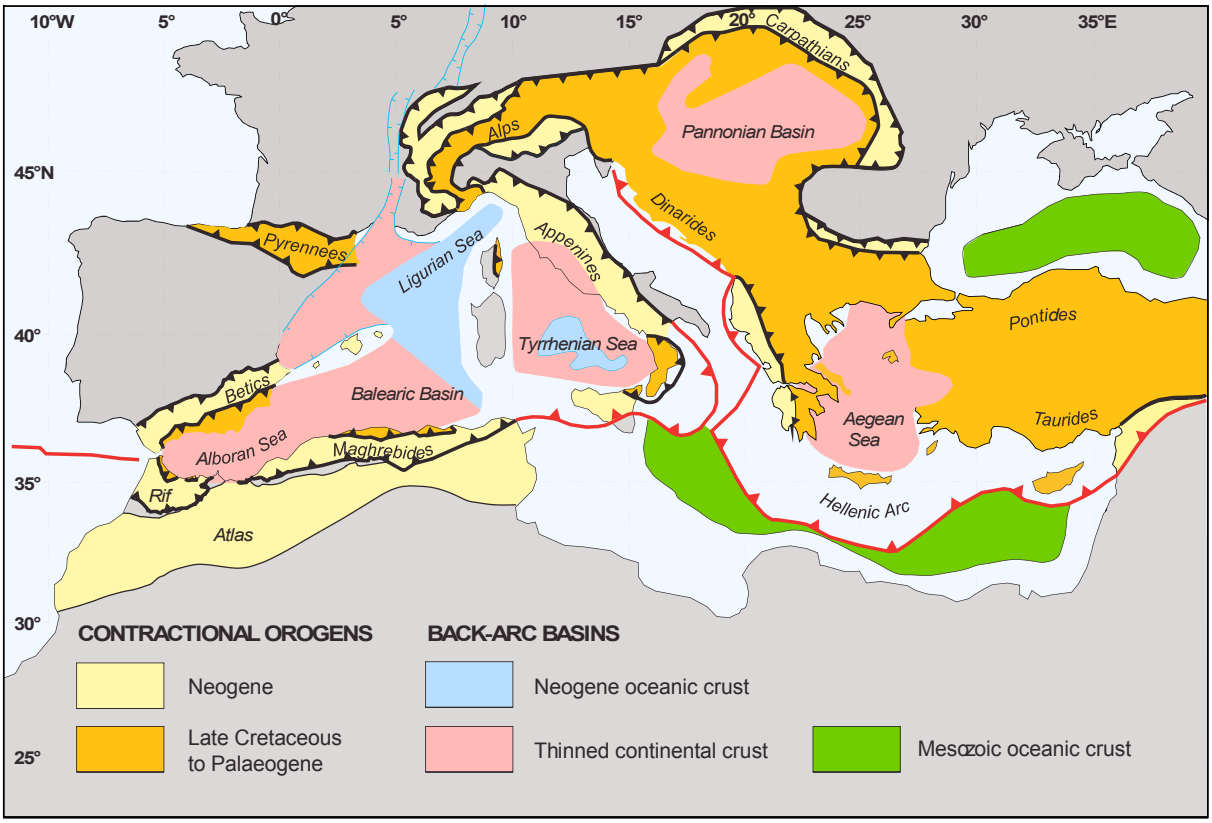

Fig. 2.1 - Schematic tectonic map of the Mediterranean region, showing Mesozoic–Tertiary contractional orogens and Neogene extensional basins. Africa–Eurasia plate boundary is shown in red; it should be noted that the plate boundary cannot be defined everywhere, because of the widely distributed pattern of deformation (after Platt, 2007).

In the northern Tyrrhenian area (Fig. 2.2), extensional tectonics developed since early Miocene in Alpine Corsica (Jolivet et al., 1990), progressively shifting eastward with an overall E-W direction of extension (Carmignani et al., 1995; Piana Agostinetti and Amato, 2009; Carminati et al., 2012). Extension resulted in the development of shallowly eastward-dipping ductile extensional shear zones, which initially (brittle-ductile transition) accompanied the nearly isothermal exhumation of the deep-seated metamorphic rocks and, successively (late Miocene-Pliocene) triggered a pronounced magmatic activity (Fig. 2.2, Jolivet et al., 1998 and references therein). The eastward migration of the compressional front generated the opening of the northern Tyrrhenian Basin characterised by thinned continental crust (25-20 km; Fig. 2.2; Piana Agostinetti and Amato, 2009; Carminati et al., 2012). The related crustal extension results from a early-middle Miocene activity of low-angle faults (extension rate up to 120%), that led to the elision of parts of the Tuscan Nappe in southern Tuscany (Brogi, 2008). The following late Miocene to Pleistocene stage is characterised by high-angle NW-SE faults, producing horst-and-graben structures with an up to 10% total extension (e.g. Carmignani et al., 1994; Decandia et al., 2001). Moreover, N-S-trending dextral fault segments along the coastline of southern Tuscany have been recognized as active features during pluton emplacement (Acocella et al., 2000; Rossetti et al., 2001). These faults have been interpreted as accommodating strain compatibility in the brittle crust during crustal-scale extensional simple shearing at depth (Rossetti et al., 2000). Finally, during late Miocene to Pleistocene, a post-collisional magmatism involved southern Tuscany and the northern Tyrrhenian Sea (Innocenti et al., 1992; Serri et al., 1993). The products of this magmatism are traditionally ascribed to the so-called Tuscan Magmatic Province (Fig. 2.3; e.g., Marinelli, 1967; Peccerillo, 1999; Dini et al., 2002).

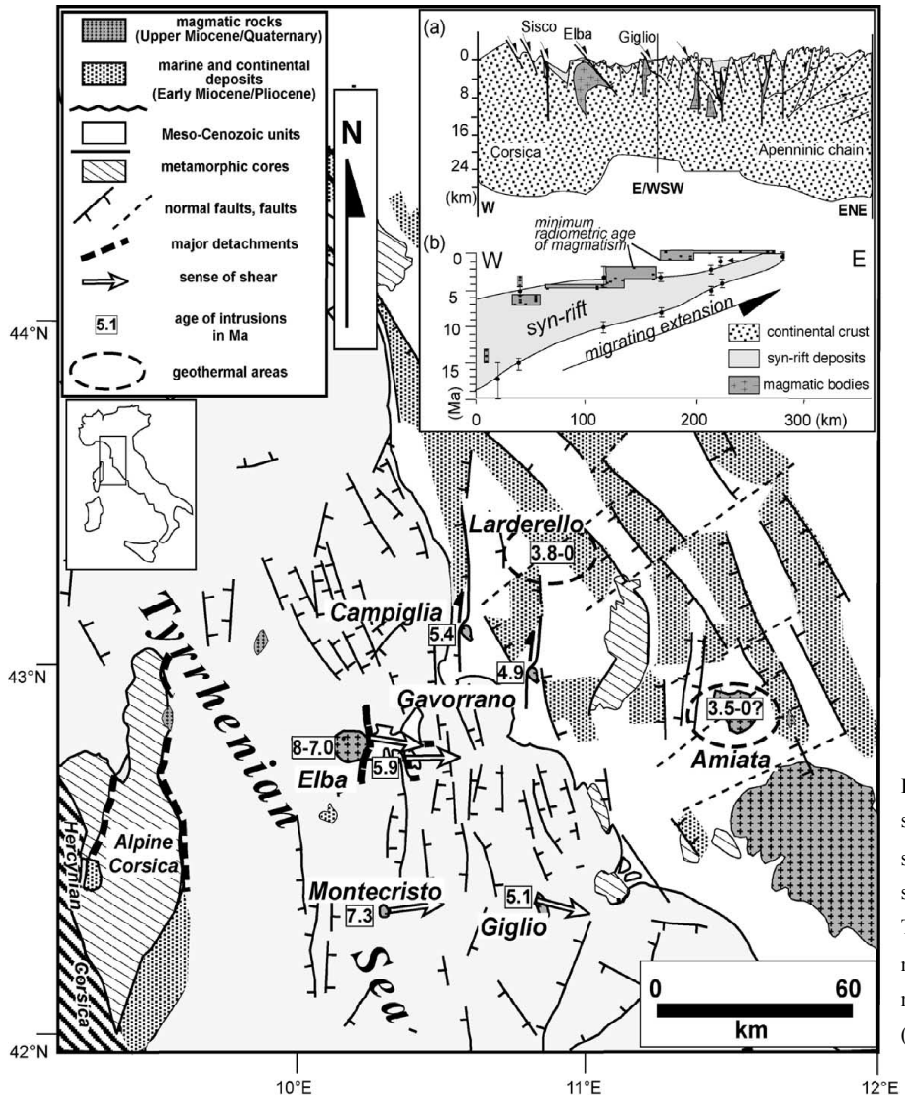

Fig. 2.2 - Schematic map of the main structural and magmatic features of southern Tuscany, Italy. (a) Ideal E–W section through the central part of the Tuscan Magmatic Province; (b) eastward migration of extension and related magmatism along an ideal section (modified after Acocella, 2002).

Tuscan Magmatic Province

The igneous activity of the Tuscan Magmatic Province (TMP) generated an association of anatectic (granites and peraluminous rhyolites) and mantle-derived (high-K calcalkaline, shoshonitic, alkaline potassic and ultra-K lamproites) intrusive and effusive rocks that crop out over a wide area in Tuscany. These activities occurred from E, in the Tuscan Archipelago (Capraia, Elba, Montecristo, and Giglio islands), to W in several localities of southern Tuscany and northern Latium (e.g. San Vincenzo, Roccastrada, Mt. Amiata, Mts. Cimini, Tolfa-Manziana-Cerite) (e.g. Barberi et al. 1971; Peccerillo et al. 1987; Poli et al. 2002). According to the eastward movement of the subduction zone, the ages range from about 14.5 Ma (Sisco, Corsica) to 200 ka (Monte Amiata), and decrease from west to the east (Fig. 2.3; Barberi et al., 1967; Innocenti et al., 1992; Dini et al. 2002; Peccerillo, 2005; Carminati et al., 2012, Perugini and Poli, 2003; Rocchi et al., 2003). This activity is linked to elevated heat flow, with peaks in the Larderello geothermal area (up to 2700 mW/m^2; Gianelli et al., 1997; Gianelli and Ruggeri, 2002; Dini et al., 2005). This thermal anomaly leads to speculate on the presence of large, still hot, magma bodies (acidic) and deeper intrusions (mafic magma). This framework and the geophysical modelling suggest the existence of a long-lived and still active magmatic system in the Larderello geothermal area (Gianelli et al., 1997; Mongelli et al., 1998) and in the mining area of Gavorrano (Castel di Pietra pluton, Franceschini et al., 2000).

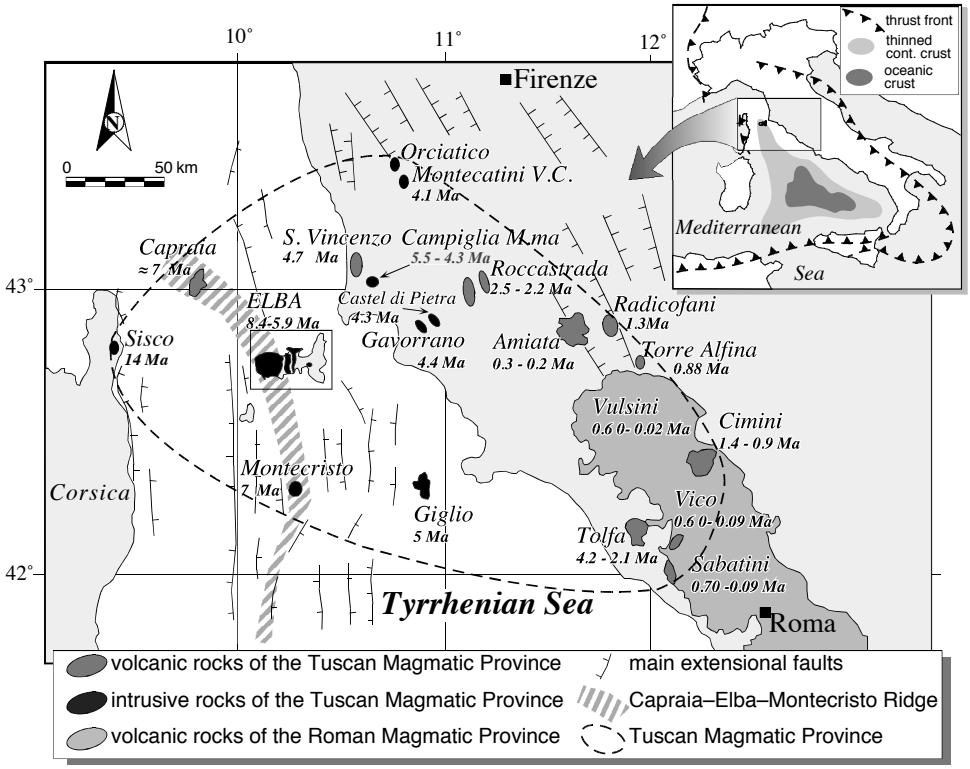

Fig. 2.3 - Location map for the Tuscan Magmatic Province. Also reported are the younger potassic-ultrapotassic volcanic rocks of the Roman Magmatic Province (modified from Dini et al. (2002).

A Total Alkali vs. Silica classification diagram for all the igneous rocks, together with an ANOR-Q' normative classification diagram of granitoids, show as acidic compositions are the most abundant in the TMP (Fig. 2.4), with the largest intrusive bodies occurring at Montecristo, Giglio and Elba islands. Other silicic intrusions crop out at Campiglia and Gavorrano, and occur as hidden bodies in several places of southern Tuscany, notably in the Mt. Amiata and Larderello area (e.g. Dini et al. 2005). Rhyolitic lava flows and domes are found at San Vincenzo, Roccastrada, and Tolfa-Manziana-Cerite area. Silicic-intermediate rocks also include the older products of Monti Cimini and Mt. Amiata. Mafic-intermediate lavas and hypoabyssal rocks occur at Montecatini Val di Cecina, Orciatico, Torre Alfina,

Radicofani, Monti Cimini, Amiata, Capraia, Campiglia, central-eastern Elba, and at Sisco. Mafic-intermediate rocks also occur as enclaves within the granitoid rocks. Compositions range from calcalkaline-shoshonitic basalt-basaltic andesite to potassic and ultrapotassic shoshonite and latite (Fig. 2.4). SiO_2 vs. K_2O/Na_2O diagram (Fig. 2.4) allows to visualise the extreme compositional variability in Tuscany igneous rocks. As an example, some rocks show high silica contents (SiO_2 > 70), have K_2O/Na_2O = 2, and are peraluminous (ASI > 1; Table 1 in Poli and Peccerillo, 2016). These composition is characteristic of both effusive and intrusive bodies (e.g. San Vincenzo and Roccastrada rhyolites, as well as Campiglia, Elba and Giglio plutons).

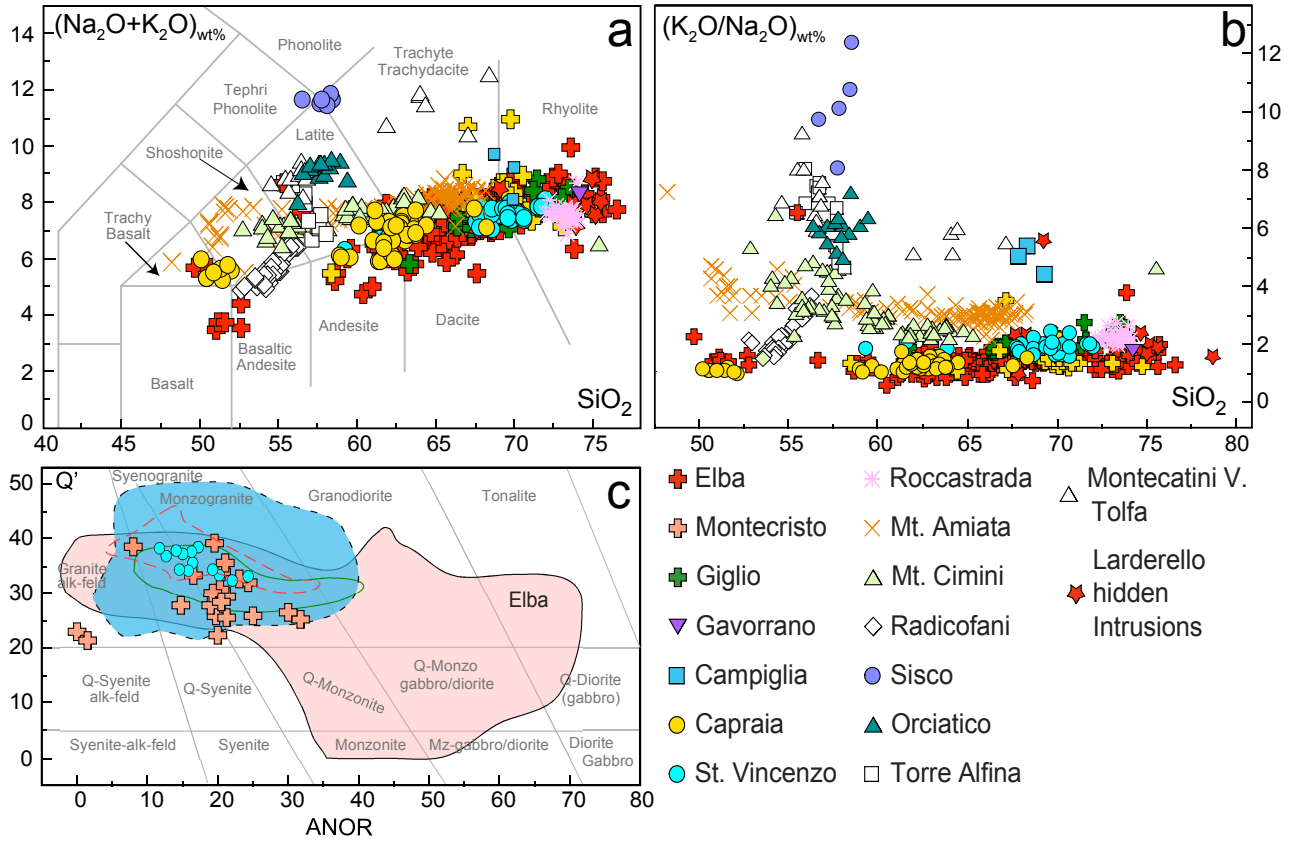

Fig. 2.4 - (a) Total alkali vs. silica diagram (Le Maitre, 2002) for the rocks of Tuscany Magmatic Province; (b) SiO_2 vs. K_2O/Na_2O diagram; (c) Q'-ANOR classification diagram for plutonic rocks (Streckeisen and Le Maitre, 1979). Q'=100*[Qtz/(Qtz+Ab+O+An)] and ANOR=100*[An/(An +Or)], where Qtz, Ab, Or, An are normative quartz, albite, orthoclase and anorthite. The compositions of the Elba and Campiglia rocks are reported as red area and blu area, respectively. The compositions of Larderello and Giglio bodies are reported as red and green dotted lines, respectively Poli and Peccerillo, 2016.

The variability observed in this magmatic province cannot be explained through differentiation processes from a unique parental magma type. Moreover, almost all the magmatic rocks recorded mixing processes between a crustal-anatectic magma and a mantle-derived magma end-members (Dini et al., 2005; Peccerillo and Donati, 2003). For the silicic igneous rocks a large amount of petrological, geochemical and isotopic data ($^{87}Sr/^{86}Sr$) are consistent with a mixing between crustal anatectic and mantle-derived mafic magmas (e.g., Poli, 1992; Peccerillo, 2005; Dini et al., 2005). Only a few rocks, such as those with the highest $^{87}Sr/^{86}Sr$ and the lowest $^{143}Nd/^{144}Nd$ (rhyolites from San Vincenzo Roccastrada) are inferred to represent magmas exclusively generated by partial melting of the crust (Peccerillo and Donati, 2003). According to Poli (2004), the formation of the silicic rocks of Tuscany, including the San Vincenzo rhyolites, involved 19-22% of batch modal melting of Paleozoic crustal rocks (gneiss and garnet micaschist) with $^{87}Sr/^{86}Sr$ initial ratio similar to those of the peraluminous silicic rocks. However, modal melting normally does not

happen in nature, where non-modal (eutectic) melting processes control the preferential breakdown of certain minerals in the crustal source (e.g., Ersoy, 2013).

On the other hand, the mafic rocks (MgO over 4 wt%) form small plutonic bodies, lava flows and enclaves in felsic rocks. The high values of Ni, Cr and Mg# in ultramafic xenoliths reflect a mantle-derived magma. These rocks are characterised by a highly variable geochemical and isotopic composition that indicates strong heterogeneity in the mantle sources (Peccerillo and Donati, 2003). Moreover, they identify a continuous trend between potassic rocks with lamproitic affinity, to ultrapotassic calcalkaline and shoshonitic rocks. Lamproitic rocks have been found in Montecatini Val di Cecina, Orciatico, Torre Alfina and Sisco, and are characterised by low CaO, Al_2O_3 and Na_2O and high K_2O. Other peculiarity are the relatively high SiO_2 content with silica over-saturation and the geochemical fingerprint of crustal materials rather than mantle ones. Capraia and Radicofani igneous products show the lowest concentrations of incompatible elements among the Tuscan mafic rocks. At Capraia, Sr isotope ratios are the lowest in the Tuscan province ($^{87}Sr/^{86}Sr$ = 0.708-0.709), while higher values are found at Radicofani ($^{87}Sr/^{86}Sr$ = 0.713-0.716). These data suggest a genesis by a mantle source rocks metasomatised by subducted upper crust materials. Experimental studies suggest origin by melting of upper mantle peridotites depleted in clinopyroxene (e.g., residual harzburgite) and enriched in a K-rich phase, such as phlogopite (Peccerillo and Donati, 2003).

Botro ai Marmi pluton emplacement

The mobility of magmas in the upper crust plays a key role during several geological processes, such as volcanic eruptions, ore deposition, and establishment of geothermal fields. The necessary permeability in country rocks is commonly activated by tectonic activity, focussing magmas and fluids in structural traps. In particular, the Campiglia Marittima area was affected by igneous activity during the late Miocene-early Pliocene, resulting in the occurrence of metasomatic rocks and ore bodies (Barberi et al., 1967). The geometry of the different lithologies and the intensity of their deformation are clearly spatially related to the location and shape of the Botro ai Marmi pluton and its thermal metamorphic aureole (Fig. 2.5). Intensity of deformation decreases with distance from the pluton, and deformation type changes accordingly, showing both ductile and brittle styles (Vezzoni et al., in revision). The roof morphology of the Botro ai Marmi stock, reconstructed by geological surveys, exploratory boreholes, and seismic-gravimetric data (Fig. 2.6; Vezzoni et al., in revision), indicated that magma and hydrothermal fluids followed similar structural patterns in the upper crust. But overall, the migration and emplacement of fluids and magmas were ruled by the lateral displacement of the thermally weakened carbonate overburden of a pluton, a process which interacted with regional extension working on transfer zones (Fig. 2.5; Vezzoni et al., in revision).

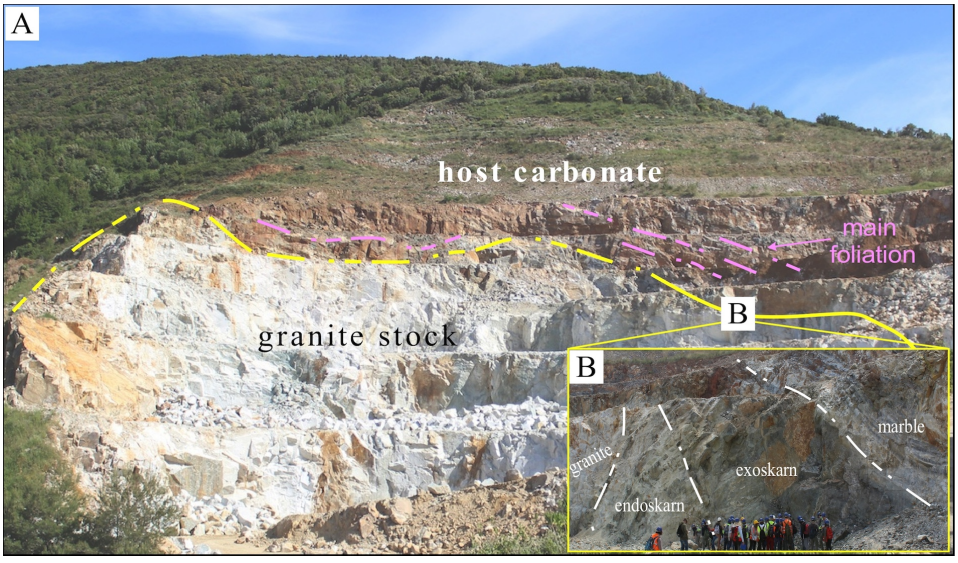

Fig. 2.5 - (A) Panoramic view of the Botro ai Marmi mine. In yellow the pluton-marble contact, and in pink the main foliation characterising the carbonate body. (B) Endoskarn and exoskarn bodies at the contact.

The Campiglia Marittima magmatic-hydrothermal system

The Campiglia Marittima area is characterised by a N-S trending horst surrounded by a Jurassic-Eocene ophiolitic sequence (Fig. 2.6). The horst, developed in the inner part of the Apennine thrust-and-fold belt as a consequence of extensional tectonics, is bounded by high-angle extensional and strike-slip faults (Acocella et al., 2000; Rossetti et al., 2000). During late Miocene, the Campiglia carbonate sequence was intruded by the Botro ai Marmi monzogranite pluton (~5.44 Ma, see chapter 7), altered by high-temperature saline fluids shortly after emplacement (Leoni and Tamponi, 1991). Mafic and felsic porphyritic dykelets crosscut the contact aureole produced by the pluton. Metasomatic products and mineralized skarn occur in close spatial association with the intrusive rocks as (i) minor metasomatic bodies (exoskarn) at the pluton-carbonate contact and as veins in the host rock, (ii) endoskarn vein in the monzogranitic body, (iii) low-grade veins and disseminations Sn-W-As-Bi ore (Venerandi-Pirri and Zuffardi, 1982), and (iv) several bodies and veins of Fe-Cu-Zn-Pb(-Ag) skarn deposit, that crop out discontinuously and occasionally surround small intrusions of mafic porphyry (Vezzoni et al., 2016). Later felsic dikes crosscut all the system. To the west of the carbonate host the early Pliocene rhyolitic extrusive complex of San Vincenzo is found (ca. 4.4 Ma, Feldstein et al., 1994).

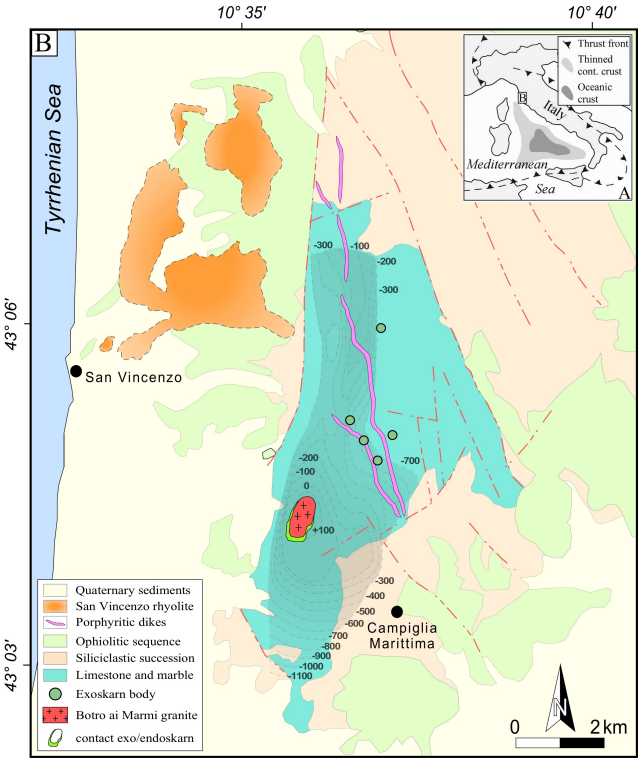

Fig. 2.6 - Schematic geological map of the Campiglia Marittima area, showing the pluton roof reconstructed by borehole log (modified after Vezzoni et al., 2016).

Botro ai Marmi granite

The Botro ai Marmi peraluminous monzogranitic pluton intruded a carbonate rock, made of white-grey marble overlain by white reef limestones and red nodular limestones (Acocella et al., 2000; Rossetti et al., 2000), generating a pervasive contact aureole (Figs. 2.6, 2.7). The granite was altered after emplacement by high-temperature fluids, resulting in proximal metasomatic bodies, both within the granite (endoskarn) and in the host carbonate (exoskarn). The primary igneous assemblage of the monzogranite consists of quartz, K-feldspar, plagioclase and biotite, along with late-magmatic tourmaline, as well as accessory cordierite, apatite and zircon. Its peraluminous feature is highlighted by the widespread occurrence of accessory cordierite and by high alumina saturation index value (ASI = 1.1-1.3). This mineral association is rarely preserved due to the hydrothermal alteration processes, resulting in the almost complete replacement of biotite and occurrence of hydrothermal calc-silicates, albite, phlogopite, HFSE/REE-bearing minerals. Metasomatism involving late-to post-magmatic hydrothermal fluids, with minor interaction with carbonate host rocks (Poli et al., 1989; Lattanzi get al., 2001), resulting in the increase of K_2O (up to 10 wt%) and loss of major elements (Rodolico, 1945; Barberi et al., 1967 and this study), which make the granite suitable for quarrying as a raw material for ceramics. This project is focused onto the granite-host rock transition, well exposed thanks to the ongoing mining activity.

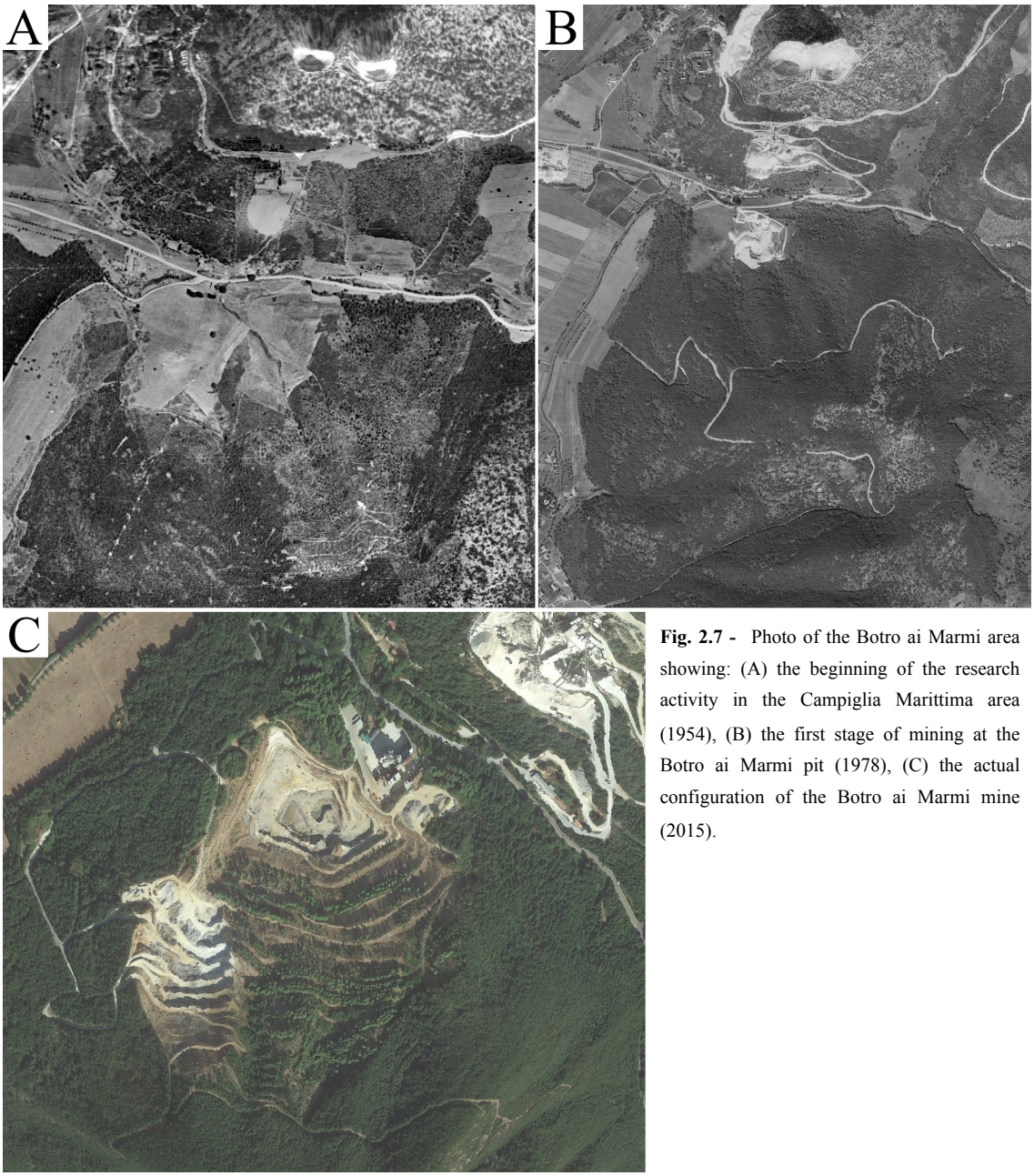

Fig. 2.7 - Photo of the Botro ai Marmi area showing: (A) the beginning of the research activity in the Campiglia Marittima area (1954), (B) the first stage of mining at the Botro ai Marmi pit (1978), (C) the actual configuration of the Botro ai Marmi mine (2015).

Mafic porphyry dykes

Mafic porphyry dykes occur as isolated sub-vertical dykelets (0.3–2 m thick and up to 30 m long) and they are found only spatially related with distal skarn bodies (Temperino mine; Vezzoni et al., 2016). These porphyritic rocks are commonly found within skarn bodies and, rarely, at the skarn marble contact (yet never intruding the marble). They vary in size from several dm^3 to several m^3 and crosscut the primary surrounding skarn as irregular masses matching their spheroidal shape. The boundaries between skarn and porphyry reveals that the mafic magma was emplaced after skarn formation. The primary paragenesis consists of phenocrysts of plagioclase, biotite, clinopyroxene, orthopyroxene, and olivine, along with abundant coarse-grained sanidine and quartz xenocrysts, all set in a fine-grained groundmass. The groundmass is completely recrystallised into a fine-grained aggregate of K-feldspar, quartz and chlorite, with mafic phenocrysts replaced by actinolite, epidote, chlorite and carbonates. The only relicts are biotite and rare clinopyroxene, as well as accessory minerals as chromite, apatite, zircon, monazite, and ilmenite (Vezzoni et al., 2016).

Felsic porphyry dykes (Coquand and Ortaccio)

The Coquand porphyry is formed by two dykes (10s m thick) cropping out discontinuously for ca. 2 km in a SE-NW direction and connecting several skarn bodies. Moreover, they crosscut both the skarn and the mafic porphyry at Temperino mine. The Ortaccio felsic porphyry dyke crops out continuously for about 8 km (thickness up to about 20 m). This dyke crosscuts the other magmatic and metasomatic rocks (Temperino skarn and mafic porphyry, as well as the Coquand felsic dikes). The two types of felsic porphyritic dykes show similar mineralogical features, with phenocrysts of quartz, sanidine (cm-size), plagioclase, biotite and cordierite (pinitised) set in a fine-grained groundmass completely recrystallised in K-feldspar, quartz and minor "chlorite". Rare mafic enclaves up to 10 cm in size are also present (Vezzoni et al., 2016).

San Vincenzo rhyolite

The San Vincenzo rhyolite represents the closing igneous event of the late acidic activity in the Campiglia system (ca. 4.4 Ma, Feldstein et al., 1994). The rhyolites cover an area of about 10 km^2 and they were emplaced as a viscous lava flow/dome to the west of the Campiglia horst. The rhyolite is characterised by a porphyritic texture with antecrysts of quartz, K-feldspar, plagioclase, biotite, along with lesser amounts of cordierite, as well as accessory apatite, monazite, zircon, ilmenite, and epidote (Ferrara et al., 1989; Ridolfi et al., 2016). Rare small mafic enclaves and clinopyroxene xenocrysts are also present.

3. Magmatic-hydrothermal systems and metasomatic processes

Heat-flux events, such as igneous intrusions emplaced into cold crustal rocks, will result not only in release of heat to the surrounding environment, but also in the transport of volatile components, which are responsible for metasomatic processes. Some of the most significant effects of these processes are fenitisation (K- and Na-metasomatism), skarns generation (Ca-metasomatism) and tourmalinisation (B-metasomatism) (Table 3.1, Pirajno, 2013).

A metamorphic process involves changes in the mineral content/composition and microstructure of a rock, dominantly in the solid state, up to partial melting, and may also involve minor changes in the chemical composition of the rock (mostly in volatile components). This process is controlled by the different physico-chemical conditions between the rock and its host. Indeed, metasomatism and metamorphism of silicate rocks are tightly correlated. Mass transfer, controlled by fluid-rock interaction, and the related mineral re-equilibration/replacement are the distinctive features of a metasomatic process. Fluid-rock interaction is controlled by the rock porosity and the chemical reactivity of a fluid. Minerals replacement (e.g. crystallization of calc-silicate, oxide, sulphide, and a variety of accessory minerals) due to the fluid-rock interaction occur as the result of a coupled metasomatic alteration and re-precipitation process. Fluid flow through the rock could results in chemical zoning (e.g. patchy zoning), partial to complete mineral replacement, reaction textures (e.g. pseudomorph), trails of fluid inclusions. Moreover, the dating of hydrothermal accessory minerals (i.e. zircon, titanite, xenotime, monazite, apatite) can give informations about the timing and chemistry of the fluid-rock interactions. Metasomatism is distinct from other endogenic processes by (e.g. Zharikov et al., 1998):

(i) the element substitutions in minerals by mechanisms involving synchronous metasomatic alteration and precipitation of new minerals, maintaining a constant volume (Lindgren's rule, 1925) during metasomatism (i.e., pseudomorphic replacement, solid-state solutions of metasomatic minerals preserving the former shape and volume);

(ii) processes including the infilling of cavities or cracks, magma crystallization, and fluid-rock interactions, by the preservation of the solid state of rocks during replacement (the volume of infilling solution is negligible in comparison with the whole rock volume);

(iii) isochemical metamorphism by substantial changes in the chemical composition by either the addition or subtraction of major elements other than H_2O and CO_2. Changes in water and/or carbon dioxide content are allowed in isochemical metamorphism, thus hydration/dehydration or carbonation/decarbonation reactions are not specific of metasomatism. Only H_2O and CO_2 are perfectly mobile during metamorphic processes, whereas during metasomatic reactions other rock- or ore-forming components may become perfectly mobile (HFSE, REE, major elements). The number of coexisting minerals in metasomatic zones is usually less than in the replaced rock unless the former rock was monomineralic,

(iv) metasomatism generating a regular set of zones, characterised by a typical metasomatic pattern. This zonal pattern represents chemical exchange between two rocks or between a rock and a circulating fluid. A metasomatic zone pattern is the complete sequence of metasomatic zones characterizing an individual metasomatic body.

(v) focused fluids in the crust are involved in metamorphic, magmatic, hydrothermal, and ore body formation processes. "High level" fluids could exploit the existing fracture network or generate new fractures, whereas porosity waves could provide a mechanism for temporal focusing of metamorphic fluid fluxes with the potential to increase the efficacy of heat and mass transport (Connolly, 1997). Hydrothermal veins are the best indicators of hydrothermal fluid flow. During contact metamorphism, once fluids are released from magma and wall rocks, thermal-chemical buoyancy and deformation of rocks interact to allow fluid circulation (e.g. Mazzarini et al., 2014; and reference therein). Textural variations and morphology of vein crystals provide some valuable informations on the nature of the hydrothermal system from which the veins were sourced. The simplest hydrothermal deposit to

visualise is a vein, which forms when a hydrothermal solution flows through an open fracture. Metasomatic veins commonly occur close or at the top of intrusive igneous rocks because their igneous rocks serve as heat sources that create convective flows of circulating fluids. Minerals precipitation is usually caused by cooling of the hydrothermal solution, or by chemical reactions between the fluids and rocks lining the fissure. Much of the hydrothermal mineral systems that are associated with igneous intrusions are primarily characterised by vein systems that are spatially and genetically associated with these intrusions.

Metasomatic alteration takes place because the mineral assemblages in the wall rocks are in physico-chemical disequilibrium with the hydrothermal fluids, and tend to re-equilibrate by forming new mineral assemblages that are stable under the new conditions. A mineral assemblage refers to a group of minerals that formed more or less at the same time and are stable together. A mineral assemblage essentially defines the physico-chemical conditions of the system. A mineral association, on the other hand, is a group of minerals that occurs together, but are not necessarily in equilibrium and did not form at the same time (e.g. Seedorff et al. 2005).

Table 1.3 Main representative examples of metasomatic processes

Type and general direction of increasing temperature		Minerals; reactions	Enrichment	Depletion
Carbonate		Calcite: $CaCO_3$ Ankerite: $Ca(Fe, Mg, Mn)(CO_3)_2$ Dolomite: $CaMg(CO_3)_2$ Magnesite: $MgCO_3$ Siderite: $FeCO_3$	CO_2, Fe	SiO_2, Al, Na, K
Fluorite and topaz alteration		CaF_2 $Al_2(SiO_4)(F,OH)_2$	F	SiO_2
Steatitisation		Talc: $Mg_3(OH_2)(Si_2O_5)_2$	SiO_2, H_2O	
Rodingite		Diopside, grossular garnet, vesuvianite	CaO_2	SiO_2, Na_2O
Silicification		Secondary quartz, chalcedony, chert, opal	SiO_2	Mg, Ca, Fe, Mn, CO_2
Tourmaline		$XY_3Al_6(BO_3)_3(Si_8O_{18})(OH)_4$ X = Na, Ca; Y = Al, Fe, Li, Mg	Al, Mg, Ca, Fe, Na, Li, B, H_2O	SiO_2, CO_2
Listvenite		Serpentine => talc => Fe, Mg carbonates, quartz, albite, Cr-muscovite, ± sulphides	Ca, K, Na, CO_2, S, As	SiO_2, Mg, Fe, Cr, H_2O
Skarn		(i) PROGRADE STAGE: e.g. Ca-skarn garnet, pyroxene, (±scheelite, sulphides)	SiO_2, Mg, Fe, S, As, B, f, Cl, W, Mo, P, Be, Sn	Ca, CO_2
		(ii) RETROGRADE STAGE: amphiboles, scapolite, epidote, vesuvianite, sulphides, carbonate	S, H_2O, Cu, Fe	Cl
Potassic alteration	Biotite	$K(Mg,Fe)_3[(OH)_2(Al,Fe)Si_3O_{10}]$	SiO_2, Al, Mg, Fe, K, H_2O	
	Feldspar	Microcline, Adularia: $K(AlSi_3O_8)$	Al, K	
Albitisation of K-feldspar (ion-exchange)		$K(Al_2Si_3O_8) + Na^+ => Na(AlSi_3O_8) + K^+$	Na	K
Greisen		Fluorite, topaz, quartz, sericite, muscovite (phengite), tourmaline, albite	SiO_2, S, Cl, Be, B, Li, F, W, Sn	

Volatile role in metasomatic processes

The role of volatiles in granitic melts is two-fold. First of all, they modify the physico-chemical behaviour of the fluids and its crystallization products, additionally, as the result of the volatiles tendency to partition into the residual fluid phases, they play a key role in the complexing and transporting of major and trace elements. The addition of volatiles (i.e. B, F, Cl, H_2O) to a mineral assemblage undergoing high-grade metamorphism lowers the temperature of the assemblage.

Both F and Cl produce distortion of the silicate-structure, allowing to accommodate in the minerals structure other elements such as Ni, Co, V, Cr, etc. Fractionation processes enhance the concentration in the residual melts of volatiles and incompatible elements, such as Sn, W, Mo, Th, U, Zr, Ta, Nb, Hf, as well as minor Cu, Zn, Pb. Thus the increase in volatiles not only depolymerises the melt but also provides ligands for complexing trace elements (e.g. Pirajno, 2009). Moreover, the key to observed REE mobilisation was mostly the formation of chloride complexes ($REECl^{2+}$, $REECl^{+2}$), whereas the mobility of Zr depended on the formation of hydroxy fluoride complexes such as $ZrF(OH)_3$ and $ZrF_2(OH)_2$ (Gysi and Williams-Jones, 2013; Migdisov et al., 2009, 2011). The formation of hydroxy fluoride complexes is favoured by high pH, while the transport as Cl-complexes is typically favoured by low pH. Changing temperature also affects metal mobility by promoting dissolution of minerals. Usually solubility of minerals increases with increasing

temperature (including REE-bearing minerals), whereas for some minerals, such as zircon, the solubility increases with decreasing temperature (Migdisov et al., 2011; Gysi and Williams-Jones, 2015). In addition, temperature affects the relative mobility of the LREE and HREE, with the former being more mobile at high temperature and the latter at low temperature (Gysi and Williams-Jones, 2013). This is due to the increased stability of LREE chloride complexes with increasing temperature (Migdisov et al., 2009).

Metasomatic processes

Magmatic-hydrothermal systems are often accompanied by extensive aureoles of metasomatic alteration in the surrounding country rocks and provide a clear demonstration of fluid activity in the crust. Among the most extreme examples of chemical interaction between infiltrating hydrothermal fluids and rocks there are zones of acid metasomatism (Fig. 3.1, e.g. Pirajno, 2009). Metasomatic alteration can take place under magmatic subsolidus conditions (e.g. infiltration of supercritical fluids), or at lower temperature. Essentially, circulating fluids chemically attack the mineral constituents of the wall rocks, which tend to re-equilibrate by forming new mineral assemblages in equilibrium with the new conditions. During these processes occurs a chemical exchange between the fluids and the wall-rocks, which is controlled by the nature of wall rocks (e.g. permeability), the composition of fluids (e.g. K/Na, Ca, F, Cl, CO_2, H_2O), the temperature and pH. Several metasomatic processes may be distinguished by composition and alteration effects produced on the wall-rock (e.g. Pirajno, 2009; Zarikov et al., 1998; Harlov and Austrheim, 2013).

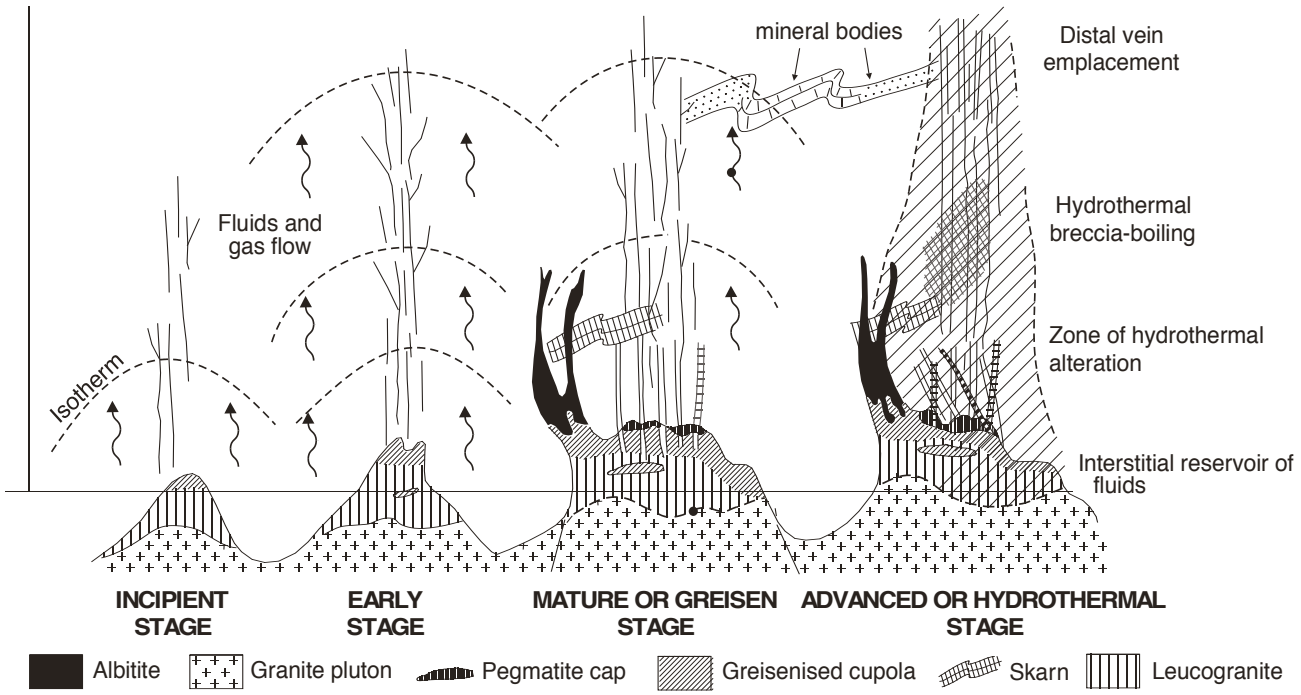

Fig. 3.1- Conceptual genetic model illustrating the different styles of intrusion-related greisen deposits (modified after Pirajno, 2009). Volatile-rich granitic cupola-like intrusions are emplaced in siliciclastic and carbonate metasedimentary rocks. Albitisation and pegmatitic caps develop as a result of fractionation and alkali-metasomatism at and near the upper portions of a cupola. Stages of degassing and fluid evolution range from incipient to advanced, from left to right in the figure, resulting in different levels of mineralisation-alteration.

Alkali metasomatism

Autometasomatism, which usually occurs at the top of a magmatic body (Figs 3.1, 3.2) during the early post-magmatic stage, is mainly characterised by alkali metasomatic processes, such as albitisation in granitic plutons. The alkali metasomatism comprises (i) Na-metasomatism with albitisation of the granite, in which primary K-feldspar was replaced by albite, and (ii) K metasomatism (potassic metasomatism), in which albite was replaced by K-feldspar. These processes can be described by the reaction:

$$(Kfs)\ KAlSi_3O_8 + Na^+ \leftrightarrow (Ab)\ NaAlSi_3O_8 + K^+$$

This reaction is controlled by the overall solubility, that increases with increasing temperature and chlorine content. The right-hand side of reaction (formation of albite) would be favoured at higher temperatures, and the left-hand of this reaction (formation of K-feldspar) at lower temperatures. Moreover, increasing volatile content during crystallisation enhance Ab content, while the fluid phase is enriched in K (decreasing Na/K in the fluid phase), resulting in transfer of K from fluid to the wall rocks. At the contrary, when volatiles are lost from the system, the residual melt becomes enriched in K, while Na is transferred to the fluid phase. K-feldspar crystallizes and Na in the fluid is transferred to the wall rocks. The evolution of an alkali-rich residual fluid phase from a nearly consolidated igneous body results in a series of post-magmatic and subsolidus growth of minerals (Bowden, 1985).

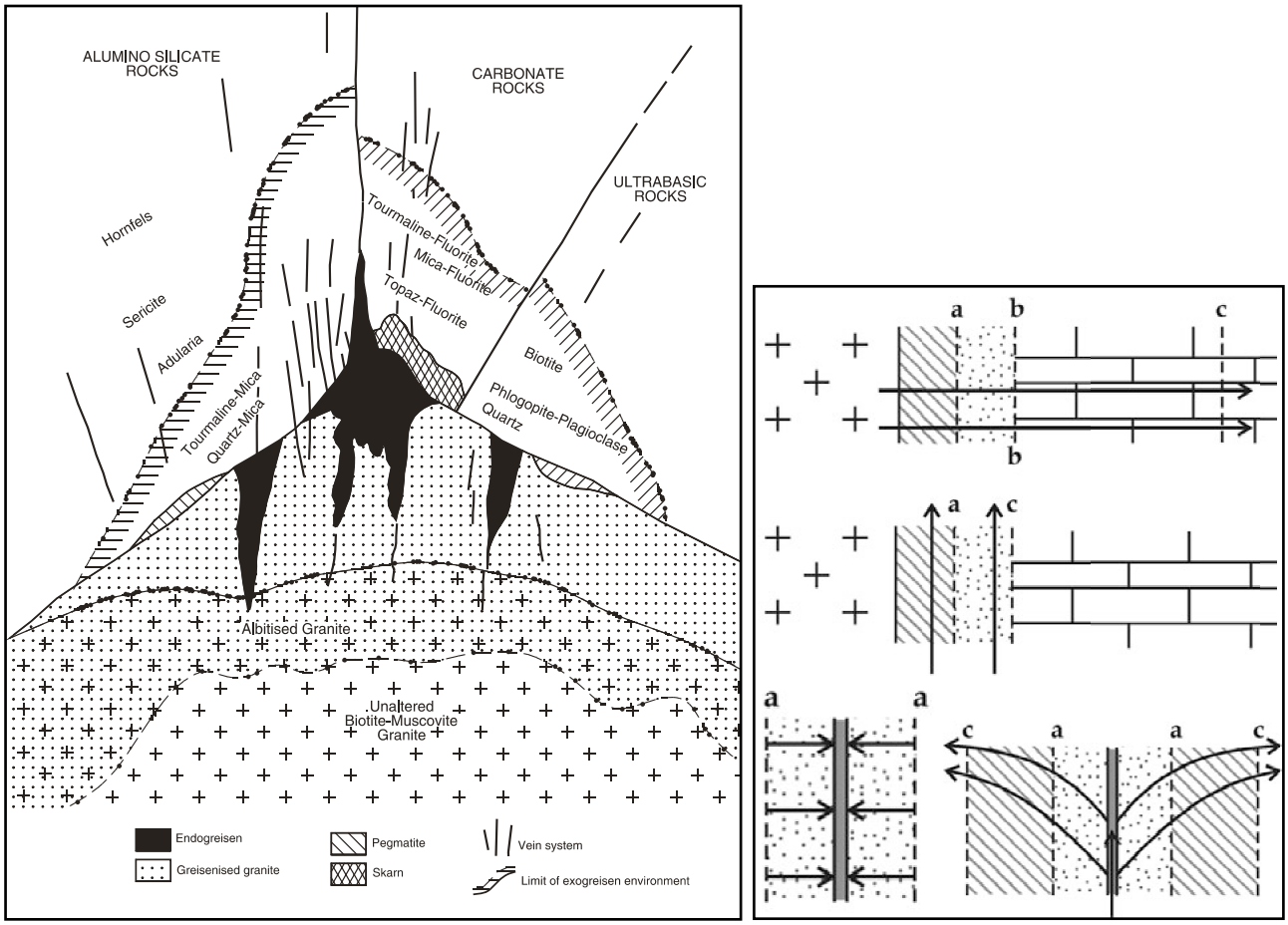

Fig. 3.2- (a) Genetic model for endo- and exoskarn systems in aluminosilicate, carbonate and ultramafic rocks. After; the endoskarn may have unidirectional solidification textures (after Pirajno et al., 2009; and reference therein). (b) series of possible relationships between contacts, mineralogical fronts (a,b), an oxygen isotope front (c) and fluid flow and/or diffusion (arrows). Lithologies are granite (crosses), marble (brick symbol), quartz veins (dark stipple), metasomatic zones (light stipple and hatching), and sandstone (coarse dots) (after Rubenhac, 2013).

In a peraluminous granites, sodic metasomatism can generate textural and colour changes. Growth of new micas, such as siderophyllite, also may occur (e.g. Pirajno, 2009). Geochemically, the rock is enriched in Nb, Zr, U, Th and minor REE. Colour changes are also related to replacement of K in perthite by Na, which leads to the development of albite. Albitisation is followed by incipient H^+ metasomatism, usually characterised by the growth of sericite and varying amounts of fluorite and topaz. Experimental work on silicate systems and fluid inclusion studies of quartz ascribes to sodic metasomatism a range of temperatures between 400 and 600°C at pressures of 1 kbar or less (Pollard, 1983).

K-metasomatism

Potassic metasomatism commonly occurs at high temperatures, and is mostly important in porphyry and epithermal mineralizing systems. This process is typically represented by the replacement of albitic plagioclase by microcline or orthoclase. Other products of K for Na exchange reactions include the growth of new micas (annite, Fe-rich phlogopite), amphibole, with compositions characteristic of Fe^{2+}-rich members (ferroedenite and ferroactinolite), and adularia, mostly in epithermal systems (Bowden, 1985). Potassic metasomatism is usually accompanied by sulphide formation (chalcopyrite, pyrite, molybdenite). Anhydrite is a common associated mineral in porphyry environments. Biotite is often green in colour and Fe-rich. Potassium silicate metasomatism leads to replacement of plagioclase and mafic silicate minerals, at temperatures between 600–450°C. Common assemblages are K-feldspar-biotite-quartz, K-feldspar-chlorite, K-feldspar-biotite-magnetite, accompanied by variable amounts of other minerals such as albite, sericite, anhydrite, apatite, and also occasionally rutile, derived from the breakdown of biotite (e.g. Pirajno, 2009). Moreover, Bowden et al. (1984) stated that K-metasomatism may post-date Na-metasomatism, which is generally confined to fractures in the roof zones of granitic plutons, and is related to the early stages of vapour separation. K-metasomatism generally results in significant enrichment in K_2O, Rb, Ba, Pb, and Sb, along with depletion in Na_2O, CaO, and Sr. The lack of significant deviation for TiO_2 and Al_2O_3 indicates no significant mass loss or gain in the rock. Elements such as K_2O and Rb appear to be controlled primarily by the stability of the metasomatic assemblage produced upon plagioclase dissolution. In contrast, Na_2O and Sr are depleted as a result of plagioclase instability and are removed from the system upon metasomatic processes (Ennis et al., 2000).

Acidic metasomatism

The acidic metasomatism (Korzhinskii, 1953; Hemley and Jones, 1964) is a process that generates a wide variety of metasomatic assemblages characterised by a general mobilisation of elements such as Fe, Mg and Ca, along with alkaline elements (K and Na), coupled with increasing of total acidity of the rock by addition of halogen-rich fluids.

Ca-metasomatism

The metasomatic processes occurring near to the contact between a magmatic body and the host rock may be linked to various stages of the magmatic evolution. Endoskarn zones develop by replacement of the magmatic rocks and exoskarn zones are formed by replacement of the host rocks. These processes, occurring at high temperatures (350-550 °C), usually affect the contact of magma with a carbonatic host rock and, less commonly Ca-rich silicate rocks. When occurring at the contact with a carbonatic host, Ca-rich fluid released from the host mainly trigger Ca-metasomatic alteration, involving isochemical contact heat transfer, fluids and metals release from a cooling plutonic body to the surrounding wall rocks. These systems are typically zoned in response to temperature variations and fluid evolution. The main representative metasomatic minerals are Ca-Mg-Fe-silicates (e.g. pyroxene, garnet, titanite, epidote, vesuvianite, phlogopite, etc.). Exo- and endoskarns can form high aspect ratio bodies along the contact (contact skarns) or occur as veins, pipes, etc. crosscutting the carbonate and/or the silicate rocks (vein skarns). Although many skarn minerals are typical rock-forming minerals, some are less abundant and most have compositional variations that can

yield some significant informations about the environment of formation. Some minerals, such as quartz and calcite, are present in almost all skarns. Other minerals, like phlogopite, are typical of magnesian skarns (Mg-rich protolith), but are absent from most of other skarn type (e.g., Aleksandrov et al., 2000). During this stage, increasing acidity (H^+, F, Cl abundance) may trigger the mobilisation of HFSE and REE to produce Ca-bearing REE-HFSE minerals (Salvi and Williams-Jones, 1997; and reference therein). At this point, temperature variation controls the occurring metasomatic reaction (decreasing temperature increases the dissociation of acids and thus the supply of H^+). Indeed, high temperature Ca-rich fluids could generate calc-silicates crystallization post-dated by low temperature F-metasomatic alteration, able to mobilise greater amount of trace elements (e.g. HFSE, REE, etc.). Changing temperature also affects metal mobility by promoting dissolution of minerals (e.g., Gysi et al., 2016).

Ca-Cl-F-metasomatism

Acidic-metamorphism, which involved low-pH F-Cl-fluids, produces complex metasomatic assemblages, which vary with temperature and the extent of the rock buffered pH. Acidic F-Cl-rich fluids (low activity of alkalis) reacting with granitic rocks are typical of greisenization processes, with formation of quartz and quartz-topaz greisens as well as fluorite and F-bearing micas (e.g. Burt, 1981).

During high-temperature acidic metasomatism, fluorite is more soluble, and permits a closed-system with calc-silicates formation in the system (Gysi et al., 2016). The release of F, the metasomatic alteration (mainly chloritization) of biotite as well as other magmatic minerals (Pirajno, 2009), and the protracted Ca-segregation (calc-silicate crystallisation) lead to a selective enrichment of the metasomatic fluid in HF. These acidic fluids promote, in addition to leaching of major minerals, the selective alteration of accessory minerals (e.g., monazite, apatite, zircon). Phosphates are more easily mobilised with respect to zircons or other HFSE-silicates.

At this point, the formation of chloride complexes promotes the mobilisation of ($REECl^{2+}$), whereas the mobility of HFSE mostly depends on the formation of hydroxy fluoride complexes such as $ZrF(OH)_3$ and $ZrF_2(OH)_2$ (Gysi and Williams-Jones, 2013; Migdisov et al., 2009, 2011). This processes are supported by low pH, decreasing temperature (it increases the dissociation of acids, supplying of H^+ circulation), and the degree of fluid-rock interaction. Changing temperature also affects metal mobility by promoting dissolution of minerals. Usually, the solubility of minerals increases with increasing temperature (including REE-bearing minerals), whereas for some minerals, such as zircon, the solubility increases with decreasing temperature (Migdisov et al., 2011; Gysi and Williams-Jones, 2015). In addition, temperature affects the relative mobility of the LREE and HREE, with the former being more mobile at high temperature and the latter at low temperature (Gysi and Williams-Jones, 2013). This is due to the increased stability of LREE chloride complexes with increasing temperature (Migdisov et al., 2009). Thus, decreasing temperature would explain the mobilisation of these elements and the pseudomorphic replacement of calc-silicates crystallised during an earlier stage. Indeed, the presence of Ca would inhibit the mobilisation of Zr by destabilising Zr hydroxy fluoride species, together with the release of cations such as Al^{3+}, during metasomatic alteration of minerals like feldspar, which may lead to the formation of complexes like AlF^{+2}. On the other hand, AlF^{+2} will break down in very acidic conditions, releasing F^- in concentrations sufficient to promote accessory Zr solubility as hydroxy fluoride complexes (Gysi and Williams-Jones, 2013). The results of this process is the diffuse crystallization of REE-bearing minerals, as well as the pseudomorphic replacement and/or patch zoning of REE-HFSE-rich calc-silicates. With decreasing temperature, HFSE-REE may be remobilised by dissolution of these calc-silicate, due to increasing activity of acidic fluids, and generate a late crystallization of HFSE-REE-bearing minerals (Cl-F-metasomatism), also in late fluorite-sulphides-quartz veins. However, the paucity of thermodynamic data for REE minerals and REE aqueous species is an important limitation on the reliable evaluation of the mobility of REE and associated metals. Moreover, REE mobility was controlled by stability of accessory minerals (e.g. zircon, apatite, monazite, allanite, etc.), for which there are very poor, if any, thermodynamic data.

Finally, the activity of acidic fluids may also give rise to phyllitic metasomatic textures with late-stage replacement of silicate minerals (i.e., K-feldspar±cordierite±calc-silicates±phyllosilicates) by K, Fe, and Al phyllosilicates. Phyllitic metasomatism is generally marked along fractures in the granite or at the pluton/host contact, where it is extensive (e.g. Gysi et al., 2016).

Sulphide mobilisation

As pointed out by experiments, during acidic and alkalic metasomatism of granites it is possible to observe ore metal deposition, showing differences in the migration properties of rare metals (e.g. W, Mo and Sn) distinctly controlled by composition of the leaching hydrothermal solution. The release of F, together with the alteration (mainly chloritisation) of the biotites at depth, would result in the leaching of metals and their complexing with F and subsequent transport upward in the evolving system (Pirajno, 2009). Two classes of complexes are important for the transport of ore metals in hydrothermal solution, sulphide (HS^- and H_2S) and chloride (Cl^-). Both these complexes are capable of transporting large quantities of metals in natural aqueous systems. With sulphide complexing, however, the concentration of reduced sulphur atoms in solution must be far greater than that of the metals if the complexes are to remain stable (Krauskopf 1979; Skinner 1979). It follows that loss of H_2S caused, for example, by boiling, cooling, oxidation or sulphide precipitation will result in an increase in pH, decrease in HS activity, and subsequent precipitation of sulphides and other metals, if they are present in sufficient quantities.

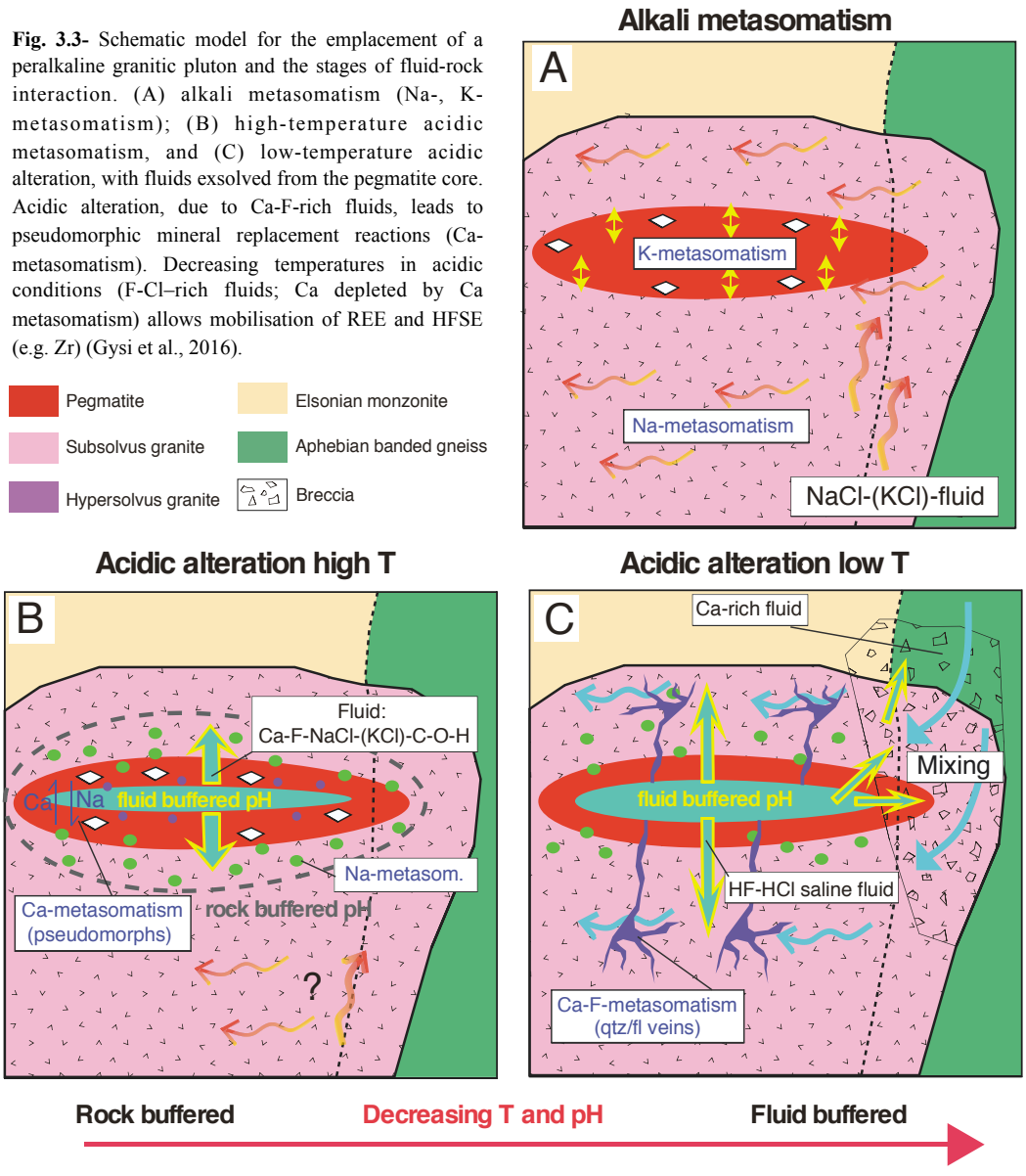

Fig. 3.3- Schematic model for the emplacement of a peralkaline granitic pluton and the stages of fluid-rock interaction. (A) alkali metasomatism (Na-, K-metasomatism); (B) high-temperature acidic metasomatism, and (C) low-temperature acidic alteration, with fluids exsolved from the pegmatite core. Acidic alteration, due to Ca-F-rich fluids, leads to pseudomorphic mineral replacement reactions (Ca-metasomatism). Decreasing temperatures in acidic conditions (F-Cl–rich fluids; Ca depleted by Ca metasomatism) allows mobilisation of REE and HFSE (e.g. Zr) (Gysi et al., 2016).

4. Analytical Methods

Samples were collected from the upper, central and lower portion of the outcropping Botro ai Marmi granite, as well as the overlying and surrounding marble. Imaging and semi-quantitative mineral identification, major and trace element analysis of bulk-rock, were carried out in the lab of the Earth Science department of Pisa. Trace element analysis of selected samples were carried by acid dilution of bulk-rock and analysis with a Nexion 300X ICP mass spectrometer.

Petrogeochemical analysis

Scanning electron microscopy (SEM-EDS)

Minerals paragenesis was reconstructed from textural relationship involving the different minerals, using a combination of optical microscopy, and scanning electron microscopy. Several polished sections were investigated using a Philips XL 30 Scanning Electron Microscope (SEM) equipped with solid state back-scattered electron (BSE) and energy dispersive spectroscopic (EDS) detectors (EDAX PV 9900). Some minerals were identified from semi-quantitative EDS analysis.

Electron microprobe (EMP)

Selected minerals were analysed quantitatively (Si, Ti, Al, Fe, V, Mn, Mg, Ca, Na, K, F, Nb, La, Ce, Sm, Nd) using a JEOL JXA 8200 electron microprobe equipped with five wavelength dispersive spectrometers (WDS) and a PulseTor Maxim EDS detector (University of Milan). Analysis were performed at 15 kV, with a 30 nA beam current and a beam diameter of 5 µm. Natural and synthetic minerals were used as standards. All standards were calibrated within 0.5 % at one standard deviation. Raw data were corrected using a Phi–Rho–Z quantitative analysis program. Representative WDS analysis of mineral phases are reported in the Supplementary Material. Owing to the small crystal size, it was not possible to use the electron microprobe to quantitatively analyse all the phases. Some minerals were identified from element maps and semi-quantitative EDS analysis using the SEM.

X-Ray fluorescence

Major elements (Na, Mg, Al, Si, P, K, Ca, Ti, Mn, Fe) analysis of selected samples were performed via X-ray fluorescence (XRF), using fused glass discs prepared by mixing 0.875 g of powdered rock samples with 6,125 g of lithium tetra-borate. The method was calibrated on twenty two international rock standards and twelve additional samples prepared by mixing available standards. The margin of error was calculated to be between 4-7%, 2-4% and about 1% respectively for abundances ranging from 0 to 1%, 1 to 10% and 10 to 65%. Overall, the analytical data obtained via the proposed method are superior to those acquired by processing briquette rock samples and comparable to those obtained using powdered rock samples dissolved in a lithium borate glass (Franzini et al., 1976; Tamponi et al., 2002).

QEMSCAN

Automated mineral analysis and textural imaging of the studied samples were performed using an FEI QEMSCAN® Quanta 650F facility at the Department of Earth Sciences, University of Geneva, Switzerland. The system is equipped with two Bruker QUANTAX light-element energy dispersive X-ray spectrometer (EDS) detectors. Analysis were conducted at high vacuum, accelerating voltage of 25 kV, and a beam current of 10 nA on carbon-coated polished thin sections. FieldImage operating mode (Pirrie et al., 2004) was used for analysis. About 221 individual fields were measured per sample, with 1500 pixels per field, and point spacing of 5 µm. The standard 1000 counts per point were acquired, thus yielding a limit of detection of approximately 2wt% per element for mineral classifications and X-ray elemental maps. Measurements were performed using iMeasure v5.3.2 software and data processing using

iDiscover® v5.3.2 software package. Final results consist of: i) high-quality spatially resolved and fully quantified mineralogical maps; ii) BSE images with identical resolution as the mineralogical maps; iii) X-ray element distribution maps.

Bulk-rock ID-ICP-MS

For each sample, about 50 mg of powders were dissolved by acid dissolution (HF + HNO_3). The powders were transferred into 20ml Savilex vials with 4ml HF + 1ml HNO_3 and evaporated at 190° for about 24h, and then re-dissolved overnight in closed vials with 4ml HF + 1ml HNO_3. After adding 1ml HNO_3, samples were dried down again at 190° and redissolved in 2ml HNO_3. After evaporation the residue were dissolved again in 3ml 3N HNO_3. After appropriate dilution with ultrapure water (Millipore Milli-Q, > 18.2 MOhm cm), the sample solutions were analyzed for Sc, V, Cr, Co, Ni, Cu, Zn (kinetic energy discrimination mode; cell gas = 3.7 ml/min He) and Li, Be, Ga, Rb, Sr, Y, Zr, Nb, Mo, Ag, Sn, Sb, Cs, Ba, REE, Hf, Ta, W, Tl, Pb, Bi, Th, U (standard mode), with a A 20 ng/ml solution of Rh and Re (internal standards) was mixed on-line with the sample solution just before reaching the nebuliser. The instrument was calibrated with the BE-N rock international standard. The detection limit in µg/L is < 0.0001 for Li, Co, Cu, Rb, Sr, Y, Zr, Nb, Sb, Cs, Ba, REE, Hf, Ta, W, Tl, Pb, Th, U, and < 0.001 for Be, Sc, V, Cr, Ni, Zn, Ge, Mo, Ag, Sn.

Laser Ablation Inductive Coupled Plasma Mass Spectrometer (LA-ICP-MS) - trace elements analysis

A Thermo Scientific iCAP-Q ICP-QMS coupled with a Photon Machine G2 193nm excimer Laser Ablation system, at the University of Perugia, was used for high spatial resolution trace element determination (Li, Be, Sc, V, Cr, Mn, Co, Ni, Cu, Zn, Ga, Rb, Sr, Y, Zr, Nb, Sn, Sb, Cs, Ba, REE, Hf, Ta, Pb, Bi, Th, U) of selected minerals, both from thin-thin section and separated minerals mounted in epoxy. The laser system is characterised by a maximum stabilised energy output of 12 mJ with fluctuations, expressed as relative standard deviation (RSD), below 2%. The pulse duration was <4 ns and the irradiance on the sample surface could be adjusted up to about 4 GW/cm2. Frequencies could be varied from 1 Hz to 300 Hz. The beam delivery apparatus was contained in a fully N2- purged optical path to prevent formation of ozone and concomitant energy loss on the target. A rotating beam homogeniser improved the homogeneity of the laser beam through its surface; a fast-change mask varied the shape and dimension of the laser beam on the sample surface.

LA-ICP-MS operating conditions were optimised before the analytical session on a continuous ablation of NIST SRM 612 reference material glass in order to provide the maximum signal intensities and stabilities for the ions of interest while suppressing oxides formation. The stability of the system was evaluated on ^{139}La, ^{208}Pb, ^{232}Th and ^{238}U by a short-term stability test, consisting of 5 acquisitions (one minute each) on a linear scan of NIST SRM 612 reference material glass. The analytical protocol for high spatial resolution trace element determination consisted in the analysis of 10–15 unknown samples bracket by four acquisitions of the NIST SRM 610 reference material. The diameter of the laser beam was varied between 50 and 20 µm for the unknown samples whereas the reference material was always analyzed at a beam size of 20 µm in order to improve the counting statistics on calibration analysis (Petrelli et al., 2007).

Data reduction was performed using the protocol reported in Longerich et al. (1996). ^{42}Ca, ^{29}Si and ^{47}Ti were used as internal standards. Major elements on unknown samples were analyzed with an Electron Probe Micro-Analyzer (hereafter EPMA). LLDs calculated following Longerich et al. (1996) for selected elements vary between 0.006-2 µg/g, at laser beam diameters of 15 µm, relative to the USGS BCR2G reference material at 8 Hz and 4.5 J/cm^2 (Petrelli et al., 2016). LLDs are of the same magnitude of those reported by Tiepolo et al. (2003) and Pearce et al. (2011) using a sector field ICP-MS coupled with a solid state 213 nm and an Excimer 193 nm laser ablation system, respectively.

U-Pb dating by CA-ID-TIMS and LA-ICP-MS

CA-ID-TIMS

Zircon separation and concentration methods - All samples (3-10 kg) were crushed with Jaw crusher and disk mill at University of Pisa (Italy). Zircon grains were concentrated by standard methods using a Wilfley table, Franz electromagnetic separator and heavy liquid separation with methylene iodide (ρ = 3.32 g cm^{-3}). Prior to U-Th-Pb CA-ID-TIMS dating zircon grains from all samples were mounted in epoxy resin, polished, and imaged by cathodoluminescence (CL) and back scattered electrons (BSE). The analytical protocol of dating the single zircon grains is similar to the one described in Schoene et al. (2010) and Wotzlaw et al. (2012). All U-Th-Pb analysis were performed using the CA-ID-TIMS method at the University of Geneva.

Chemical abrasion and chemistry - After imaging single zircon grains were extracted from the epoxy resin, washed in water and individually annealed at 900°C for 48 h in quartz crucibles in muffle furnace. Subsequently, individual zircon grains were transferred into 3ml screw-top Savillex vials with 3N HNO_3 and ultrasonically cleaned twice for about 15 min each time. In order to minimize the effects of secondary lead loss each individual zircon grain was placed into pre-cleaned Savillex capsule and chemically abraded in HF + trace HNO_3 at 180°C for 15 h in Parr bombs (Mattinson, 2005). After the partial dissolution step, each zircon together with the leachate was again transferred into 3ml screw-top Savillex vial. The leachate was completely pipetted out and the remaining zircons were rinsed in ultrapure water and then fluxed for several hours in 6N HCl on a hotplate at a temperature of ca. 80C. After removal of the acid, the zircons were again rinsed several times in ultra-pure water and 3N HNO_3 in an ultrasonic bath. The weight of each single zircon grain was estimated by the measurements of the crystal dimensions and using ρ=4.714 $g.cm^{-3}$. Each single zircon grain was loaded for dissolution into pre-cleaned Savillex capsules, spiked with 12-20 mg of the EARTHTIME ^{202}Pb-^{205}Pb-^{233}U-^{235}U tracer solution (ET 2535, http://www.earthtime.org/) and dissolved in 70 µl HF and traces of HNO_3 at 210 °C for about 60h in Parr bombs. After evaporation the residue was re-dissolved overnight in 25 µl 6N HCl. Samples were then dried down again and redissolved in 80µl 3N HCl. Lead and uranium were separated by anion exchange chromatography (Krogh, 1973) in 40 µl columns using ultra-pure HCl and H2O, and finally dried down with 3 l of 0.05N H_3PO_4.

Mass-spectrometry and blank - The isotopic analysis were performed at University of Geneva on a TRITON mass spectrometer equipped with a MasCom discrete dynode electron multiplier. The linearity of the multiplier was calibrated using U500, Sr SRM987, and Pb SRM982 and SRM983 solutions. The dead-time for the SEM was determined to be constant at 23 ns for up to 1.3 Mcps and at a Faraday/SEM yield between 93–94%. During the time of the measurements isobaric interferences from $BaPO_2^+$ or Tl^+ were monitored by measuring masses 201 and 203 and masses 202, 205 in unspiked samples. Since no statistically significant signal was observed on the controlled masses no correction was applied. Lead isotopic fractionation was corrected based on the certified value of $^{202}Pb/^{205}Pb$ = 0.99924±0.03%, 1σ of the EARTHTIME ^{202}Pb-^{205}Pb-^{233}U-^{235}U tracer. The U mass fractionation for the same analysis was calculated using the ^{233}U-^{235}U ratio of the double spike solution (0.99506±0.01%, 1σ). The average Pb and U fractionation factors determined by EARTHTIME ^{202}Pb-^{205}Pb-^{233}U-^{235}U tracer were 0.13±0.02 %/amu and 0.10±0.02 %/amu (1σ) respectively. Both lead and uranium were loaded with 1 µl of silica gel–phosphoric acid mixture (modified after Gerstenberger and Haase, 1997) on outgassed single Re-filaments. Pb isotope compositions were measured on the electron multiplier, while U (as UO_2) isotopic measurements were made in static Faraday mode (using amplifiers equipped with $10^{12}\Omega$ resistors) or, in case of insufficient U beam size - on the electron multiplier. Isobaric interference of $^{233}U^{18}O^{16}O$ on $^{235}U^{16}O^{16}O$ was corrected using a $^{18}O/^{16}O$ ratio of 0.00205. The measured uranium isotopic ratios were corrected assuming a sample $^{238}U/^{235}U$ ratio of 137.818 ± 0.045 (2σ, Hiess et al., 2012). All common Pb in the zircon analysis was attributed to the procedural blank. Over the course of this study 15 total procedural blanks were

measured, yielding the following blank isotopic composition: $^{206}Pb/^{204}Pb$ = 18.30±0.71, $^{207}Pb/^{204}Pb$ = 15.47±1.03, $^{208}Pb/^{204}Pb$ = 37.60±0.97 (1σ %). U blanks are <0.1 pg and do not influence the degree of discordance at the age range of the studied samples, therefore a value of 0.05 pg ±50% was used in all data reduction.

Data reduction, reporting ages and errors - The initial statistics, data reduction and age calculation were done using the TRIPOLI and Redux software (Bowring et al., 2011). All $^{206}Pb/^{238}U$ and $^{207}Pb/^{206}Pb$ ratios were corrected for initial disequilibrium in $^{230}Th/^{238}U$ using Th/U [magma] calculated from the lattice strain model for zircon-melt partitioning of Th and U (Blundy and Wood 2003). The accuracy of the measured data was assessed by repeated analysis of the 2Ga synthetic solution (Condon et al., 2008) and international R33 standard zircon (Black et al. 2004), which was pre-treated by chemical abrasion (Mattinson, 2005). Both yielded an internal reproducibility in $^{206}Pb/^{238}U$ dates of better than 0.05%. The 2Ga synthetic solution measured with EARTHTIME ^{202}Pb-^{205}Pb-^{235}U-^{238}U tracer yielded mean $^{207}Pb/^{206}Pb$ = 1999.41±0.23/0.40/6.0 Ma (MSWD=0.74, n=23). The standard zircon R33 (Black et al. 2004) was measured with EARTHTIME ^{202}Pb-^{205}Pb-^{235}U-^{238}U tracer at an average $^{206}Pb/^{238}U$ age of 419.58±0.05 Ma (MSWD=1.5, n=22). All uncertainties reported are at the 2 sigma level, following x/y/z systematic of Schoene et al. (2006). All data are reported in the table S1 with internal errors only, including counting statistics, uncertainties in correcting for mass discrimination, and the uncertainty in the common (blank) Pb composition. The MSWD values of weighted mean from all samples are within the range of acceptable values at 95% confidence level and for n-1 degrees of freedom, defined by Wendt & Carl (1991).

LA-ICP-MS

A Thermo-Finnigan Element 2 sector field ICP-MS coupled with a 193 nm ArF Excimer Resonetics RESOlution M-50 LR laser at the University of Bergen was used to measure U/Pb and Pb/Pb isotopic ratios in the zircons. The sample introduction system was modified to enable simultaneous nebulization of the ablated solid sample and a tracer solution (Horn et al., 2000). The tracer solution consisted of natural Tl ($^{205}Tl/^{203}Tl$=2.3871; Dunstan et al., 1980), ^{209}Bi and enriched ^{233}U and ^{237}Np (>99%). The laser produced an energy density of 5-7 J/cm2 with a repetition rate of 5 Hz. The samples were placed in a Laurin two-volume sample cell mounted on a computer-driven motorized microscope stage. During ablation, the stage was moved beneath the stationary laser beam to produce a linear raster of approximately 19x60 μm. Each analysis consisted of 35 seconds background measurement of the aspirated tracer solution and the gas blank, followed by 110 seconds of measurement of U and Pb signals from the zircons together with the signal from the tracer solution. Each analysis was followed by a 45 second wash cycle.

Detrital zircons were analysed together with three zircon age standards; the 91500 (1065 Ma; Wiedenbeck et al., 1995), the GJ-1 (609 Ma; Jackson et al., 2004) and the Plešovice (337 Ma; Sláma et al., 2008) standards. The Plešovice standard was used as the primary standard to correct for instrument drift. Calibrated against the Plešovice standard, the 91500 and GJ-1 standards yielded ages of 1064±2 Ma and 604±1 Ma, respectively.

The LA-ICP-MS data have been filtered in order to provide a robust dataset. Analysis with 1σ errors of the measured isotopic ratios >10% and/or a probability of concordance <0.05 were excluded. The excluded analysis are provided in Appendix A, but have not been used for any figures, calculations or interpretations.

All detrital single-grain ages reported in this thesis are single grain concordia ages with the corresponding 2σ errors calculated by Isoplot (version 4.15; Ludwig, 1998; Ludwig, 2012). For unimodal grain distributions mean ages with 2σ standard deviations are given. Following suggestions by Vermeesch (2004) and Andersen (2005), detection limits have been calculated for all samples, giving the size of the smallest age fraction still detected with 95 % confidence (Figs. 3, 5 and 6).

5. Evolving metasomatic alteration of a peraluminous granite intruding a limestone/marble host (Campiglia Marittima, Tuscany)

Gabriele Paoli [a,*], Andrea Dini [b], Sergio Rocchi [a]

[a] *Dipartimento di Scienze della Terra, Università di Pisa, Via Santa Maria 53, 56126 Pisa, Italy*

[b] *CNR, Istituto di Geoscienze e Georisorse, Via Moruzzi 1, 56124 Pisa, Italy*

Keywords

Magmatic-hydrothermal system, fluid-rock interaction, mass balance, acidic metasomatism

Abstract

Metasomatic alteration is a complex process involving textural, mineralogical, and chemical changes, as the result of the interaction of hot aqueous fluids with the rocks through which they circulate, under evolving physicochemical conditions. Intense circulation of fluids released in subsolidus conditions by an igneous intrusion commonly occurs in contact aureoles. Fluid circulation may generate vein systems and metasomatic bodies showing intricate mutual cross-cutting relationships. At Campiglia Marittima area, the time-transgressive circulation of magmatic/metasomatic fluids generated a tangled sequence of replacement and new crystallised minerals, either in the intrusive Botro ai Marmi peraluminous monzogranite than in the limestone/marble host rocks. Field observations, mineral paragenesis, and bulk-rock chemistry suggested that the system experienced evolving conditions, generating a significant exchange of major and trace elements between granite, metasomatic fluids, and host rock. The alteration processes resulted in the metasomatic replacement of the granite (mostly along magmatic joints) and the intense replacement of the contact carbonate (pluton boundary and folded layers).

At the top of the pluton, a system of magmatic joint has been formed during the magmatic stage, contributing to the later fluids circulation. The metasomatic activity can be subdivided into (i) late magmatic stage, (ii) K-metasomatism, (iii) high temperature Ca-rich metasomatism and (iv) lower temperature acidic metasomatism. Shortly after emplacement or during a late-magmatic stage, circulation of B-rich fluid form disseminated tourmaline-quartz orbicules, which tends to be particularly abundant in zones of fracturing forming veinlets systems. Later on, high-temperature metasomatic fluid generated a pervasive K-metasomatism. The granite experienced deep metasomatic alteration of plagioclase (replaced by K-feldspar), biotite (replaced by phlogopite-chlorite-titanite), ilmenite (replaced by titanite-rutile) and apatite, with mobilisation of Fe, Na, P, Ti and minor HFSE and REE. The altered granite is enriched in Mg, K, Rb, Ba, Sr and depleted in Fe and Na. High-temperature, Ca-rich fluids led to the acidic alteration (Ca-metasomatism) of the system. This stage is characterised by the crystallization of a great variety of calc-silicates (e.g., diopside, vesuvianite, epidotes, garnet), particularly abundant at the host-granite contact (exoskarn), and along fractures into the granite (endoskarn). The granite experienced the Ca-metasomatic alteration along magmatic joint, resulting in the exchange of HFSE (e.g., Ti, Nb, Ta, Zr) and LREE with hydrothermal fluids. The mobilised elements at contact with Ca-rich fluids provoked the crystallisation of metasomatic minerals, such as phlogopite, titanite, diopside, ekanite, apatite, cheralite. Upon cooling, fluids became more acidic, with the increase of fluorine activity. The increasing acidity is supported by the widespread crystallisation of fluorite, corresponding to the textural disequilibrium of calc-silicates crystallised during the Ca-metasomatism. Thus, the formation of a metasomatic front at the pluton-host boundary, where fluids would be accumulated and pH buffered to low values as temperature decreased, provoked the increasing mobilisation of REE and HFSE and the late crystallisation of REE-HFSE minerals.

5.1. Introduction

Most large skarn deposits are associated with relatively shallow magmatic systems emplaced within or near carbonate rocks. In the simplest scenario, these deposits form by the transfer of heat, fluid, and metals from a cooling magma to the surrounding rocks, leading also to hydrothermal alteration (skarnification; Meinert et al., 2005). Metasomatic-hydrothermal alteration is a complex process involving textural, mineralogical, and chemical changes, as the result of the interaction of hot aqueous fluids with the rocks through which they circulate, under evolving physicochemical conditions. Intense circulation of fluids released in subsolidus conditions by an igneous intrusion commonly occurs in contact aureoles (Pirajno, 2009, and reference therein). Fluid circulation may generate vein systems and metasomatic bodies showing intricate mutual cross-cutting relationships. At the lowest temperature and pressure, exsolution of gas and hydrothermal fluids induce rock transformation as the result of disequilibrium generated by H^+, OH^- and other volatile constituents (e.g. B, CO_2, F, Cl). Components such as B and F are usually concentrated in evolved, late-stage magmas. This enrichment is responsible for a series of processes both in the magmatic and post-magmatic stages characterizing a magmatic-hydrothermal systems (i.e., fractionation/crystallisation, fluid phase evolution, wall-rock alteration, metal transport and deposition). Evidences for an enrichment occurred during the magmatic stage could be the crystallisation of fluorite, tourmaline, Li-mica, etc. while at the post-magmatic stage, a witness could be the development of a similar suite of hydrothermal minerals (Pollard et al., 1987). Therefore, hydrothermal fluid-rocks interaction produced a redistribution of chemical components, forming new mineral assemblages in equilibrium with the new intensive parameters. On the other hand, the fluids may change their composition as a result of the interaction with the country rocks. Thus, the main factors controlling alteration processes are the nature of the country rocks, along with the composition, concentration, activity and chemical potential of the hydrothermal fluids (e.g. H^+, HF, HCl, CO_2, K^+; Harlov and Austrheim, 2013).

Multi-stage metasomatic events can superimpose through time, generating complex mineral associations. For example, when hydrothermal fluids are channelled out of a granite in a carbonate-rich rock, mineral-fluid equilibria become much more complex due to the reactive nature of the host rock. These processes are highlighted by the frequent occurrence of mineralisations and of a wide variety of skarn/replacement deposits at the pluton-host boundary (Einaudi et al., 1981). Thus, a magmatic-hydrothermal system fed by evolving fluids (e.g., Dini et al., 2005) could produce superimposing metasomatic parageneses (e.g., Gysi et. al., 2016). Understanding the relative timing and the relationships between these events could provide crucial knowledge on generation, segregation, and transfer of magmatic-hydrothermal fluids, a fundamental process that involves element, mass and heat transfer throughout these systems. The relationships between igneous intrusions, fluid transfer and mineralization can be determined after detailed field, geochemical, petrological, and chronological investigations. Moreover, outline geometries and spatial relationships of the main geological bodies, mineralogical parageneses and mineral zoning of a magmatic-hydrothermal system is important for reconstructing the hydrothermal fluid pathways and shedding light on the processes of fluid-rock interaction (e.g. Pirajno, 2009, 2013; Harlov and Austrheim, 2013).

The Campiglia Marittima magmatic-hydrothermal system is characterised by multiple igneous events followed by multi-stage hydrothermal episodes (Vezzoni et al., 2016). The shallow-level intrusion (depth of ~4-6 km; Leoni and Tamponi, 1991) of the Botro ai Marmi monzogranite produced the thermal metamorphism and the deformation of the carbonate host-rock (Acocella et. al 2002; Rossetti et. al., 2000). These processes are highlighted by exoskarn bodies occurring as massive zones at the pluton contact or as replacement of the ductilely folded host-rock (Vezzoni et al., in revision). Moreover, calc-silicate endoskarn veins follow brittle fractures in the granite pluton to join the exoskarn. All these features are useful to detect element mobility processes between granite and metasomatic products triggered by hydrothermal fluids. In this study, a detailed textural, mineralogical and chemical investigation of the monzogranite, the

host carbonate rocks, and their hydrothermal-metasomatic alteration products, it is carried out in the field, under the optical and electron microscope, by QEMSCAN and EPMA analysis.

5.2. Geological background

The Campiglia Marittima area is characterised by a Mesozoic carbonate horst, trending N-S, confined by a Jurassic-Eocene ophiolitic/cover sequence (Fig. 5.1; Da Mommio et al., 2010). The horst, developed in the inner part of the Apennine thrust-and-fold belt as a consequence of extensional tectonics, is bounded by high-angle extensional and strike-slip faults (Vezzoni et al., in revision). In this area, a Miocenic extension produced a thinned crust (~22 km), widespread magmatism involving both crustal anatectic and mantle-derived products, and diffuse hydrothermal-metasomatic activity (Barberi et al., 1967; Dini et al., 2005; Bertini et al., 2006).

The magmatic activity started during the latest Miocene (5.442±0.012 Ma; Paoli et al. in prep. - chapter 7), when the Campiglia carbonate horst was intruded by the Botro ai Marmi peraluminous monzogranite pluton (Fig. 5.1). The monzogranitic pluton is well exposed in an open-pit (~500 m^2) in the Botro ai Marmi area. Drilling logs and geophysical data evidenced the existence of a larger, N-S elongated pluton. The monzogranite has been altered by high-temperature (500-550°C) saline (38wt% NaCl and 19wt% KCl) fluids (fluid inclusions from metasomatic K-feldspar; Caiozzi et al., 1998; Fulignati et al., 1999). The magmatic intrusion (~0.10-0.15 GPa) produced a scattered thermal aureole in the carbonatic host rock (Leoni and Tamponi, 1991). The large contact-metamorphic aureole shows foliation and deformation structures preferentially oriented with a NE-SW to N-S dip (Fig. 5.1; Vezzoni et al., in revision.). Minor, irregular exoskarn bodies occurred at the pluton-carbonate contact and as veins into the host rock, as well as endoskarn veins were observed in the monzogranitic body.

Much more voluminous Fe-Cu-Zn-Pb(-Ag) skarn deposits are found ~1 km above the pluton, hosted by a withe marble resulting from the contact metamorphism (Vezzoni et al., 2016). The skarn is crosscutted by mafic and felsic porphyritic dykes, all affected by potassic alteration (Vezzoni et al., 2016). The youngest age of these events is constrained by whole-rock K-Ar age of 4.30±0.13 Ma (Borsi et al., 1967). Other metasomatic bodies and ore concentrations, spatially related to the main intrusive body (Monte Valerio area), are represented by low-grade veins and disseminated Sn-W-As-Bi ore (Venerandi-Pirri and Zuffardi, 1982). Finally, the early Pliocene peraluminous San Vincenzo rhyolites (Ferrara et al., 1989; Ridolfi et al., 2016) have been emplaced to the west of the carbonate horst (4.38±0.04 Ma; Feldstein et al., 1994).

Pluton morphology and marble deformation structures

In the Campiglia area, the deformation styles and the rocks morphologies are spatially related to the shape of the monzogranitic pluton. Indeed, the intensity of the deformation decreases with distance from the pluton (Vezzoni et al., in revision). The pluton' roof is N-S elongated, with length/width ratio of 3 to 6, and an E-W strongly asymmetric profile (western side > 70° dipping, eastern and southern flanks ~25-30° dipping). The minimum pluton area can be estimated to be about 18 km^2 (up to 50 km^2), outcropping at the top of a bulge in an open-pit mine. The granite shows a widespread cooling fracturation there (Vezzoni et al., in revision).

The pluton emplacement produced transient ductile conditions in the carbonatic host-rocks. They were thermally weakened, flowing laterally, accumulating downslope of the pluton roof mainly towards the east. The metamorphosed carbonate host was pervasively foliated, defining a broad antiform with NE-SW to N-S sub vertical axial plane (Vezzoni et al, in revision). The dip of the foliation planes decreases with distance from the pluton roof. Moreover, the first tens metres from the pluton contact are characterised by decametric folds generally gently dipping sub-parallel to the pluton-marble contact. The limbs of the main folds are characterised by minor cm-sized isoclinal folds highlighted by the different alternate colours of the layers (dark grey, light grey, and white; Vezzoni et al, in revision).

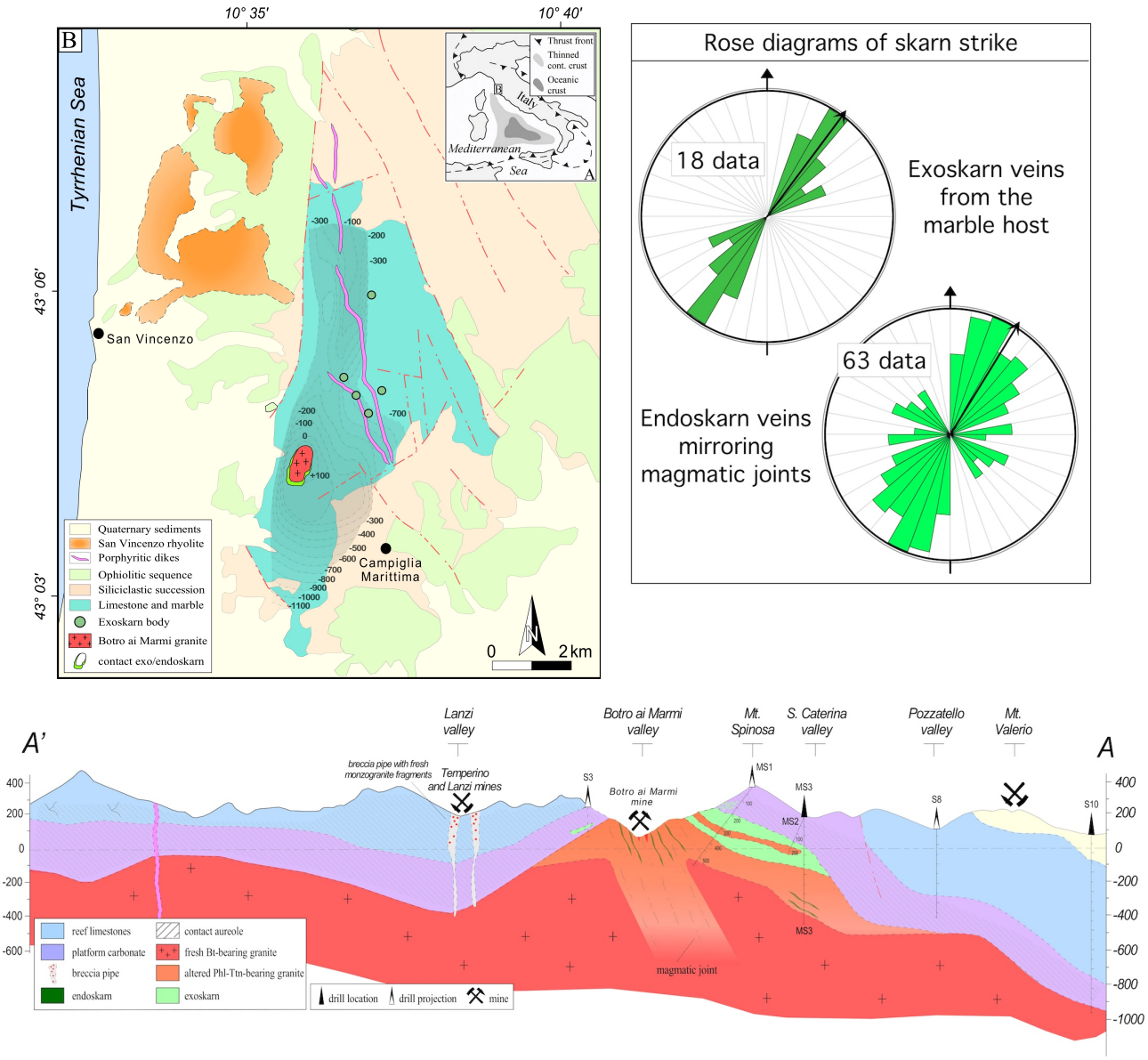

Fig. 5.1 - (a-b) Schematic geological map of the Campiglia Marittima area, showing the pluton roof reconstructed by borehole log (modified after Vezzoni et al., submitted); (c) Northeast-Southwest section (A-A') showing lithological distribution with depth and the location of drill core (modified after Dini et al., 2013). The spatial relationships with the outcropping skarn bodies are also reported. (d) Rose diagrams showing the average direction of the endoskarn and exoskarn veins.

5.3. Analytical methods

Samples were collected from the upper, central and lower portion of the outcropping granite, as well as the overlying and surrounding marble. The imaging and mineral identification were carried out at University of Pisa by SEM-EDS. Major element analysis was performed via X-ray fluorescence (XRF), while trace element analysis of selected whole-rock samples were carried out by acid digestion and elemental determination by ICP mass spectrometer. Both major and trace elements analysis were performed in the lab of the Earth Science department of Pisa. Moreover, automated mineral analysis and textural imaging of the studied samples were performed using an FEI QEMSCANQuanta 650F facility at the Earth Sciences Department of Geneva University. Selected minerals were quantitatively analysed at the University of Milano, using a electron microprobe equipped with five wavelength dispersive spectrometers and a EDS detector (the detailed analytical methods are reported in *Methods* chapter).

Porosity measurement were performed at University of Pisa, to quantify total porosity ($Ø_t$) and density (ρ) of the samples. Actual densities (ρ_r) were computed from the modal abundances of the single samples. Apparent density (ρ_a) measurements were performed on rock samples previously dried at 70°C x 24h in a ventilated oven. The samples were totally imbibed by distilled water and the total porosity, expressed in percentage, was computed as: $Ø_t = 100 \times [(W_2-W_d)/(W_2-W_1)]$ where W_1 is the hydrostatic weight, W_2 the weight of the imbibed sample and W_d is the weight of the dry sample.

5.4. Field and petrographic evidences

At Campiglia Marittima, the main monzogranite body crops out over a limited area at Botro ai Marmi, and is found in boreholes at Mt. Spinosa and Mt. Valerio, 3 km south of the outcrop (Fig. 5.1). The outcropping granite is mainly characterised by intense metasomatic alteration. Unaltered granite is found: (i) in a few small outcrops inside the quarry, (ii) to the north, deep portions of monzogranite were brought at shallow depth by breccia pipe outcropping at the Temperino mine (Fig. 5.1), and, (iii) moving to the south, it is found at increasing depth in several borehole (Fig. 5.1; MS1=550m; MS3=500m; S10=950m). The Botro ai Marmi quarry provides a window into the granitic intrusion that triggered the Campiglia Marittima hydrothermal system. In that area the top of the Botro ai Marmi granitic body crops out, along with its metasomatic products and the carbonate host rock (Fig. 5.2). The asymmetric pluton roof reaches its maximum elevation in this area, where the host rock carbonate is progressively thinner. The arrangement of the contact aureole shows strong variations from southern to eastern side.

Field relationships

The exposed lithologies can be easily distinguished between (i) an unaltered, biotite-bearing monzogranite, showing a typical grayish colour, contrasting with (ii) an altered, pinkish-whitish, phlogopite-titanite-bearing granite. The altered granite occupies more than the 95 vol% of the pit exposures and it is the most representative lithology down to ~400 m of depth (see deep borehole description). The unaltered monzogranite is found only in a few small outcrops (Fig. 5.2). These lithologies do not show any mutual crosscutting relationship and have identical U-Pb zircon ages (Paoli et al., in prep. - chapter 7).

A sharp-bordered, greenish endoskarn characterised by intense textural changes due to calc-silicate crystallisation occurred along fractures crosscutting the granite, likely developed during monzogranite cooling (Figs 5.2). The veins system (from centimetric to decimetric/metric in thickness) is structurally controlled by NE-SW to E-W sub-vertical brittle magmatic joints in the granite pluton (Fig. 5.2). The endoskarn is mainly characterised by calc-silicates (40-60 vol%), calcite, phlogopite, accessory epidote, apatite and minor zircons. At the pluton-marble contact it is possible to discern between different exoskarn lithologies according to their mineralogy (Fig. 5.3). These bodies locally reflect the host carbonate original composition (marble with impurities), but usually present peculiar colour, mineral composition and texture. A dark green diopside-titanite-phlogopite skarn is usually located at the pluton contact. Moving toward the marble contact, diopside is accompanied by vesuvianite and garnet crystallisation. Garnet increases and vesuvianite decreases, generating a reddish garnet-vesuvianite-quartz exoskarn, occasionally showing radial vesuvianite crystals, at the contact with marble. In these transitional area, wollastonite occasionally replaced early metasomatic calc-silicate. Folded grey marble, probably reflecting a lithological layering, is replaced by brownish phlogopite-diopside-calcite-albite exoskarn, accompanied by minor amphibole and trace olivine. This exoskarn do not show any evidence of deformation, postdating the deformation processes. In this study a full petrographic description of the observed lithologies is presented, underlining differences between mineralogical paragenesis (Table 1). In this work, *endoskarn* and *exoskarn* are used as lithologic terms and do not strictly refer to their genetic evolution (although endoskarn

replaces igneous rocks and exoskarn replaces host rock). Indeed, in our interpretation, the origin of these bodies is not directly related to the Botro ai Marmi monzogranite emplacement (see discussion).

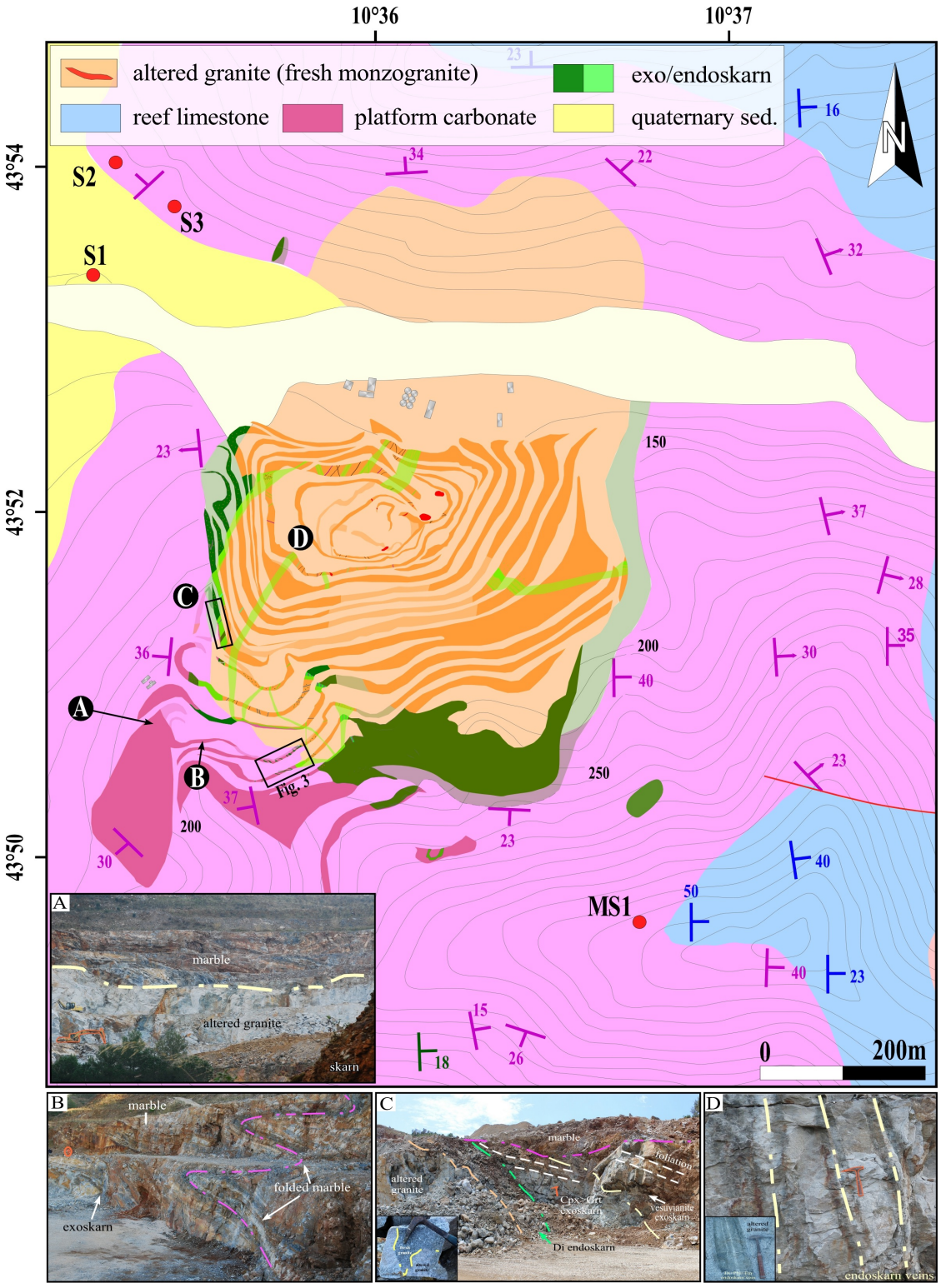

Fig. 5.2 - Geologic map of the Botro ai Marmi mine, showing the spatial relation between the granitic pluton, the metasomatic bodies and the host carbonate. Hydrothermal veins are also shown. The darker colours indicate the outcropping lithologies. A) Panoramic view of deformation structures at the granite-marble transition. B) Marble folding at marble-pluton contact. Some folds are replaced by exoskarn. C) Granite-endoskarn-exoskarn contact. In the inset is shown the contact between fresh and altered granite. D) Endoskarn veins.

Physical properties of studied samples

The main physical properties of the analysed lithologies are reported in Table 2. The actual densities (ρ_r) have been computed from the mineral modal abundances, assuming calculated density of the main representative minerals (e.g., 2.71 g/cm^3 for calcite, 2.86 g/cm^3 for dolomite, 2.65 g/cm^3 for quartz). The computed real density values range from (i) 2.711 to 2.84 g/cm^3 for the marbles, depending on dolomite and accessory minerals (mainly sulfides) content, (ii) 2.65 to 2.67 g/cm^3 for the granite, up to 2.69 g/cm^3 in the endoskarn veins. Here the density varies mainly according to titanite and diopside abundance. On the other hand, (iii) the density of the exoskarn bodies range from ~3.35 to 3.53 g/cm^3 based on calc-silicates mineralogy (garnet, vesuvianite, diopside, epidote). An exception is represented by the phlogopite-rich skarn that shows a density of 2.92 g/cm^3, due to the high phlogopite amount. The measured apparent densities (ρ_b) are comparable with the computed real density values. The derived connected porosity ($Ø_t$) don't vary significantly (values from 0.11 to 0.37 vol%). No significant correlation has been observed between the $Ø_t$ values and any other chemical, mineralogical or physical properties.

Petrographic observations

Fluid-rock interaction and metasomatic alteration effects which occurred at Botro ai Marmi include hydrothermal contact metamorphism, likely related to the emplacement of the granite body, and the by-products of sin- to post-intrusion igneous events occurred in the Campiglia area (mafic porphyry and San Vincenzo rhyolite emplacement). Evaluation of the mineral paragenesis is based upon field observation, petrography and scanning electron microscope (SEM-EDS) analysis. Metasomatic alteration took place because the mineral assemblages in the wall rocks are in physico-chemical disequilibrium with the hydrothermal fluids, and tend to re-equilibrate forming new stable mineral assemblages. In this context, minerals were interpreted as magmatic according to textural relationships, for example if they occur as phenocrysts (e.g., K-feldspar), or as isolated relict crystals displaying dissolution textures. Metasomatic minerals were recognised on the basis of replacement and dissolution/precipitation textures and their presence in veins. Moreover, the metasomatic bodies developed at the contact between the monzogranite and the host marble offers an excellent opportunity to study metasomatic reactions related to emplacement of a peraluminous monzogranite in a carbonatic sequence (now a pure marble). Indeed, at Botro ai Marmi, both the monzogranite and the marble host are extensively altered and replaced by metasomatic calc-silicates (e.g diopside, vesuvianite, garnet, titanite, epidote), F-rich phlogopite, REE-rich accessory minerals (e.g. allanite, apatite) and sulfides. The altered monzogranite and endoskarn are enriched/depleted in major and trace elements relative to the unaltered monzogranite. The same observations came from the comparison of the marble and the exoskarn products.

Marble host

At Botro ai Marmi the pluton crops out in a window through the upper host rock (Triassic limestones), that have been extensively metamorphosed (~8 km^2 metamorphic aureole; Vezzoni et al., in revision) by the intrusion to medium/coarse-grained white-rose marble with grey impurities, such as marl-rich sediments (Figs 5.2, 5.3). Metamorphic paragenesis includes calcite and dolomite, as well as minor quartz, phyllosilicates (Ms, Phl) and Cu-Fe-Pb-Zn sulfides. Marble show some disequilibrium geometries with a granoblastic sutured texture, typical of HT-LP contact metamorphism (quick recrystallisation of carbonates). Based on the initial thickness of the carbonatic sequence, the depth of the pluton emplacement has been estimated at 4-6 km (0.10-0.15 GPa; Leoni and Tamponi, 1991), as observed in other crustal setting of southern Tuscany (Dini et al., 2008). Temperature of 550 to 430 °C are obtained using the calcite-dolomite geothermometer (Franzini et al., 2010). Lobate to sutured grain boundaries, as well as tabular phlogopite crystals grown along the calcite grain boundaries suggests the presence of highly interconnected porosity (Franzini et al., 2010).

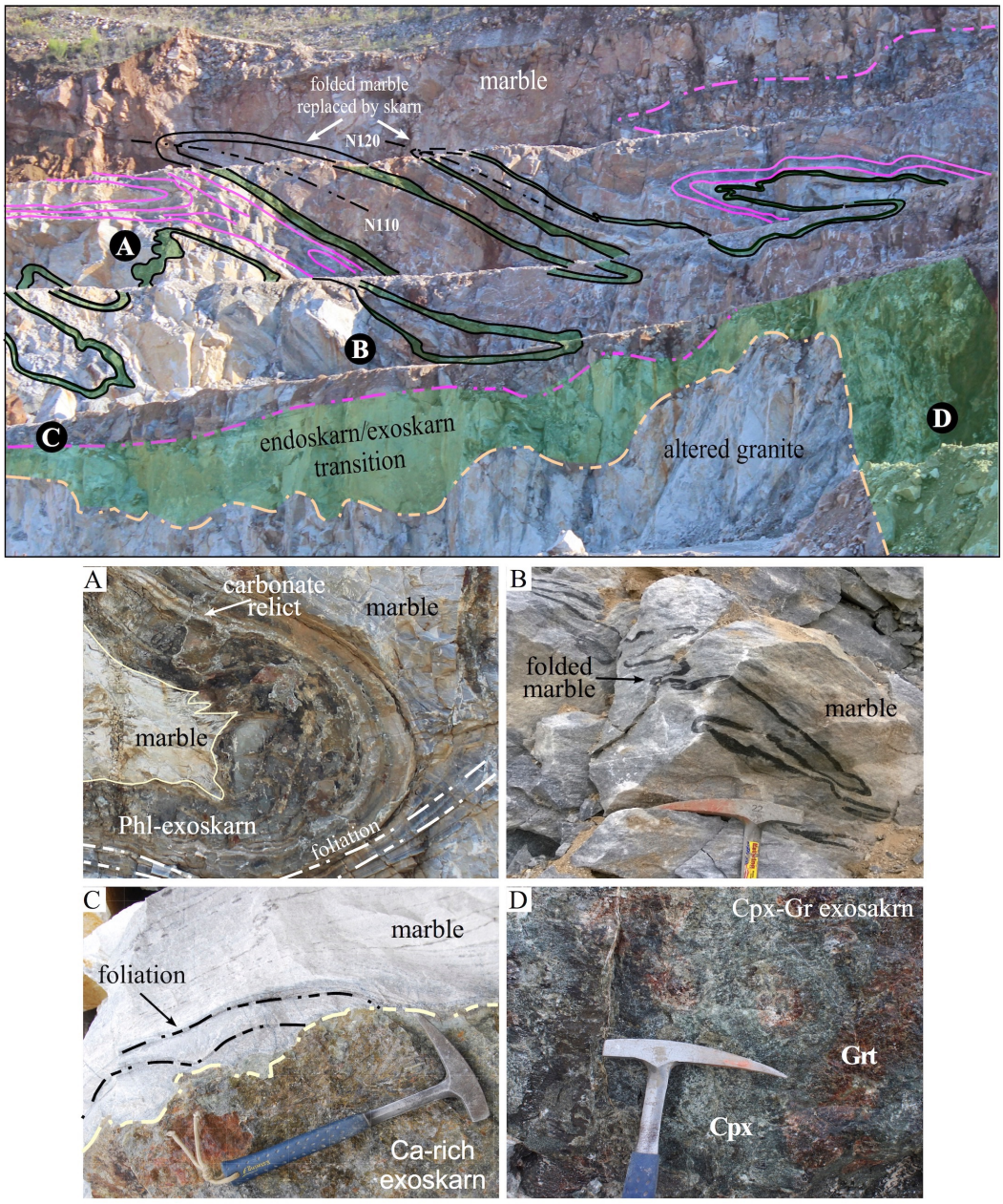

Fig. 5.3 - Representative photographs of the different exoskarn bodies at the pluton-host contact. A) Formerly fold replaced by phlogopite-diopside exoskarn, into layered grey marble. The core of the fold shows indented contact. B) Centimetric folds into white-grey marble. C) Diopside exoskarn at contact with white marble, showing foliation and replacement front. D) Vesuvianite-garnet exoskarn with calcite veins.

Unaltered biotite-bearing monzogranite

Previous studies (Barberi et al., 1967; Caiozzi et al., 1998; Lattanzi et al., 2001; Rodolico, 1945) described the Botro ai Marmi pluton as a medium-grained monzogranite, consisting in quartz, K-feldspar, plagioclase and biotite, along with accessory titanite, apatite, zircon and late-stage tourmaline. Moreover, they argue that a pervasive hydrothermal alteration has been responsible for the increase of K_2O (up to 10 wt%), occurrence of replacement K-feldspar, loss of Ca-Fe-S, and the abundant replacement of biotite.

In the present study, samples collected from the unaltered fraction of the pluton display a biotite-bearing monzogranite, scarcely affected by metasomatism (slight alteration of biotite; Fig. 5.4). The unaltered granite is also found in a few small outcrops at the Botro ai Marmi pit (Fig. 5.2), and in deep borehole (see borehole description). It is a medium-grained rock with rarely porphyritic texture (K-feldspar). The primary igneous assemblage of this unaltered

monzogranite consists of K-feldspar (30-35 vol%), quartz (30-35 vol%), plagioclase (20-30 vol%), and biotite (5-10 vol %), along with late-magmatic tourmaline and accessory cordierite, apatite, and zircon (Table 5.1; Fig. 5.4). Cordierite represents the most abundant accessory mineral, indicating the peraluminous character of these rocks. Tabular K-feldspar (ortose, Or_{85-90}, n=7) frequently occurs as megacrysts (up to ~5-6 cm), showing rare pertite with Ab. Interstitial Kfs is also present. Plagioclase (An_{35-45}, n=11) usually shows the enrichment in the albitic component moving from core to rim. The rim is characterised by a thin oligoclase overgrowth (An_{10-15}, n=6). Biotite is the only mafic mineral. Its composition is annite/siderophyllite (according to Deer et al., 1992) or Fe-biotite/siderophyllite (according to Foster et al., 1960), with a Fe# values comprise between 0.4-0.6, comparable with other peraluminous magmas from Tuscany (i.e., Monte Capanne pluton - Farina et al., 2010; San Vincenzo rhyolite - Ridolfi et al., 2016). Major element data for K-feldspar and biotite are reported in *Supplementary Table 1*.

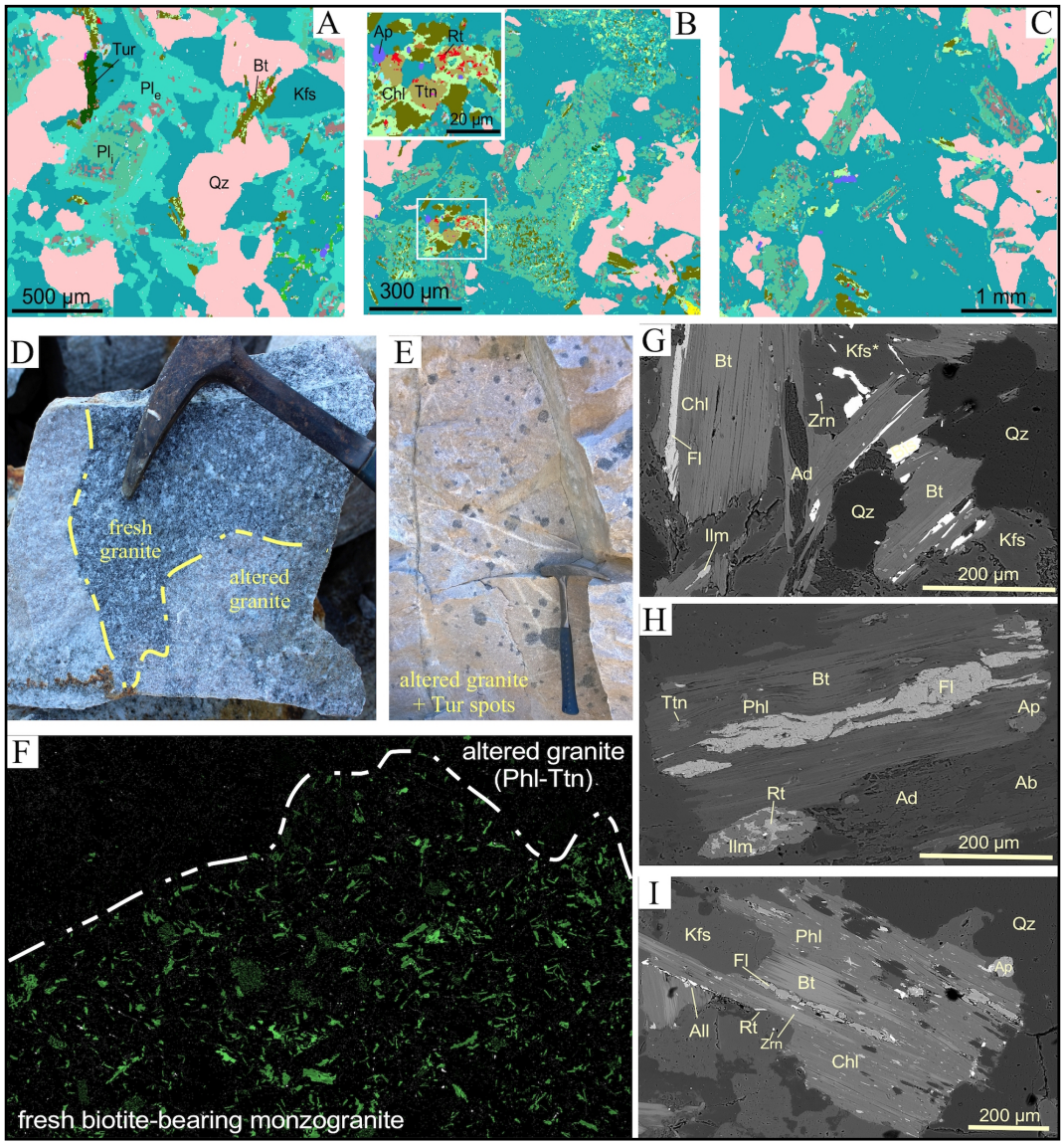

Fig. 5.4 - A-B-C) QEMSCAN images showing the alteration of plagioclase from fresh monzogranite (A) to increasingly altered granite (B-C). Secondary K-feldspar replace plagioclase (Plg_i = An_{35-45}, Plg_e = An_{10-15}). Biotite is replaced by Chl+Ttn+Phl, while ilmenite is replaced by Ttn+Rt.. D) Contact between fresh and altered granite. E) Altered granite with tourmaline spot. F) QEMSCAN element map of Fe distribution between altered and fresh granite. G-H-I) Backscattered electron images of altered biotite with fluorite and late sulfides. Biotite is replaced by Chl+Phl+Ttn. Moreover, in G ilmenite is replaced by titanite and rutile. Apatite and zircons occurred both into the biotite and on its border. For abbreviations see Whitney and Evans, 2010.

Altered phlogopite-titanite-bearing monzogranite

The metasomatic alteration of the biotite-bearing granite produced a pinkish-white altered granite (95 vol% of outcropping granite). It is characterised by the almost complete replacement of biotite by phlogopite (Mg# = 0.5), chlorite, titanite and Ti-oxide. The rare biotite remnants show abundance of FeO (up to 25 wt%) and TiO_2 (up to 4 wt %), diffuse alternation of chlorite and/or phlogopite, as well as replacement by numerous metasomatic minerals (i.e., titanite, fluorite, rutile, adularia; Fig. 5.5) between the layers (Fig. 5.4). In close spatial relation with deeply altered biotite is frequently observed a strong recrystallisation of accessory minerals (apatite, zircon, minor monazite).

Feldspars show peculiar characteristics (Fig. 5.4). The oligoclase abundance is considerably reduced up to ~5 vol% (Table 5.1; Fig. 5.4). The outer part of the plagioclase (mainly the oligoclase rim) is almost completely, isotropically replaced by irregularly shaped K-feldspar (average Or_{80-90}). Replacement of plagioclase also occurred along polysynthetic twinning and, to a smaller extent, along fractures. Scattered K-feldspar island in highly altered plagioclase were also observed. The progressive replacement of plagioclase (oligoclase) by K-feldspar is directly proportional with the proximity to endoskarn veins. Closer to endoskarn veins, occurred minor, widespread metasomatic diopside, amphibole and accessory minerals. Late calcite usually fill up open micro-fractures.

Modal (vol%) abundance for the main lithologies sampled at the Botro ai Marmi mine

	Mineral paragenesis	Fresh Bt-beraing monzogranite	Altered Phl-Ttn-Chl beraing granite	Endoskarn	Exoskarn		
					Di-Ttn-Phl	Phl-rich	Grt>Vs and Vs>Grt
Igneous minerals	***Quartz***	30-35	45-50	5-10	< 5	rare	trace
	K-feldspar	30 -35	25-30	< 5	< 5	< 5	–
	Plagioclase (An_{35-45})	5-10	5-10	5-10	5-10	trace	trace
	Plagioclase (An_{10-15})	15-20	< 5	< 5	< 5	< 5	
	Biotite	5-10	< 1	trace	–	–	–
	Turmaline	< 3-5	< 3-5	–	–	–	–
Metasomatic minerals	***Phlogopite***	–	5-10	5-10	5-10	30-35	5-10
	Titanite	–	1-3	5-10	5-10	5-10	5-10
	Diopside	–	–	15-25	25-35	20-25	5-10
	Vesuvianite	–	–	trace	< 5	< 5	20-40
	Garnet	–	–	trace	< 5	< 5	10-30
	Albite	–	–	< 3-5	< 3-5	5-10	< 3-5
	Allanite	–	trace	< 5	< 5	< 5	< 5
	Calcite	–	trace	5-15	10-20	10-15	< 5
	Sericite	< 3-5	< 3-5	< 3-5	–	–	–
	Chlorite	<1	1-3	< 3-5	< 3-5	< 3-5	< 3-5
	Sulphides	< 3-5	< 3-5	< 3-5	< 3-5	< 3-5	< 3-5
	Accessory	Zrn, Ap, Tur, Mnz, Ttn, Rt	Zrn, Ap, Tur, Rt, Aln, Cal, Fl, Thr, Urn	Zrn, Ap, Rt, Fl, Ep, Thr, Urn	Zrn, Ap, Ep, Fl, Thr, Urn	Ap, Zrn, Ep, Fl	Zrn, Ap, Ep, Fl,

Table 5.1 - modal (% vol) abundance of the different lithologies outcropping at the Botro ai Marmi mine. Granite–Bt = unaltered Bt bearing monzogranite; Granite–Phl-Ttn = altered facies of the granite rich in Phl and Ttn; Granite–Di = altered facies of the granite rich in Di-(Phl-Ttn).

Accessory minerals usually show evidences of replacement and/or recrystallisation with particularly relevant textures (Figs 5.4-5.6). (i) Cordierite, a typical mineral of the crustal-derived products of the Tuscan province (i.e., San Vincenzo rhyolite, Roccastrada rhyolite), is commonly strongly altered or replaced by "pinite". Thus, it is mainly identified from its shape and from the composition of its remnants. (ii) Ilmenite, another common accessory mineral of crustal magmas from Tuscany, is usually extensively replaced by titanite and rutile aggregates. Only few unaltered crystals are observed included in biotite. Crystals up to 100-150 μm, observed at contact with altered biotite, likely represent a secondary crystallisation postdated by Ti-rich minerals replacement. (ii) Primary monazite is strongly affected by metasomatic alteration. Indeed, most of the crystals (< 50 μm) are observed in altered biotite showing clear dissolution textures. On the other hand, likely metasomatic unaltered monazite are observed as small, euhedral crystals (5-10 μm) widespread into interstitial K-feldspar, quartz, or as aggregate with bigger apatite and zircons. (iii) Zircons

consist of crystals included in biotite (50-250 µm), contrasting with small (5-20 µm), euhedral crystals, mostly forming aggregate with apatite and monazite bordering altered biotite. An evidence of metasomatic origin for some zircon crystals it is represented by their occurrence at border of spongy-textured metasomatic titanite. (iv) Apatite crystals vary in size from small euhedral crystals (50 µm), usually forming aggregate with other accessories, up to 300-500 µm, indicating a possibly metasomatic origin. These minerals are occasionally observed included in unaltered or slight altered biotite, while commonly form aggregate of crystals in close contact with deeply altered biotite (chlorite-titanite-rutile-phlogopite).

Iron sulfides, chalcopyrite and minor Zn-Pb sulfides occurred as fracture and cavities infill. Furthermore, numerous quartz and calcite-sulfides-oxides bearing veins (few millimetres to decimetres in width) are irregularly developed within the granitic rock following the fractures system of the pluton. The igneous body is cut and altered by a stock-work of late veins and micro fractures (millimetric to centimetric thickness). The monzogranite is partially sericitised and chloritised where this stock-work occurs.

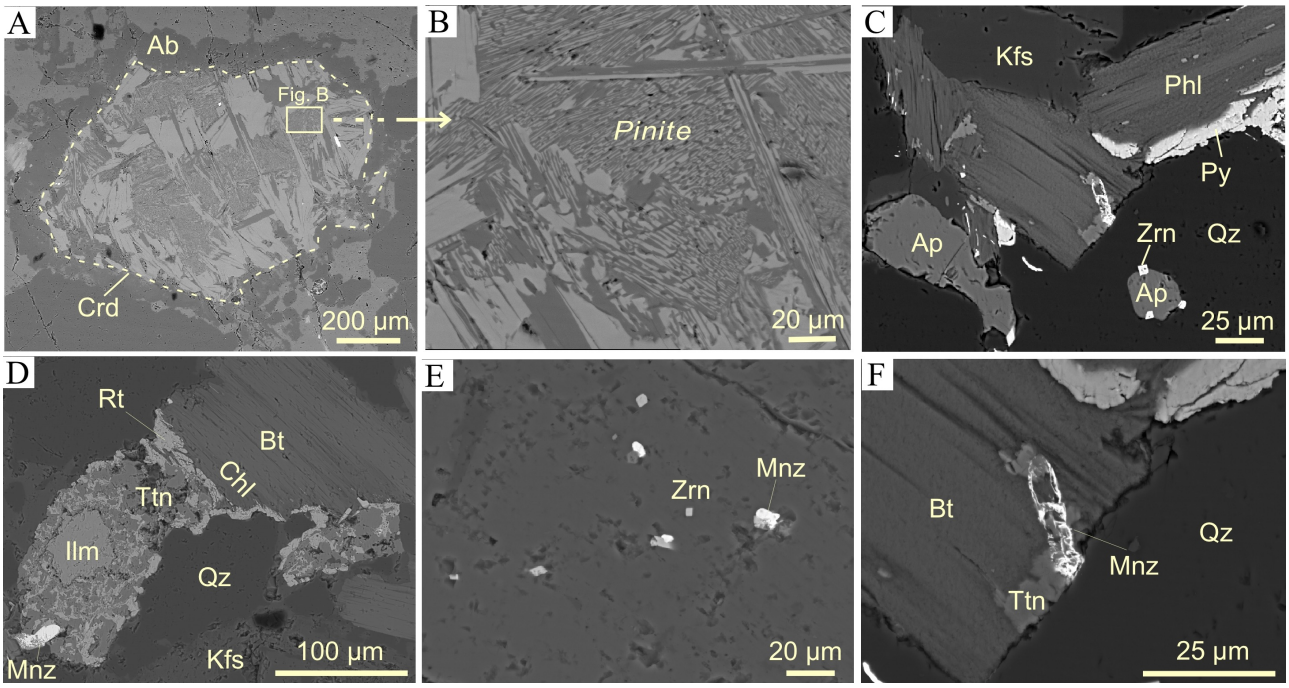

Fig. 5.5 - Backscattered electron images showing altered and replacement accessory minerals in granite. A-B) Pinitized cordierite in monzogranite. C) Apatite, zircon, pyrite and monazite in altered granite. D) Ilmenite replaced by titanite and rutile. E) Metasomatic monazite and zircon in secondary K-feldspar. F) Relict of monazite in biotite (magnification of C).

Endoskarn

Endoskarn bodies (Fig. 5.2) are a system of veins crosscutting the main pluton body resulting from the Ca-metasomatic alteration of the original granite. The veins are connected to the exoskarn aureole. They form close to the contact with the marble host. Development of endoskarn began with early potassic alteration resulting in the replacement of the magmatic minerals by K-feldspar+phlogopite+chlorite+titanite. Primary igneous textures are preserved. Later, all the remnants and the new minerals are partially replaced by diopside+calcite+epidote+rutile ±apatite and zircon during a Ca(-Mg) alteration. Remnants of the original granite (i.e., K-feldspar) are also observed. Biotite (5-10 vol%) is completely replaced by diopside-phlogopite-titanite-chlorite association, as well as by recrystallisation of accessory minerals. Accessory HFSE-REE (up to 5 vol%; epidote) and Th-U bearing minerals, as well as sulfides (up to 5 vol%), were observed in multiple generations. Sulfides include pyrrhotite-altered to pyrite, chalcopyrite, and minor arsenopyrite and sphalerite.

The abundance of metasomatic minerals (mainly diopside) decreases moving away from the vein core, coupled with the increase of newly crystallised titanite, indicating a local circulation of Ti and a more efficient circulation of Fe and Mg. Occasionally, centimetric, euhedral crystals of titanite occur in veins with diopside and quartz. These crystals show varying texture, from homogeneous to patchy zoned, together with multiple cracking and frequent sets of fluid inclusions (Fig. 5.5). Two generations of accessory epidote are discriminated according to their colour in hand sample, different brightness and composition by SEM-EDS analysis. The first is greenish, less bright, and Fe-rich, therefore is classified as epidote. The other, brownish to black, shows high REE contents and is classified as allanite. Usually epidote shows clear dissolution/recrystallisation textures and patchy zoning, resulting in the crystallisation of euhedral, strongly zoned, allanite. Fluorite is widespread in veins and inclusions, occasionally inter-layered in the magmatic biotite. The calcite+fluorite+sulfides aggregates post-date the formation of the calc-silicate skarn, occurring as fracture infill (Fig. 5.7). Typically lower temperature phyllitic alteration (chlorite-sericite) is generally marked close to fractures and core of endoskarn veins, where the abundance of multiple generation of low temperature iron sulfides (replacing high temperature sulfides) and fluorite increase and calc-silicate are frequently replaced by late accessory minerals.

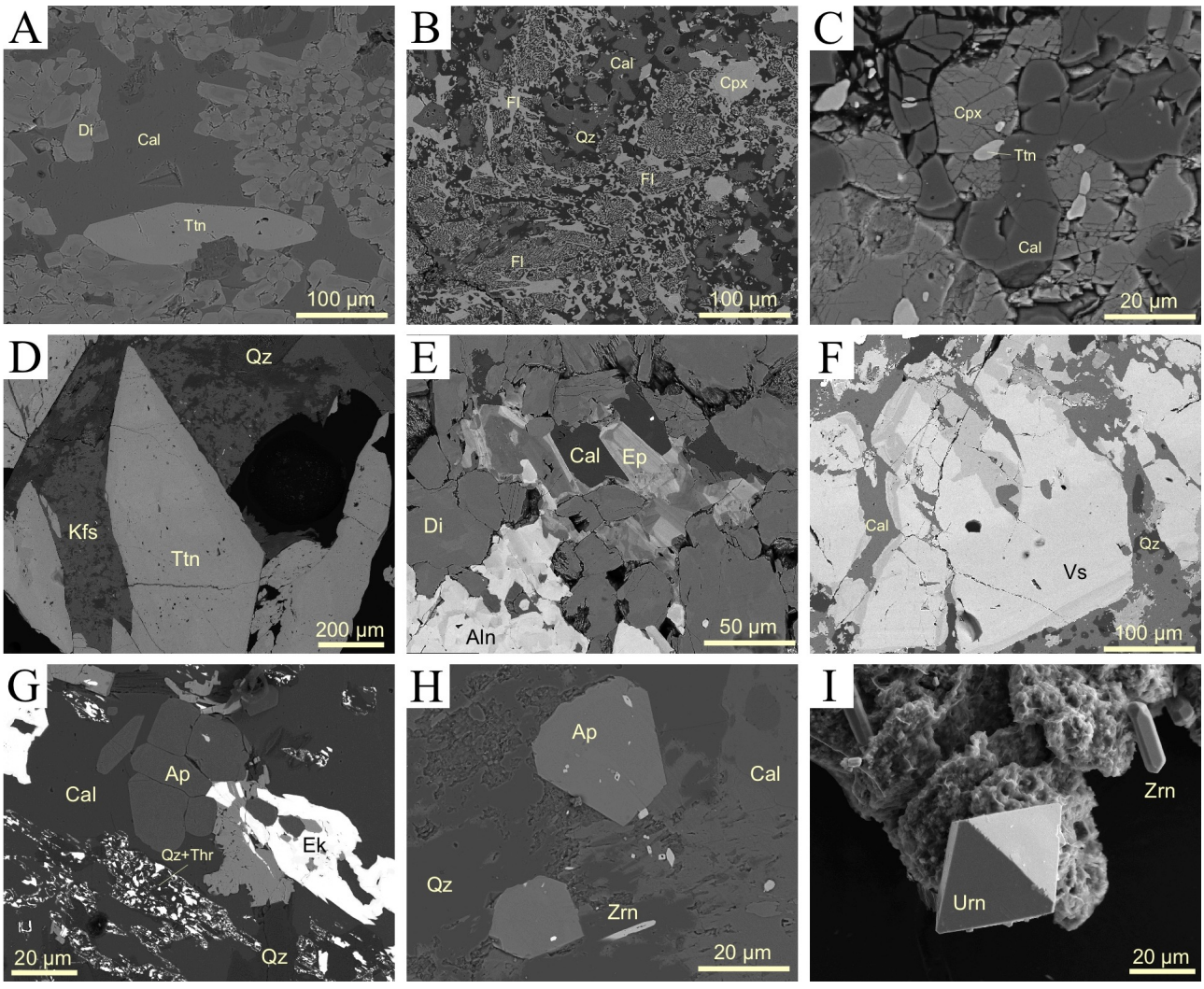

Fig. 5.6 - A) Filling fractures diopside-titanite and late calcite exoskarn. B) Fluorite-calcite-quartz-diopside pseudomorphs in Cpx-rich exoskarn. C) Dissolution texture of diopside, titanite, with late calcite. D) Euhedral zoned titanite with relict K-feldspar and quartz, in veinlet. E) Late allanite replacing epidote in Di-rich exoskarn. F) Zoned vesuvianite with fractures filled by REE-enriched overgrowth. G) Pseudomorph of thorite+quartz after ekanite,with apatite, quartz and calcite in Cpx-rich exoskarn. H-I) Apatite, zircon and uraninite resulting from metasomatic alteration of biotite (H) and titanite (I).

Exoskarn

The pervasive alteration of the bedded marble host rock by hydrothermal fluids commonly resulted in the formation of banded skarn pockets and veins (Fig. 5.2 and 5.6). Massive bodies occurred at the pluton-marble contact, while veins are observed as selective replacement of the ductilely folded carbonatic host-rock inside the marble body (Fig. 5.3). Patches of marble remained inside the exoskarn. The stage of folding and marble development are probably coeval with the Botro ai Marmi pluton emplacement (Vezzoni et al., in revision). Later on, metasomatic alteration developed from the monzogranite. The metasomatic minerals are mainly represented by diopside+garnet+vesuvianite+titanite +phlogopite±scapolite±adularia±allanite. Accessory minerals include zircon, apatite, magnetite, pyrrhotite-altered to pyrite, minor chalcopyrite, sphalerite, arsenopyrite together with multiple generation of fluorite. In only few cases the replacement of folded marble produced a decimetric band of metallic mineralisation.

Some minerals, such as quartz and calcite, are present in almost all skarns, with calcite decreasing toward the pluton contact. On the other hand, the metasomatic alteration produced alternating layers (decimetres to metres in thickness) of garnet-dominated and pyroxene-dominated skarns. Moving from the granite to the marble it is possible to observe: (i) proximal diopside-titanite-phlogopite bodies, (ii) vesuvianite-diopside > garnet-vesuvianite bodies (iii) garnet > vesuvianite bodies, (iv) mainly phlogopite-albite replacing folded marble. Occasionally, at the exoskarn-marble contact early calc-silicates are replaced by pyroxenoid (mainly wollastonite). Diopside and red vesuvianite show massive to radiating textures, spectacularly regular zoning, as well as secondary metasomatic textures marked close to the pluton/ marble contact (i.e., vesuvianite and early REE-rich epidote replaced by late REE-poor epidote). Garnet are euhedral, red to brown in colour, with concentric zoned growth, which do not manifest any consistent compositional trends (detectable by SEM-EDS analysis). Titanite is widespread in the overall exoskarn bodies, showing a slight increase close to the granite contact. It is usually characterised by patchy zoning and *spongy* textures. Phlogopite abundance is likely related to the initial marl levels content in the host rock. Indeed, exoskarn bodies, following early marble folded level, show association of metasomatic phlogopite (>50 vol%), subhedral diopside, albite, as well as accessory apatite, amphibole, and rare olivine, all fixed in a fine-grained calcite matrix. Epidote is widespread in all these bodies both as prograde and retrograde mineral. Indeed hydrous minerals do not necessarily represent retrograde alteration (e.g., ilvaite crystallisation at Temperino distal skarn; Vezzoni et al., 2016). For example, the high fluorine activity in Sn-skarns is observed to stabilise many hydrous minerals at high temperatures during early skarn alteration stages (e.g., Lost River, Alaska; Dobson, 1982). On the contrary, minerals with a probable retrograde origin are amphibole and chlorite, as well as other hydrous phases overprinting the prograde sequence. Accessory HFSE-REE and Th-U minerals increase close to the granite contact. Here occurs the crystallisation of accessory calc-silicate such as epidote, allanite (see endoskarn), ekanite ($ThCa_2Si_8O_{20}$), as well as Ca-rich phosphates like cheralite ($CaTh(PO_4)_2$). These minerals frequently experienced a secondary alteration and could be replaced by other phases, such as apatite, zircon, thorite, uraninite accompanied by crystallisation of quartz and fluorite. Moreover, secondary accessories resulted from the alteration of main calc-silicates, such as titanite. Indeed, such minerals are frequently bordered by uraninite, thorite, and/or zircon, reflecting coupled reactions in which dissolution of primary, HFSE/REE-rich phases are replaced by secondary HFSE-REE and Th-U accessory minerals (Fig. 5.6). This coupled dissolution/recrystallisation reaction evidences a multi-stage mobilisation of REE and HFSE during fluid–rock interaction. This multi-stage metasomatic crystallisation makes more difficult to distinguish between different growing events. As previously observed in the altered granite and the endoskarn bodies, high- to low-temperature sulfides (i.e., Py, Po, Ccp, Sp) are widespread through the exoskarn system filling open-space, forming veins, as isolated crystals, and showing multiple textures of intergrowth and mutual replacement (Fig. 5.7).

Thus, a multi-stage heavy elements mobility is suggested by the occurrence of accessory minerals replacing calc-silicates, the multi-stage replacement of REE-bearing minerals (i.e. ekanite → thorite+quartz), and the occurrence of metasomatic zircon and apatite in close relation with titanite and phlogopite. These evidences mark a local mobilisation

of commonly poorly mobile elements (e.g., Zr, Th, REE, Hf, Nb), usually recalling transport via hydroxy-fluoride complexes (high F^-–ligands) in a hydrothermal context. The abundant precipitation of HFSE-REE and Th-U minerals, the zoning/replacement of calc-silicates, and the common occurrence of pseudomorphs with fluorite, support the idea of acidic-fluids as carrier of HFSE an REE during metasomatism.

Late hydrothermal veins

A late low-temperature hydrothermal veins system cross-cut the granite body. They are characterised by abundant chlorite, low temperature sulfides, calcite, quartz and fluorite, as well as accessory HFSE-REE and Th-U bearing minerals (Fig. 5.5). Late-crystallised anhydrous minerals such as quartz and orthoclase are present as minor interstitial minerals. The main sulfides are pyrrhotite (FeS), pyrite (FeS_2), sphalerite (ZnS), chalcopyrite ($CuFeS_2$), and minor galena (PbS). Single- and poly-phase sulfide grains occur (i) as isolated interstitial grains at the contact between unaltered grains of magmatic minerals, (ii) in veins crosscutting the systems or along cleavage planes and fractures of fresh igneous minerals, and more rarely (iii) as inclusions near the margins of the same minerals. Individual grains are typically subhedral and varying from μm to centimetre in size. Single grains of sulfide and polyphase assemblages commonly are accompanied by late-crystallising quartz, fluorite, and HFSE-REE and Th-U accessory minerals (Fig. 5.6, 5.7).

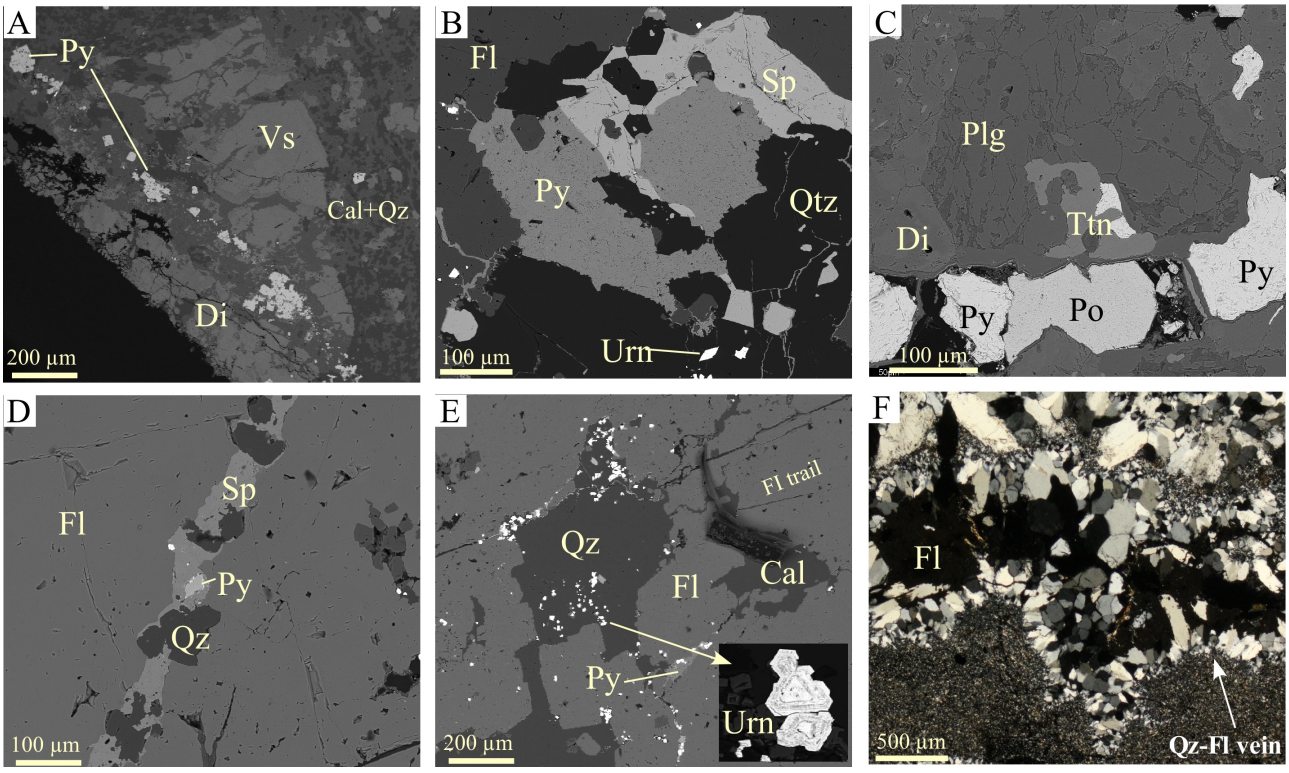

Fig. 5.7 - BSE image of: A) Cpx-rich exoskarn with Py trail and late quartz-calcite aggregates; B) pyrite-sphalerite aggregates in quartz-fluorite vein, with uraninite inclusions; C) pyrrhotite-pyrite vein in diopside-titanite endoskarn; D) sphalerite-pyrite-quartz vein in centimetric fluorite crystal; E) widespread uraninite crystals in quartz-fluorite vein; F) quartz-fluorite veinlet in altered granite.

Petrographic variations with depth

The analysis of several exploratory borehole logs (Samim, 1983), which reached the magmatic body at different depth, is performed to investigate the lithological variations with depth through the carbonate host to the granite. In particular, the MS3 borehole extend from the metamorphosed carbonate rock through a thick metasomatised body to the granite, which has been reached at 225 m below the surface.

The following lithological variations refer to the borehole progressive depth (Supplementary Fig. 5.1). Pure marble extends from the surface to about 200 m of depth. This rock is characterise by a medium to coarse-grained white-rose marble, with common grey impurities due to increase in a marly component and grain size decrease. The marble presents some disequilibrium geometries with a granoblastic sutured texture, with dominant calcite, dolomite (increasing with depth), minor quartz, phyllosilicates and sulfides. Moving toward the pluton contact the following metasomatic rocks has been observed: (i) between 50 and 120 m occurred a diffuse crystallisation of metasomatic phlogopite, accompanied by minor K-feldspar, and rare diopside, as well as accessory fluorite, chlorite, and muscovite, (ii) between 170 and 230 m occurred several metasomatic minerals, mostly calc-silicate aggregates, that increased moving close to the pluton contact. From top to bottom, aggregates of phlogopite±K-feldspar±scapolite±plagioclase are replaced by fine-grained exoskarn bodies, predominantly characterised by diopside±phlogopite±K-feldspar and minor vesuvianite±garnet±scapolite. Secondary minerals are epidote, fluorite, chlorite, and sulfides. A weak mineralisation with pyrite and magnetite is also present. Moving closer to the granite contact the modal amount of garnet and epidote increase, while diopside is frequently found with scapolite and vesuvianite. At ca. 220 m, the drill core reached a brownish-pinkish leucogranite mainly characterised by K-feldspar (50 vol%), quartz (30 vol%), plagioclase (10-15 vol %), and phlogopite-titanite assemblages (5-10 vol%). Millimetric to centimetric veins, mainly consist of quartz and late-alteration minerals, such as chlorite, fluorite, calcite and sulfides crosscut the granite,. Between 320 and 400 m (in the granite profile) a petrographic and chemical variation has been observed and linked to the occurrence of a series of endoskarn veins, mainly characterised by the association of diopside±titanite±phlogopite±epidote. Late sulfides, calcite and chlorite are also present. Below 400 m (until 550 m) the profile is totally made of granite showing variable metasomatic alteration grade, determined by the varying metasomatism of biotite (mostly replaced by titanite). The last 70 m of the profile are mainly characterised by a biotite-rich granite showing few if any metasomatic minerals.

General alteration patterns

The evolution of the textures and mineral assemblages of the Botro ai Marmi granite and marble host rock are summarised in Figure 5.8. An initial magmatic stage is characterised by the crystallisation of the main magmatic minerals, probably at depth - biotite, plagioclase (andesine in composition), K-feldspar (up to 5 cm), quartz, cordierite, together with accessory minerals such as zircon, apatite, ilmenite and late tourmaline. The transfer and emplacement of the monzogranitic magma at a shallower (emplacement) level determined a drop in pressure promoting the crystallisation of a thick oligoclase rim on andesinic plagioclase, together with crystallisation of interstitial quartz and K-feldspar. Around the granite body the metamorphism of the host carbonatic sequence led to the crystallisation of an almost pure marble.

The monzogranite body was completely altered during the prominent and widespread alteration stage. Plagioclase is replaced by K-feldspar, while biotite is almost completely replaced by phlogopite, chlorite and titanite. Accessory minerals originally included in biotite are dissolved and recrystallised at biotite border or in exoskarn bodies. Ilmenite is replaced by titanite and rutile, while apatite recrystallised in close spatial association with biotite. Along the main magmatic fractures crosscutting the granite, the replacement of the original monzogranite paragenesis reached its climax, with crystallisation of calc-silicates forming endoskarn veins.

Marble is affected by calc-silicate crystallisation evolving from diopside, through vesuvianite, to garnet. Phlogopite and titanite characterised the whole metasomatic process (Fig. 5.8). Sulfides crystallised during the whole metasomatic process. Pyrrhotite is frequently altered to pyrite. The occurrence of accessory minerals replacing early calc-silicates, the multi-stage replacement of REE-bearing minerals, as well as the occurrence of metasomatic zircon and apatite bordering titanite and phlogopite, highlight the evolution of the system toward more acidic condition. This stage is characterised by abundant precipitation of HFSE-REE and Th-U accessory minerals, the zoning/replacement of calc-silicates, and the common occurrence of pseudomorphs with fluorite. These evidences support the positive correlation between the acidity of F-rich fluid and the increasing mobilisation of REE, HFSE, and trace elements.

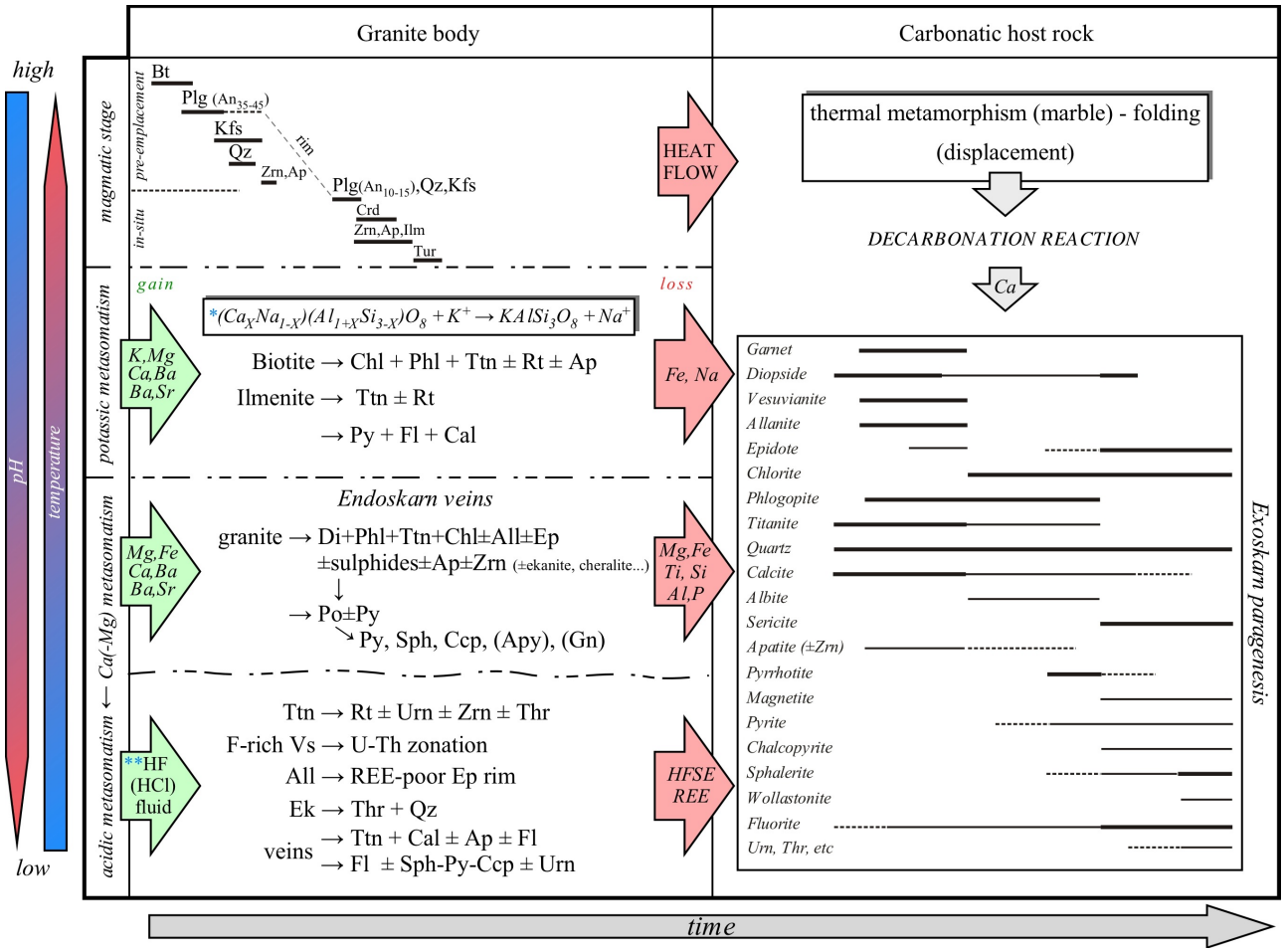

Fig. 5.8 - Mineral paragenesis summarising the original and metasomatic mineralogy from the granite body and the carbonate host rock. *Plg rim (An_{10-15}) completely replaced by Kfs, while Plg core (An_{35-45}) partially replaced. **calc-silicates dissolution/ replacement, HFSE and REE local mobilisation, chemical zoning (i.e.,Vs-Ttn-Di-Grt).

5.5. Whole-rock compositions

Based on the above petrographic evidences, the unaltered biotite-bearing monzogranite is interpreted to represent the primary magmatic granite. The sparse occurrence of outcrops of unaltered monzogranite allow to assume that the protolith was fundamentally similar to this rock. Chemical and petrographic alteration of the original monzogranite produced an altered (phlogopite-titanite bearing) granite, in which biotite has been completely replaced by titanite and phlogopite-chlorite. Along magmatic joints, the alteration is pronounced and biotite is replaced by titanite, phlogopite and diopside. Whole-rock analysis from the main representative lithologies (unaltered and altered granite, endoskarn, exoskarn, marble) collected at the Botro ai Marmi mine, allow to better characterise the geochemical variability occurred at the pluton-marble contact, also in term of trace element and REE. The comparison with data obtained from borehole reports (MS3 core; Samim, 1983) allows to identify geochemical variation with depth. In this context, geochemical data are related to petrographic observations. Samples from drill cores have originally collected at 3 m intervals. These intervals typically do not cross metasomatic alteration boundaries or lithological contacts.

The compositional data for samples collected at the Botro ai Marmi mine have been obtained by X-ray fluorescence on whole-rock for major elements and by ICP-MS on acid digested powders for trace elements. Both these procedures has been performed at the Earth Science Department of Pisa. Whereas, whole-rock composition of the drill cores samples has been obtained by X-ray fluorescence (XRF) at the Rimin laboratory during exploratory investigations.

Geochemistry of outcropping lithologies at the Botro ai Marmi mine

Whole-rock composition of the Botro ai Marmi lithologies is reported in Table 5.2. The granite has a syenogranitic to monzogranitic composition (SiO_2=70-72 wt%) and a peraluminous character (ASI=1.1-1.3). The normative composition diagram and the SiO_2 vs. K_2O/Na_2O diagram (Fig. 5.9) shows values similar to other peraluminous igneous products from southern Tuscany (i.e., Gavorrano, Montecristo, and Giglio Island intrusions; Dini et al., 2002; Pinarelli et al., 1989; Poli and Peccerillo, 2016). Same similarities result from major and trace elements comparison. The comparison between unaltered and altered granite shows significant patterns, using a decrease in SiO_2 as an index of progressive alteration. Indeed, silica content decreases from the unaltered granite (71-69 wt%), to the altered granite (66-64 wt%) and to the endoskarn veins (55 wt%). Na_2O shows a negative linear correlation versus silica. A similar pattern also holds for Sr, Rb and Ba variations. MgO/FeO_t ratio shows a positive correlation with silica, defining a significative increase if compared with phlogopite-titanite bearing granite and a slight increase if compared with endoskarn veins (Fig. 5.9). CaO and P_2O_5 exhibit a prominent positive linear correlation, highlighted from the endoskarn vein samples. A quite similar, more scattered, positive pattern is defined by K_2O, that on contrary shows the same values for unaltered monzogranite and endoskarn. MgO, TiO_2, and Al_2O_3 values remain almost unvaried.

The transition from the unaltered to the altered granite is characterised by the decrease of FeO_{tot} from values of about 2.5 wt% to values lower than 0.25 wt%. Total FeO_{tot} increases significantly in the endoskarn veins (up to 10 wt %). Higher values of FeO_{tot} are coupled with an increase of Al_2O_3 content up to 21 wt% (15-16 wt% in the original granite). The same systematic variation is also observed for MgO. The abundance of TiO_2 is constant in both the altered and unaltered granite (0.35-0.45 wt%). Na_2O content decreases with the alteration, while K_2O increases from the original granite to the phlogopite-titanite granite (from 5 wt% up to 10 wt%). Na/K ratio shows a positive correlation with Sr and negative correlation with Rb values (Fig. 5.10). The endoskarn bodies, where plagioclase is completely replaced by K-feldspar, show the maximum value of K_2O. The abundance of Rb and Ba show a positive correlation with K_2O, and in some altered granite Rb and Ba rising over 500 ppm. The CaO content increases from 1-2 wt% in the original granite to 3 wt% in the altered granite. A net increase occurred in the endoskarn bodies, up to value of 10 wt%. Th concentration increases from 14 ppm in the unaltered granite to 18 ppm in the altered granite (up to picks of 24 ppm), while decreases in the endoskarn to 9 ppm. Initial U concentration is between 12-14 ppm and vary with metasomatic alteration from 11 to 4 ppm. Endoskarns show values between 7 and 8 ppm.

	GBM-2NA	GBM4	GBM-5	GBM-2A	GBM13	GBM-19A	202R	301R	GBM-19B	202V	GBM 12	GBM16	201A	201C	201L	GBM-22	GBM28N	GBM-23	GBM-7	GBM-9	GBM47	GBM-28B	GBM-28	MB
Rock type	*fresh granite*	*granite–Bt*	*granite–Bt*	*granite–Phl-Ttn*	*granite–Phl-Ttn*	*granite–Phl-Ttn*	*granite–Phl-Ttn*	*granite–Phl-Ttn*	*granite–Di*	*granite–Di*	*endoskarn*	*endoskarn*	*endoskarn/granite*	*endoskarn core*	*endoskarn rim*	*exoskarn–Phl*	*exoskarn–Phl*	*exoskarn–Di*	*exoskarn–Cpx*	*exoskarn–Cpx*	*exoskarn–Grt-Vs*	*grey marble*	*grey marble*	*white marble*
Major element (ppm)																								
SiO2	70.66	67.43	68.86	68.85	66.96	66.45	69.8	66.49	64.4	69.18	39.03	42.96	63.29	57.08	55.97	39.08	39.52	53.68	52.61	49.65	39.61	2.65	3.87	1.57
TiO2	0.39	0.37	0.36	0.33	0.44	0.38	0.4	0.36	0.5	0.32	0.88	0.05	0.33	0.27	0.31	0.94	0.82	0.04	0.08	0.06	0.21	0.02	0.02	0.04
Al2O3	14.79	15.91	15.75	15.37	15.53	17.22	15.53	15.67	15.66	14.52	21.61	0.97	15.38	17.24	16.87	21.32	21.26	0.67	0.83	0.78	16.21	0.87	1.11	0.41
FeO	1.73	2.42	2.86	0.13	1.75	0.23	0.48	0.21	1.35	0.19	5.19	8.83	0.09	1.73	1.49	4.87	5.19	8.53	11.95	19.59	9.9	0.33	0.25	0.11
MnO	0.04	0.06	0.06	0.01	0.04	0.02	0.04	0.02	0.06	0.02	0.08	0.07	0.02	0.03	0.03	0.08	0.07	0.16	0.25	0.36	0.45	0.02	0.01	0.02
MgO	0.91	0.92	0.97	0.93	1.02	1.25	0.94	0.7	1.04	0.4	9.95	11.88	0.68	2.35	2.82	9.46	11.23	13.37	11.85	5.83	1.54	4.3	4.97	0.87
CaO	1.79	1.87	1.82	3.11	2.5	2.65	3.27	2.76	4.77	2.96	7.73	20.55	3.7	9.44	9.96	8.87	6.24	23.42	22.42	22.07	31.35	49.62	48.65	53.77
Na2O	2.30	2.90	3.34	2.79	2.40	2.02	3.76	1.62	2.60	2.25	0.06	0.15	0.96	3.20	3.23	0.08	0.01	0.10	0.11	0.12	0.07	0.01	0.15	0.05
K2O	6.78	6.5	5.07	6.39	7.38	7.48	3.57	10.78	6.96	7.25	5.06	4.14	11.21	5.81	5.14	4.91	5.56	0	0	0	0.02	0.29	0.47	0.05
P2O5	0.17	0.2	0.17	0.18	0.17	0.25	0.26	0.24	0.2	0.27	0.14	0.01	0.29	0.26	0.28	0.15	0.18	0.02	0.02	0.02	0.21	0.03	0.02	0.09
LOI	1.11	1.38	1.22	1.63	1.8	2.71	1.71	1.63	2.49	1.52	9.9	10.42	2.97	2.88	2.55	10.85	8.9	0.97	1.52	2.09	1.29	41.87	41.91	43.07
Trace element (ppm)																								
Li	60.77	95.24	82.57	99.00	44.40	89.98	86.00	26.92	29.54	17.23	318.52	31.73	75.88	27.69	29.25	297.56	316.80	40.34	62.15	40.55	19.43	6.73	8.21	1.98
Be	10.69	10.77	11.48	11.75	8.11	15.32	10.68	3.74	11.73	7.20	5.67	4.04	2.01	18.44	18.49	5.26	6.06	2.24	4.96	3.09	6.70	0.22	0.23	0.09
Sc	27.88	27.14	30.25	30.26	39.28	27.71	4.75	3.27	33.85	4.10	121.32	7.86	3.42	5.06	5.73	110.14	2.77	11.30	21.36	19.01	5.37	0.89	7.07	0.91
V	81.77	177.13	67.67	120.23	134.46	89.51	28.80	23.31	82.77	20.56	134.75	7.59	16.37	35.34	38.48	133.81	107.35	18.19	9.09	8.49	20.68	5.80	8.92	1.65
Cr	81.80	177.10	6.80	120.20	134.50	89.50	28.90	26.30	82.80	16.80	134.70	7.60	15.20	15.50	15.70	133.80	110.90	18.20	0.90	0.80	25.70	5.80	8.90	1.70
Co	5.41	10.42	10.10	7.74	6.73	1.23	4.57	2.24	5.20	1.48	8.68	2.87	1.00	5.10	4.19	8.49	8.93	8.59	11.03	14.93	9.26	1.02	1.51	0.56
Ni	44.28	58.96	55.80	40.40	34.96	19.24	11.33	21.48	50.97	3.53	19.34	3.93	5.46	47.96	35.21	17.55	16.57	23.14	21.44	23.31	8.44	4.02	17.95	2.31
Cu	14.81	24.12	29.27	4.38	10.33	22.75			11.30	4.77	37.03	3.48	3.95	3.95	3.00	48.17	25.23	26.65	23.63	17.40	9.64	4.77	3.09	108.84
Zn		65.21			22.06	174.31	0.14	11.59		0.14	63.23	272.85	23.06	23.06	14.24	18.34	44.88	77.46	83.43	164.42	69.18	3.26		116.13
Ga	21.95	25.13	24.58	24.35	22.36	26.70	20.66	26.65	25.05	19.28	29.06	66.20	23.55	40.68	41.69	27.45	27.59	4.23	5.87	6.71	35.85	0.90	1.24	0.34
Rb	374.09	405.24	330.92	431.36	370.79	479.34	213.66	545.44	406.75	384.84	336.88	68.02	573.75	301.88	268.78	352.65	331.17	1.76	10.83	3.34	5.68	28.48	35.30	1.69
Sr	148.94	200.98	140.77	278.80	294.98	221.34	182.68		402.38		579.59	552.80		554.49	328.24	485.99	20.25	39.50	50.57	56.34	170.01	304.24	541.10	167.18
Y	13.19	14.84	13.32	14.58	12.15	14.68	11.07	15.79	21.11	10.65	17.32	5.81	10.88	14.80	14.80	17.97	14.00	1.36	2.90	1.44	14.38	2.28	2.36	5.76
Zr	35.39	2.08	22.27	27.03	3.12	20.87	10.54	7.68	19.68	9.84	24.52	2.71	8.72	15.20	13.85	40.57	23.68	2.33	5.69	4.80	62.50	1.58	1.78	2.06
Nb	10.85	11.82	12.63	12.66	11.35	8.53	11.50	10.52	17.25	9.54	19.85	0.53	9.13	12.11	12.29	20.27	18.85	0.13	0.66	0.19	35.46	0.80	0.87	0.59
Mo	1.13	1.58	1.33	0.88	1.07	1.10	1.77	0.52	0.93	0.43	0.30	0.16	0.52	0.31	0.44	0.15	0.39	0.04	0.10	0.19	1.28	0.34	0.20	0.17
Ag	0.28	0.00	0.12	0.13	0.00	0.12	0.00	0.00	0.12	0.00	0.00	0.00	0.12	0.10	0.10	0.21	0.15	0.02	0.04	0.03	0.00	0.00	0.01	0.00
Cd	0.04	0.00	0.03	0.03	0.00	0.12	0.00	0.01	0.04	0.00	0.00	0.00	0.01	0.03	0.03	0.07	0.00	0.01	0.01	0.01	0.04	0.00	0.01	0.00
Sn	5.83	12.33	14.06	5.24	6.17	4.30	6.53	9.36	11.89	8.25	8.22	0.00	9.00	8.75	8.89	44.53	1.18	4.44	7.01	10.08	0.00	0.92	2.81	1.15
Sb	1247.60	237.20	241.83	299.11	157.30	636.43	0.49	0.68	432.02	0.57	0.00	0.00	0.39	0.51	0.45	18.33	2.61	1.12	0.00	0.00	2.70	6.50	0.37	0.18
Cs	15.42	29.36	22.10	15.26	15.86	25.08	9.68	12.52	8.97	8.20	18.73	6.24	13.26	8.47	7.91	19.16	22.88	0.35	1.06	0.53	1.25	4.64	5.67	0.10
Ba	454.37	323.16	314.99	350.39	460.55	438.05	259.79	772.49	509.48	418.19	543.73	77.41	728.49	674.75	582.13	516.56	546.48	4.20	23.08	7.36	11.14	6.18	7.63	3.07
La	29.73	29.97	29.58	19.74	31.35	30.03	15.73	14.85	25.18	12.07	44.93	25.16	9.04	44.62	42.41	30.42	23.21	3.63	21.12	4.84	39.29	3.46	3.68	3.79
Ce	59.48	62.58	61.78	48.94	65.86	65.67	36.56	40.41	62.73	28.76	78.11	32.67	23.27	67.22	64.92	52.77	43.82	6.74	28.18	7.91	60.70	6.86	7.12	3.75
Pr	6.83	7.43	7.09	6.20	7.83	7.46	4.74	5.95	8.09	3.87	7.93	2.80	3.26	6.55	6.31	5.91	5.15	0.78	2.37	0.86	5.16	0.85	0.90	0.78
Nd	25.56	27.51	26.52	23.94	29.22	27.22	18.15	25.39	31.94	14.76	26.06	8.43	13.03	20.97	20.34	20.87	18.64	2.80	6.86	2.98	15.25	3.53	3.72	3.08
Sm	5.13	5.84	5.33	5.23	5.83	5.47	4.06	6.66	7.15	3.33	4.06	1.55	3.15	4.33	4.19	3.89	3.49	0.58	1.13	0.55	3.08	0.79	0.82	0.60
Eu	1.15	0.83	1.10	1.03	0.92	1.14	0.83	0.46	1.03	0.58	0.41	0.21	0.37	0.34	0.30	0.63	0.34	0.05	0.08	0.08	0.73	0.13	0.13	0.14
Gd	4.37	4.29	4.46	4.45	4.18	4.74	3.23	5.42	6.12	2.72	3.23	1.32	2.68	3.60	3.60	3.78	2.86	0.41	0.88	0.39	2.74	0.65	0.61	0.74
Tb	0.53	0.62	0.55	0.58	0.57	0.61	0.46	0.73	0.80	0.41	0.49	0.21	0.41	0.59	0.56	0.53	0.45	0.06	0.11	0.05	0.46	0.09	0.09	0.11
Dy	2.59	3.07	2.67	2.86	2.75	2.95	2.39	3.57	4.02	2.19	3.03	1.14	2.25	3.22	3.11	3.17	2.82	0.29	0.59	0.27	2.54	0.48	0.47	0.69
Ho	0.43	0.50	0.44	0.48	0.44	0.48	0.39	0.56	0.69	0.37	0.62	0.19	0.38	0.56	0.53	0.66	0.58	0.05	0.10	0.05	0.46	0.08	0.08	0.15
Er	1.06	1.18	1.06	1.22	1.00	1.17	1.01	1.35	1.76	0.94	1.86	0.49	0.96	1.41	1.38	2.02	1.72	0.12	0.28	0.18	1.30	0.23	0.23	0.42
Tm	0.14	0.14	0.13	0.16	0.12	0.14	0.13	0.16	0.24	0.13	0.29	0.07	0.13	0.19	0.18	0.31	0.27	0.02	0.05	0.04	0.19	0.03	0.03	0.06
Yb	0.81	0.75	0.74	0.94	0.63	0.79	0.77	0.86	1.29	0.70	1.77	0.46	0.70	1.04	1.04	1.92	1.68	0.18	0.45	0.57	1.20	0.19	0.20	0.34
Lu	0.11	0.09	0.09	0.13	0.08	0.10	0.10	0.11	0.17	0.09	0.25	0.08	0.09	0.13	0.13	0.27	0.23	0.03	0.10	0.14	0.16	0.03	0.03	0.05
Hf	1.10	0.10	0.72	0.94	0.15	0.73	0.51	0.48	0.97	0.47	1.20	0.18	0.44	0.69	0.70	1.65	1.14	0.15	0.38	0.31	1.89	0.08	0.07	0.13
Ta	1.74	1.84	1.79	1.84	1.84	1.05	1.55	1.40	2.44	1.36	1.30	0.13	1.26	2.07	2.85	1.37	1.44	0.01	0.07	0.01	1.73	0.18	0.06	0.31
Tl	2.34	2.35	2.70	1.06	1.31	0.72	0.90	1.48	1.89	1.06	0.83	0.93	1.75	0.94	0.86	0.90	3.24	1.03	4.24	0.11	0.06	0.24	0.66	0.04
W	58.13	51.05	50.97	30.71	46.65	37.91	0.00	0.00	26.46	0.00	15.69	1.37	0.00	0.00	0.00	26.31	0.00	2.20	1.54	2.71	0.00	0.00	2.09	0.00
Pb	31.09	51.00	3.31	1.54	46.60	1.38	10.66	12.45	1.87	11.19	15.70	1.40	7.44	2.83	2.66	4.03	9.08	14.65	12.78	3.11	0.02	0.57	0.49	3.72
Bi	14.96	15.87	15.97	17.63	16.58	18.10	0.00	0.00	24.20	0.00	13.16	1.36	0.00	0.00	0.00	12.34	0.00	0.32	0.43	0.32	0.00	0.00	0.85	0.00
Th	10.25	9.98	14.39	11.64	6.26	10.77	17.56	5.78	15.00	12.30	3.30	0.96	9.59	2.33	1.92	3.64	6.80	0.24	0.36	0.24	2.59	0.79	4.81	0.31
U	4.73	4.01	4.91	5.41	5.70	4.51	9.12	4.23	4.52	7.88	18.16	5.20	7.27	2.17	1.62	17.17	3.37	0.80	1.25	0.56	5.14	3.69	0.96	0.06
As	0.00	177.00	0.00		134.00	0.00	0.00	0.00	0.00	0.00	135.00	7.60	0.00	0.00	0.00	0.00	0.00	0.00	0.00	0.00	0.00	0.00	0.00	0.00
∑REE	138	145	142	116	151	148	89	106	151	71	173	75	60	155	149	127	105	16	62	19	133	17	18	15
Mg#	60	52	49	95	63	69	84	90	94	84														
ANOR	16	17	21	22	18	20	41	5	21	16														
Q'-F'	28	22	27	24	20	16	28	12	21	25														
Density	*2.64*	*2.64*	*2.64*	*2.66*	*2.66*	*2.66*	*2.66*	*2.66*	*2.67*	*2.67*	*2.69*	*2.69*	*2.69*	*2.70*	*2.70*	*2.92*	*2.92*	*3.34*	*3.34*	*3.34*	*3.53*	*2.83*	*2.83*	*2.71*

Table 5.2 - Whole-rock composition of the Botro ai Marmi lithologies

The exoskarn bodies show an increasing silica content moving to the pluton-marble contact, from 40 wt% up to 50 wt%. Total Fe and Mg show maximum values of 20 wt% and 13 wt%, respectively, in the vesuvianite-garnet rich exoskarn. Ti shows common values of 0.25-0.3 wt%, with maximum amount of 0.8 wt% in the phlogopite-rich exoskarn. K_2O and Na_2O show low values in all the exoskarn bodies (lower than 1 wt%). The CaO content, values from 20 to 24 wt%, shows a positive correlation with distance from the pluton. An exception is represented by the phlogopite-rich exoskarn, showing common values of 7-9 wt%. Th and U are lower than 3 ppm.

The chondrite-normalised REE-Y patterns for the Botro ai Marmi monzogranite, endoskarn, exoskarn, and marble are shown in Fig. 5.11. The Botro ai Marmi monzogranite (both unaltered and altered) exhibit moderate HREE fractionated pattern and moderate Eu anomaly (Eu/Eu*=0.55-0.60) comparable with those reported for other peraluminous bodies from southern Tuscany (Dini et al., 2002, 2005; Poli, 2016; Ridolfi et al., 2016). Comparing the patterns resulted from the different lithologies it is possible to observed slight but significant variations. The patterns of the endoskarn bodies, as well those of the phlogopite and vesuvianite-garnet rich exoskarns show a slight enrichment in HREE. The marble shows a comparable pattern, with lower concentration. Only the phlogopite-rich exoskarn presents a strong positive anomaly of Y. In contrast, the pyroxene-rich exoskarn shows LREE and HREE enriched pattern, with lower concentration of middle REE and a strong negative anomaly of Y.

The continental crust-normalised multi-element patterns resulting from the monzogranites (Fig. 5.12) show, again, characteristic common of crustal products from southern Tuscany (Dini et al., 2002, 2005; Poli, 2016; Ridolfi et al., 2016). The plotted data show a general positive anomaly of U, K, and Rb, together with negative anomalies of Ba, Hf, and Sr. A significant negative anomaly of Ti is also observed. Endoskarn bodies show comparable patterns, except for a marked negative anomaly of Th. On the other side, the exoskarn bodies show negative anomaly of Cs, Rb, Ba, and K. As for the REE pattern, the phlogopite and vesuvianite-garnet exoskarn patterns are comparable with the granite one. The pyroxene exoskarn shows a intermediate composition between granite and marble, with a pronounced negative anomaly of Nb. Moreover, Th is progressively depleted from granite, through endoskarn, to garnet and then diopside exoskarn. The overall multi-element patterns of the different lithologies are similar, except for the pyroxene exoskarn.

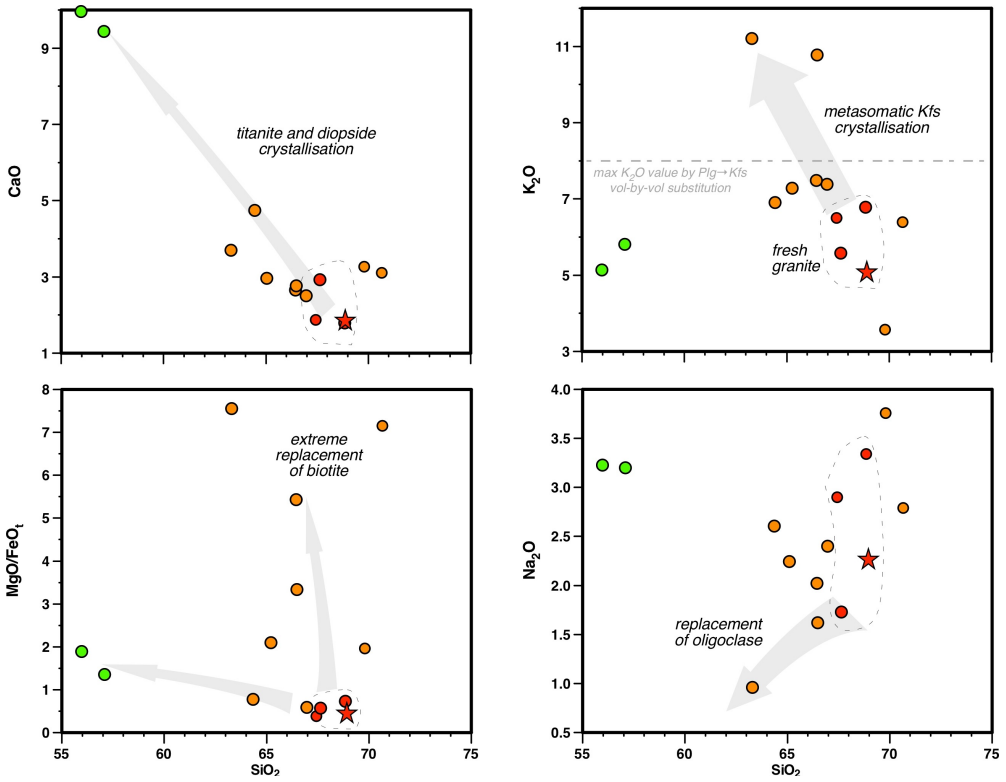

Fig. 5.9 - Selected oxide diagrams for the Botro ai Marmi fresh monzogranite (red), altered granite (orange) and endoskarn vein (green). The red star indicate the monzogranite initial composition (sample GBM5).

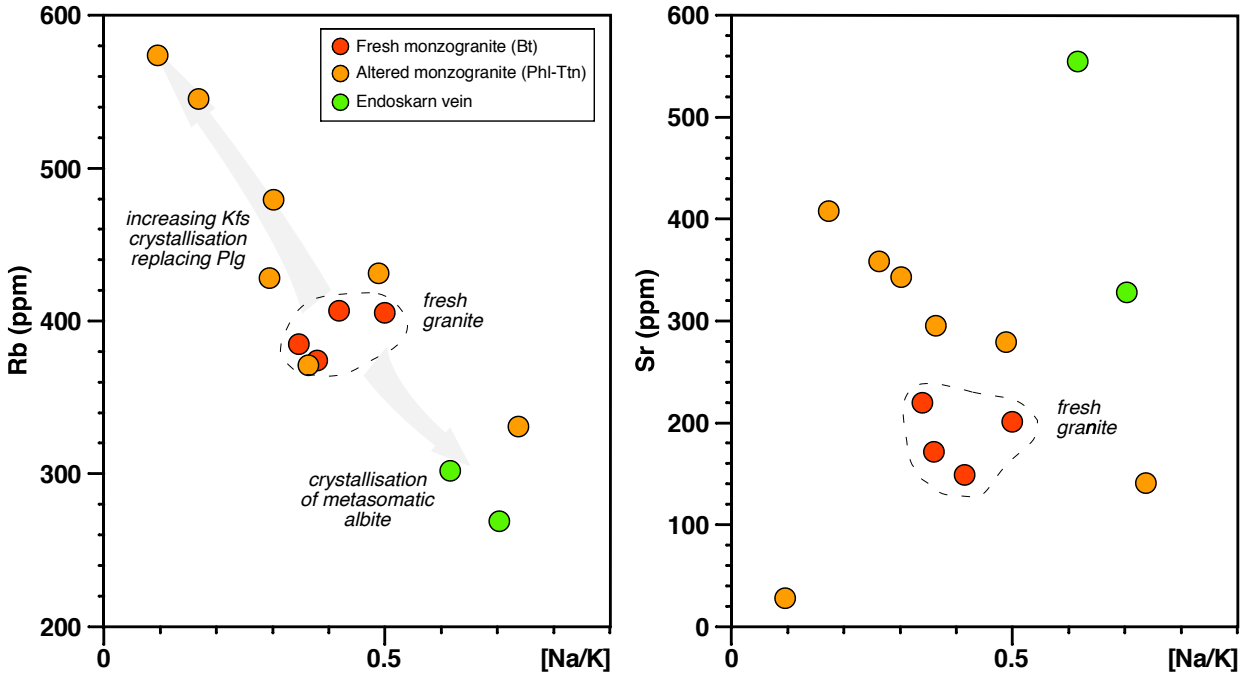

Fig. 5.10 - Na/K (cationic) vs. Rb (ppm) and Sr (ppm) showing the results of plagioclase replacement by K-feldspar.

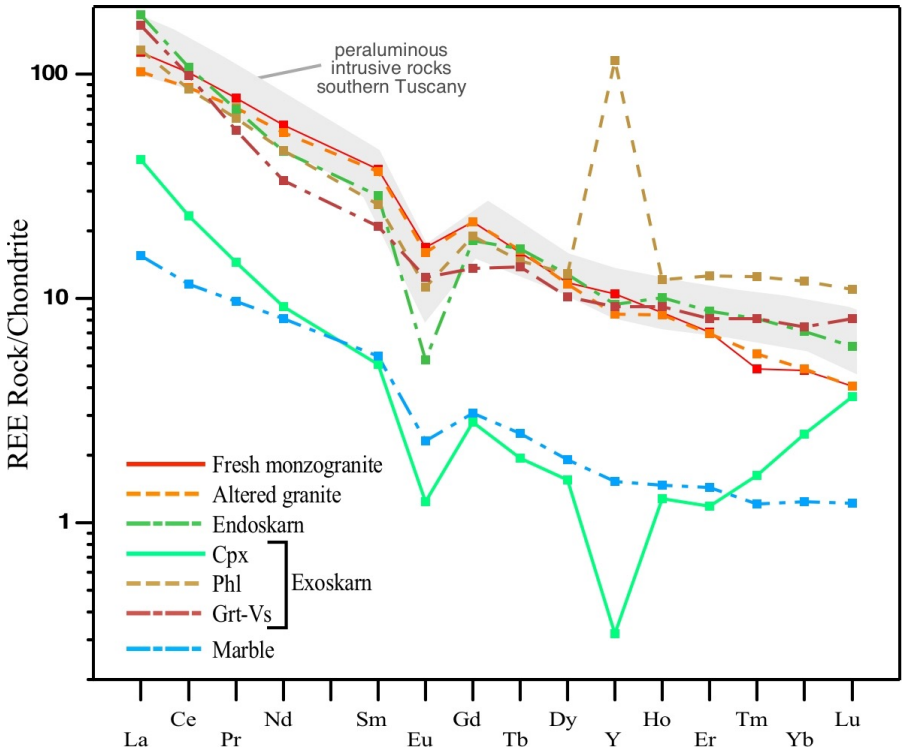

Fig. 5.11 - Chondrite normalised REE patterns for Botro ai Marmi granite, endoskarn, exoskarn, and marble. The shaded field represent the REE composition of the peraluminous intrusive rocks from southern Tuscany (after Pinarelli et al., 1989; Poli and Peccerillo, 2016). Normalising values after Sun & McDonough (1989).

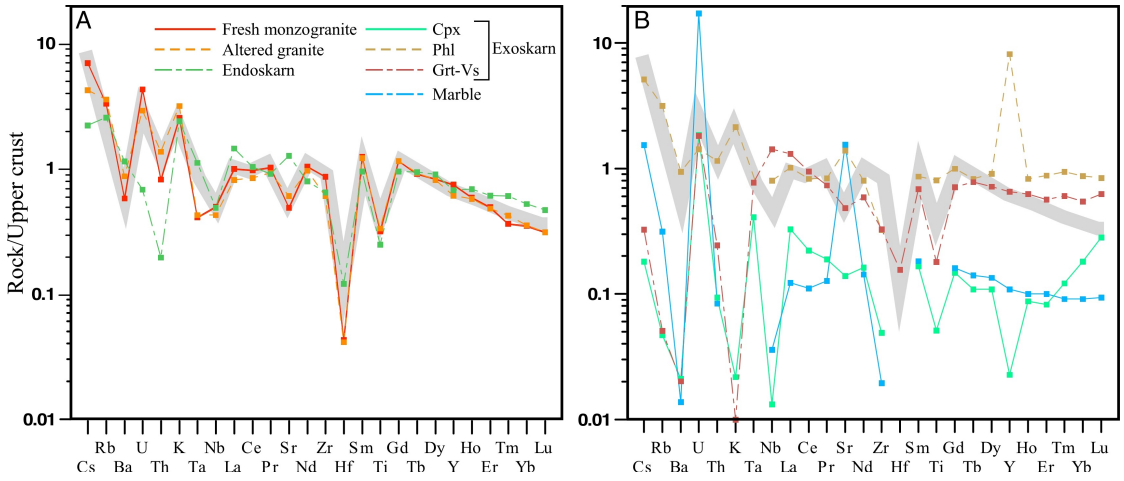

Fig. 5.12 - Upper-crust normalised multi element spider diagrams. A) Granitic rocks from Botro ai Marmi compared with the composition of the peraluminous intrusive rocks from southern Tuscany (shaded field; after Poli et al., 1989, 2016). B) Comparison between the lithologies observed at the Botro ai Marmi mine Normalising values after Sun & McDonough (1989).

Lithological and geochemical distribution with depth: the MS3 borehole

The relative concentration of elements varying with depth outlines the occurrence of metasomatic alteration boundaries or lithological contacts (Figs 5.13, 5.14). The pure marble shows a net decrease of the CaO/MgO ration with depth. These results correspond to the decrease in dolomite content, moving from stratified black limestone to massive limestone. Zn shows is maximum value at the top of the perforation (up to 500 ppm) with tendency to decrease with depth. No significant concentration of Zn-minerals were observed, except for small hemimorphite ($Zn_4Si_2O_7$ (OH) $2H_2O$) and sphalerite (ZnS) crystals (Samim, 1983). Li and F values show a positive correlation, increasing in correspondence of pyrrhotite and scheelite mineralisation. Worth of note are the high values of Sr in the marble (up to 900 ppm), that showed a general decrease with depth in accordance with the decreasing of CaO/MgO ratio. In the granite fraction, Sr shows a twofold positive correlation with depth, starting from values of about 200 ppm (values obtained in this study from samples of fresh granite collected at the Botro ai Marmi mine). Between 220 and 400 m, Sr increases up to values of 500 ppm. After a sudden decrease to initial values (at 420 m), Sr increases again up to 450 ppm. Nb values define a similar trend. Between 80 and 150 m the occasional increase of Co, Cr, Ni, Nb, Rb, V, Ti, Y, Zr, and Zn correspond to mineralised exoskarn bodies (Fig. 5.13). Between 180 and 220 m occurred a fine-grained exoskarn (Samim, 1983) characterised by high values of Fe and Cu, corresponding to pyrrhotite-pyrite-magnetite mineralisation. F values increase with depth, showing occasional maximum likely related to phlogopite crystallisation (Fig. 14). The transition between the exoskarn and the monzogranite is characterised by few metres of endoskarn. Worth of note are the high values of Fe, Cu (up to 800 ppm) and F (up to 5 wt%), corresponding to mineralisations of pyrrhotite, fluorite and minor chalcopyrite (Samim, 1983). Sn reaches values up to 700 ppm in correspondence of endoskarn veins crosscutting the monzogranite (cassiterite, adularia, green fluorite, pyrite, garnet).

At 220 m of depth occurred the top of the granite body. The Al_2O_3/FeO_{tot} ratio shows high value until 300 m, then decrease until 400 m, as consequence of Fe-rich calc-silicate crystallisation. P shows constant values of 0.15-0.2 wt% in the granite and 0.02 wt% in the marble fraction. The occasional increase up to 0.1 wt% (in the marble) and up to 0.35 wt% (in the granite) correlate with higher apatite abundance (apatite effect). The Al_2O_3 values show a general increase with depth (mirroring the twofold trend of Sr), with a transition area between 350 and 400 m, that reset the system to initial values. Occasional increase of Zn, Pb, Cu, and S correlate with pyrite-sphalerite-galena mineralisations (Samim, 1983). The overall granite section shows high values of K (5-9 wt%), respect to values of the fresh granite (3.5-4 wt%; this study), until 520 m of depth where decrease rapidly to the protolith value. These evidences correspond to a significative, diffuse replacement of plagioclase by K-feldspar.

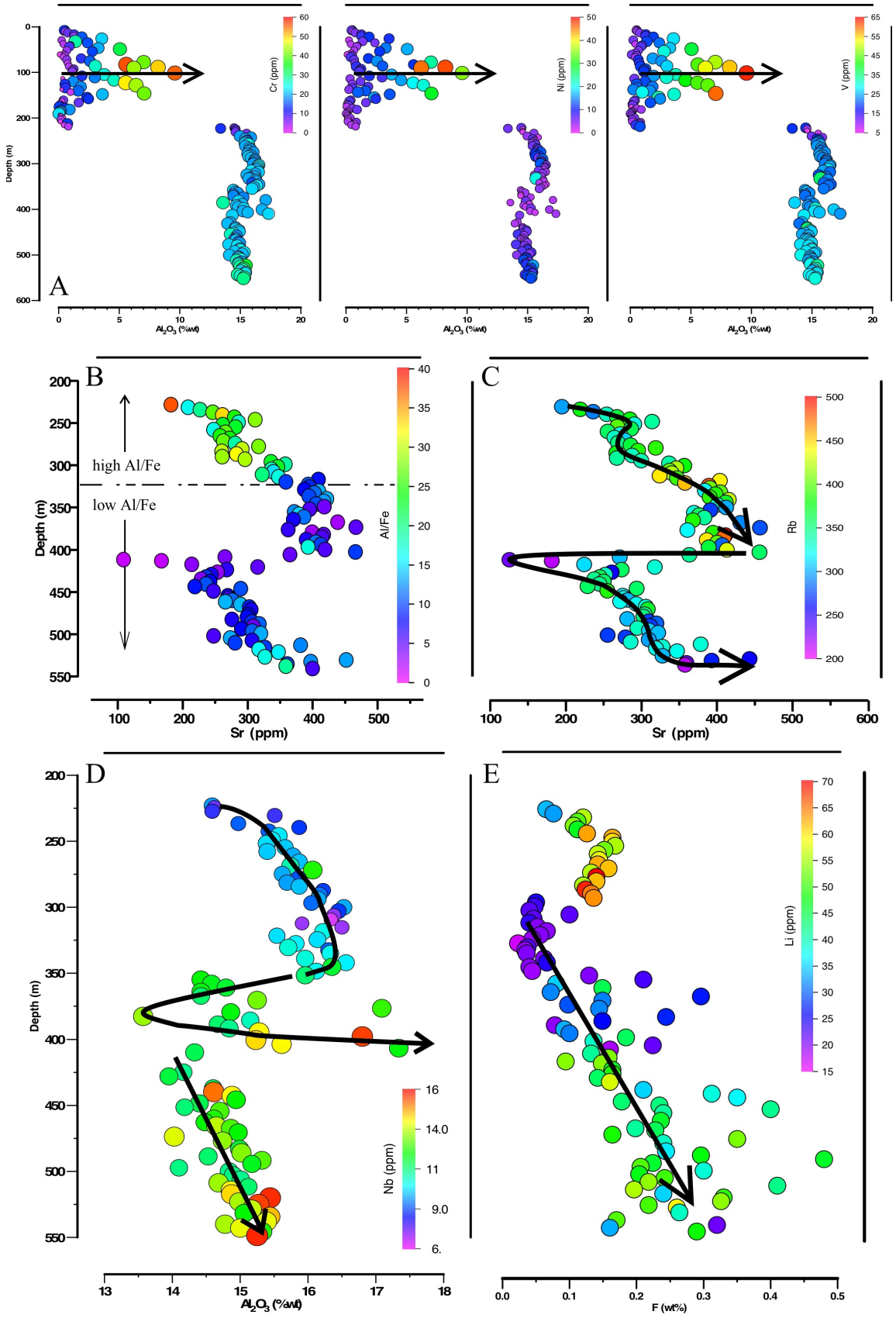

Fig. 5.13 - Selected diagrams showing the geochemical variation with depth in the MS3 borehole. Major elements oxides as wt.%, trace elements as ppm. Arrows indicate the main patterns.

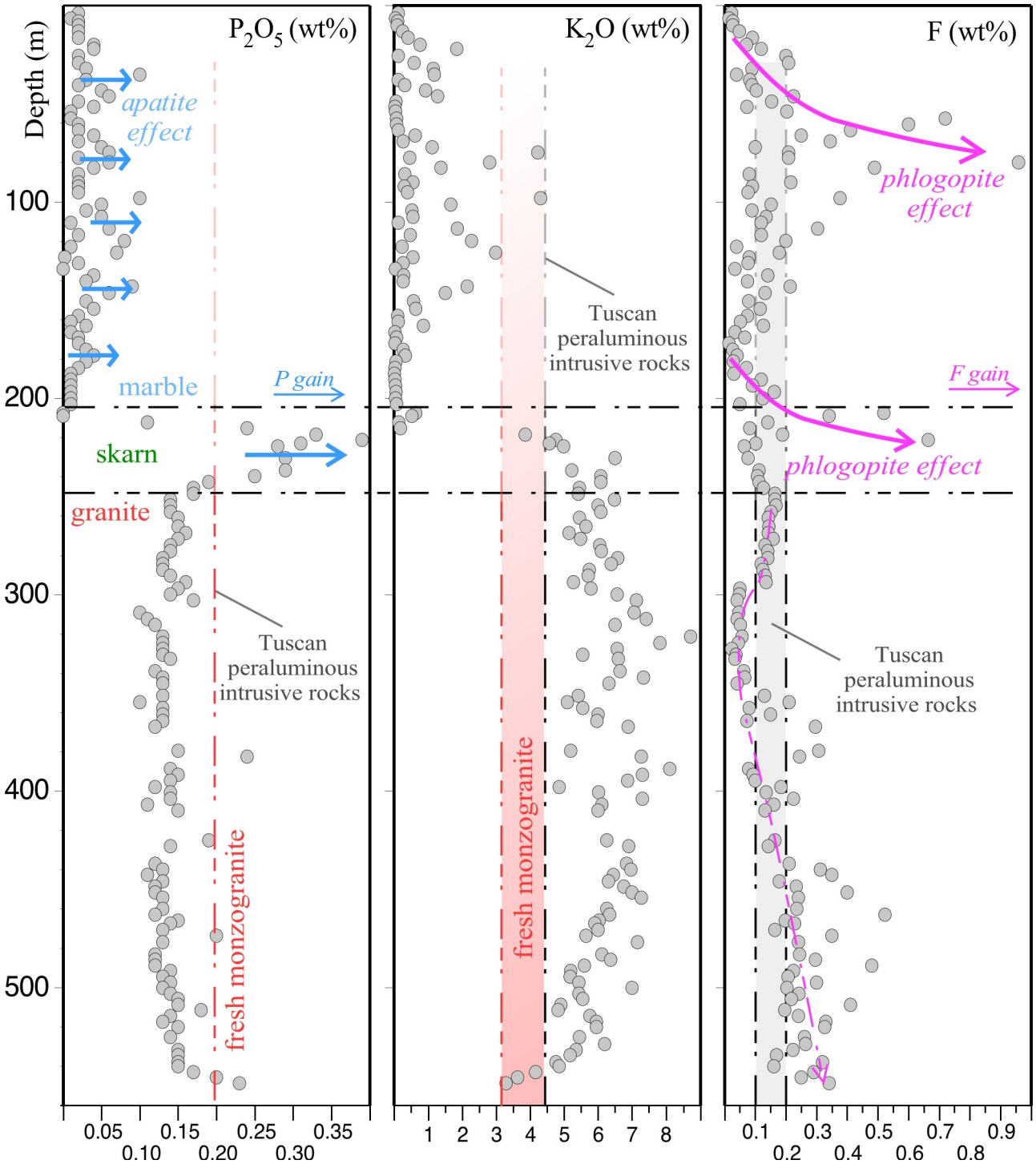

Fig. 5.14 - P_2O_5, K_2O, and F (wt%) variation with depth in the MS3 borehole. The dashed lines indicated the mean composition of the fresh granite (red) and of the peraluminous intrusive rocks from southern Tuscany (black). The arrows indicate the progressive crystallisation of apatite (blue) and phlogopite (violet). Values of intrusive bodies from southern Tuscany are from Poli et al. (2016).

5.6. Discussion

Interpretations of field relations

Field observations, petrographic evidences, and geochemical data allow to constrain the metasomatic processes affecting the Campiglia magmatic-hydrothermal system. The monzogranitic pluton shows a N-S structure reaching an apophyses in the Botro ai Marmi area. The outcropping portion of the pluton is at the top of this bulge, exposed mostly thanks to row ceramic mining activity. The results obtained from field observations and borehole analysis show that the metasomatic alteration reached its peak in this structural maximum. These observations suggest that fluid(s) circulation exploited this preferential pathway to produce diffusive potassic alteration of the monzogranite. Alteration propagated in the monzogranite decreasing toward the unaltered monzogranite relicts, as highlighted by decreasing replacement of plagioclase by K-feldspar. Moreover, endoskarn veins formed along the main magmatic joints show a similar orientation respect to the main pathway and a decreasing alteration approaching the border. These evidences support the preferential circulation of fluids along fractures. Similar observations, suggesting magmatic joints as preferential pathway for fluid circulation, have been obtained for the Gavorrano pluton (southern Tuscany). There, quartz-pyrite hydrothermal veins exploited magmatic joints (Rocchi et al., 2003), but no calc-silicates are found along veins or close to the pluton-host contact. However, metamorphic temperature of 550-600 °C obtained from the surrounding carbonate and Paleozoic deposits are comparable with those from the Botro ai Marmi intrusion. Moreover, at Campiglia the main exoskarn bodies are distributed along marble bedding, or selectively replace the ductively folded carbonate host rocks. The main metasomatic activity is concentrated in the area above the pluton bulge, corresponding to the mostly altered monzogranite fraction. Moreover, exoskarn bodies sampled by boreholes at distance from the pluton bulge support the ability of fluid to exploit marble bedding for migrating at long distance. Furthermore, the significative displacement to south of the metamorphosed carbonatic sequence due to the granite emplacement testify a preferential pathway for element circulation toward the border of the pluton body. This interpretations, together with evidences of Fe, Sn, and minor W mobilisation during granite metasomatism, allow to speculate on the origin of the distal Sn-Fe(-W) deposits of Mt. Valerio, 3 km south of the monzogranite outcrop (Fig. 5.1). Indeed, the most peraluminous plutons world-wide are associated with Sn skarns, a skarn type which has been linked to melts of continental crust containing a significant sedimentary component (Meinert et al., 2005).

Elemental gain/loss during metasomatism

When plutonic igneous rocks have been modified on a large scale by the introduction of some elements and the subtraction of other elements so that the chemical composition (and mineralogy) of a igneous rock would progressively be changed, an investigation of these changes is needed. Thus, have been developed calculations of mass-balance quantities of the elements that have been added and/or subtracted. During alteration, the volumes of plagioclase and biotite would become less, phlogopite would replace biotite, while K-feldspar would replace plagioclase and increase in abundance. Such calculations to be accurate would also have to take into account density and volume changes because the newly formed minerals in the more granitic rocks have lower densities and different volumes from that existing in the original rock. Some assumptions also have to be made, i.e., whether to balance the chemistry assuming that at least one element is immobile (e.g., Baugartner and Olsen, 1995; Grant, 1986, 2005; Gresen, 1967; López-Moro, 2012). In this context, a series of isocon diagrams (e.g., Baugartner and Olsen, 1995; Grant, 1986, 2005; López-Moro, 2012) for selected samples have been realised to quantify the relative losses, gains or immobility of elements during the alteration processes. Indeed, chemical mass transfer, resulting from metasomatic processes, are basically quantified by comparing the chemical composition of an unaltered (initial) and an altered rock (Durand et al., 2009). The initial composition of the granite has been selected according to petrographic and geochemical observations. The sample has been collected as

far as possible from the contact with the altered granite and is apparently unaffected by metasomatism (unaltered biotite). The initial composition has been compared with the phlogopite-titanite-bearing monzogranite (altered granite) and the endoskarn. The main major and trace element changes resulting from the metasomatic alteration are illustrated in Fig. 5.15 andFig. 5.16. The quantification of volume changes and mass-balance modelling (isocon diagram) has been realised according to López-Moro (2012). The selection of immobile elements for isocon diagram construction is performed according to volume factors and clusters of slopes (López-Moro, 2012).

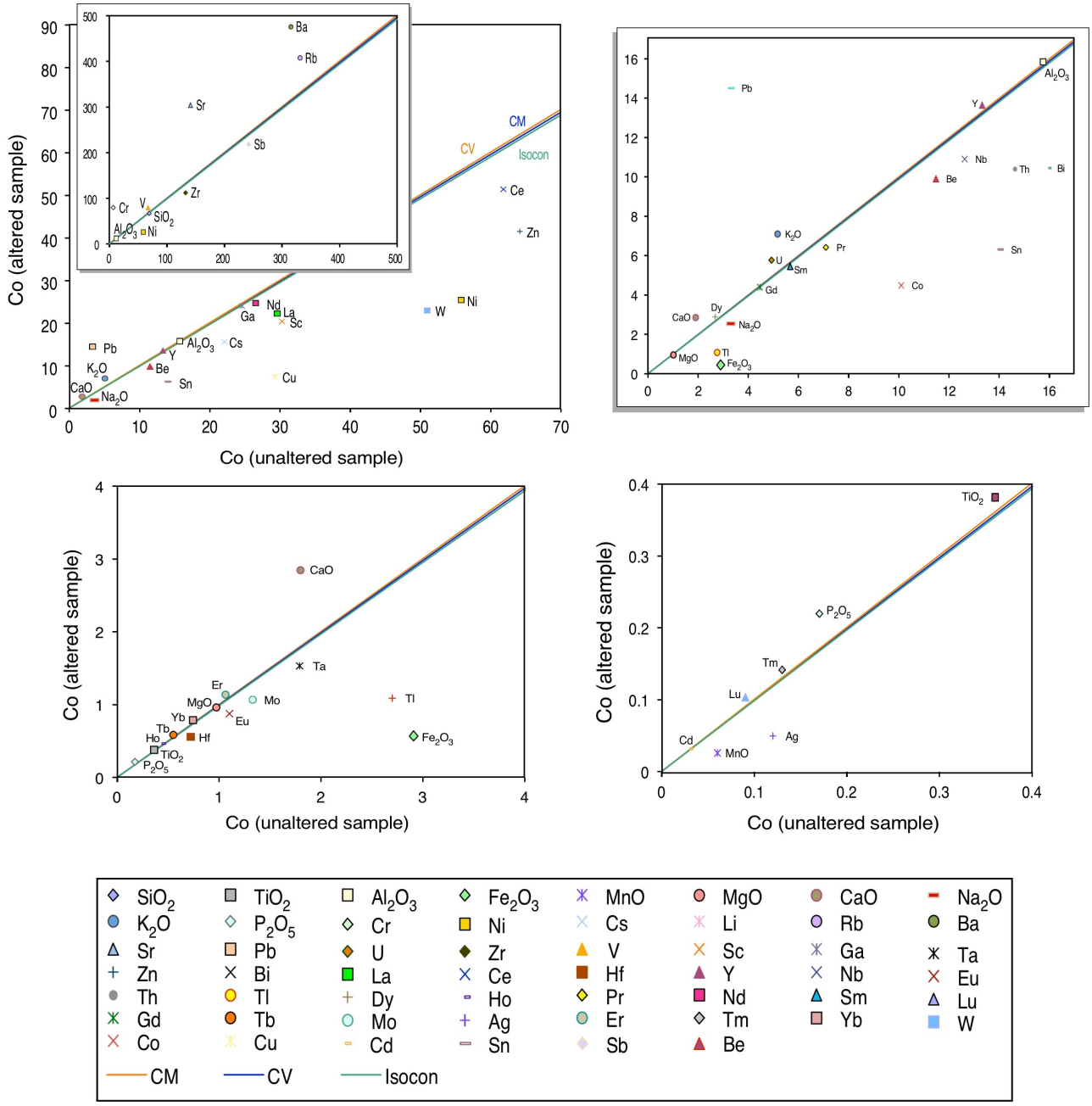

Fig. 5.16 - Main isocon diagrams of fresh granite against endoskarn vein from rim (circle) to middle (square) and to core (triangle). Best-fit isocon (green) using the cluster of slopes method. Isocon at constant mass (blue) and constant volume (orange) are also shown.

The mass-balance resulted from comparison between biotite-bearing and phlogopite-titanite-bearing granite is illustrated in Fig. 5.15. Al_2O_3, TiO_2, and SiO_2 are selected as immobile elements (slope and Fv=~1). The resulting overall volume and mass changes are less than 1%. Total Mg and Ti do not show significant variations. An explanation for Ti invariance could be its redistribution from biotite, in the unaltered granite, to titanite, in the altered granite. This interpretation is supported by the gain of Ca, that in turn is supported by gain of P (apatite crystallisation). The massive loss of Fe, the significant loss of Na, and the increase of K are caused by the complete alteration of biotite and the plagioclase replacement by K-feldspar in the altered granite. The abundant crystallisation of K-feldspar could also explain the Rb, Ba, and Sr enrichment. Indeed, Rb and Sr are rather compatible in K-feldspar and biotite, but highly incompatible in plagioclase. Moreover, the positive correlation between Sr vs. Na/K and the negative correlation between Rb vs. Na/K ratio (Fig. 5.15) are compatible with plagioclase replacement by K-feldspar. Moreover, because the composition of metasomatised rocks are likely to be somewhat variable as consequence of accessory minerals concentration, the isocon analysis of the trace elements yield variable results. The main evidences are the general loss of metals (Cu, Zn, Zr, Ni, Mo, Sb, Tl) and the major depletion of Sn and W in the altered granite. On the other hand, the results obtained from samples from the borehole evidenced the loss with depth of MgO, Cr, Ni, Nb, and Sr, probably linked to the increasing metasomatic alteration of biotite and K-feldspar (replaced by adularia).

The gains and losses during the metasomatic stage(s) forming the endoskarn veins (average of five samples) are much more significative (Fig. 5.16). The apparent gains an losses during the acidic metasomatism is shown in Fig. 5.16, Al is selected as immobile elements to realise a tentative isocon. The resulting overall mass and volume losses are about -5%. Si and Na show a significative loss, mostly as the result of the replacement of plagioclase by K-feldspar. Biotite lisciviation caused a massive Fe loss. The apparent Ca, Al, Mg, P, and K gain is likely to be caused by both the acidic and potassic metasomatic processes. In particular, diopside and apatite crystallisation are likely responsible for Ca, Mg, and P gain, while metasomatic K-feldspars is the better candidate to account for the gain of Al and K. As observed for the phlogopite-titanite bearing granite, Rb, Ba, and Sr are gained during the metasomatic processes, while metals are lost. Endoskarn veins, from border to core, show the increasing lost of Si, K, Rb, Ba, and Sr probably resulting from the replacement of K-feldspar by albite. On contrary, gain of Fe, Mg, Ca, and Na is likely linked to the massive crystallisation of calc-silicates at the vein core. Moreover, gain of REE could be ascribed to the crystallisation of accessory allanite. The other trace elements remain almost unvaried (Fig. 5.16).

Chemical mass transfer has been quantified between the original composition of the marble and the different exoskarn products. The marble protolith composition has been calculated by averaging three unaffected marble samples from the host rock. They consist of medium to coarse-grained white-rose calcite marble, with calcite content above 90% and marl-rich grey impurities. The main accessories are dolomite, quartz, phyllosilicates and minor sulfides. The samples have been collected as far as possible from the contact with the monzogranite. On the other hand, exoskarn bodies are mainly characterised by metasomatic diopside, vesuvianite, titanite, phlogopite, garnet, epidote, quartz, and accessory apatite, zircon, and fluorite. Mass balance calculations suggest an overall strong decrease of total Ca and Sr (up to 70%), correlating with the decrease of calcite content as the contact is approaching. Most other chemical elements are gained during metasomatism. Strong gain of Si, Fe, Mn, and Ti, as well as Cr, Sc, and Zn have a mutual relationship with calc-silicates crystallisation. The gain of REE, Zr, Y is ascribable to the crystallisation of HFSE/REE accessory minerals, such as zircon, allanite and/or to REE-rich calc-silicates (e.g., vesuvianite, titanite). The content of W, Sn, Pb and other metals increase toward the contact with the intrusion, showing the lowest values in the garnet-vesuvianite skarn. The Al content increases from diopside-, through garnet-vesuvianite- to phlogopite-skarn, correlating with phlogopite abundance. P content is strictly related to the abundance of apatite, that increase in phlogopite and garnet-vesuvianite skarn. The REE distribution, as observed in endoskarn, is mostly related to calc-silicates and accessory minerals abundance. For example, the enrichments of La and Ce are petrographically testified by allanite crystallisation. Usually diopside exoskarn shows a loss of REE (except for La, Ce), while phlogopite and garnet-

vesuvianite skarns show their gain, with positive anomalies of HREE. Garnet may be a good candidate to account for the gain of HREE. Indeed, garnet has very high partition coefficients for the HREE (Gaspar et al., 2008). Thus garnet contains most of the HREE budget of the whole-rock. As stated by field and petrographic observations, the phlogopite-rich exoskarn derived from ductilely folded marl-rich marble fraction. Comparing these lithologies emerges (i) the gain of Rb, Sr, Ba, K and Al, correlated with phlogopite, K-feldspar, and albite crystallisation, (ii) the prominent depletion in Ca, corresponding to the abundant transformation of calcite, and (iii) the strong gain of metals and trace elements such as Sn, W, Sb, and Nb. (iv) Moreover, the significant gain of LREE correlates with the crystallisation of accessory allanite. Indeed, allanite has a very high partition coefficient for LREE (Bea, 1996; Herman, 2002).

The mineralogical and geochemical evolution from marble to exoskarn documents the elements transfer during metasomatism. The general volume loss, up to 25% in the Grt-Vs skarn, probably resulting from the marble decarbonation never correlate with significant mass loss. Indeed, the increase of the density (up to 70% in the Grt-Vs skarn), due to new calc-silicate crystallisation, compensate the mass loss resulting from the decarbonation process.

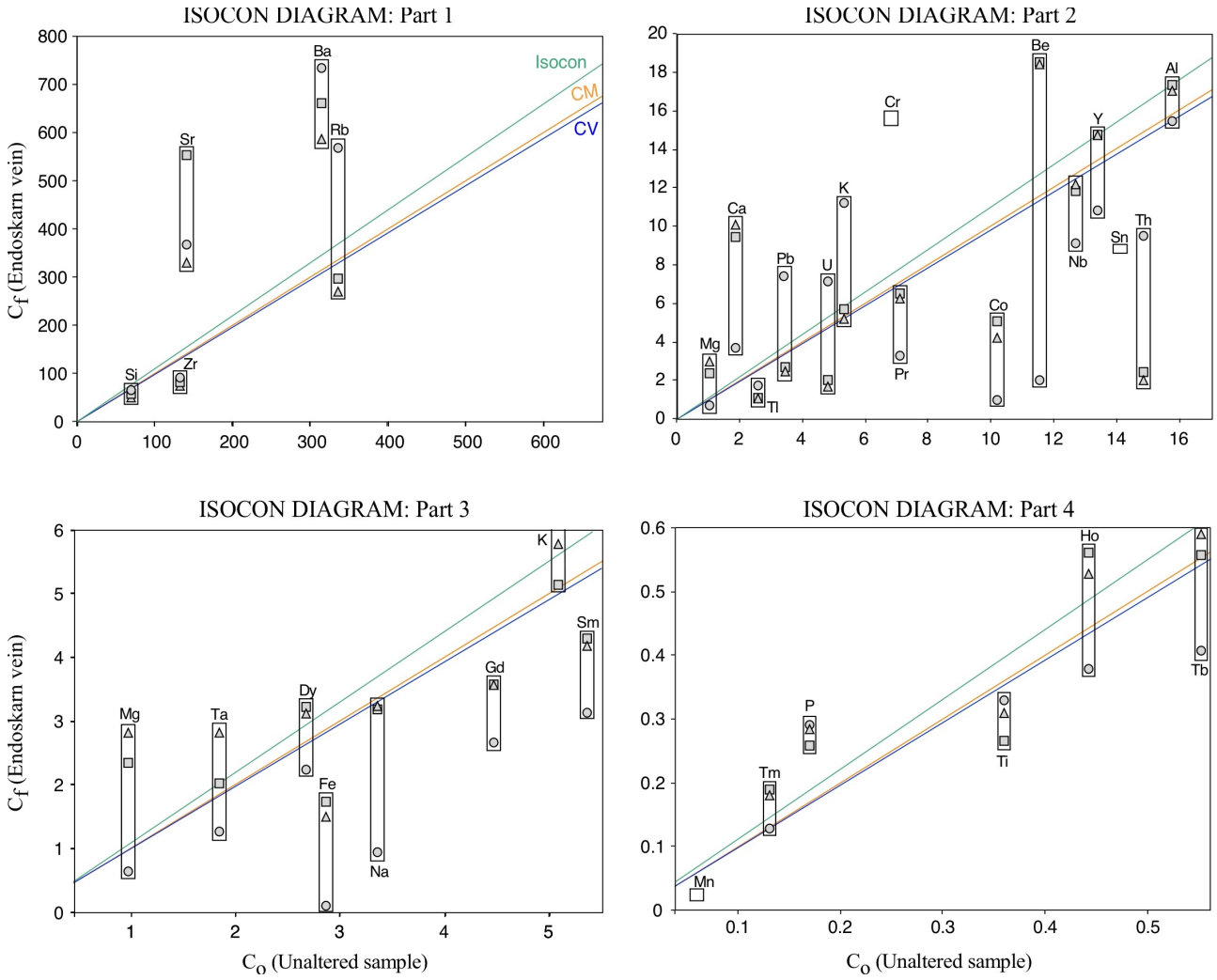

Fig. 5.16 - Main isocon diagrams of fresh granite vs. endoskarn vein from rim (circle) to middle (square) and to core (triangle). Best-fit isocon (green) using the cluster of slopes method. Isocon at constant mass (blue) and constant volume (orange) are also shown.

General metasomatic patterns: mineral assemblages during metasomatism

The evolution of the Botro ai Marmi granite and skarn could be subdivided into different stages related to different rock textures and mineral assemblages. These are a magmatic stage, an alkali metasomatic stage, a Ca(-Mg)-metasomatic stage and a final acidic hydrothermal stage (Fig. 5.8). Thus, relatively simple patterns of alteration could be complicated by the overlap of multiple metasomatic events. Reactive transport models are generally too poorly constrained to offer unique solutions, while equilibrium calculations are at best an approximation. Even in systems where local fluid-rock equilibrium is not attained, however, reactions generally progress along a vector similar to that defined by equilibrium models. Equilibrium models can therefore provide a qualitative indication of system behaviour (Meinert, 2005). In this context, we proposed a genetical interpretation for the mineral assemblages observed at the Botro ai Marmi mine, relating different mineral paragenesis to different alteration stages.

Magmatic stage

The timing of feldspars crystallisation is critical to understand the magmatic evolution of the Botro ai Marmi monzogranite. Compositions and textural observations indicate the presence of at least two generations of igneous plagioclase. The first generation is represented by the andesine cores (~An_{35-45}), which show a weak calcic-sodic core to rim compositional zoning. The low-An oligoclase (An_{10-15}) rim is interpreted as a second generation according to the clear compositional gap with the andesine cores. This marked zoning requires a physical change in melt conditions, which would alter the stability of andesine to the point where oligoclase would nucleate. A sudden decreases in pressure is the preferred catalysts (e.g., Plümper and Putnis, 2009). Thus, first generation of plagioclase (An_{35-45}) would likely has crystallised early in the magma chamber with biotite, K-feldspar, quartz, cordierite, as well as accessory zircon, apatite, and ilmenite. The rapid ascent and the sudden change in pressure condition allow the crystallisation of a thick oligoclase rim on andesinic plagioclase. Late exsolution of B-rich fluids resulted in the crystallisation of tourmaline-quartz orbicules. Indeed, tourmaline has been found to crystallise during the late-magmatic to post-magmatic stage in many granite types, although represent a common magmatic mineral in some felsic, peraluminous granites (Pichavant and Manning, 1984). The emplacement of the monzogranitic pluton resulted in the metamorphism of the host carbonatic sequence and the crystallisation of an almost pure marble. Shortly after emplacement or during a late-magmatic stage, circulation of B-rich fluid formed disseminated tourmaline-quartz orbicules, which tend to be particularly abundant in zones of fracturing forming veinlets system. Fluid enrichment in B is possibly inherited from a source region containing evaporites (similar features are reported for several granite world wild; e.g., Pirajno, 2009; Pirajno and Schlögl, 1987; Pollard, 1987).

Potassic metasomatism

After emplacement, the biotite bearing monzogranite was affected by an intense, pervasive potassic alteration (K-metasomatism). Potassium metasomatism converted the fresh monzogranite - K-feldspar+andesine (An_{35-45})+oligoclase (An_{10-15})+quartz+biotite±ilmenite-apatite-zircon-monazite - to the alteration mineral association - K-feldspar+andesine (An_{35-45})+phlogopite+chlorite+titanite±rutile±apatite-zircon-monazite±fluorite.

In a closed system subject to thermal gradients K/Na activity ratio of a fluid in equilibrium with two alkali feldspars at high temperature would be great than that of a fluid in equilibrium with the same assemblage at lower temperature. If such a system was open (e.g., porphyry copper system), infiltration of fluid from a higher temperature environment to a lower temperature environment would promote exchange of potassium in the fluid for sodium in the wall rock. Complete replacement of oligoclase, and partial replacement of andesine by K-feldspar could be ascribed to a mechanism of alkali ion exchange between fluid and feldspar phases controlled by a replacement reaction (e.g., Orville, 1963; Moore and Liou, 1979):

$$(NaAlSi_3O_8)_{solid} + (K^+)_{aq} \rightarrow (KAlSi_3O_8)_{solid} + (Na^+)_{aq}$$

Irregularly shaped K-feldspar, mostly replacing the oligoclase rim, has a composition similar to that in the original granite, suggesting that the the pre-existing oligoclase is converted directly to K-feldspar. Its abundance decreases from about 30 vol% in the unaltered monzogranite to 5 vol% in the phlogopite-titanite granite. Replacement of plagioclase also occurs along polysynthetic twinning and, to a smaller extent, along fractures. The alteration increases with distance from the unaltered granite relicts. The local Si gain, in some of the altered granite, corresponds to crystallisation of albite and quartz. The reaction between K-feldspar and plagioclase implies the mobility of Al^{3+} (that may be incorporate in sericite), Na^{+} and Ca^{2+}. The elements liberated in the reaction might have been fixed by calcite, epidote and fluorite. Isotropic replacement of plagioclase by K-feldspar supports a pervasive circulation of fluids between grain boundaries. The same evidence is highlighted by crystallisation of metasomatic minerals around the igneous grain boundaries. Thus, the selective replacement of plagioclase along its oligoclase rim is the result of a greater interaction with metasomatic fluids. Moreover, loss of sodium from plagioclase could produce local crystallisation of albite.

During this stage of potassic alteration biotite is completely replaced by phlogopite (50%)+chlorite (30%)+titanite (20%) association. Titanite has been partially converted to rutile during a later stage. Parry and Downey (1982) describe the hydrothermal alteration of biotite considering both iso-volumetric and Al-conservative reactions. They conclude that the process conserves Al and requires variable additions of K and Mg, as well as significative subtractions of Fe. Thus, the alteration resulted in a significative volume loss (up to 30%) filled by the products of other reactions (titanite, rutile, minor quartz and adularia). Mg^{2+} ions were added, while Fe^{2+} ions were lost. The overall reaction conserves Ti+Al within the pseudomorphic chlorite-titanite-phlogopite assemblage. Fe^{2+} likely contributes to the crystallisation of new Mg-Fe calc-silicate in the exoskarn bodies. Moreover, the accessory minerals included in the biotite crystals are interested by intense metasomatic alteration. Primary deposition of iron sulfides accompanied potassic alteration. These sulfides were remobilised and redistributed during both acidic and late phyllitic alteration.

Ca(-Mg)-metasomatism

The increasing acidity of metasomatic fluids due to mixing with high-temperature Ca-rich fluids triggered a Ca-metasomatism stage. Calcic alteration affected the monzogranite along magmatic joints, and, in the upper end of the pit, the monzogranite adjacent to the contact with the host marble. The distribution and density of new Ca-rich assemblage is directly correlated to the distribution and intensity of the calcic-metasomatism. Indeed, the preferential fluid circulation along magmatic joints lead to the development of endoskarn veins, characterised by significative replacement of the original magmatic paragenesis by crystallisation of Ca-Mg-rich assemblages with diopside +phlogopite+chlorite+titanite±epidote±calcite. The metasomatic replacement is highlighted at the core of the veins, showing higher calc-silicates concentration correlated with Ca and Mg increase. These reactions promoted mass transfer of SiO_2 and MgO. The mineral assemblage of the original monzogranite required a significative input of Mg and Ca to produce the resulting mineral assemblage. On contrary, deeply altered monzogranite at contact with endoskarn veins shows the highest values of K and the complete replacement of plagioclase by K-feldspar and sericite. At the same time, the increase of Rb, Ba and Sr values, whit Na decreases, correlates with K-feldspar crystallisation. Thus, simultaneously reactions involving plagioclase, K-feldspar, biotite, and accessory minerals converted the rock to a new Ca-rich mineralogical association.

In the upper end of the pit, pervasive overprinting of the bedded marble resulted in a banded exoskarn. A rock composed essentially by calcite±dolomite±micas has been replaced by diopside+hydrogrossular garnet+vesuvianite +allanite+titanite+phlogopite±scapolite assemblage. The distribution and density of these minerals reflect the relative mobility of major elements, and in a lesser extent the host carbonate composition. For example, the occurrence of Mg-rich phlogopite exoskarn, along previously folded marble level, may be related to a lithological variation with greater abundance of marly impurities (micas-rich fraction). These observation highlight the selective process of circulation of Fe and Mg also several metres into the marble. On contrary, Ti (usually behaves as immobile element) shows only a

local mobilisation. Indeed, abundant crystallisation of titanite and rutile occurred in close spatial relation with deeply altered biotite. In the endoskarn veins titanite is more abundant at the border, decreasing moving to the cores. Moreover titanite abundance decreases in distal exoskarn (Phl-rich exoskarn). However, monomineralic veins of centimetric titanite has been found. Thus, this system required the input of total Si, Mg, Fe and Ti from an external source. This implies a relative decrease in concentration for immobile elements like, for example, CaO. This element input is coeval with the formation of calc-silicates and the release of CO_2 by the decarbonation reaction (Harlov and Austrheim, 2013). This results in a composition close to that of the studied samples in the vicinity of the contact.

Sulfides post-date the formation of the calc-silicate skarns, occurring as fracture infill, disrupted primary cavities and brecciated portions of the metasomatic bodies. In a late stage, muscovite±oxides may partially replace biotite and chlorite. Sericite also occurs owing to the break-down of plagioclase. Furthermore, numerous quartz and calcite+sulfide +oxide bearing veins, from few millimetres to decimetres in width, are irregularly developed in the system following the main fractures of the pluton and folded marble in the host rock.

Thus, the interaction between monzogranitic and CO_2-rich fluids, released during calc-silicate reactions, can explain the high K_2O and Ba, and to a lesser extent, the Sr content in the altered samples. Hydrothermal fluids released from an external source may be responsible for high Rb, as well as K_2O, MgO, Fe concentrations in altered samples, in as much as country rocks have very low abundances of these elements. Hydrothermal fluids can also account for the existence of isotopic disequilibrium among coexisting phases. Assimilation of marble country rocks can account for the high CaO and Sr contents observed in the altered samples. However, this process can only justify CaO and Sr abundances in granite samples very close to the granite/wall-rock interface. In fact, the assimilation is limited by the amount of heat available and by the surface area of the assimilated rocks (Durand et al., 2009).

Acidic alteration

The increasing acidity of circulating fluids, possibly related to mixing with acidic-fluids released at depth by the magmatic body, is testified by patchy zoning (i.e., titanite), as well as dissolution-recrystallisation texture, pseudomorphs, and pronounced zoning in calc-silicates (Figs 5.5, 5.6, 5.7). This stage could be responsible for the strong metasomatic alteration of biotite, interesting also the accessory minerals which includes (apatite, zircon, monazite, ilmenite). These interpretations are supported by crystallisation of aggregates of euhedral accessory minerals (apatite, zircon, monazite) bordering the deeply altered biotite. Moreover, deeply chloritised biotite is frequently interlayer by fluorite crystals. The crystallisation during this stage of Ca-REE-rich minerals, such as allanite, ekanite, cheralite, supports the mobilisation of HFSE/REE by fluids characterised by increasing acidity (Fig. 5.5). The continuous crystallisation of calc-silicates (Ca sequestration) increases the acidity of the fluids, leading to the alteration of earlier calc-silicates with diffuse crystallisation of accessory minerals (e.g. thorite, uraninite, zircon), usually on their surface or into fractures. Again, F-rich fluids circulation is supported, in endoskarn, by pseudomorph textures developed as fluorite-pyroxene-calcite-quartz aggregate replacing diopside-calcite-quartz assemblages, or in exoskarn, by the pseudomorphic replacement of Ca-REE-silicates (i.e., ekanite replaced by thorite-quartz pseudomorphs). The abundance of quartz-fluorite veins associated with crystallisation of HFSE-REE and Th-U accessory minerals (mostly uraninite) aggregates, in veins and inclusions widespread through the system, indicates that this stage postdated alkali- and Ca-metasomatism. Moreover, whereas the K-metasomatism alteration type involved pervasive replacement restricted to the granite, the acidic metasomatism extended also into the surrounding host rock and involved the formation of veins filling fractures in the granite, massive body at pluton-marble contact, and replacement of the marble along earlier folding (Fig. 5.3). The ubiquitous presence of fluorite in the skarn, in the granite and in quartz-fluorite veins suggests that the acidic F-rich fluids circulate in the system during the whole metasomatic activity. Moreover, data from quartz-hosted fluid inclusions in the Botro ai Marmi granite containing 38 wt% NaCl and 19 wt% KCl (Caiozzi et

al., 1998; Fulignati et al., 1999) show that Cl-fluids should be taken into account for the increasing acidity of the system and for the progressive mobilisation of REE (Gysi et al., 2013).

Phyllitic alteration

The final circulation of low-temperature acidic fluids gave rise to a phyllitic alteration characterised by the late crystallisation of K-, Fe-, and Al-phyllosilicates (e.g. saponite, kaolinite, muscovite). These type of alteration is generally enhanced along fractures in the granite, and at the pluton-marble contact.

Accessory minerals behaviour during metasomatic alteration

As commonly observed in peraluminous granites, the content of REE and HFSE is controlled by the abundance of accessory minerals, which are mostly included in biotite or other phyllosilicates (Clarke, 1981; Villaseca et al., 2008). Peraluminous granite from Tuscany show similar characteristics (e.g., Dini et al., 2005). In particular, for what it concerns, accessory minerals are mostly included in biotite. Thus, the metasomatic alteration of phyllosilicates could promote the mobilisation of HFSE and REE into the system. In this context, the Botro ai Marmi peraluminous monzogranitic pluton shows the prominent metasomatic alteration/recrystallisation of accessory minerals included in biotite, thus mobilisation of HFSE and REE. This process of alteration is attributed to F(-Cl)-rich fluids for several reasons: (i) the frequent occurrence of fluorite interlayer in the biotite structure, generating a localised chloritic alteration, (ii) the process of dissolution/precipitation of accessory minerals, that frequently re-crystallised at or across the rim of biotite. Other evidences are, (iii) the great abundance of uncommonly big apatite, as well as small euhedral monazite and zircon bordered altered biotite. (iv) Monazite is really uncommon in biotite, except for few crystals showing pseudomorphic textures. On the contrary, it is frequently found as 5-20 μm crystals in interstitial K-feldspar and quartz, or forming trail of crystals in interstitial K-feldspar (10-15 μm monazite-zircon aggregate). Zircon is the accessory mineral most resistant to metasomatic alteration processes, according to its abundance not only into fresh but also into altered biotite. The most significative evidences are the crystal-shape and size. Indeed, zircons included in biotite are usually bigger (50 up to 200 μm) and show variable euhedral shapes. Instead, zircons found at border of biotite or in endoskarn veins are usually smaller than 30-50 μm, showing morphological feature such as no prism faces, no or rare inclusions, possibly indicating late, low-temperature crystallisation (Schaltegger, 2007). A clear hydrothermal origin for apatite and zircon can be inferred by their presence in exoskarn bodies. Recent works showed extensive evidences for hydrothermal zircon crystallisation from volatile-rich partial melts metasomatised mantle, beneath old continental roots, later sampled accidentally by kimberlite (Griffin et al., 2000). Again, hydrothermal zircon may form during metasomatic alteration of ophiolitic rocks (Dubinska et al., 2004) and during the metasomatism of harzburgite by basaltic liquid and accompanying fluids (Grieco et al., 2001). Finally, few evidences exist for hydrothermal zircons derived from metasomatism of a granitic rock (Yang et al., 2009; Park et al., 2016) and no evidences for hydrothermal zircons from metasomatic alteration of a peraluminous granite body. Recognising the hydrothermal nature of zircon could be pivotal to reconstruct metasomatic processes by U-Pb dating. U-Pb dating of reliably identified hydrothermal zircon would complement less-precise and multiply biased U-Pb ages of apatite, monazite, rutile and titanite from hydrothermal metasomatic deposits.

5.7. Conclusions

The complicated patterns of alteration and mineralisation in the Botro ai Marmi mine resulted from the superimposition of alteration and mineralisation patterns associated with multiple metasomatic events. Potassic and calcic metasomatism are associated with fluids released by a deep mafic source (Fig. 5.17). Indeed, metasomatic alteration produced the significant gain of Mg, Fe, Ca, as well as gain of metals. Potassic alteration interested the whole exposed monzogranite, while calcic and more acidic metasomatism is confined along the magmatic jointing (endoskarn veins) and adjacent to de contact between the pluton and the host marble (exoskarn). Fluid flow away from the intrusion generated Mg-rich skarn in the folded marble. Moreover, Ca-rich bodies are affected by secondary dissolution/ replacement textures, suggesting the increasing acidity of hydrothermal fluids. Reciprocal reactions involving replacement of (i) plagioclase by K-feldspar, (ii) biotite by phlogopite+chlorite+titanite, (iii) biotite by diopside+titanite +phlogopite±allanite, and (iv) calcite+dolomite±micas by garnet±vesuvianite±diopside±phlogopite±epidote reflect the exchange of mass between fluid and wall rock. Moreover, hydrothermal circulation of HFSE, REE, Th, U, P, Zr, Ti resulted in the local crystallisation of HFSE-REE and Th-U accessory minerals.

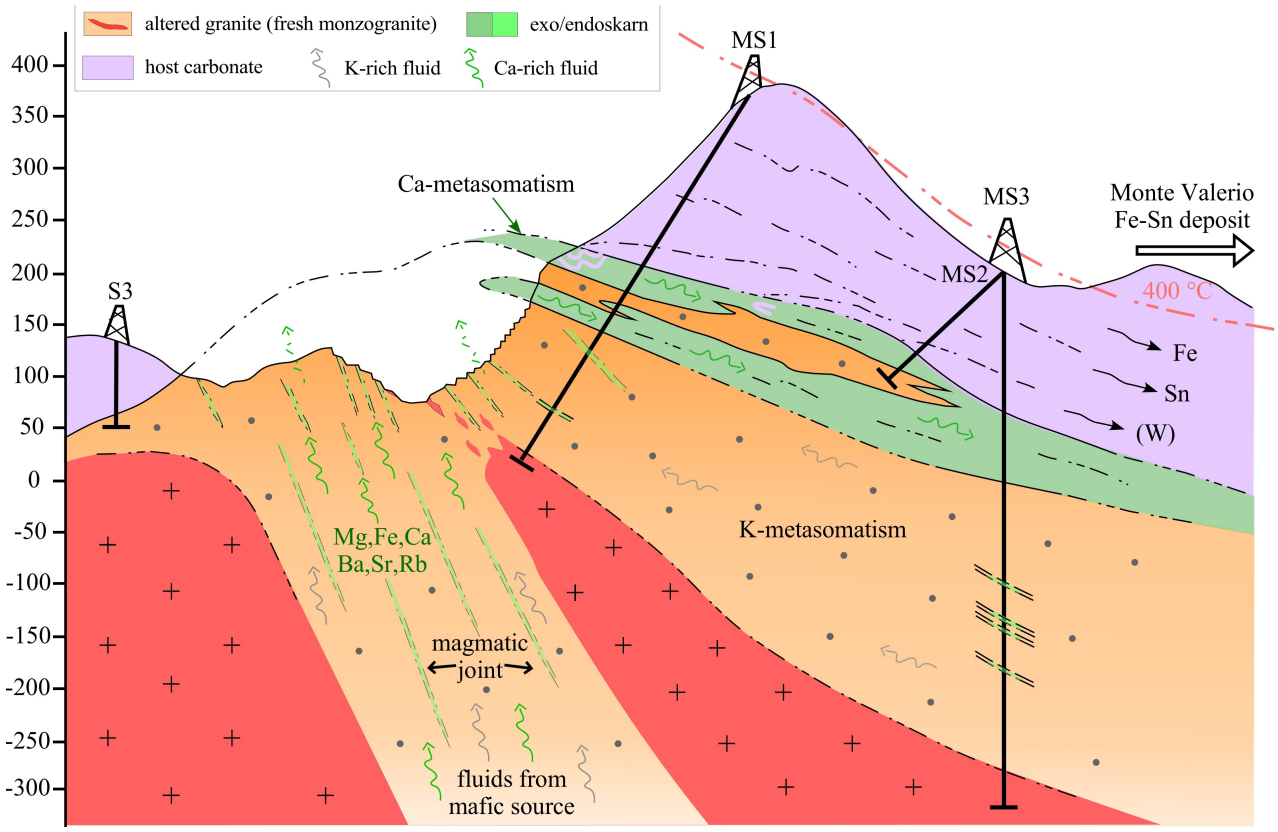

Fig. 5.17 - Schematic cartoon for the metasomatic alteration of the Botro ai Marmi peraluminous monzogranite and carbonatic host. The magmatic jointing promote the circulation of K-rich fluid (black) and Ca-rich fluid (green) in the granite body, while the foliation and folding allow the formation of the contact exoskarn in the host.

Fluid(s) circulation is enhanced by the diffuse jointing at the top of the pluton, probably generated by the continuous release of volatiles from the magmatic reservoir. Shortly after emplacement or during a late-magmatic stage, circulation of B-rich fluid formed disseminated tourmaline-quartz orbicules, which tend to be particularly abundant in zones of fracturing forming veinlets systems. The intrusion generates a widespread contact aureole and an almost pure marble.

Successively, a high-temperature, mafic fluid generated a pervasive potassic metasomatism. During this process plagioclase has been intensively replaced by K-feldspar, while biotite has been replaced by phlogopite-chlorite-titanite aggregates. Almost simultaneously, the circulation of Ca-Mg-rich fluids resulted in the crystallization of a variety of calc-silicates (e.g., diopside, vesuvianite, garnet, epidote), particularly abundant at the carbonate-granite contact, and along veins into the granite. During this stage, the monzogranite experienced loss of Fe and Na and gain of Mg, K, Rb, Ba, Sr. Trace elements, REE, Ti and P show only a local mobilisation/recrystallisation effect. Upon cooling, fluids became more acidic, with the increasing fluorine activity. The increasing acidity is testified by the widespread crystallisation of fluorite frequently related to the occurrence of textural disequilibrium (fluorite-Ca-silicates pseudomorphs, patchy zoning of calc-silicates, dissolution/precipitation textures). The metasomatic alteration of earlier calc-silicates increased the mobilisation of REE and HFSE. During this process, low-temperature and low pH as well as availability of F and Cl to complex with HFSE and REE support the destabilisation of accessory minerals, such as zircons, apatite, monazite. Once the fluid mixed with the Ca-bearing fluid a new generation of metasomatic accessory minerals precipitated on a large scale, both in the granite and metasomatic bodies (e.g., zircon, apatite, allanite, thorite, uraninite as well another HFSE-REE-bearing minerals).

Thus, the present study allows to speculate on the mechanism responsible for the metasomatic alteration of a shallow level, peraluminous monzogranite (Fig. 5.17). High fluid pressure (input from a mafic reservoir) would be responsible for the bulge structure of the monzogranite pluton. Magmatic joints, marble bedding, and carbonate folding probably have been promoted the fluid circulation, also at long distance (up to 3 km). The diffusive alteration outward from endoskarn veins testify pervasive fluid-rock reactions. The character of the metasomatic alteration, typical of porphyry copper systems (Ca-Mg-Ba-Sr gains), supports the idea of fluid released by a mafic reservoir. The role of hydrothermal chlorine brines exsolved from the magmas during the late stage of crystallisation could be also considered essential as carrier of metals (Fe, Cu, Sn, Zn, As, W) for the nearby ore deposits.

Acknowledgements

This project was partially funded by the Progetto di Ricerca di Ateneo (PRA_2016_33). Thanks are due to K. Kouzmanov for providing QEMSCAN data, M. Tamponi for performing XRF analysis, W. Philippe and F. Martenot for help in the cleaning laboratory, and to M. D'Orazio for critical support during ICP-MS analysis.

References

Acocella, V., Rossetti, F., Faccenna, C., Funiciello, R., Lazzarotto, A., 2000. Strike-slip faulting and pluton emplacement at Campiglia Marittima (southern Tuscany). Bollettino della Società Geologica Italiana 119, 517-528.

Barberi, F., Innocenti, F. and Mazzuoli, R., 1967. Contributo alla conoscenza chimico-petrografica e magmatologica delle rocce intrusive, vulcaniche e filoniane del Campigliese (Toscana). Memorie Società Geologica Italiana 6, 643-681.

Baumgartner, L.P. and Olsen, S.N., 1995. A least-squares approach to mass transport calculations using the isocon method. Economic Geology 90, 1261-1270.

Bea, F., 1996. Residence of REE, Y, Th, and U in granites and crustal protoliths; implications for the chemistry of crustal melts. Journal of Petrology 37, 521- 552.

Bertini, G., Casini, M., Gianelli, G., Pandeli, E., 2006. Geological structure of a long-living geothermal system, Larderello, Italy. Terra Nova 18, 163-169.

Borsi, S., Ferrara, G. and Tongiorgi, E., 1967. Determinazione con il metodo K/Ar delle età delle rocce magmatiche della Toscana. Bollettino Società Geologica Italiana 86, 403-411.

Caiozzi, F., Fulignati, P., Gioncada, A., Sbrana, A., 1998. Studio SEM-EDS dei minerali figli nelle inclusioni fluide del granito di Botro ai Marmi (Campiglia Marittima) e possibili implicazioni minerogenetiche. Atti Società Toscana Scienze Naturali, Memorie- Serie A, 105, 65-73.

Charoy, B., 1982. Tourmalinisation in Cornwall, England. In A.M. Evans Metallization associated with acid magmatism (Wiley Interscience, New York), 63-70.

Clarke, D. B., 1981. The mineralogy of peraluminous granite: a review. Canadian Mineralogist, 19, 3-17.

Da Mommio, A., Iaccarino, S., Vezzoni, S., Dini, A., Rocchi, S., Brocchini, D., Guideri, S., Sbrilli, L., 2010. Valorizzazione del geosito <<Sezione Coquand>>, Miniera del Temperino (Parco Archeominerario di San Silvestro Campiglia Marittima). Atti Società Toscana di Scienze Naturali, Memorie, Serie A 115, 55-72.

Deer, W. A., Howie, R. A., Zussman , J., 1992. An Introduction to the Rock Forming Minerals, 2nd ed., Longman, London, pp. 696.

Dini, A., Innocenti, F., Rocchi, S., Tonarini, S., Westerman, D. S., 2002. The magmatic evolution of the laccolith-pluton-dyke complex of Elba Island, Italy. Geological Magazine 139, 257-279.

Dini, A., Gianelli, G., Puxeddu, M., Ruggieri, C., 2005. Origin and evolution of Pliocene-Pleistocene granites from the Larderello geothermal field (Tuscan Magmatic Province, Italy). Lithos 81, 1-31.

Dini, A., Westerman, D.S., Innocenti, F., Rocchi, S., 2008. Magma emplacement in a transfer zone: the Miocene mafic Orano dyke swarm of Elba Island, Tuscany, Italy. Geological Society of London, Special Publication 302, 131-148.

Dobson , D. C., 1982. Geology and alteration of the Lost River tin-tungsten-flourine deposit, Alaska. Economic Geology 77, 1033-1052.

Dubínska, E, Bylina, P, Kozlowski, A, Dörr, W, Nejbert, K, Schastok, J, Kulicki, C., 2004. U–Pb dating of serpentinization: hydrothermal zircon from a metasomatic rodingite shell (Sudetic ophiolite, SW Poland). Chemical Geology 203, 183-203.

Durand, C., Marquer, D., Baumgartner, L., Goncalves, P., Boulvais, P., Rossy, M., 2009. Large calcite and bulk-rock volume loss in metacarbonate xenoliths from the Quérigut massif (French Pyrenees). Contributions to Mineralogy and Petrology 157, 749-763.

Einaudi, M.T., Meinert, L.D., and Newberry, R.J., 1981. Skarn deposits: Economic Geology 75th Anniversary Volume, 317–391.

Feldstein, S. N., Halliday, A. N., Davies, G. R., Hall, C. M.,1994. Isotope and chemical micro-sampling: Constrains on the history of an S-type rhyolite, San Vincenzo, Tuscany, Italy. Geochimica et Cosmochimica Acta 58, 943-958.

Ferrara, G., Petrini, R., Serri, G. and Tonarini, S., 1989. Petrology and isotope- geochemistry of San Vincenzo rhyolites (Tuscany, Italy). Bulletin Volcanologique 51, 379-388.

Franzini, M, Lezzerini, M., Origlia F., 2010. Marbles from the Campiglia Marittima area (Tuscany, Italy). European Journal of Mineralogy 22, 881-893.

Fulignati, P., Gioncada, A., Sbrana, A., 1999. Rare-earth element (REE) behaviour in the alteration facies of the active magmatic-hydrothermal system of Vulcano (Aeolian Island, Italy). Journal of Volcanology and Geothermal Research 88 (4), 325-342.

Gaspar, M., Knaack, C., Meinert, L., Moretti, R., 2008. REE in skarn Systems: A LA-ICP-MS study of garnets from the Crown Jewel gold deposit. Geochimica et Cosmochimica Acta 72, 185-205.

Grant, J. A. , 1986. The isocon diagram- a simple solution to Gresens' equation for metasomatic alteration. Economic Geology 81, 1976-1982.

Grant, J. A., 2005. Isocon analysis: a brief review of the method and applications. Physics and Chemistry of the Earth 30, 997-1004.

Gresens, R.L., 1967. Composition-volume relationship of metasomatism. Chemical Geology 2, 47-55.

Grieco, G., Ferrario, A., von Quadt, A., Koeppel, V., Mathez, E.A., 2001. The zircon bearing chromitites of the phlogopite peridotite of Finero (Ivrea Zone, Southern Alps): Evidence and geochronology of a metasomatized mantle slab. Journal of Petrology 42, 89-101.

Gysi, A.P. and Williams-Jones, A.E., 2013. Hydrothermal mobilization of pegmatite-hosted REE and Zr at Strange Lake, Canada: A reaction path model. Geochimica et Cosmochimica Acta, 122, 324-352.

Gysi, A.P., William-Jones, A. E., Collins, P., 2016. Lithogeochemical Vectors for Hydrothermal Processes in the Strange Lake Peralkaline Granitic REE-Zr-Nb Deposit. Society of Economic Geologists, Inc. Economy Geology 111, 1241-1276.

Griffin, W.L., Pearson, N.J., Belousova , E., Jackson, S.E., Van Achterbergh, E., O'Reilly, S.Y., Shee, S.R., 2000. The Hf isotope composition of cratonic mantle: LAM-MC-ICPMS analysis of zircon megacrysts in kimberlites. Geochimica et Cosmochimica Acta 64, 133-147.

Harlov, D. E., Austrheim, H., 2013. Metasomatism and Chemical transformation of Rock: Rock-Mineral-fluid Interaction in Terrestrial and Extraterrestrial Environments. (Lecture Notes in Earth System Sciences), 1-16.

Hermann, J., 2002. Allanite: thorium and light rare earth element carrier in subducted crust. Chemical Geology 192, 289-306.

Lattanzi, P., Benvenuti, M., Costagliola, P., Maineri, C., Mascaro, I., Tanelli, G., Dini, A., Ruggieri, G., 2001. Magmatic versus hydrotermal processes in the formation of raw ceramic material deposits in southern Tuscany. Proceedings 10th Int. Symposium on Water-Rock interaction, Villasimius(Italy), 10-15 June 2001, 725-728.

Leoni, L., Tamponi, M., 1991. Thermometamorphism in the Campiglia Marittima aureole (Tuscany, Italy). N. Jb. Miner. Mh. 4, 145–157.

López-Moro, F.J., 2012. EASYGRESGRANT–A Microsoft Excel spreadsheet to quantify volume changes and to perform mass-balance modeling in metasomatic systems. Computers & Geosciences 39, 191-196.

Meinert, L.D., Dipple, M.G., Nicolescu, S. 2005. World Skarn Deposits. Economic Geology 100th Anniversary Volume: 299-336.

Moore,D.E. and Liou, J.G., 1979. Chessboard-twinned albite from Franciscan metaconglomerates ifs the Diablo Range, California. American Mineralogist 64, 329-336.

Orville, P.M., 1963. Alkali-metasomatism and feldspar: Norsk GEological Tidsskr. 42, 283-316.

Park, C., Song, Y., Chung, D., Kang, I.-M., Khulganakhuu, C., Yi, K., 2016. Recrystallization and hydrothermal growth of high U–Th zircon in the Weondong deposit, Korea: Record of post-magmatic alteration. Lithos 260, 268-285.

Parry, W., Downey, L., 1982. Geochemistry of hydrothermal chlorite replacing igneous biotite. Clay Miner. 30, 81–90.

Pichavant M, Manning D (1984) Petrogenesis of tourmaline granites and topaz granites; the contribution of experimental data. Phys. Earth Planetary Int. 35, 31–50.

Pinarelli, L., Poli, G. and Santo, A., 1989. Geochemical characterization of recent volcanism from the Tuscan Magmatic Province (Central Italy): the Roccastrada and San Vincenzo centers. Periodico di Mineralogia 58, 67-96.

Pirajno, F., 2009. Hydrothermal processes and mineral systems. Springer, Berlin.

Pirajno, F., 2013. Effects of Metasomatism on Mineral Systems and Their Host Rocks: Alkali Metasomatism, Skarns, Greisens, Tourmalinites, Rodingites, Black-Wall Alteration and Listvenites, in Metasomatism and the Chemical Transformation of Rock: The Role of Fluids in Terrestrial and Extraterrestrial Processes. Berlin, Heidelberg, Springer Berlin Heidelberg, 203-251.Poli, G., 1992. Geochemistry of Tuscan Archipelago granitoids, central Italy: the role of hybridization processes in their genesis. Journal of Geology 100, 41-56.

Pirajno, F., Schlögl, H.U., 1987. The alteration-mineralisation of the Krantzberg tungsten deposit, South West Africa/ Namibia. South African Journal of Geology 90, 499–508.

Plümper, O. and Putnis, A., 2009. The complex hydrothermal history of granitic rocks: Multiple feldspar replacement reactions under subsolidus conditions. Journal of Petrology 50, 967–987.

Poli, G., Peccerillo, A., 2016. The Upper Miocene magmatism of the Island of Elba (Central Italy): compositional characteristics, petrogenesis and implications for the origin of the Tuscany Magmatic Province. Mineralogy and Petrology 110, 421-425.

Pollard, P.J., Pichavant, M., Charoy, B., 1987. Contrasting evolution of fluorine- and boron-rich tin systems. Mineralium Deposita 22, 315–321

Ridolfi, F., Renzulli, A., Perugini, D., Cesare, B., Braga, R., Del Moro, S., 2016. Unravelling the complex interaction between mantle and crustal magmas encoded in the lavas of San vincenzo (Tuscany, Italy). Part II: Geochemical Overview and Modelling. Lithos 244, 233-249

Rodolico, F., 1945. Ragguagli sul granito del Campigliese. Atti della Società Toscana di Scienze Naturali 73, 62-74.

Rossetti, F., Faccenna, C., Acocella, V., Funicello, R., Jolivt, L., Salvini, F., 2000. Pluton emplacement in the northern Tyrrenian area, Italy. Geological Society, London, Special Publications 174, 55-77.

Rocchi, S., Dini, A., Mazzarini, F., Poli, G., 2003. Campiglia Marittima and Gavorrano intrusive magmatism. Periodico di Mineralogia 72, 127-132.

Samim, 1983. Note di commento ai sondaggi di Monte Spinosa. (http://www.neogeo.unisi.it/dbgmnew/)

Seedorff, E., Dilles, J.H., Proffett, J.M., Einaudi, M.T., Zurcher, L., Stavast ,W.J.A., Johnson, D.A., Barton, M.D., 2005. Porphyry deposits: characteristics and origin of hypogene features. Economic Geology 100, 251-298.

Schaltegger, U., 2007. Hydrothermal zircon. Elements 3, 51.

Venerandi-Pirri, I. and Zuffardi, P. (1982). The Tin Deposit of Monte Valerio (Tuscany, Italy): Pneumatolytic-Hydrothermal or Sedimentary-Remobilization Processes? Ore Genesis. G. C. Amstutz, G. Frenzel, C. Kluth et al., Springer Berlin Heidelberg 2, 57-65.

Vezzoni, S., Dini, A., Rocchi, S., 2016. Reverse telescoping in a distal skarn system (Campiglia Marittima, Italy). Ore Geology Reviews 77, 176-193.

Villaseca, C., Pérez-Soba, C., Merino, E., Orejana, D., López-García, J.A., Billstrom, K.., 2008. Contrasted crustal sources for peraluminous granites of the segmented Montes de Toledo Batholith (Iberian Variscan Belt). Journal of Geosciences, 263-280.

Yang WB, Niu HC, Shan Q, Luo Y, Yu XY, 2009. Ore-forming mechanism of the Baerzhe super-large rare and rare earth elements deposit. Acta Petrol Sin 25, 2924–2932

Supplementary material

Supplementary Fig. 5.1

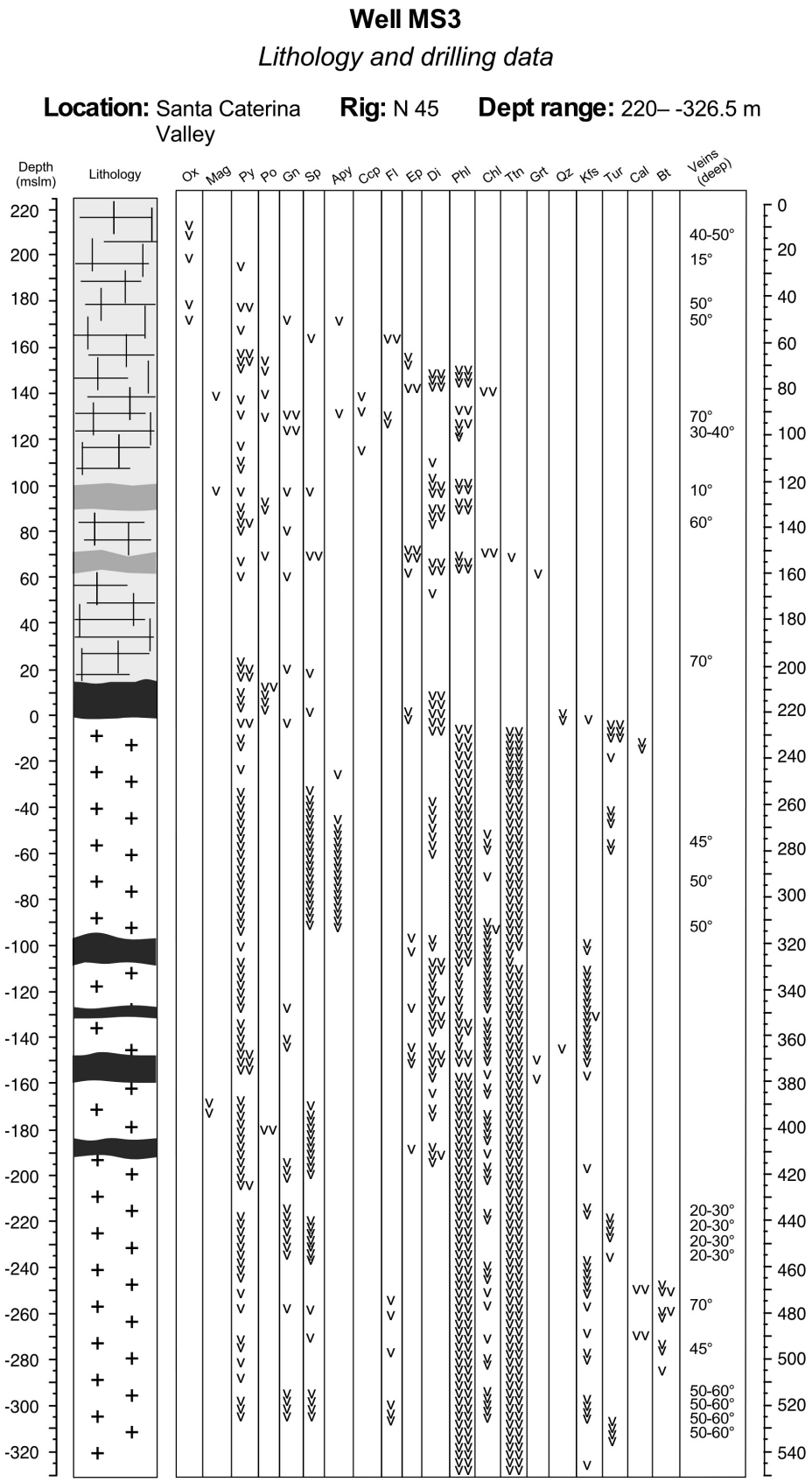

Supplementary Fig. 5.1 - Lithology and paragenetic distribution in the MS3 borehole. Data from Samim, 1983.

EMP analysis for feldspar from Botro ai Marmi granite

Rock type	***Biotite-bearing granite***			***Phlogopite-itanite-bearing granite***				***Biotite-bearing granite or sligtly alteredgranite***										
Mineral	***Kfs1***	***Kfs2***	***Kfs3***	***Kfs4***	***Kfs5***	***Kfs6***	***Kfs7***	***Plg1***	***Plg2***	***Plg3***	***Plg4***	***Plg5rim***	***Plg5mid***	***Plg5core***	***Plg6rim(1)***	***Plg6(2)***	***Plg6(3)***	***Plg6core(4)***
SiO_2	65.70	65.70	66.00	65.90	65.40	65.50	65.80	64.30	65.00	67.40	68.90	67.30	60.40	57.70	66.40	63.70	60.00	57.60
TiO_2	0.00	0.00	0.02	0.02	0.01	0.03	0.00	0.03	0.00	0.00	0.00	0.00	0.02	0.00	0.00	0.02	0.02	0.00
Al_2O_3	19.50	19.20	19.50	19.60	19.50	19.30	19.80	23.10	23.10	21.40	20.60	21.50	26.00	27.80	21.90	24.00	27.30	28.20
Cr_2O_3	0.02	0.00	0.00	0.00	0.03	0.00	0.00	0.03	0.00	0.05	0.00	0.00	0.00	0.00	0.00	0.00	0.00	0.00
FeO	0.00	0.00	0.05	0.03	0.00	0.20	0.00	0.00	0.02	0.00	0.00	0.02	0.00	0.20	0.30	0.10	0.00	0.12
Mno	0.00	0.01	0.00	0.00	0.00	0.00	0.00	0.00	0.02	0.00	0.02	0.00	0.01	0.02	0.02	0.00	0.05	0.02
MgO	0.02	0.02	0.00	0.00	0.03	0.00	0.00	0.00	0.00	0.04	0.00	0.00	0.00	0.01	0.00	0.00	0.02	0.01
CaO	0.08	0.03	0.10	0.10	0.08	0.04	0.10	3.50	3.50	0.98	2.60	2.96	6.90	8.70	1.89	4.50	7.60	8.20
Na_2O	1.92	1.70	1.66	1.99	1.63	1.36	2.10	9.20	8.90	9.90	8.40	8.80	7.20	6.00	10.10	8.60	6.60	5.70
K_2O	14.20	15.00	14.30	13.80	14.70	15.00	14.10	0.23	0.31	0.76	0.24	0.23	0.16	0.18	0.18	0.21	0.23	0.18
Totale	101.4	101.7	101.6	101.4	101.4	101.4	101.9	100.4	100.9	100.5	100.8	100.8	100.7	100.6	100.8	101.1	101.8	100.0
Structural formula, oxygen equivalents p.f.u. = 8																		
Si	2.97	2.98	2.98	2.97	2.97	2.97	2.96	2.82	2.83	2.93	2.97	2.92	2.67	2.56	2.89	2.78	2.62	2.57
Ti	0.00	0.00	0.00	0.00	0.00	0.00	0.00	0.00	0.00	0.00	0.00	0.00	0.00	0.00	0.00	0.00	0.00	0.00
Al	1.04	1.02	1.04	1.04	1.04	1.03	1.05	1.19	1.19	1.10	1.05	1.10	1.35	1.46	1.12	1.23	1.41	1.48
Cr	0.00	0.00	0.00	0.00	0.00	0.00	0.00	0.00	0.00	0.00	0.00	0.00	0.00	0.00	0.00	0.00	0.00	0.00
Fe^{2+}	0.00	0.00	0.00	0.00	0.00	0.01	0.00	0.00	0.00	0.00	0.00	0.00	0.00	0.01	0.01	0.00	0.00	0.00
Fe^{3+}	0.00	0.00	0.00	0.00	0.00	0.00	0.00	0.00	0.00	0.00	0.00	0.00	0.00	0.00	0.00	0.00	0.00	0.00
Mn	0.00	0.00	0.00	0.00	0.00	0.00	0.00	0.00	0.00	0.00	0.00	0.00	0.00	0.00	0.00	0.00	0.00	0.00
Mg	0.00	0.00	0.00	0.00	0.00	0.00	0.00	0.00	0.00	0.00	0.00	0.00	0.00	0.00	0.00	0.00	0.00	0.00
Ca	0.00	0.00	0.00	0.00	0.00	0.00	0.00	0.16	0.16	0.05	0.12	0.14	0.33	0.41	0.09	0.21	0.36	0.39
Na	0.17	0.15	0.15	0.17	0.14	0.12	0.18	0.78	0.75	0.84	0.70	0.74	0.62	0.52	0.85	0.73	0.56	0.49
K	0.82	0.87	0.82	0.79	0.85	0.87	0.81	0.01	0.02	0.04	0.01	0.01	0.01	0.01	0.01	0.01	0.01	0.01
Totale	5.00	5.02	4.99	4.99	5.01	5.00	5.01	4.98	4.96	4.96	4.86	4.91	4.97	4.97	4.98	4.97	4.96	4.95
Sito Z	4.01	4.00	4.02	4.02	4.01	4.01	4.01	4.02	4.02	4.03	4.02	4.02	4.02	4.03	4.03	4.02	4.03	4.05
Sito X	0.99	1.02	0.97	0.97	1.00	0.99	1.00	0.96	0.93	0.92	0.84	0.89	0.95	0.94	0.95	0.95	0.93	0.89
Ab %	17	15	15	18	14	12	18	82	81	90	84	83	65	55	90	77	60	55
An %	0	0	0	0	0	0	0	17	18	5	14	15	34	44	9	22	38	44
Or %	83	85	85	82	85	88	81	1	2	5	2	1	1	1	1	1	1	1

6. Element mobilities during the evolving metasomatic alteration of a peraluminous granite (Campiglia Marittima, Italy)

Gabriele Paoli [a,*], Andrea Dini [b], Maurizio Petrelli [c], Sergio Rocchi [a]

[a] *Dipartimento di Scienze della Terra, Università di Pisa, Via Santa Maria 53, 56126 Pisa, Italy*

[b] *CNR, Istituto di Geoscienze e Georisorse, Via Moruzzi 1, 56124 Pisa, Italy*

[c] *Dipartimento di Fisica e Geologia, Università di Perugia, Piazza dell'Università, 1, 06123 Perugia, Italy*

Keywords

Elements mobilities, metasomatic minerals, LA-ICP-MS, HFSE/REE mobility

Abstract

Comparison of whole-rock specimens is frequently useful to trace the element mobility during metasomatic alteration. Indeed, it is necessary to know whether the constituents, being added or subtracted, have really entered or left the system. However, when certain components have been transported only locally, the comparison of whole-rock analysis could hide some micro-scale processes (i.e., replacement and pseudomorphism). The evolution of fluid composition may be recorded within individual zones in metasomatic minerals. For such reason, the analysis of major (EMP) and trace (LA-ICP-MS) elements on selected minerals has to be integrated with geological datas (e.g. field relationships, textural evidences, mineral parageneses, etc.). This kind of analysis allows to better appreciate the individual minerals contribution to the overall change in fluid composition, and to identify possible litho-geochemical vectors of the metasomatic alteration.

At Botro ai Marmi mineralogical, textural and geochemical investigation of granite, endoskarn and exoskarn bodies provided evidence for a potential contribution of elements from an external source. The granitic pluton underwent intense hydrothermal alteration during post-magmatic fluid-rock interaction processes. The system is affected by two metasomatic stages characterised by K-rich fluid and Ca(-Mg)-rich fluid circulation. Initially, a potassic metasomatic event led to the complete metasomatic alteration of magmatic biotite, plagioclase, and ilmenite, promoting major element mobilisation and crystallisation of K-feldspar, phlogopite, chlorite, titanite, and rutile. Significant gain of K, Ca, Rb, Ba, Sr, were accompanied by loss of Fe and Na. Metals (i.e., Cu, Zn, Sn, W, Tl) show a significant mobility during metasomatism. The increasing fluids acidity due to interaction with Ca-rich fluids resulted in a diffuse Ca-metasomatism. During this stage occurred a wide variety of calc-silicates (e.g. diopside, titanite, vesuvianite, garnet, epidote), particularly abundant at the carbonate-granite contact and along veins into the granite. Ca-F-rich fluids enhanced the acidic alteration of accessory minerals and the mobilisation of HFSE and REE. This stage is characterised by the exchange of major elements (Ti, Ca, Fe, Al) with HFSE and REE in the forming metasomatic minerals (i.e., titanite, vesuvianite), and the crystallisation of HFSE-REE minerals. Moreover, the common textural disequilibrium of newly formed minerals (pseudomorphs, patchy zoning, dissolution/precipitation textures) testifies the evolution of metasomatising fluids toward more acidic condition.

Concluding, the selective mobilisation of such components was related to a change in fluid composition, pH and temperature. This study emphasises the importance of relating field studies to petrographic observation and detailed geochemical analysis. Moreover, it shows how such linkage can lead to the construction of litho-geochemical model for element mobilisation in crustal magmatic-hydrothermal setting.

6.1. Introduction

Any hydrothermal fluid can give rise to metasomatism when it interacts with an intrusive body during or subsequent to consolidation, modifying its original mineralogy. Fluid compositions can be buffered by local host rocks, and/or it could reflects different reaction rates of different host minerals. It is therefore important to evaluate the chemical changes that could accompany such exchange reactions, since most major and trace elements are known to be sensitive to these processes (e.g., Pirajno, 2009, 2013; Harlov and Austrheim, 2013).

In heterogeneous system, the components may be redistributed among the phases in the system (closed-system), or there may be a redistribution of matter between the system and its surroundings, either and exchange or transfer of components (open-system; Thompson 1982).

Comparison of whole-rock specimens is frequently useful to trace the element mobility during metasomatic alteration. Indeed, it is necessary to know whether the constituents, being added or subtracted, have really entered or left the system or whether they contribute volumetrically to the system as constituents of other minerals. However, when certain components have been transported only locally (within the limits of the hand specimen), the comparison of whole-rock analysis could hide some micro-scale processes (i.e., replacement and pseudomorphism). For example, the evolution of fluid composition may be recorded within individual zones in metasomatic minerals, as observed for garnet (e.g., Jamtveit, 1993), Ti-bearing minerals (e.g., Gierè, 1990), and HFSE-REE accessory minerals (e.g., Gysi et al., 2016), from metasomatic environments where minerals growth reflects the interplay of heating and fluid infiltration. For such reason, the analysis of major (EMP) and trace (LA-ICP-MS) elements on selected minerals has to be integrated with geological datas (e.g. field relationships, textural evidences, mineral paragenesis). This kind of analysis allows to better appreciate the individual minerals contribution to the overall change in fluid composition and to identify possible litho-geochemical vectors of the metasomatic alteration. Moreover, performing a detailed geochemical investigation of single minerals involved in a metasomatic process could provide a way of evaluating the element mobility during such process. Thus, the aim of this study is to investigate how alteration affects the mobilisation/ concentration of elements in a shallow peraluminous granite. In this context, the reconstruction of geochemical vectors is pivotal to relate geochemical changes at the mineral, rock, and deposit scale to changes in specific processes involving element mobilisation. Moreover, this study attempts to determine the chemistry of hydrothermal fluids, according to the different metasomatic stages, investigating the changes in trace element composition of the main rock-forming minerals, defining key metasomatic alteration reactions linking mineral textures and chemistry.

At Botro ai Marmi (Campiglia Marittima), mineralogical and geochemical variations in the altered granite were initially (Pinarelli et al., 1989) attributed to the interaction between granitic magma and CO_2-rich fluids released during calc-silicate reactions in the heated country rocks, and/or auto-metasomatism caused by late-stage hydrothermal fluids emanating from the crystallising magma. However, mineralogical, textural and geochemical investigation of granite, endoskarn and exoskarn bodies (Paoli et al., in prep. - see chapter 5) provided evidence for a potential contribution of elements from an external source. At Botro ai Marmi two metasomatic stages characterised by K-rich fluid and Ca(-Mg)-rich fluid circulation were defined. Significant gain of K, Ca, Rb, Ba, Sr, were accompanied by loss of Fe and Na. Metals (i.e., Cu, Zn, Sn, W, Tl) show a significant mobility during metasomatism. The occurrence of a wide variety of calc-silicates (e.g. diopside, titanite, vesuvianite, garnet, epidote), particularly abundant at the carbonate-granite contact and along veins into the granite, allows to investigate the fluid evolution during metasomatism. Moreover, the common textural disequilibrium of newly formed minerals (pseudomorphs, patchy zoning, dissolution/precipitation textures) testifies the evolution of metasomatising fluids. Thus, the Campiglia area represents an excellent case study to investigate the element mobilities resulting from the metasomatic alteration of a peraluminous granite.

The combination of (i) detailed mineralogical and textural investigation, and of (ii) geochemical analysis, which defines the relative and absolute mass changes involved during the metasomatic event(s), with (iii) new micro-scale

ICP-MS analysis allows to speculate on the origin and geochemistry of the metasomatic fluid(s) responsible for the alteration processes.

6.2. Geological background

The Campiglia Marittima area (hereafter Campiglia) is characterised by a Mesozoic carbonate rocks horst, trending N-S, confine in a Jurassic-Eocene ophiolitic sequence. This area is characterised by an intense metasomatic activity started with the shallow crustal (~4-6 km) emplacement of the Botro ai Marmi monzogranite pluto. Later, mafic and felsic porphyritic bodies crosscut the contact aureole produced by the pluton into the host carbonates (~8 km^2; Vezzoni et al., 2016). Finally, to the west of the horst, cropped out the early Pliocene rhyolitic extrusive complex of San Vincenzo. In the Campiglia horst, it is possible to distinguish between metasomatic and ore bodies, in close spatial association with the Botro ai Marmi granite. In detail, these lithologies occur as: (i) two important granite typologies, an unaltered biotite granite and a pinkish-white granite. The latter is characterised by an intense metasomatic alteration of biotite replaced by chlorite, phlogopite and Ti-rich minerals. (ii) A system of endoskarn resulting from the metasomatism of the igneous rock, developed along fractures into the granite body and (iii) a variety of exoskarn resulted from the metasomatic replacement of the host carbonate (Fig. 5.1), and (iv) the main Campiglia Fe-Cu-Zn-Pb(-Ag) skarn deposit, consisting in several bodies and veins that crop out discontinuously. Moreover in this area occurred (v) minor Sn-W-As bodies (Venerandi-Pirri, 1982; Dini et al., 2013).

The Botro ai Marmi pluton (BM) has a syenogranitic to monzogranitic composition (SiO_2=68-72 wt%) and a peraluminous character (ASI=1.1-1.3). The unaltered granite is found in a few small outcrops at the Botro ai Marmi mine. It is a medium-grained rock with rarely porphyritic texture (K-feldspar). The primary igneous assemblage of this unaltered monzogranite consists of K-feldspar (30-35 vol%), quartz (30-35 vol%), plagioclase (20-30 vol%), and biotite (5-10 vol%), along with late-magmatic tourmaline and accessory cordierite, apatite, and zircon. Tabular K-feldspar (ortose, Or_{85-90}, n=7) frequently occurs as megacrysts (up to ca. 5 cm). Plagioclase (An_{35-45}, n=11) usually shows the enrichment in albitic component moving from core to rim. The rim is characterised by a clear thin oligoclase overgrowth (An_{10-15}, n=6). The pinkish-white altered granite (95 vol% of outcropping granite), resulting from the metasomatic alteration of the biotite granite, is characterised by the almost complete replacement of biotite by phlogopite (Mg# = 0.5), chlorite, titanite and Ti-oxide. Biotite remnants show abundance of Fe (up to 25 wt%) and Ti (up to 4 wt%), diffuse layering of chlorite and/or phlogopite, as well as numerous inclusion of metasomatic minerals (i.e., titanite, fluorite, rutile, adularia). In this rock, the content of oligoclase is considerably reduced to ~5 vol%. This mineral is usually replaced by interstitial K-feldspar (Or_{80-90}), that shows a composition similar to the ortose in the unaltered granite. The widespread occurrence of minor diopside, amphibole and accessory minerals (including apatite and zircon) represents an important evidence of metasomatic reactions. The Ca-metasomatic alteration of the original granite generated a system of endoskarn veins (from centimetric to decimetric in thickness), following brittle fractures in the granite pluton to join the exoskarn aureole, pointing out complex fluid circuits. The endoskarn is mainly characterise by calc-silicates (50-60 vol%) such as diopside, titanite (5-10 vol%; occasionally up to few centimetres), phlogopite (10-15 vol%), relicts of K-feldspar(10-15 vol%), minor epidote, albite, apatite, and zircon, together with accessory sulfides and calcite (5-10 vol%). On the other side, exoskarn bodies occur as massive bodies at the pluton-marble contact or as the replacement of the ductilely folded carbonatic host-rock, suggesting preferential path-way for metasomatic fluids. The most representative metasomatic minerals are calc-silicates (i.e., diopside, vesuvianite, garnet, titanite, epidote; up to 60 vol%), calcite (up to 30 vol%) as well as phlogopite, minor scapolite, and sulfides. Multiple effects of hydrothermal fluids circulation overlap through time, resulting in complexes mineral associations, like replacement texture (epidote, REE-bearing, and pyroxenoid replacing garnet, pyroxene, titanite), pseudomorphism and clear mineral zoning. Widespread crystallization of clay minerals, calcite and sulfides generally fill veins and cracks.

Finally, a late low-temperature hydrothermal veins system cross-cut the granite body. This late manifestation is characterised by an abundance of chlorite, sulfides, calcite, quartz and fluorite, as well as accessory HFSE-REE and Th-U accessory minerals.

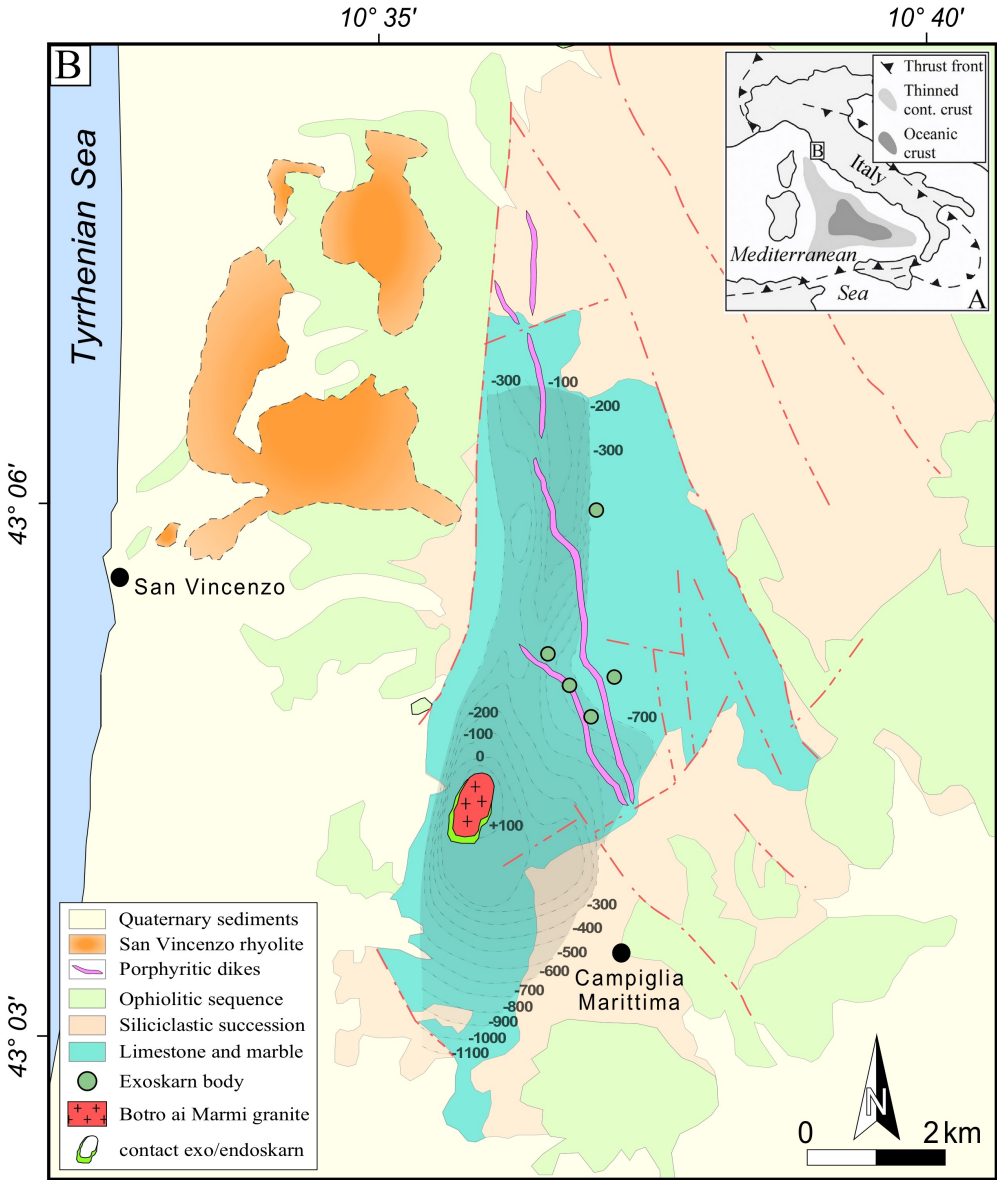

Fig. 6.1 - (A) Location map of the Campiglia area and (B) schematic geological map (modified from Da Mommio et al., 2010). The pluton roof morphology is also reported (grey lines).

6.3. Methods

Major elements of selected minerals were analysed using a JEOL 8200 electron microprobe equipped with five wavelength dispersive spectrometers (WDS) and a PulseTor Maxim EDS detector, at the University of Milano. The WDS analysis were conducted at 15 kV, with a 30 nA beam current and a beam diameter of 5 µm. Due to the small crystal size, it was not possible to use the electron microprobe to quantitatively analyse all the phases, indeed some minerals were identified from element maps and semi-quantitative SEM-EDS analysis. Moreover, a Thermo Scientific iCAP-Q ICP-QMS coupled with a Photon Machine G2 193 nm excimer Laser Ablation system was used for high spatial resolution trace element determination of the same minerals, at the University of Perugia. ^{42}Ca, ^{29}Si and ^{47}Ti, previously determined by EMP, were used as internal standards.

6.4. Results: mineral microtextures and chemistry

Textural evidences from outcrop and thin sections, along with SEM imaging (Table 6.1), have been used as the basis to select the minerals involved in the metasomatic reactions, in order to perform major and trace element analysis. The minerals chemistry has been used to document the mobility of elements between granite, marble and metasomatic products. Variations in the mineral chemistry of feldspars, micas, calc-silicates, Ti-bearing minerals and accessory minerals indicate multiple processes of mineral-fluid interaction and reflect the metasomatic fluid evolution. Complete mineral chemistry data are provided in Supplementary Table 6.1.

Table 6.1 - Metasomatic minerals

General group	End members	Abbreviation	General formule	Composition	Main impurities/particularity	Occurrence
Phyllosilicate	Biotite	Bi	$X_2Y_{4\text{-}6}Z_8O_{20}(OH,F)_4$	TiO_2 > 3 wt%, Fe > Mg	high Ti	unalt. granite
	Phlogopite	Phl		Mg >> Fe, no K	F, Nb, Nd, La, Ce	alt. granite, endoskarn, Di-exoskarn
	Chlorite	Chl		Mg >> Fe, K	F	Chl-veims, Phl-Bt alteration
Ti-minerals	Titanite	Ttn	$CaTiSiO_4(O,OH,F)$	*Ca-site:* REE, Al; *Ti-site:* Nb, Ta, Zr, Al; *O-site*: F	high Al, Th, U, Zr, Nb, Y, Ta, LREE, F	alt. granite, endoskarn, exoskarn
	Rutile	Rt	TiO_2	*Ti* => Al^{3+}, V^{3+}, Cr^{3+}, Fe^{3+}, Nb^{5+}, Ta^{5+}, Sn^{4+}	Nb, Cr, V, Al, Zr, Sc, Sn	altered granite
Pyroxene	Diopside	Di	$X^{2+}Y^{2+}Z_2^{4+}O_6$	$(Ca, Na)(Mg, Zn)Si_2O_6$	Zn, Na	endoskarn, exoskarn
	Hedenbergite	Hd		$(Ca, Na)(Fe, Zn)Si_2O_6$	Zn, Na	Pyroxene-exoskarn
Epidote	Epidote	Ep	$A_2M_3Si_3O_{12}(OH, F)$	*A-site*: Ca > REE; *M-site*: Al > Fe;	Sr, Sn, Sb, Th, U	Pyroxene-exoskarn
	Allanite	All		*A-site*: REE > Ca; *M-site*: Al ≥ Fe;		Pyroxene-exoskarn, altered granite
Plagioclase	Albite	Ab	$XAl_{1\text{-}2}\ Si_{3\text{-}2}\ O_8$	$NaAlSi_3O_8$	not determined	granite, endoskarn, minor in transitional exoskran
	Anorthite	An		$CaAl_2Si_2O_8$		
	K-feldspar	Kfs		$KAlSi_3O_8$		
Garnet	Grossularite	Gr	$X_3Y_2Z_3O_{12}$	$Ca_3Al_2Si_3O_{12}$	not determined	Grt-Vs-exoskarn, accessory in other exoskarn
	Andradite	Ad		$Ca_3Fe_2Si_3O_{12}$		
Other	Vesuvianite	Vs	$X_{19}Y_{13}Si_{18}O_{68}(OH,F,O)_{10}$	*X-site:* Ca, Na, $LREE^{3+}$; *Y-site:* Al, Mg, $Fe^{3\text{-}2+}$	Th, U, LREE, F, Li, Be, Zn, Zr	Vs-exoskarn, Pyroxene-exoskarn
Accessory minerals						
Phosphates	Apatite	Ap		$Ca_5(PO_4)_3(OH,Cl,F)$	F	altered granite, endoskarn, exoskarn, e.g. replacement of calc-silicates or earlier generation of accessory minerals
	Monazite	Mnz		$(Ce,Nd,Y,Dy,Sm,Nd,Th)(PO_4)$	not detected	
	Cheralite	Cher		$CaTh(PO_4)_2$	not detected	
Th-U minerals	Ekanite	Ek		$Ca_2ThSi_8O_{20}$	U, REE	
	Uraninite	Urn		UO_2	Th	
	Thorite	Thr		$Th(SiO_4)$	U	
Other	Zircon	Zrn		$Zr(SiO_4)$	under development	

Table 6.1 - Main metasomatic minerals observed in the Botro ai Marmi system.

Magmatic minerals

Feldspar group

The alkali feldspar, the main mineral in the granite facies (50-30 vol%), is represented by two generation of crystals. The first usually occurs as medium-size euhedral crystals, occasionally forming tabular phenocrysts up to 3-5 cm in size and as late magmatic interstitial grains. A secondary generation isotropically replaced the plagioclase rims. Replacement of plagioclase also occurs along polysynthetic twinning, along fractures, and scattered K-feldspar island were also observed in highly altered plagioclase. There are no significant chemical variability between core and rim of the crystals and between the two generation of K-feldspar (orthoclase, $Or_{85\text{-}90}$, n=7). Plagioclase (up to 30 vol%) crystals are

subhedral to euhedral commonly showing a compositional zoning from An_{35-45} (n=11) core to An_{10-15} (n=6) rim. With progressing granite metasomatic alteration, the oligoclase rim is almost completely replaced by K-feldspar. Sericitic alteration increases towards the centre of the grains, and is widespread mostly in the altered granite.

Mica group

Biotite is the only mafic mineral (together with late-magmatic tourmaline) observed in the granite (Fig. 6.1). Its composition varies between annite/siderophyllite (according to Deer et al., 1992) or Fe-biotite/siderophyllite (according to Foster et al., 1960), with a Fe# values comprise between 0.4-0.6, comparable with other peraluminous magmas from southern Tuscany (Fig. 6.2). Data plotted on a MgO-Al_2O_3 discriminating diagram (Abdel-Raham, 1994) show a biotite composition typical of peraluminous granites, according to petrographic evidences (e.g., cordierite) as well as the aluminium saturation index of the rock (ASI=1.1-1.3). Moreover, biotites show a high TiO_2 content (up to 4 wt%). Fluorine content is extremely variable, from 0.5 wt% in primary biotite up to 3 wt% in secondary phlogopite. The overall fluorine value define two distinct trend well correlated with Ti content and Mg# or Fe# (Fig. 6.3).

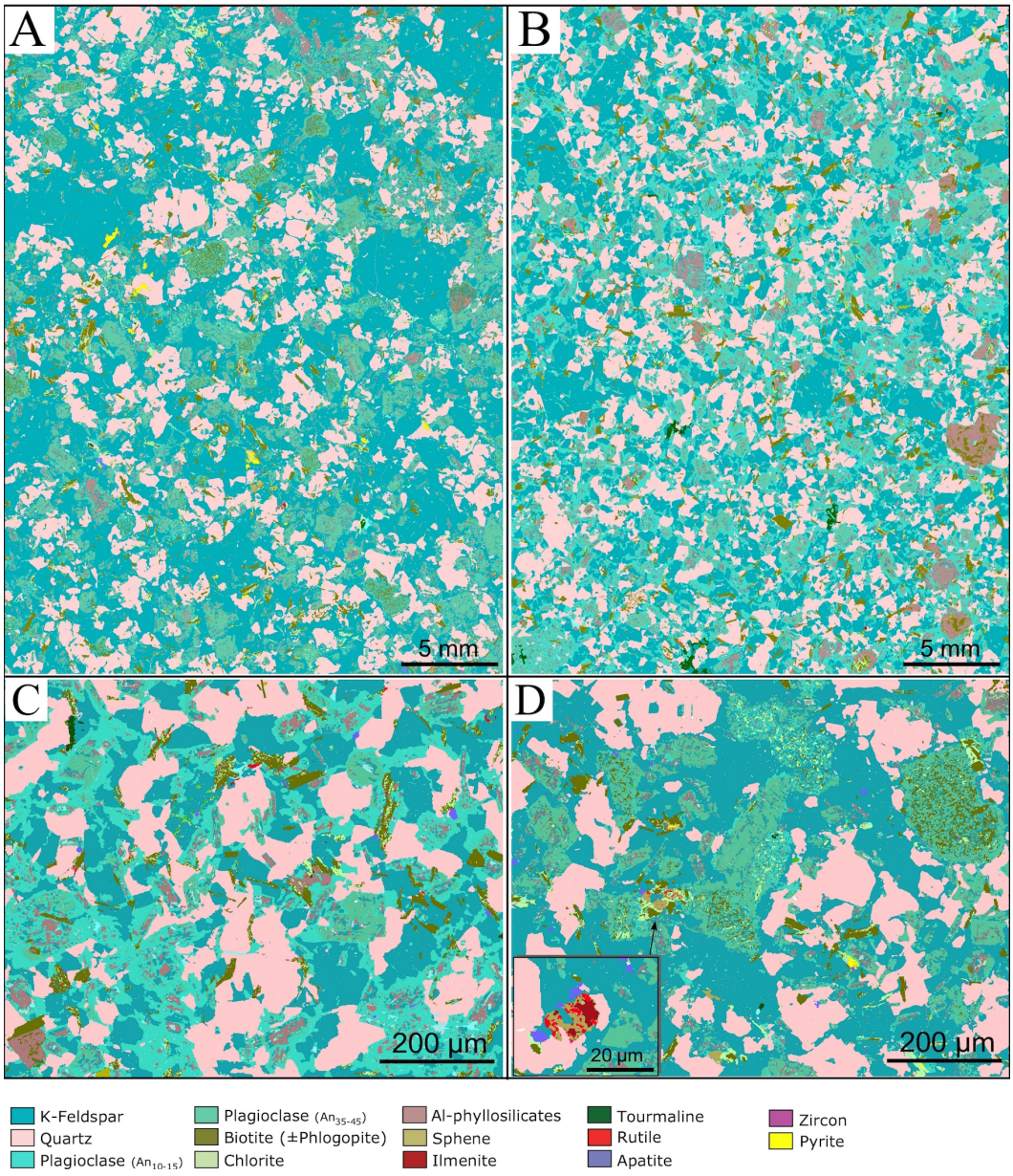

Fig. 6.2 - QEMSCAN images of two samples of granite. A) Thick overgrowth of oligoclase (An10-15) on andesine plagioclase (An35-45). B) K-feldspar replace albite and increase from 30 vol% to about 50 vol%.

Accessory minerals

Accessory minerals show particularly relevant textures (see chapter 5). Cordierite represents the most abundant accessory mineral, indicating the peraluminous character of the rock. This mineral, which is abundant in the crustal magmatic products of Tuscany (i.e., San Vincenzo rhyolite, Roccastrada rhyolite), is strongly altered and *is* commonly replaced by pinite and thick coronas of albite, supporting alkali metasomatism.

Ilmenite is commonly extensively replaced by titanite and rutile aggregates. Its metasomatic alteration is enhanced in crystals included in biotite, which are strongly affected by metasomatic replacement.

Monazite is usually represented by small euhedral crystals (5-15 μm) located at the boundary of metasomatic quartz and K-feldspar, or it is occasionally represented by trail of 5-10 μm monazite-zircon aggregates included in hydrothermal K-feldspar. Rare bigger crystals (up to 30 μm) are observed into altered biotite and show evidence of interaction with fluids (e.g. dissolution/pseudomorphic textures).

Zircon crystals vary from 30-250 μm euhedral and slightly altered crystals to 5-10 μm euhedral bipyramidal crystals. The biggest crystals are usually included in biotite, while the smallest crystals usually form aggregates with apatite and monazite. Crystals smaller than 30 μm are frequently observed in secondary K-feldspar, more frequently in quartz and in such cases they form monazite-zircon trail of inclusion in secondary K-feldspar. Zircon-apatite aggregate are frequently observed also in endoskarn and exoskarn bodies (mobilisation of P and Zr in hydrothermal fluids). Moreover, zircon crystals bordering titanite grains are interpreted to result from the mobilisation of Zr during metasomatic alteration of titanite by acidic fluids.

Metasomatic minerals

At the granite-marble contact, the exchange reactions between metasomatic fluids, granite and host carbonate resulted in the intense replacement of primary minerals by calc-silicates, oxides, HFSE-REE and Th-U minerals, as well as multiple generation of sulfides. Chemical zoning in metasomatic minerals, and in particular oscillatory zoning, is a common phenomenon generally interpreted as a primary growth texture, that expresses the feedback between mineral surface and its environment (e.g., Shore and Fowler, 1996; Halden, 1996). During mineral growth, fluids interacting with mineral surface can promote particular exchange reactions inhibiting others, generating a chemical potential gradients at the mineral surface (Halden, 1996). A growing mineral may be surrounded by a thin layer depleted in those elements with distribution coefficients that favour the solid phase, or by elements that are more rapidly adsorbed at the mineral surface. However, if the mineral growth rate is constant and low, the chemical variations mostly depend from the fluid composition. These changes are indirectly responsible for changes in the growth rate. Thus, it is difficult to isolate a single event in an open environment, such as in a metasomatic system like Botro ai Marmi (Shore and Fowler, 1996).

Metasomatic minerals from Botro ai Marmi display simple to complex zoning characterised by major and trace element variability. The concentric zoning has been interpreted to result from evolving metasomatic fluids. Metasomatic minerals showing complex irregular zoning increase according to the proximity with the granite-host rock transition. They are interpreted to result from multiple metasomatic events characterised by increasing activity of metasomatic fluids. Pyroxene, titanite, and epidotes crystals from the exoskarn bodies show the most complex textures.

Phyllosilicates

The composition of the phyllosilicates (Supplementary table S.6.1) yielded important information on the metasomatic alteration of primary minerals, such as K-feldspar and biotite, and the mobility of Fe, K, Al, Mg, Ti, Ca and Si. This, in turn, provided constraints on the physic-chemical conditions prevailing during fluid-rock interaction in the granite. The phyllosilicates were distinguish according to their chemistry (Fig. 6.2). The subdivision of the phyllosilicates into separate groups based on their chemistry is consistent with petrographic observations of fine

'intergrowth' of either Mg-phyllosilicates and Fe-phyllosilicates, as well as hydrothermal chlorite. The metasomatic alteration of magmatic biotites produced exchange of Fe-Ti-Mg-Si, resulting in the complete replacement of biotite by phlogopite (Mg#=0.5) and chlorite, as well as new crystallisation of Al-rich titanite and rutile. The unaltered granite shows abundance of normal biotite (siderophyllite-annite series), while biotite from the altered granite is a Mg-rich phlogopite (Fig. 6.3). Phlogopite results slightly enriched in LREE-Nb, and quite enriched in F (3 wt% vs 0.5 wt% in biotite). Chlorite, commonly replacing biotite in the altered granite, shows F contents up to 0.25 wt% and it is observed in close spatial relation with fluorite intra-layers. Diagrams of Fig. 6.4 (Fe/Mg vs Ti, F vs Ti, and F vs Fe#) evidence the exchange reactions occurred during the alteration of biotite, involving $TiMgFe_{-2}$, $(OH)F_{-1}$, KNa_{-1} exchange, generating phlogopite and chlorite replacement (e.i., Thompson, 1982). Moreover SEM-EDS analysis occasionally show Fe-enriched biotite fractions (FeO=35-40 wt%). Commonly, Fe-rich biotite (annite) has been interpreted to result from a K-Na exchange reaction during a process of alkali metasomatism (Pirajno et al., 2013). The depletion of Fe/Mg ratio is directly related to the Ti decrease, allowing to distinguish between phlogopite and the other micas (Fig. 6.3).

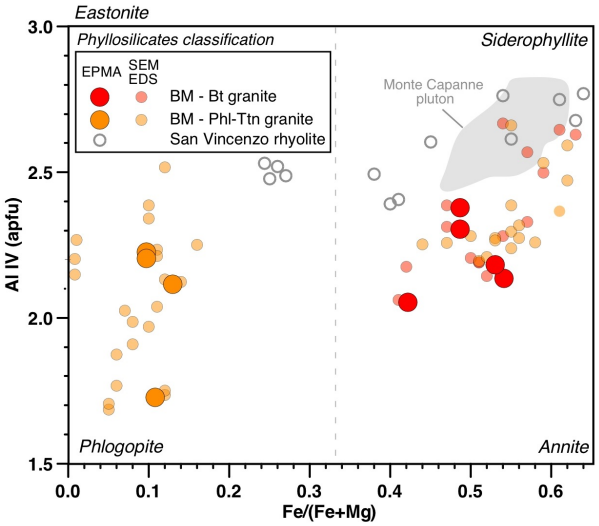

Fig. 6.3 - Classification diagram of phyllosilicates from the Botro ai Marmi granite (big circle = EPMA analysis; small circles = SEM-EDS analysis). For comparison are shown a series of phyllosilicates EPMA analysis from the San Vincenzo rhyolite (Dini, unpublished) and from the Monte Capanne pluton (Farina et al., 2010).

The chondrite-normalised REE pattern (Fig. 6.4) obtained from bulk analysis on biotite and phlogopite collected from granite and exoskarn, reflect the pattern of the host rock. Biotite and phlogopite from the unaltered and altered granite, respectively, show a slight enrichment in LREE and depletion in HREE. In contrast, phlogopite collected from exoskarn bodies shows a flatter pattern, compatible with the whole-rock diopside-phlogopite-exoskarn pattern (see discussion).

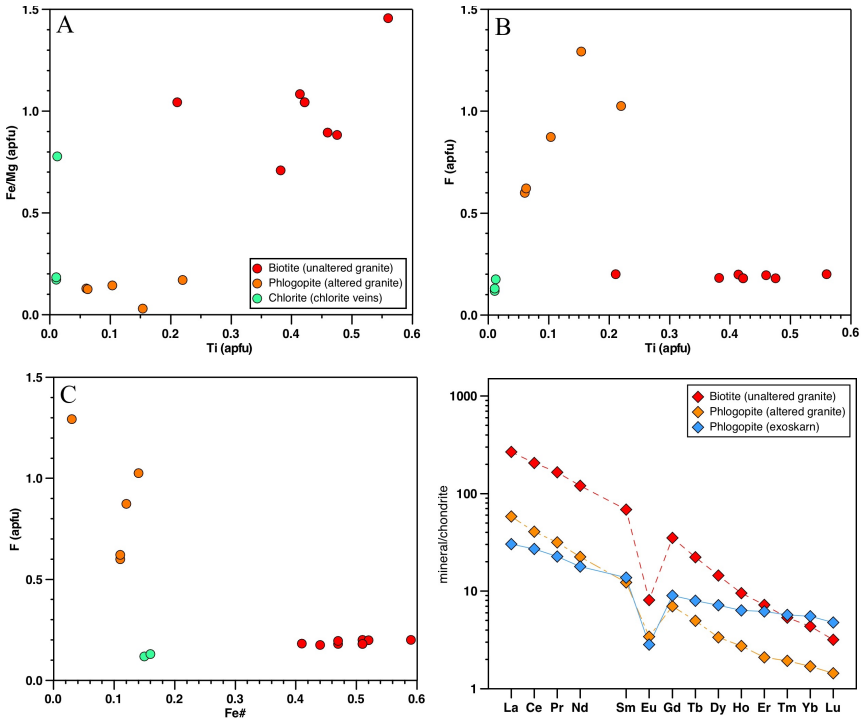

Fig. 6.4 - Composition diagrams for selected major and minor elements of biotite from unaltered granite (red), of phlogopite from altered granite (orange), and of chlorite from hydrothermal veins (green). A) Ti vs Fe/Mg, B) Ti vs F, and C) Fe# vs F content.

Fig. 6.5 - Chondrite normalised REE pattern for biotite (red) and phlogopite (orange) from the Botro ai Marmi granite, and phlogopite from exoskarn (blu).

Titanium minerals

Metasomatic titanite and rutile are widespread in samples from the Botro ai Marmi mine and they are usually observed as replacement of ilmenite and/or new crystals related to altered biotite. Ilmenite is partially to completely replaced by titanite, which seems to be altered in rutile during an ensuing stage. Titanite is also observed in endoskarn veins, forming euhedral, centimetric, patchy zoned crystals. Rutile aggregates replacing titanite could enter the same chemical impurities. Ti^{4+} may be replaced by major amounts of Fe^{3+}, Nb^{5+} and Ta^{5+}, minor amounts of $A1^{3+}$, V^{3+}, Cr^{3+}, and Sn^{4+} or by trace amounts of Mg^{2+}, Mn^{2+}, Fe^{2+}, Ca^{2+} and Si^{4+} (e.g. Deer et al., 1992).

Titanite - Titanite occurs as euhedral to subhedral crystals and is crystallised in multiple generations (Fig. 6.6; Paoli et al., in prep. - chapter 5). Accurate SEM-EDS observations show variable textures, possibly reflecting variable degrees of fluid-mineral interaction and changes in trace element composition. The most common textures are (i) simple zoning, (ii) patchy zoning, (iii) rim dissolution/corrosion (spongy texture), and (iv) later zones that truncate and embay earlier ones, showing sharp boundaries against adjacent zones (Paoli et al., in prep. - chapter 5). Intensively altered titanite crystals, common in exoskarn and endoskarn, are frequently replaced by apatite, zircon, thorite, uraninite (similar examples are reported for several context world wild; e.g., Pan et al., 1993; Allen et al., 1986). Similar occurrences are previously reported for hydrothermal titanite from other systems (e.g. Vico volcanic complex; Della Ventura et al., 1999), in which titanite has been commonly observed in close spatial relation with fluorite, apatite and other accessory minerals (multiple events of mineral-fluid exchange reactions). At Botro ai Marmi, some properties are common for titanite from each lithology, such as Al, Zr, Th, U, and REE enrichment. The textural variability for titanite from the different environment correspond to a compositional zoning. Moreover, titanite crystals show variable amount of Sr, Ba, Cr, Mn, Fe, and F (Table S.6.1), indicating that such a large number of elements were exchanged during its growth. The average composition of titanite crystals from the different environments is particularly high in Al_2O_3 content, ranging from mean values of 3.5 wt% up to of 5.5 wt% (titanite in veins). Variation in the aluminium content is partially responsible of the mineral zoning (Fig. 6.7). Al shows a positive correlation with F (0.25-0.79 wt%) and Ti. Moreover, a perfect correlation exist between Ti and F and a good correlation is also shows by Al+Fe vs F. The compositional variation could be described by exchange reaction involving $AlFTi_{-1}O_{-1}$ and vector (Markl and Piazolo, 1999). Ca shows a perfect correlation with REE and Zr, while, M^{3+} correlate with Ca+Ti content. Th (20-500 ppm) shows a positive correlation with U (20-700 ppm), reaching maximum values in centimetric, patchy zoned titanite from metasomatic veins. REE concentration shows a negative correlation with U/Th ratio (Fig. 6.6), from core to rim.
The maximum REE content is obtained from titanite of the unaltered granite. Other important enrichment are Zr (200-6000 ppm), Nb (180-2500 ppm), Y (up to 5370 ppm), and Ta (up to 250 ppm). Nb and Ta show a perfect positive correlation. Thus, titanite crystals from the different environments show variable chemical composition, resulting in variable internal texture/zoning. Indeed, typical BSE images of titanite from the granite show homogeneous crystals or simple zoning with distinct dark and bright overgrowths. On the other hand, titanite grains from endoskarn and exoskarn show more complex patterns, with later zones that truncate and embay earlier ones. Each zone appears to be internally homogeneous with sharp boundaries against adjacent zones.

Titanite displays almost two distinctly different chondrite-normalised REE profile, one that is generally flatter or enriched in middle REE and slightly depleted in La, Ce, and HREE, and another generally enriched in LREE (slight decrease in La and Ce) and strongly depleted in HREE (Fig. 6.7). Profiles with intermediate slopes are unusual, while the abundance of REE vary significantly. The flatter profile correspond to euhedral titanite from titanite veins, endoskarn and few crystals from the altered granite, spatially related with titanite veins. These titanite crystals show, as the other, evident zoning that do not correspond to significant REE-pattern variation. Profiles slight enriched in LREE and strongly depleted in HREE are observed in altered granite and in rims of few crystals from biotite granite (Fig. 6.7). Thus, usually homogeneous or zoned titanite from altered granite, as well as mostly from veins and unaltered granite, do not show variation in the REE pattern during growth. In contrast exists a significant variation between different rock

typology. It is interesting to note that only a titanite crystal from the biotite granite shows variation in the REE pattern during growth.

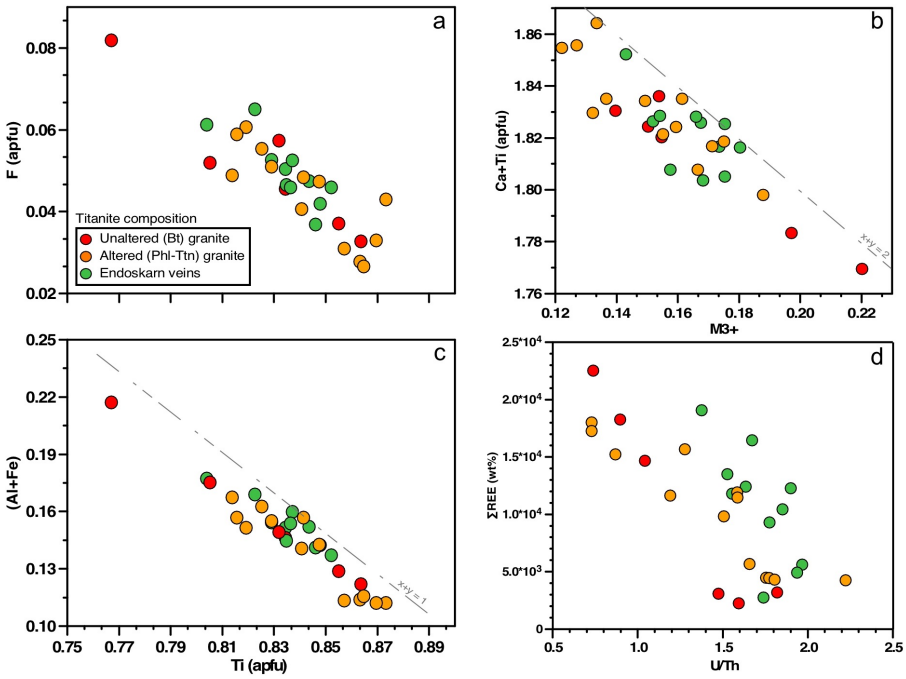

Fig. 6.6 - Selected composition diagrams of metasomatic titanite from the unaltered granite (red), from the altered granite (orange), and from endoskarn vein (green). The diagrams show the exchanging mechanism involving F, Al, and Ti. The diagram d) shows the correlation between the U/Th and REE concentration.

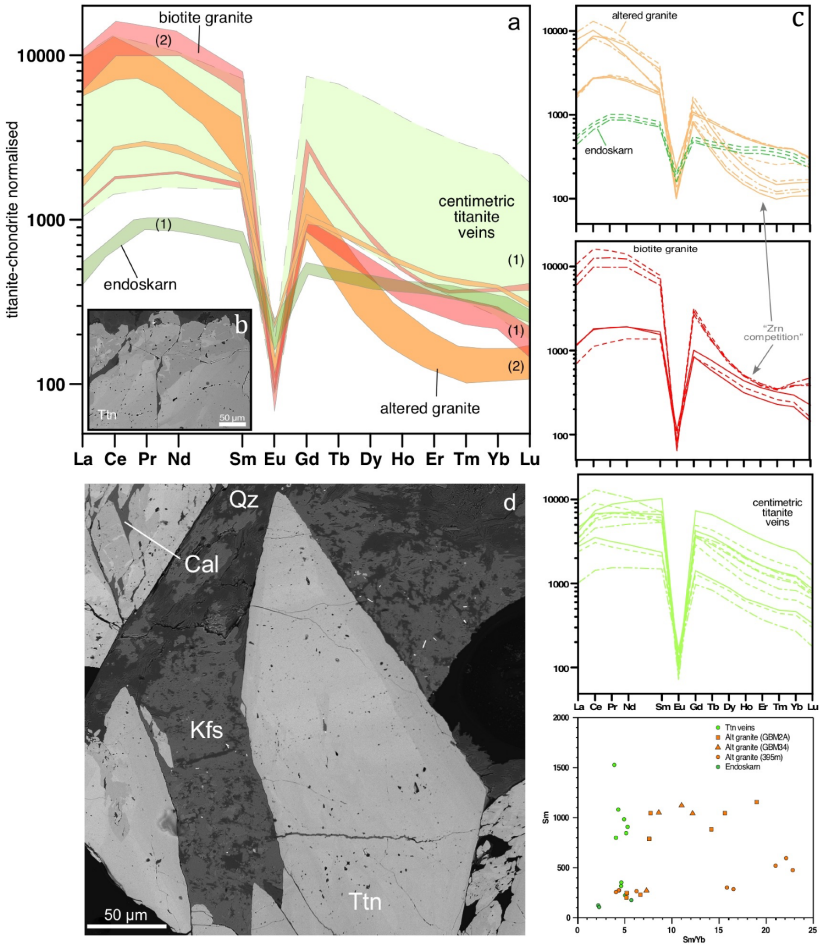

Fig. 6.7 - a) Chondrite normalised REE pattern for titanite from the biotite granite, the phlogopite titanite granite and the endoskarn veins.The symbols (1) and (2) indicate two different pattern groups. b) Backscattered electron images showing titanite zoning (altered granite). On right (c) are reported the chondrite normalised REE pattern for titanite from each lithology. d) Backscattered electron images showing zoned, centimetric titanite from endoskarn vein.

Rutile (TiO_2) - Rutile usually shows anhedral crystal observed in spatial relation with titanite, ilmenite and altered biotite. When it is observed in biotite from the altered granite, rutile form needle-shaped crystals between biotite intra-layer, testifying the exchange of $TiFe_{-1}$ with metasomatic fluids. Occasionally it is possible to observe perfectly octagonal euhedral crystals, characterised by prominent zoning linked to compositional variability (Fe, Al, Nb, Ta). However, rutile is mostly observed as replacement of ilmenite (ilmenite breakdown: $2FeTiO_3 \rightarrow 2TiO_2 + 2Fe + O_2$), and/or titanite, forming titanite-rutile aggregates. Rutile crystals reach size up to 300-500 µm, when completely replace titanite crystals. The average chemical composition of rutile are reported in Supplementary table 6.1. The analysed samples show a significant amount of Nb (0.1-2.8 wt%), Cr (up to 1.6 wt%), Fe (0-1 wt%), V (500-3500 ppm), Al (500-1000 ppm), Zr (70-700 ppm), Sc (40-340 ppm), and Sn (100-200 ppm). Zoned crystals commonly show a decreasing amount of Cr, Zr, Nb and Ta from core to rim, contrasting with the increase of Fe and Al. Low or no detectable concentration of REE is recorded. Plotting the obtained data on a Cr vs Nb diagram it is possible to distinguish between two populations of rutile (Cr/Nb ratio does not change significantly).

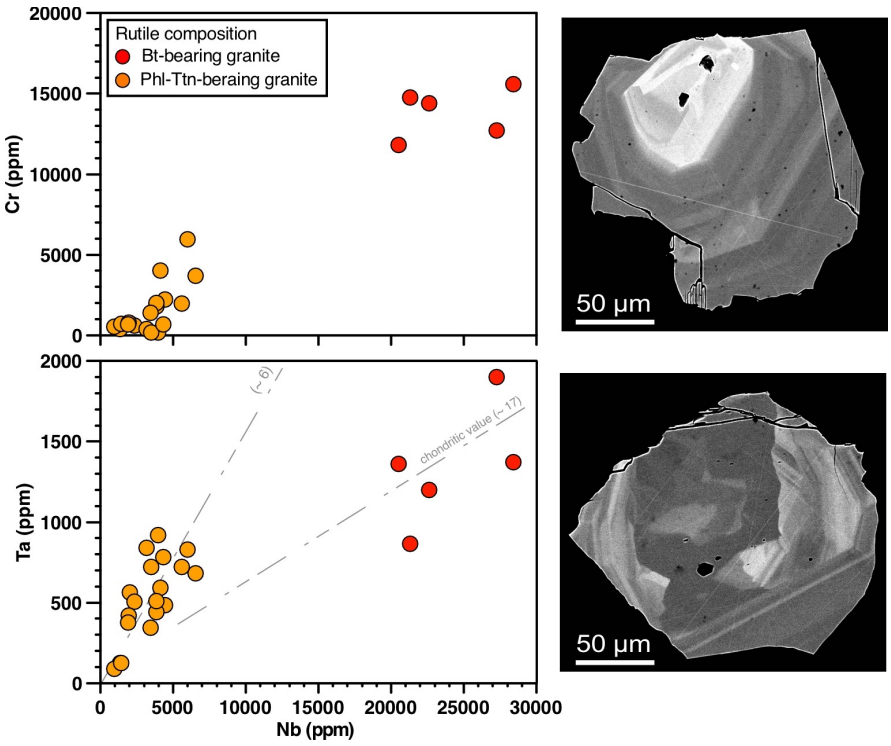

Fig. 6.8 - Selected diagram showing the mineral chemistry of metasomatic rutile after ilmenite during incipient alteration of the granite (red) and from the altered granite (orange). The diagrams show the tendency of Ta to uncouple from Nb (chondritic Ta/Nb=17.6). On right, BSE images showing the typical zoning observed in rutile crystals.

Calc-silicates (diopside, vesuvianite, garnet, epidotes)

The metasomatic minerals are mainly represented by association of calc-silicates as vesuvianite, diopside, garnet, titanite, epidote, minor ekanite, cheralite, as well as phlogopite, scapolite, zircon, apatite, sulfides and multiple generation of fluorite. Multiple fluid-mineral exchange reactions are pointed out by (i) the diffuse growing zonation of calc-silicates (garnet, vesuvianite, epidote, titanite), (ii) the multi-stage replacement of calc-silicates minerals (i.e. epidote → allanite; ekanite → thorite + quartz), (iii) the occurrence of metasomatic zircon, apatite, uraninite, thorite, replacing intensively altered calc-silicates (e.g., titanite).

Pyroxene (diopside-hedenbergite) - The typical metasomatic assemblage in the diopside-rich zone is diopside+titanite+calcite+quartz+epidote±K-feldspar±plagioclase, with variable abundance of sulfides. BSE and SEM-EDS analysed pyroxene collected from the Botro ai Marmi metasomatic bodies show wide ranges of solutions of the Ca-Mg-Fe pyroxenes, mostly falling in the diopside-hedenbergite field (Fig. 6.9; Morimoto et al., 1988). The main evident chemical variation regards the abundance of Fe (3-22 wt%) and Mg (3-16 wt%), giving pyroxene from En_{35-45} to En_{15-10}. Pyroxenes from exoskarn bodies, at the pluton-marble contact, show enrichment in Fe respect to Mg, in contrast, pyroxene from the endoskarn shows diopsidic composition, with Mg content higher then Fe. These groups

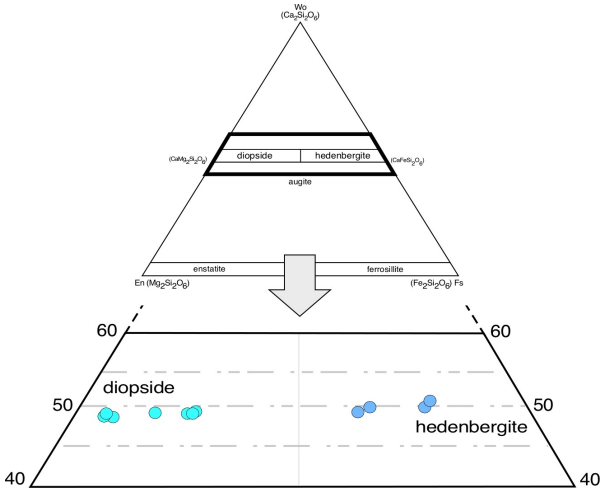

Fig. 6.9 - Mineral chemistry of metasomatic clinopyroxene (EPMA analysis). Composition ranges of the Ca-Mg-Fe clinopyroxene according to Morimoto et al. (1988).

may be classified as hedenbergite and magnesian-diopside, respectively (Fig. 6.9; Morimoto et al., 1988).Variation of Fe and Mg concentration occasionally produce growth zoning, which do not reflect other chemical changes. The content of Al is commonly lower than 0.5 wt%. Other trace elements are Mn (500-5000 ppm), Ti (0-500 ppm), Na (0-1300 ppm), and Zn (40-400 ppm). Content of F, REE, and HFSE are not significant, showing values close to the detection limit or even not detectable. Pyroxene is occasionally associated with small, interstitial amphibole, possibly resulting from its metasomatic alteration.

Vesuvianite - The chemistry and chemical variations in 16 vesuvianite crystals from exoskarn samples have been examined by EMP and then reduced to formula units on the basis of 50 cations and 78 anions. For 24 analysis, the mean Si content is 18.05 a.p.f.u., indicating that only Si occurs at the Z-group sites. The mean Ca+Na+La+Pb+Th content is 18.3 a.p.f.u., that indicate possible substitutions in the X site (usually 19). The mean Al+Mg+Fe+Ti+Mn+Cu+Zn content is 12.99 a.p.f.u., indicating that only these cations occupy the Y group site. In addition, the individual means for each group of sites support a 50-cation scheme of normalisation. For X=2^+ and Z=4^+, only an heterovalent substitution can involve Y group cations:

$$(Mg + Fe^{2+} + Mn) + Ti^{4+} \rightarrow 2(Al + Fe^{3+})$$

Groat et al. (1992) suggest that, based on ionic radii, those sites can potentially be occupied by REE cations. Indeed, REE are commonly minor constituent in vesuvianite, but can reach significant content (in this work show commonly values of LREE up to 2 wt%). There are three possible exchange reactions involving the incorporation of REE at the *X* sites. (i) Stated that the REE-rich vesuvianite contain common values of Al, it is possible to eliminate the substitutions REE^{3+}+Mg → Ca+Al and Mg+Ti → 2Al (Groat et al., 1992). (ii) Another possible mechanism involves the substitution of O^{2-} for OH^-, however, there are insufficient data on OH^- contents of vesuvianite to test the importance of this substitution. (iii) The last possible substitution proposed by Groat et al. (1992) is:

$$REE^{3+} + Na \rightarrow 2Ca \text{ and } Na + Ti^{4+} \rightarrow Ca + Al$$

Fig. 6.10 shows a perfect correlation between Na+Ti against Ca+Al or REE+Na, supporting $MgTiAl_{-2}$ as main exchange vector.

According to the chondrite-normalised pattern of the analysed vesuvianite it is possible to distinguish between two distinctly different vesuvianite group. One shows homogeneous crystals with composition typical of vesuvianite (i.e., Groat et al., 1992), while the other shows enrichment in LREE, Y, Th, and U (Fig. 6.10). Some common impurities are Zn (100-200 ppm), Li-Be (100-2000 ppm), and Zr (30-400 ppm). Bi, Sn, Sb show values in the order of 50 ppm. REE-rich vesuvianite are observed indistinctly in all the exoskarn lithology. Vesuvianite crystals from Di+Ep+Vs+Qz+Cal-exoskarn show the highest values of REE accompanied by the highest value of Th (up to 2500 ppm) and U (up to 3900 ppm), replacing Ca in the *X* site (Fig. 6.10). These elements show high values also in vesuvianite crystals from the other environments (Th=0.5-5000 ppm; U=1.5-580 ppm). Vesuvianite from Vs-Grt-rich exoskarn shows a prominent growth

zoning, with significant variability of U, Th and REE content. Some crystals show the maximum values of these components in the middle area, respect to the rim and the core, with positive correlation between U and REE. Other crystals show the increase of U and Th from rim to core and the negative correlation with REE content. Moreover, all the analyzed vesuvianite contain significant amount of F (0.68-0.88 wt%), probably replacing OH^- or O sites.

The vesuvianite chondrite-normalised REE patterns (Fig. 6.10) highlight almost two distinctly different profiles, both enriched in LREE and depleted in HREE. The patterns obtained from vesuvianite crystals sampled from Di-bearing exoskarn show a constant slope from enriched LREE to depleted HREE, with a strong negative Eu anomalies (Eu/Eu*=0.31-0.44). The others crystals, separated from vesuvianite- and garnet-rich exoskarn, show profiles characterised by a marked LREE slope, a strong depletion in middle REE and a flat HREE pattern, with a prominently positive Eu anomaly (Eu/Eu*=1.9-8.3). Thus, REE patterns show a weak negative Eu anomalies for vesuvianite enriched in REE, and, on contrary, strong positive Eu anomalies for vesuvianite crystals with a lower content of REE.

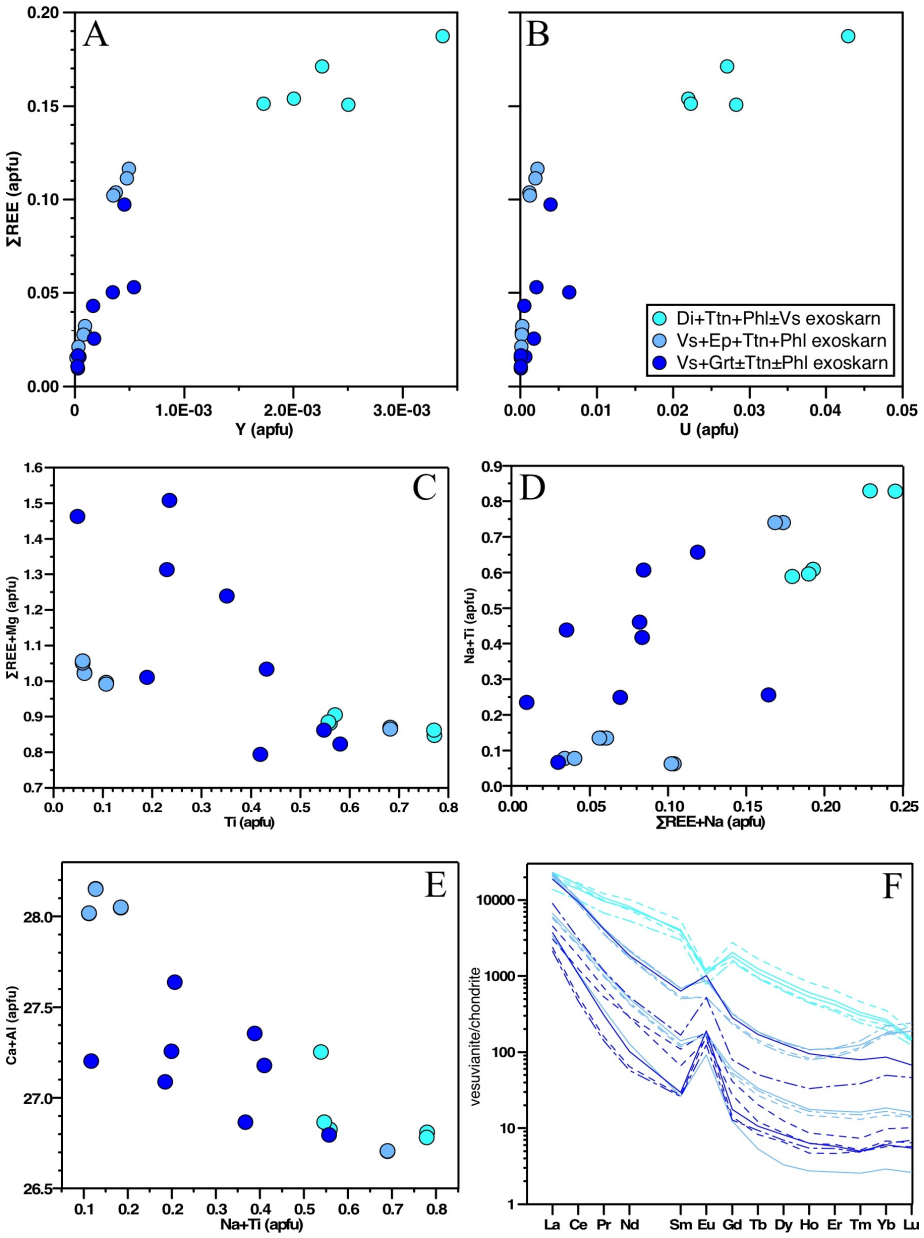

Fig. 6.10 - Selected diagram showing the mineral chemistry of metasomatic vesuvianite from different exoskarn typology. Diagrams from A to E show the correlation between REE, U, Ti, Mg, Ca, Na, and Al. F) Chondrite normalised REE pattern for vesuvianite from different exoskarn typology. It is possible to observe two different REE profiles (see text for discussion).

Garnet - Garnet-pyroxene exoskarns are predominant at the pluton-host contact (Paoli et al., in prep. - chapter 5). By petrographic observations, more than a generation of garnet has been identified in a millimetre area, attesting the extremely dynamic nature of the metasomatic system. Commonly, garnets are red to brownish, anisotropic, and exhibit low birefringence. Oscillatory zoned garnets show morphological transition from a simple dodecahedral growth, in the core, to a composite dodecahedral trapezohedron growth, near its margin. High index faces indicate fast crystal growth (e.g., Jamtveit et al., 1993). Anisotropy is not always homogeneous or sectorial and chaotic birefringence, development of lamellae, and irregular boundaries between sectors have been also observed. Minor and trace elements can also be present in garnets according to several exchange mechanisms (McIntire, 1963), such as surface adsorption and occlusion (growing kinetic effect-controlled), or substitution mechanisms and interstitial solid solution (crystal chemistry-controlled). The incorporation of REE and Y is also possible by replacement of X^{2+} cations in the dodecahedral position. Semi-quantitative analysis (SEM-EDS) on garnets from the Botro ai Marmi exoskarns define a solid solution between grossular–andradite. The compositions range from $Adr_{30}Grs_{70}$ to almost pure grossular Adr_1Grs_{99}, with spessartine, pyrope, almandine, uvarovite, etc. collectively lower than 10%. Rare $Adr_{70}Grs_{30}$ to almost pure andradite also occur (Supplementary Table S.6.1.). Slight variation are observed between (i) garnets from pyroxene-garnet exoskarn, showing pyralspite up to 12%, grossular up to 90%, and andradite between 0-15%, (ii) zoned garnets, showing pyralspite between 0-7% and mainly grossular content, and (iii) garnets from Di+Ttn+Cal+Qz±Ep ±Vs-exoskarn, showing pyralspite content lower than 10%. Garnets with oscillatory zoning usually show Al-rich cores and Fe-rich rims, but homogeneous garnets and garnets with Fe-rich cores and Al-rich rims can also be found. This is consistent with most metasomatic systems, where early prograde garnets tend to be Al-enriched and later or retrograde garnets tend to be Fe-enriched (e.g. Einaudi et al., 1981; Nakano et al., 1989; Meinert, 1997).

Epidote-group - Epidote is common in endoskarn and exoskarn, as well as frequently observed in the altered granite. This phase is characterised by multiple generations showing significant chemical variability. The general mineral formula of epidote-group minerals is $A_2M_3Si_3O_{12}(OH, F)$, with the A site containing Ca^{2+} (epidote subgroup) or Ca^{2+} $+REE^{3+}$ (allanite subgroup), and M site containing $Al^{3+} + Fe^{3+}$ (epidote subgroup) or $Al^{3+}+Fe^{2+}$ (allanite subgroup). The main control on the chemistry of epidote-group is fixed by the coupled exchange reaction $[REE^{3+}+Fe^{2+}] \rightarrow [Ca^{2+}$ $+Fe^{3+}]^{-1}$. Also the $Fe^{3+}Al^{3+}{}_{-1}$ exchange vector may control the chemistry of this phase. These coupled substitutions (Petrík et al., 1995; Poitrasson, 2002) can be depicted on an Al vs REE diagram, and Fe^{3+}/Fe^{2+} ratios can be estimated using the following equation:

$$Fe^{3+}/(Fe^{3+} + Fe^{2+}) \rightarrow (REE^{3+}/Al^{3+}) + 1$$

Fig. 6.11 displayed two different type of epidote characterised by variable chemistry (n = 15). The first group, collected from Di-bearing exoskarn, shows values of REE<0.2 a.p.f.u. and Fe^{3+}>0.8, that allow to classify the mineral as epidote ($Al^{3+}>Fe^{3+}$). The other, composed by crystals from altered granite and Vs-bearing exoskarn, generally shows value of REE>0.5 a.p.f.u. and Fe^{3+}<0.5 a.p.f.u., classifying the mineral in the allanite subgroup. Compositional data for metasomatic epidote are listed in Supplementary Table S.6.1 for granites, diopside exoskarn, and vesuvianite exoskarn. The Di-bearing exoskarn shows both the epidote varieties, with an evident substitution of Ca^{2+} with REE^{3+}, moving from cores to the rim of the crystals and spatially related (later) REE-rich epidote. On the other hand, allanite-(La,Ce) from the granite and the Vs-bearing exoskarn is more homogeneous, showing only a slight enrichment of $REE^{3+}Fe^{2+}$ moving from core to rim observed in samples from the granite body. The overall result is the occurrence of two generation of epidote, in which the REE concentration increases with decreasing Ca concentration. As suggested by Gysi et al. (2016) the allanite composition can be used to relate stages of Ca-metasomatism to the redox condition (Fe^{3+}/ Fe^{2+}) and the Al and REE concentrations of the hydrothermal fluids. As shown in Fig. 6.11, the data for epidote from diopside exoskarn plot on a linear trend of Ca against $Fe^{3+}/(Fe^{3+} + Fe^{2+})$, while the other samples, compared to general trend, show lower $Fe^{3+}/(Fe^{3+}+Fe^{2+})$ ratios with decreasing Ca concentration. For comparison, data for epidote-group

minerals from similar localities are also shown (Corupá pluton - Vlach, 2012; Strange Lake granite - Gysi et al., 2016). Moreover, the Ca vs REE diagram (allanite) yield the same linear trend, indicating a good substitution of the REE for Ca with minor fraction of other elements being involved, except Fe for the coupled substitution with Al. The average composition of epidote is occasionally enriched in Sr (800-1000 ppm), Sn (1700-3000 ppm), and Sb (up to 450 ppm) in samples from the Di+Phl+Ttn+Cal±Vs±Ep exoskarn. At the same time this epidote shows a lower Th/U ratio (< 0.5), with low value of Th (0.4-5 ppm). In contrast, the average composition of allanite from the altered granite and from the endoskarn veins shows higher Th/U ratio, with commonly higher values of Th (50-1930 ppm) respect to U (40-200 ppm). This group shows also the highest value of REE (12-26 wt%). REE show a positive correlation with Th/U ratio and F values, suggesting probable exchange reactions. Allanite shows the highest values of F (up to 0.4 wt%).

Epidote is characterised by LREE-enriched pattern and display two distinctly different chondrite-normalised REE profile, both strongly depleted in HREE (Fig. 6.12). One is generally more enriched in LREE and middle REE and strongly depleted in HREE, another is generally enriched in LREE (with lower concentration), flat for middle REE and less depleted in HREE. Profile with higher LREE enrichment correspond to allanite-(La, Ce) from endoskarn and altered granite, while the flatter pattern represent epidote from Di-bearing exoskarn, showing lower REE content and metals enrichment.

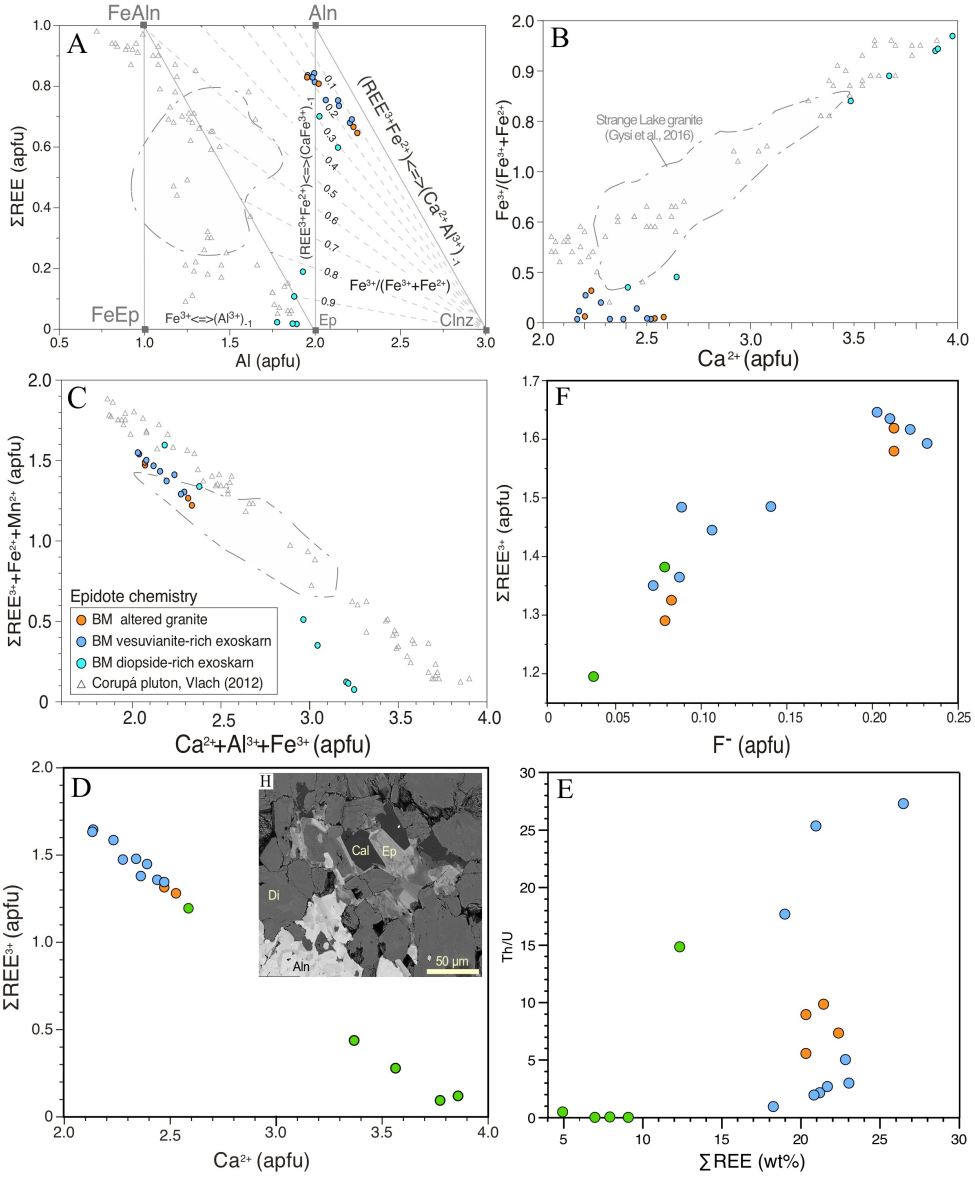

Fig. 6.11 - Mineral chemistry of hydrothermal epidotes from the altered granite (orange), the vesuvianite rich exoskarn (blu), and the diopside-rich exoskarn (light blu). a) Diagram showing the element substitution mechanisms in epidote-group minerals and the method for estimating $Fe^{3+}/(Fe^{3+}+Fe^{2+})$ of Petrík et al. (1995). b, c) Diagrams showing element substitution mechanisms involving REE, Ca, Al, and Fe. Note that allanite crystals have the lowest $Fe^{3+}/(Fe^{3+}+Fe^{2+})$ ratios. For comparison, data for epidote-group minerals from similar localities are also shown (Corupá pluton, Vlach, 2012; Strange Lake granite, Gysi et al., 2016). D, E, F) Mineral chemistry of hydrothermal epidote and allanite showing correlation between REE, Th/U ratio and F content.

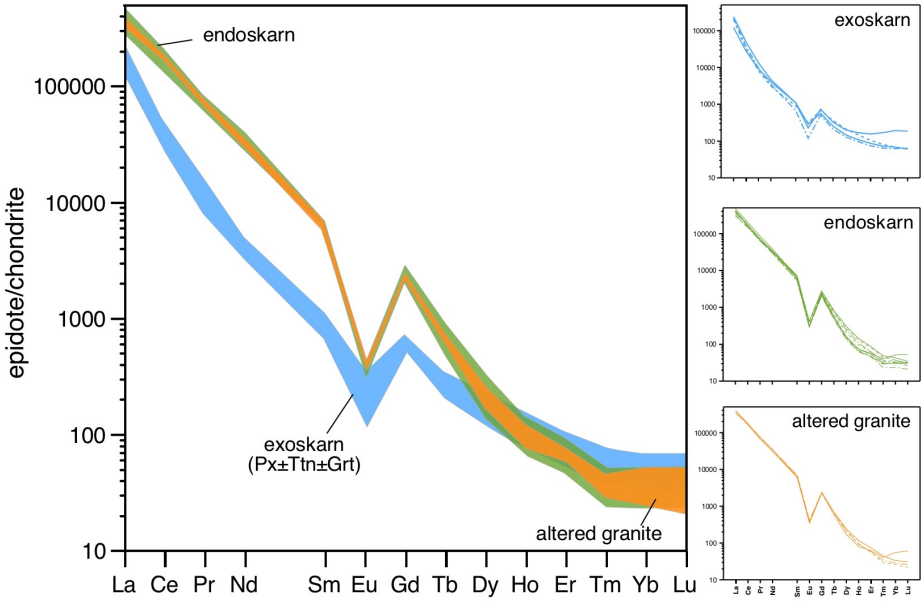

Fig. 6.12 - Chondrite normalised REE pattern for epidote from the altered granite, the endoskarn and the exoskarn bodies. It is possible to define almost two distinct REE patterns. On right are reported the REE pattern for epidote from each lithology.

Accessory minerals (magmatic-to-hydrothermal crystallisation)

HFSE-REE accessory minerals - Zircon and apatite directly precipitated from hydrothermal fluids should display consistent internal structures (oscillatory or sector zoning), also typical of magmatic grains. The best textural evidence for the hydrothermal origin of zircon or apatite is its occurrence in metasomatic rocks, such as exoskarn, mutually with other hydrothermal minerals (e.g., calc-silicate, micas, or other accessory minerals), or the presence of hydrothermal inclusions (Schaltegger, 2007).

At Botro ai Marmi it is possible to recognise both magmatic and metasomatic zircon and apatite. Zircon grains from the unaltered granite are commonly colourless and range from 50 to 250 µm in diameter. Cathodoluminescence images exhibit euhedral zircons, with typical oscillatory zoning and rare inherited cores. Metasomatic zircons resulted also from the late metasomatic alteration of calc-silicates, usually titanite. Zircon grains from metasomatic rocks are usually smaller than 30 µm in diameter, euhedral to subhedral, homogeneous with minor oscillatory zoning and rare inclusions, usually mutual with other accessory minerals (e.g., apatite, monazite, uraninite, thorite). On the other hand, metasomatic apatite from the altered granite is linked to altered biotite. Indeed, apatite, that in granitic rocks is commonly included in biotite, in this context occurred as crystals of 400-500 µm (uncommon size for magmatic apatite) grown across biotite rim or between their layering. Instead, lesser and smaller crystals are included into biotite. The metasomatic products commonly show euhedral to subhedral apatite crystals (20-100s µm in length) linked to newly crystallised calc-silicates. Apatite shows variable textures, such as complex zoning patterns, homogeneous and oscillatory zoned crystals. They are usually included in phlogopite or fill cavities as aggregate of crystals with calcite, titanite and diopside. The frequent intergrown with small euhedral zircon grains support the hydrothermal origin for apatite.

Secondary crystals of monazite, occasionally observed in trail of zircon-monazite aggregates (5-15 µm) into metasomatic K-feldspar crystals, are also observed. Moreover, at the granite-host contact, the abundant crystallisation of apatite is accompanied by the crystallisation of HFSE-REE-rich calc-silicates, such as cheralite [$CaTh(PO_4)_2$] and ekanite ($Ca_2ThSi_8O_{20}$). These minerals are commonly replaced by secondary thorite-quartz pseudomorph (ekanite) or thorite-apatite-zircon aggregates (cheralite).

Sulfides

High- to low-temperature sulfides are widespread throughout the system. The main sulfides are pyrrhotite (FeS), pyrite (FeS_2), sphalerite (ZnS), chalcopyrite ($CuFeS_2$), and minor galena (PbS). Single- and poly-phase sulphide grains occur: (i) as isolated interstitial grains at the contact between unaltered grains of magmatic minerals, (ii) in veins crosscutting the systems or along cleavage planes and fractures of fresh igneous minerals, and more rarely (iii) as inclusions near the margins of the same minerals. Individual grains are typically subhedral and varying from μm to cm in size and they are accompanied by crystallisation of quartz, fluorite, as well as HFSE-REE and Th-U accessory minerals. Iron sulfides, chalcopyrite and minor Zn-Pb sulfides occurred as fracture and cavities infill. Numerous sulfides-quartz-calcite bearing veins (few millimetres to decimetres in width) are irregularly developed within the granitic rock, following the magmatic jointing. Pyrrhotite-pyrite-sphalerite aggregates are widespread throughout endoskarn and exoskarn system, filling open-space, forming veins, as isolated crystals, and showing multiple processes of intergrowth and mutual replacement. A late, low-temperature veins system follow the granite body fracturation. It is characterised by abundance of chlorite, pyrite-sphalerite, calcite, quartz, violet fluorite, uraninite, and thorite.

Fluorite

Fluorite crystals, showing variable size and colour, are observed as widespread, euhedral and interstitial, secondary crystals in the altered granite (frequently associated with sulfides), in the metasomatic bodies (exo- and endoskarn), and forming late quartz-fluorite and chlorite-sulfides-fluorite veins. In the altered granite, fluorite commonly crystallised between biotite intra-layers, provoking an intense chloritic alteration. Fluorite crystals are commonly associated to other metasomatic minerals, such as sulfides, usually growing along fractures. The crystallisation of accessory minerals into fluorite could produce structural deformation, resulting in worthy violet to blackish fluorite crystals. Finally, fluorite-pyroxene pseudomorphs (±quartz and calcite) clearly modify a former metasomatic pyroxene-quartz-calcite association.

Colourless and withe crystals are collected from late hydrothermal quartz-fluorite-sulfides-calcite veinlets, crosscutting the granite. Pink, violet and dark violet crystals are collected from hydrothermal centimetric veins usually related to sulfides and accessory minerals (e.g., uraninite, cheralite, thorite). Finally greenish crystals are collected from late hydrothermal veins in the endoskarn veins. In the hydrothermal vein is also possible to observe fluorite crystals characterised by a colour shade from pink core, through green zones to a whitish rim. The analysed fluorites do not show significant impurities, with the exception of Sr (up to 150 ppm). On the other hand, the REE-profiles showed two principals groups of fluorite (Fig. 6.13). The green colour group is rich in REE, with LREE and HREE fractionation respect to middle REE. In contrast, the violet to colourless fluorites show less content of REE and flatter pattern, with a unusual Y positive anomalies. Dark violet or black fluorite are interpreted as violet fluorite damaged by radiation that was caused by uranium minerals included in some of the vein-type deposits. Thus colour reflect REE(+Y) content, that is mainly control by the minerals association in which fluorite crystallised.

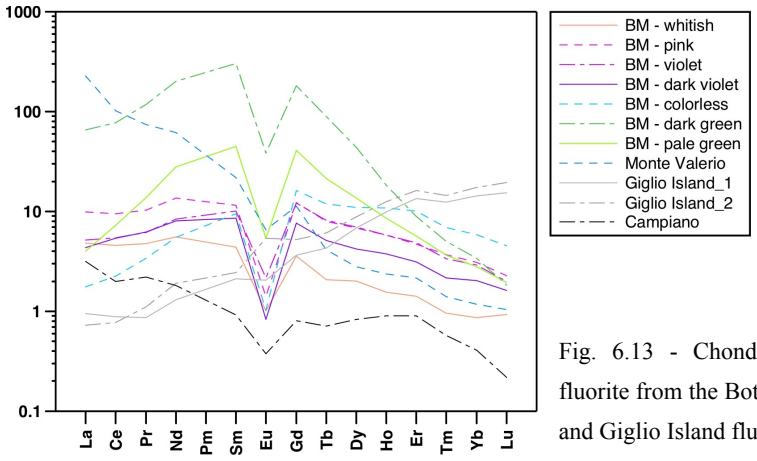

Fig. 6.13 - Chondrite normalised REE pattern for fluorite from the Botro ai Marmi system. Monte Valerio and Giglio Island fluorite are shown for comparison.

6.5. Discussion

Heat-liberating events, such as igneous intrusions emplaced into cool carbonatic rocks, will result not only in loss of heat to the surrounding environment, but also in the transport of volatile components which are responsible for metasomatic effects. Metasomatism is a process by which new minerals replaced old ones (e.g., Lindgren, 1925), that process capable of changing the bulk composition of a rock (e.g., Ramberg, 1952). Again, metasomatism is a process that involves major gain or loss of components, usually thanks to flow of large quantities of fluids through an open rock body (Best, 1982). Therefore, metasomatism is the process whereby elements are exchanged between fluids and adjacent rocks (Pirajno, 1992). The peraluminous granite of Botro ai Marmi was interested by multiple metasomatic processes provoking prominent element mobilities.

The comparison between chemical analysis of representative rock-forming minerals collected at Botro ai Marmi allow to investigate the physico-chemical variabilities of the hydrothermal fluids responsible for the alteration processes occurred in this area.

Interpretations of metasomatic processes

The primary igneous assemblage of the unaltered monzogranite consists of K-feldspar, quartz, plagioclase, and biotite, along with accessory cordierite, apatite, and zircon. Crystallisation of tourmaline-quartz orbicules is attributed to the late exsolution of B-rich fluids from the magmatic source (shortly after emplacement or during a late-magmatic stage). The intrusion of the Botro ai Marmi granite resulted in the metasomatic alteration of the carbonatic host-rocks (Fig. 6.14).

K-metasomatism

After emplacement, K-rich fluids produced a strong metasomatic alteration of the whole granite body. The alteration of igneous minerals (e.g., biotite, plagioclase, K-feldspar) produced a significant component exchange (Figs 6.3, 6.4). The content of some elements remain invariant after exchange reactions forming new phases (Ti, Al, Si), other were added (K, Mg, Ca, Rb, Ba, Sr), while other (Fe, Mg, Na) where lost from the granite. Plagioclase was replaced by K-feldspar (complete replacement of oligoclase rim, and partial replacement of andesine core), after a mechanism of alkali ion exchange between potassic fluid and feldspar phases. Metasomatic alteration of biotite (exchange of Ti, Fe, K and Al) coupled with the addition of such components (K, Mg) resulted in the replacement of biotite by phlogopite-chlorite, as well as new crystallisation of Al-rich titanite and rutile. Phlogopite is slightly enriched in LREE-Nb, and quite enriched in F (3 wt% vs 0.5 wt% in biotite). Moreover, also chlorite, usually devoid of F, shows unusual F contents up to 0.25 wt%, indicating a significant addition of F during metasomatic alteration. Indeed, intra-crystalline chlorite layers are commonly in close spatial relation with fluorite crystallised between biotite layers. Titanite and rutile present a significant enrichment in Nb, Zr, and Al, as well as similar Nb/Ta ratios (Fig. 6.8), allowing to infer a common origin, as also highlighted by the petrographic evidences of mutual replacement. The local Si gain in the altered granite correspond to crystallisation of new albite and quartz. The potassic metasomatic stage is also characterised by the partial alteration of accessory minerals included in biotite. The increase acidity of fluids, during the final stage of potassic metasomatism, provoked dissolution/precipitation reactions and the mineral-fluid exchange of P, and minor of LREE and HFSE. These processes are highlighted by the widespread crystallisation of new apatite, and by the increase concentration of LREE and HFSE in growing titanite (Figs 6.6, 6.7). Moreover, the crystallisation of iron and minor Cu-Zn-Pb sulfides evidence the gain of metals.

Ca-metasomatism

The increasing acidity of metasomatic fluids due to mixing with high-temperature Ca-rich fluids triggered a Ca-metasomatism stage. This alteration affected the monzogranite along magmatic jointing (endoskarn vein) and at the pluton-host contact, as well as the carbonate host at the contact and along folded layers. The fluids responsible for this metasomatic alteration could be related to a twofold source. In the area adjacent to the monzogranite-host contact, fluids are likely released from the host carbonate. Contrary, along endoskarn veins within the granite, far from the contact (300m of depth in borehole; Paoli et al., in prep. - chapter 5), Ca-rich fluids are likely released from a deeper, not exposed source. Reactions involving addition of Ca and Mg, together with exchange of Fe, Ti, Si, Al and trace elements lead to the alteration of the original rocks and crystallisation of new cal-silicates, aluminosilicate and REE-HFSE phases.

The replacement of the potassic altered granite resulted in the new crystallisation of diopside+titanite+phlogopite +epidote(s)±apatite±zircon association. Ca-metasomatism of the host carbonate (calcite±dolomite±phyllosilicates) resulted in the crystallisation of diopside+(hydrogrossular)garnet+vesuvianite+epidote(s)+titanite+phlogopite±scapolite ±apatite±zircon±ekanite±cheralite. This paragenesis highlight the exchange of major and trace element between fluids, metasomatised granite, and host carbonate. Moreover, the distribution and density of the new minerals reflect the local composition of the host carbonate. For example, phlogopite crystallisation increase along folded marble, probably characterised by a greater abundance of marly impurities (Mg-rich phyllosilicates).

In the Botro ai Marmi granite, as usually observed in igneous rocks, accessory minerals control the total amount of REE and mostly of HFSE. Magmatic apatite and monazite are easily altered by metasomatic alteration, generating mobilisation of P, REE, Th and other trace element. The exchange reactions with Ca-rich fluids provoke the crystallisation of secondary apatite in the altered granite, and the secondary crystallisation of trail of zircon-monazite aggregates (5-15 μm) into metasomatic K-feldspar crystals. Instead, at the granite-marble contact, the increasing activity of Ca-rich fluids produced the abundant crystallisation of apatite, as well as HFSE/REE rich calc-silicates, such as cheralite and ekanite. At the same time, patter of zoning in the new calc-silicates show the increase of Th, U, HFSE, and REE, supporting the intensification of exchange reactions between rocks and metasomatic fluids. This stage is characterised by the low activity of F supported by the occasional crystallisation of fluorite.

Declining Ca-activity and increasing F-activity

The continuous crystallisation of calc-silicates (Ca sequestration) lead to the increasing acidity of the residual fluid(s) and to the increasing activity of fluorine. These fluids are responsible for the hydrothermal alteration of HFSE/ REE magmatic minerals and of metasomatic calc-silicates, producing the mobilisation of REE/HFSE in the late stage of the metasomatic activity. The metasomatic alteration due to fluid(s) characterised by increasing acidity shows the following textures: (i) titanite, epidote(s), vesuvianite, and garnet with reaction and growth zoning characterised by the common increase, moving from core to rim, of HFSE (i.e., Nb, Ta, Zr), LREE, Th, U, as well as metals (i.e., Zn, Sn, Sb), (ii) epidote progressively replaced by Ce-La-rich allanite, suggesting the REE-Al vs Ca-Fe exchange reaction, (iii) dissolution/replacement reactions of calc-silicates (Ca-metasomatism) resulting in the crystallisation of secondary apatite, zircon, thorite, uraninite, usually bordering or in close spatial relation with the parental calc-silicate. Moreover the acidic alterations is characterised by (iv) the pseudomorphic replacement of ekanite by thorite-quartz aggregates, cheralite by thorite-apatite-zircon aggregates, and diopside-quartz-calcite by clinopyroxene-fluorite-quartz-calcite aggregates, testifying significant textural alteration processes. The cal-silicates crystallised during this late-stage shows positive correlation between F, structure-forming elements (Fig. 6.7), REE content, and Th/U ratio (Figs 6.10 and 6.11), supporting the ability of F-rich fluids to enhance the exchange of these components. Moreover, the widespread crystallisation of fluorite support the importance of F activity during the whole metasomatic process(es).

Fig. 6.14 - A schematic model for the progressive element mobility observed at the Botro ai Marmi metasomatic system. These diagrams define the main mechanism responsible for the selective mobilisation of elements indicating the possible litho-geochemical vectors for the metasomatic processes.

Elements mobilisation during metasomatism

LA-ICP-MS and EPM data of representative rock-forming minerals from Botro ai Marmi allow to identify the physico-chemical variation of the hydrothermal fluids resulting from the different alteration processes. Changes in minerals composition or elements ratios reflect the crystallisation/replacement/dissolution of certain phases respect to others. For example, the variations of REE-patterns observed in several minerals may be interpreted to reflect progressive process of metasomatic alteration and crystallisation from fluid with a variable LREE/HREE ratio, or a contemporaneous growth of minerals characterised by contrasting REE fractionation.

Most of the metasomatic minerals show the enrichment in Al, Sr, Ba, LREE, HFSE, Zr, Th, U, and Sn from core to rim. F shows unusual concentration in most of the new crystallised minerals, defining a common positive correlation with REE content. Moreover, in Al-rich titanite, F content (0.25-0.80 wt%) correlates positively with Al content (3.5-5.5 wt%), suggesting a mutual exchange reaction. Usually, LREE are more enriched respect to HREE (i.e., phlogopite), according to their relative mobility, with the former more mobile at high temperature and the latter at low temperature (Gysi and Williams-Jones, 2013). Phlogopite, titanite and rutile, including grains from the altered granite, show significant abundance of Nb (up to 2.8 wt% in rutile). Titanite and rutile show concomitant abundance of Ta the correlates positively with Nb. These components testifying the mobilisation of HFSE from the beginning of the metasomatic alteration (K-metasomatism). Phosphate are interpreted to control the mobility of P, REE and HFSE since this stage of metasomatic alteration. Indeed the granite is characterised by the significative alteration of monazite and apatite, and the whole system is characterised by newly crystallised apatite, while endoskarn and exoskarn show frequently minor cheralite grains.

Titanite, vesuvianite, and epidote(s) show the general increase of the REE content from core to rim, indicating the progressive mobilisation of these components. Titanite shows the negative correlation of REE content with Th/U ratio from core to rim, whereas the opposite is true for vesuvianite and allanite (positive correlation). These data reflect the differential mobilisation of Th and U in the different lithologies (the latter easily mobilised), thus the crystallisation of hydrothermal minerals from a fluid with variable Th/U ratio. Moreover, the abundance of Th in the fluids is probably controlled by exchange of Th between fluid and accessory minerals, either magmatic (monazite, apatite, zircon) or newly crystallised during Ca-metasomatic stage (ekanite, cheralite). The increase of REE content in growing epidote and their replacement by allanite (exchange of $CaFe^{3+}$ with $REEFe^{2+}$) testify the higher acidity of metasomatic fluids. Indeed, the continuous crystallisation of calc-silicates (Ca sequestration) lead to the alteration of calc-silicates formed during Ca-metasomatism.

Titanite is the most representative metasomatic minerals observed over-all the different environments (altered granite, endoskarn, exoskarns). Since mineral-fluid partition coefficients for the REE in titanite do not vary significantly from LREE to HREE (Henderson, 1980), the distribution of these elements in the mineral reflects their availability in the environment of formation. Titanite crystals from altered granite, veins, and unaltered granite do not show significant variations in the REE-pattern during growth. In contrast exists a significant variation between different rock typology. Euhedral titanite crystals from titanite and endoskarn veins show generally granitic pattern (flatter profile), while late-zoning of titanite from altered granite commonly shows LREE-enriched and HREE-depleted pattern (Fig. 6.7). Occasional La and Ce depletion is attributed to the coeval crystallisation of allanite or mobilisation of these elements to form secondary accessory minerals. Moreover, titanite from granite is characterised by a strong depletion in HREE,k that could be attributed to the solubility of zircon during acidic conditions.

The crystallisation from fluids with variable LREE/HREE ratio is also supported by epidote REE-profiles, commonly showing LREE-enriched pattern. La-Ce allanite from endoskarn and altered granite shows a significant LREE-enriched and HREE-depleted pattern, while epidote from Di-bearing exoskarn are characterised by flatter patterns, lower REE and metals content (Figs 6.11, 6.12). Epidote crystallisation is usually accompanied by garnet crystallisation (mainly in exoskarn). Thus, the variability in the REE-patterns could be controlled by (i) crystallisation

of garnet, commonly showing HREE-enriched patterns and high Lu/Hf and Sm/Nd ratios (Gaspar et al., 2008), and/or by (ii) the solubility of zircon, which is enhanced by low temperature and pH and high F concentration, that likely predominate during acidic metasomatic alteration.

Significant data results from the analysis of vesuvianite chondrite-normalised REE patterns (Fig. 6.10). Vesuvianite crystals from Di-bearing exoskarn show a constant slope from enriched LREE to depleted HREE, with a strong negative Eu anomalies (Eu/Eu*=0.31-0.44). Contrary, vesuvianite from Vs>Grt and Grt>Vs exoskarn, shows profiles characterised by a significant enriched LREE profile, strong depletion in middle REE and flat HREE pattern, with a prominently positive Eu anomaly (Eu/Eu*=1.9-8.3). These data cold be explained with the mutual crystallisation of allanite, explaining the variable inclination of LREE-pattern, and garnet, responsible for the HREE depletion. The existence of an Eu anomaly suggests that Eu is present as Eu^{2+}, contrasting with the Eu^{3+} state of the other REE. The widespread presence at Botro ai Marmi of magnetite and mostly pyrrhotite highlights a reduced environment (Gaspar, 2005). Under such reduced conditions Eu should be present as Eu^{2+}, which in part explains its different behaviour from the other REE and the consequent Eu/Eu* ratios. At temperatures above 250 °C, Eu^{2+} should predominate (Sverjensky, 1984), and Eu can fractionate from the other REE (Bau, 1991). Differences in the magnitude of the anomaly may be interpreted to reflects local heterogeneities of the system (protolith and metasomatic fluid) possibly generated by the metasomatic alteration of magmatic plagioclase, incorporating Eu^{2+} replacing Ca^{2+}, and/or the alteration of usually mutual metasomatic garnet characterised by positive Eu anomaly (Gaspar et al., 2008). Moreover, Sverjensky (1984) and Bau (1991) stated that Eu^{3+}/Eu^{2+} redox potential in hydrothermal fluids depends mainly on temperature and speciation, and less on pH or pressure. Speciation can extend the stability of Eu^{3+} which can be significant at low temperatures. However, at the relatively high temperatures observed in metasomatic systems, Eu^{2+} should predominate and Eu can fractionate from the other REE (Bau, 1991). Worth of note is the strong negative anomalies of Eu resulting from fluorite analysis. Indeed, Eu^{2+} is too large to enter the fluorite structure. Contrary, positive anomalies could be explain by metasomatic alteration of feldspar at high fO_2 allowing circulation of Eu^{3+} (Hill et al., 2000).

In this context, interesting results occurred from the comparison between REE-pattern of fluorite from Botro ai Marmi and other areas interested by hydrothermal activity (green fluorite from the Monte Valerio Fe-Sn(-W) deposit; colourless fluorite from the Giglio Island hydrothermal pyrite mineralisation). Two different REE-pattern groups (Fig. 6.13) are characterised one by strong enrichment in middle REE and depletion in HREE (green crystals), while the other by flatter pattern with slight depletion in HREE (white, violet, pink crystals, colourless). Thus exist a correlation between colour and REE patter. Green crystals of fluorite show the highest content of REE with a strong enrichment of middle REE, respect to violet crystals, showing flatter patterns. The green crystals are usually spatially related with late quartz-chlorite-sulfides veins, indicating a late circulation of the HFSE and the REE. Moreover, the positive anomaly of Y is common and interpreted to reflect crystallisation from enriched hydrothermal fluids after extended fluid-rock interaction (Dill et al., 2011; Munoz et al., 2005).

REE-HFSE-Zr mobilisation by fluorine activity

The answer to the REE mobilisation is the formation of aqueous chloride complexes ($REECl^{2+}$, $REECl^{2+}$), whereas the mobility of Zr mostly depended on the formation of hydroxy fluoride complexes such as $ZrF(OH)_3$ and $ZrF_2(OH)_2$ (Gysi and Williams-Jones, 2013; Migdisov et al., 2009, 2011). Moreover, this process is enhanced by low pH values, which depends from the initial concentrations of Cl and F, temperature (decreasing T correspond to increasing supply of H+), and intensity of fluid-rock exchange reactions. Usually mineral solubility increase with increasing temperature, whereas zircon go through retrograde solubility indeed are mostly mobilised at lower temperature (Migdisov et al., 2011; Gysi and Williams-Jones, 2013). Thus, the crystallisation of REE-bearing minerals in close spatial relationship with altered minerals could be explain by the scarcity of REE transporting ligands, such as chloride, together with the abundance of fluoride and phosphate, which likely play an important role as depositional ligands (Migdisov et al.,

2016). The simultaneous crystallisation of minerals with contrasting LREE/HREE partition coefficients produced variability in the REE-pattern of crystallising minerals. Increasing availability of F ions, previously reduced by Al^{3+} release during K-metasomatism alteration of plagioclase (AlF^{+2}), is possibly promoted by AlF^{+2} breakdown due to increasing fluid acidity. This process releases fluorine in sufficient concentrations to promote Zr solubility as hydroxy fluoride complexes at very low pH (Gysi and Williams-Jones, 2013). Unfortunately, LREE mobility at Botro ai Marmi was largely controlled by the stability of allanite-(Ce, La) and vesuvianite, for which there are scarce thermodynamic data. The same uncertainty occurs in evaluating HREE mobility, which was likely controlled by zircon, for which partitioning of the HREE into hydrothermal fluids are poorly constrained. Thus, the strong HREE depletion observed in the main metasomatic minerals, particularly titanite and epidote, may be controlled by the solubility of zircon, which is enhanced by low temperature and pH, as well as high F concentration. It is therefore suggested the increasing abundance of F in metasomatic fluids during the alteration processes. Indeed, F-rich fluids are extremely corrosive and must have extensively interacted with the rocks resulting in mobilisation/exchange of HFSE, REE, Zr, Th, U, and metals. Fluorite crystallisation, commonly accompanied by HFSE-REE minerals as well as Th-U minerals, support the role of F-rich fluids as carrier of these components. Moreover, circulation of F-rich fluids is confirmed by textural reworking of metasomatic minerals, such reaction pseudomorphs replacing calc-silicates formed during Ca-metasomatism. Another supporting evidence is the high content of F in several metasomatic minerals (apatite, vesuvianite, phlogopite, epidote, and titanite). Finally, fluorite crystallisation characterised the whole metasomatic activity with inclusions and veins filling fractures.

Metasomatic transport of Zr is highlighted by the occurrence of zircon grains in the different exoskarn bodies. Indeed, there are few possible processes able to explain their origin: inheritance of detrital zircons from carbonate host rock, fluids transport of magmatic zircon from the intrusion to the metasomatic assemblage, or direct precipitation from metasomatic fluid (e.g., Deng et al., 2015). At Botro ai Marmi, there are no evidences of zircon inheritance from the host rock (lacking of zircon), or transport from the granitic intrusion. In contrast, there are evidences that support a direct precipitation from hydrothermal fluids. Zircon grains from the exoskarn bodies are commonly euhedral with diameter lower 30-40 μm, and morphology common of flux grown zircons formed in hydrothermal environments (e.g., Burakov et al., 2002; Schaltegger, 2007; Yang et al., 2014). Most of the zircon grains are intergrown with apatite and their occurrence increase at the granite-host transition, where the abundance of Ca-rich fluids could be responsible for the immediate P precipitation (e.g., Wan et al., 2012). The mutual occurrence of metasomatic zircon and apatite demonstrates the mobility of P and Zr (commonly poorly mobile) in metasomatic fluids at the Botro ai Marmi system.

At Botro ai Marmi, the new metasomatic minerals association, resulting from multiple exchange reactions, as well as addition and loss of components, highlight the mobilisation of a great numbers of elements between fluids, granite and the host carbonate. Even elements considered poorly mobile, such as Ti, Zr, Th, REE, and HFSE highlight at least a local mobilisation, recalling transport via acidic fluids. Indeed, the abundant precipitation of HFSE-REE and Th-U minerals, the zoning/replacement of calc-silicates, and the common occurrence of pseudomorphs including fluorite crystallisation, support the exchange of HFSE, REE and other components between granite, Ca-F-rich fluids, and host carbonates.

Which is the nature and source of metasomatic fluids active at Botro ai Marmi?

Regrettably, this question is not easily answered, and only hypothesis/speculations can be provided, indeed, multiple sources are likely the best option. Potassic alteration is typical of porphyry copper systems, while, peraluminous plutons world-wide are mostly associated with Sn skarns. The least Al-saturated plutons have the thermic and chemical activity to form Ca-Fe skarns, which usually show a significative mantle signature and relatively little interaction with continental sedimentary material (Meinert et al., 2005). Pyroxene and garnet-pyroxene skarns typically resulted from interaction between metasomatic fluids released by a mafic-ultramafic source and a carbonatic host rock (e.g., Meinert

et al., 2005). Skarn replacing more-or-less pure marble tend to be more Ca-rich, with mineral such as hedenbergite, ilvaite, johansenite (as observed in the Temperino mine; Vezzoni et al., 2016). Instead, Mg-rich skarn are common in dolomites, with minerals such as forsterite, serpentine and phlogopite (Burt, 1977), while the available iron tend to form magnetite rather than andradite or hedenbergite (Hall et al., 1988).

At Botro ai Marmi a peraluminous monzogranite intruded an almost pure marble host (minor dolomite, about 5%, and low Mg value). The crystallisation of new metasomatic minerals, in endoskarn and exoskarn, correspond to a general gain of K, Ca, Fe, Mg, Ba, Rb, Sr. Worth of nite is the high content of metal in the unaltered granite if compared with crustal values (i.e., Sn = 7-12 vs ~2 ppm; W = max 50 vs 1.1 ppm; Tl = ~2 vs 0.5 ppm). During alteration occurred the significant loss of metals, such as Cu, Zn, Ni, Mo, Sb, Tl and mainly Sn, W and Zr. The main metasomatic minerals are K-feldspar, phlogopite, titanite, diopside, vesuvianite, and grossular (phases typically of mafic metasomatic alteration).

Fluids released from an external source as to be invoke to explain the high Rb, Ba, K, and Mg concentrations, considered that country rocks have low abundances of these components. Assimilation of marble country rocks can account for the high Ca and Sr contents observed in the altered samples. However, this process can only justify Ca and Sr abundances in granite samples very close to the granite-marble interface. In fact, the assimilation is limited by the amount of heat available and by the surface area of the assimilated rocks. Thus, a major input of Ca from an external source has imposed by the diffuse endoskarn bodies occurring at depth (borehole data). Moreover, data from the borehole evidenced the loss with depth of Mg, Cr, Ni, Nb, and Sr. A general exchange/mobilisation of metals (i.e., Fe, Sn, W) between granite and metasomatic fluids during alteration processes could result in the distal Sn-Fe(-W) deposits of Mt. Valerio (3 km south of Botro ai Marmi). Moreover, the nearest Temperino mining area is characterised by a Zn-Pb(-Ag) ore replaced by a Fe-Cu mineralization, spatially related with a batch of mafic magma (Vezzoni et al., 2016). In that model, Zn-Pb skarn predates the Fe-Cu mineralization and formed as a distal skarn having no spatial relationship with the magmatic rocks. Thus, the emplacement of mafic magma during this first stage is not required, given that deep hydrothermal fluids can be emplaced independently. Moreover, at Campiglia, a mafic reservoir is inferred to be active since the emplacement of the Botro ai Marmi granite (Paoli et al., in prep. - chapter 7).

Thus, the release of fluids from a mafic reservoir could be account for the potassic- and later calcic-metasomatism observed in the Campiglia system. As additional support to this interpretation, average orientation of endoskarn veins correlates with the bulged geometry of the pluton, both in the mine and in the deep borehole. Thus, the metasomatic alteration is channelized preferentially in a NE-SW direction. These structural and metasomatic evidences could be attributed to the action of overpressure, mafic fluids released from a deeper source.

6.6. Conclusions and genetic model

The Botro ai Marmi granitic pluton underwent intense hydrothermal alteration during post-magmatic fluid-rock interaction processes (Fig. 6.14). Initially, a potassic metasomatic event led to the complete metasomatic alteration of magmatic biotite, plagioclase, and ilmenite, promoting major element mobilisation and crystallisation of K-feldspar, phlogopite, chlorite, titanite, and rutile. At the same time, the leaching of apatite and monazite led to the local mobilisation of HFSE (e.g., Nb, Ta, Zr), U, Th, and LREE. The increasing fluids acidity due to interaction with Ca-rich fluids resulted in a diffuse Ca-metasomatism. During this stage, a significant amount of calc-silicates and accessory minerals did form, showing a progressive enrichment in HFSE and LREE. Hereafter, the contribution of F-rich fluids enhanced the acidic alteration of accessory minerals and the mobilisation of HFSE and REE. Thus, these processes produced the substitution of major elements (Ti, Ca, Fe, Al) with HFSE and REE in the forming metasomatic minerals (i.e., titanite, vesuvianite), and the crystallisation of HFSE-REE minerals. The increasing acidity of metasomatic fluids (Ca sequestration by previously formed calc-silicates), produced the re-mobilisation of HFSE/REE by metasomatic

alteration of calc-silicates and accessory minerals. The abundant precipitation of HFSE-REE and Th-U minerals, the zoning/replacement of calc-silicates, and the common occurrence of pseudomorphs including fluorite crystallisation, support the exchange of HFSE, REE and other components between granite, Ca-F-rich fluids, and host carbonates until low temperatures.

Concluding, the selective mobilisation of such components was related to a change in fluid composition, pH and temperature. This study emphasises the importance of relating field studies to petrographic observation and detailed geochemical analysis. Moreover, it shows how such linkage can lead to the construction of litho-geochemical model for element mobilisation in crustal magmatic-hydrothermal setting.

Acknowledgements

This project was partially funded by the Progetto di Ricerca di Ateneo (PRA_2016_33). Thanks to Kouzmanov K. for providing QEMSCAN data and to D'Orazio M. for help during ICP-MS analysis.

References

Allen, P., Condie, K.C., Bowling, G.P., 1986. Geochemical characteristics and possible origins of the Closepet Balholith, south India. J. Geol., 94, 283 99.

Bau, M., 1991. Rare-earth element mobility during hydrothermal and metamorphic fluid-rock interaction and the significance of the oxidation state of europium." Chemical Geology 93(3), 219-230.

Best, M.G., 1982. Igneous and metamorphic petrology. Freeman, San Francisco, 630.

Burakov, B.E., Hanchar, J.M., Zamoryanskaya, M.V., Garbuzov, V.M., Zirlin V.A., 2002. Synthesis and investigation of Pu-doped single crystal zircon, (Zr, Pu)SiO4. Radiochim Acta 90, 95–97.

Burt, D.M., 1977. Mineralogy and petrology of skarn deposits: Rendiconti della Società Italiana di Mineralogia e Petrologia 33, 859–873.

Deer, W.A., Howie, R.A., Zussman, J., 1992. An Introduction to the Rock Forming Minerals, 2nd ed., Longman, London, pp. 696.

Della Ventura, G., Bellatreccia, F., Williams, C.T., 1999. Zr- and LREE-rich titanite from Tre Croci, Vico Volcanic complex (Latium, Italy). Mineralogical Magazine 63 (1), 123–130.

Deng, X.D., Li, J.W., Wen, G., 2015. U-Pb geochronology of hydrothermal zircons from the early Cretaceous iron skarn deposits in the Handan-Xingtai district, north China craton. Economic Geology 110: 2159–2180.

Dill, H.G., Hansen, B.T., Weber, B., 2011. REE contents, REE minerals and Sm/Nd isotopes of granite- and unconformity-related fluorite mineralization at the western edge of the Bohemian Massif: With special reference to the Nabburg-Wölsendorf District, SE Germany. Ore Geology Reviews 40(1), 132-148.

Dini, A., Orlandi, P., Vezzoni, S., 2013. Temperino e Lanzi. Le paragenesi primarie dello skarn: Rivista Mineralogica Italiana Campigliese. Min. Miner. 1, 28–39.

Einaudi, M.T., Meinert, L.D., Newberry, R.J., 1981. Skarn deposits: Economic Geology 75th Anniversary Volume, 317–391.

Foster, M.D., 1960. Interpretation of the composition of trioctahedral micas. U.S. Geol. Surv. Prof. Pap. 354-B, 11-46Franzini, M, Lezzerini, M., Origlia F., 2010. Marbles from the Campiglia Marittima area (Tuscany, Italy). European Journal of Mineralogy 22, 881-893.

Gaspar, M., Knaack, C., Meinert, L., Moretti, R., 2008. REE in skarn Systems: A LA-ICP-MS study of garnets from the Crown Jewel gold deposit. Geochimica et Cosmochimica Acta 72(1), 185-205.

Gieré R., 1990. Hydrothermal mobility of Ti, Zr and REE: examples from the Bergell and Adamello contact aureoles (Italy). Terra Nova 2, 60-67.

Groat, L.A., Hawthorne, F.C., Ercit, T.S., 1992. The chemistry of vesuvianite. Canadian Mineralogist 30, 19-48

Gysi, A.P. and Williams-Jones, A.E., 2013. Hydrothermal mobilization of pegmatite-hosted REE and Zr at Strange Lake, Canada: A reaction path model. Geochimica et Cosmochimica Acta, 122, 324-352.

Gysi, A.P., William-Jones, A.E., Collins, P., 2016. Lithogeochemical Vectors for Hydrothermal Processes in the Strange Lake Peralkaline Granitic REE-Zr-Nb Deposit. Society of Economic Geologists, Inc. Economy Geology 111, 1241-1276.

Halden, N.M., 1996. Determination of Lyapounov exponents to characterize the oscillatory distribution of trace elements in minerals. Can. Mineral. 34, 1127–1135.

Hall, D.L., Cohen, L.H., Schiffman, P., 1988. Hydrothermal alteration associated with the Iron Hat iron skarn deposit, eastern Mojave Desert, San Bernardino County, California. Economic Geology 83, 568–587.

Harlov, D.E., Austrheim, H., 2013. Metasomatism and Chemical transformation of Rock: Rock-Mineral-fluid Interaction in Terrestrial and Extraterrestrial Environments. (Lecture Notes in Earth System Sciences)1-16.

Henderson, P., 1980. Rare earth element partition between sphene, apatite and other coexisting minerals of the Kangerdlugssuaq intrusion, E. Greenland. Contrib. Mineral. Petrol. 72, 81 5.

Hill, G.T., Philip, A.R.C., Kyle, R., 2000. Geochemistry of southwestern New Mexico fluorite occurrences implications for precious metals exploration in fluorite-bearing systems. Journal of Geochemical Exploration 68, 1-20.

Jamtveit, B., Wogelius, R.A., Fraser, D. G., 1993. Zonation Patterns of Skarn Garnets - Records of Hydrothermal System Evolution. Geology 21(2), 113-116.

Lindgren, 1925. Metasomatism: Geological Society of America Bulletin 36, 247–261.

Markl, G., and Piazolo, S., 1999. Stability of high-Al titanite from low-pressure calcsilicates in light of fluid and host-rock composition. American Mineralogist 84, 37-47.

McIntire, W.L., 1963. Trace element partition coefficients-a review of theory and applications to geology. Geochim. Cosmochim. Acta 27, 1209–1264.

Meinert, L.D., 1997. Application of skarn deposit zonation models to mineral exploration. Explor. Min. Geol. 6, 185–208.

Meinert, L.D., Dipple, M.G., Nicolescu, S., 2005. World Skarn Deposits. Economic Geology 100th Anniversary Volume: 299-336.

Migdisov, A.A., William-Jones, A.E., Wagner, T., 2009. An experimental study of the solubility and speciation of the rare earth elements (III) in flouride-and chloride-bearing aqueous solutions at temperatures up to 300°C. Geochimica et Cosmochimica Acta 73, 7087-7109.

Migdisov, A.A., Williams-Jones, A.E., Van Hinsberg, V., Salvi, S., 2011. An experimental study of the solubility of baddelite (ZrO2) in flouride-bearing solutions at elevated temperature. Geochimica et Cosmochimica Acta 75, 7426-7434.

Morimoto, N.C., 1988. Nomenclature of Pyroxenes. Mineralogy and Petrology 39, 55-76.

Munoz, M., Premo, W.R., Courjault-Radé, P., 2004. Sm Nd dating of fluorite from the worldclass Montroc fluorite deposit, southern Massif Central, France. Mineralium Deposita 39, 970–975.

Nakano, T., Takahara, H., Norimasa, N., 1989. Intracrystalline distribution of major elements in zoned garnet from skarn in the Chichibu mine, central Japan; illustration by color-coded maps. Can. Mineral. 27, 499–507.

Oberti, R., Smith, D.C., Rossi, G, and Caucia F., 1991. The crystal-chemistry of high-aluminium titanites. Eur. Z Mineral. 3, 777 92.

Pan, Y., Fleet, M.E., MacRae, N., 1993. Late alteration in titanite (CaTiSiOs): redistribution and remobilization of rare earth elements and implications for U/Pb and Th/Pb geochronology and nuclear waste disposal. Geochim. Cosmochim. Acta 57, 355 67.

Petrík, I., Broska, I., Lipka, J., and Siman, P., 1995. Granitoid allanite-(Ce): Substitution relations, redox conditions and REE distributions (on an example of I-type granitoids, Western Carpathians, Slovakia): Geologica Carpathica 46, 79-94.

Pinarelli, L., Poli, G. and Santo, A., 1989. Geochemical characterization of recent volcanism from the Tuscan Magmatic Province (Central Italy): the Roccastrada and San Vincenzo centers. Periodico di Mineralogia 58, 67-96.

Pirajno, F., 2009. Hydrothermal processes and mineral systems. Springer, Berlin.

Pirajno, F., 2013. Effects of Metasomatism on Mineral Systems and Their Host Rocks: Alkali Metasomatism, Skarns, Greisens, Tourmalinites, Rodingites, Black-Wall Alteration and Listvenites, in Metasomatism and the Chemical Transformation of Rock: The Role of Fluids in Terrestrial and Extraterrestrial Processes. Berlin, Heidelberg, Springer Berlin Heidelberg, 203-251.

Pirajno, F., and Smithies, R.H., 1992. The FeO/(FeO+MgO) ratio of tourmaline: a useful indicator of spatial variations in granite-related hydrothermal mineral deposits. Journal Geochem. Expl. 42, 371–382.

Poitrasson, F., 2002. In situ investigations of allanite hydrothermal alteration: Examples from calc-alkaline and anorogenic granites of Corsica (southeast France): Contributions to Mineralogy and Petrology, v. 142, p. 485–500.

Schaltegger, U., 2007. Hydrothermal zircon. Elements 3, 51.

Shore, M., and Fowler, A.D., 1996. Oscillatory zoning in minerals: a common phenomenon. Can Mineral. 34, 1111–1126.

Sverjensky, D.A., 1984. Europium redox equilibria in aqueous solution. Earth Planet. Sci. Lett. 67 (1), 70–78.

Thompson, J.B., 1982. Composition space; an algebraic and geometric approach. Reviews in Mineralogy and Geochemistry 10, 1-31.

Venerandi-Pirri, I., and Zuffardi, P., 1982. The Tin Deposit of Monte Valerio (Tuscany, Italy): Pneumatolytic-Hydrothermal or Sedimentary-Remobilization Processes?. In: Amstutz, G.C., Frenzel, G., Kluth, C., Ore Genesis 2, 57–65.

Vlach, S., 2012. Structural and compositional variations of hydrothermal epidote-group minerals from a peralkaline granite, Corupá pluton, Graciosa Province, south Brazil: Anais da Academia Brasileira de Cienccias 84, 407–425.

Wan, B., Xiao, W., Zhang, L., Han, C., 2012, Iron mineralization associated with a major strike–slip shear zone: radiometric and oxygen isotope evidence from the Mengku deposit, NW China: Ore Geology Reviews 44, 136-147.

Yang, W.-B., Niu, H.-C., Shan, Q., Sun, W.-D., Zhang, H., Li, N.-B., Jiang, Y.-H., Yu, X.-Y., 2014. Geochemistry of magmatic and hydrothermal zircon from the highly evolved Baerzhe alkaline granite: implications for Zr–REE–Nb mineralization. Miner Deposita 49, 451-470.

Supplementary material

Supplementary Table S.6.

Feldspar

Rock type	*Biotite-bearing granite*				*Phlogopite-tianite-bearing granite*						*Biotite-bearing granite or slightly alteredgranite*							
Mineral	***Kfs1***	***Kfs2***	***Kfs3***	***Kfs4***	***Kfs5***	***Kfs6***	***Kfs7***	***Plg1***	***Plg2***	***Plg3***	***Plg4***	***Plg5rim***	***Plg5mid***	***Plg5core***	***Plg6rim(1)***	***Plg6(2)***	***Plg6(3)***	***Plg6core(4)***
SiO_2	65.70	65.70	66.00	65.90	65.40	65.50	65.80	64.30	65.00	67.40	68.90	67.30	60.40	57.70	66.40	63.70	60.00	57.60
TiO_2	0.00	0.00	0.02	0.02	0.01	0.03	0.00	0.03	0.00	0.00	0.00	0.00	0.02	0.00	0.00	0.02	0.02	0.00
Al_2O_3	19.50	19.20	19.50	19.60	19.50	19.30	19.80	23.10	23.10	21.40	20.60	21.50	26.00	27.80	21.90	24.00	27.30	28.20
Cr_2O_3	0.02	0.00	0.00	0.00	0.03	0.00	0.00	0.03	0.00	0.05	0.00	0.00	0.00	0.00	0.00	0.00	0.00	0.00
FeO	0.00	0.00	0.05	0.03	0.00	0.20	0.00	0.00	0.02	0.00	0.00	0.02	0.00	0.20	0.30	0.10	0.00	0.12
Mno	0.00	0.01	0.00	0.00	0.00	0.00	0.00	0.00	0.02	0.00	0.02	0.00	0.01	0.02	0.02	0.00	0.05	0.02
MgO	0.02	0.02	0.00	0.00	0.03	0.00	0.00	0.00	0.00	0.04	0.00	0.00	0.00	0.01	0.00	0.00	0.02	0.01
CaO	0.08	0.03	0.10	0.10	0.08	0.04	0.10	3.50	3.50	0.98	2.60	2.96	6.90	8.70	1.89	4.50	7.60	8.20
Na_2O	1.92	1.70	1.66	1.99	1.63	1.36	2.10	9.20	8.90	9.90	8.40	8.80	7.20	6.00	10.10	8.60	6.60	5.70
K_2O	14.20	15.00	14.30	13.80	14.70	15.00	14.10	0.23	0.31	0.76	0.24	0.23	0.16	0.18	0.18	0.21	0.23	0.18
Totale	101.4	101.7	101.6	101.4	101.4	101.4	101.9	100.4	100.9	100.5	100.8	100.8	100.7	100.6	100.8	101.1	101.8	100.0
Structural formula, oxygen equivalents p.f.u. = 8																		
Si	2.97	2.98	2.98	2.97	2.97	2.97	2.96	2.82	2.83	2.93	2.97	2.92	2.67	2.56	2.89	2.78	2.62	2.57
Ti	0.00	0.00	0.00	0.00	0.00	0.00	0.00	0.00	0.00	0.00	0.00	0.00	0.00	0.00	0.00	0.00	0.00	0.00
Al	1.04	1.02	1.04	1.04	1.04	1.03	1.05	1.19	1.19	1.10	1.05	1.10	1.35	1.46	1.12	1.23	1.41	1.48
Cr	0.00	0.00	0.00	0.00	0.00	0.00	0.00	0.00	0.00	0.00	0.00	0.00	0.00	0.00	0.00	0.00	0.00	0.00
Fe^{2+}	0.00	0.00	0.00	0.00	0.00	0.01	0.00	0.00	0.00	0.00	0.00	0.00	0.00	0.01	0.01	0.00	0.00	0.00
Fe^{3+}	0.00	0.00	0.00	0.00	0.00	0.00	0.00	0.00	0.00	0.00	0.00	0.00	0.00	0.00	0.00	0.00	0.00	0.00
Mn	0.00	0.00	0.00	0.00	0.00	0.00	0.00	0.00	0.00	0.00	0.00	0.00	0.00	0.00	0.00	0.00	0.00	0.00
Mg	0.00	0.00	0.00	0.00	0.00	0.00	0.00	0.00	0.00	0.00	0.00	0.00	0.00	0.00	0.00	0.00	0.00	0.00
Ca	0.00	0.00	0.00	0.00	0.00	0.00	0.00	0.16	0.16	0.05	0.12	0.14	0.33	0.41	0.09	0.21	0.36	0.39
Na	0.17	0.15	0.15	0.17	0.14	0.12	0.18	0.78	0.75	0.84	0.70	0.74	0.62	0.52	0.85	0.73	0.56	0.49
K	0.82	0.87	0.82	0.79	0.85	0.87	0.81	0.01	0.02	0.04	0.01	0.01	0.01	0.01	0.01	0.01	0.01	0.01
Totale	5.00	5.02	4.99	4.99	5.01	5.00	5.01	4.98	4.96	4.96	4.86	4.91	4.97	4.97	4.98	4.97	4.96	4.95
Sito Z	4.01	4.00	4.02	4.02	4.01	4.01	4.01	4.02	4.02	4.03	4.02	4.02	4.02	4.03	4.03	4.02	4.03	4.05
Sito X	0.99	1.02	0.97	0.97	1.00	0.99	1.00	0.96	0.93	0.92	0.84	0.89	0.95	0.94	0.95	0.95	0.93	0.89
Ab %	17	15	15	18	14	12	18	82	81	90	84	83	65	55	90	77	60	55
An %	0	0	0	0	0	0	0	17	18	5	14	15	34	44	9	22	38	44
Or %	83	85	85	82	85	88	81	1	2	5	2	1	1	1	1	1	1	1

Method	EMP															SEM-EDS	SEM-EDS	SEM-EDS
Sample	BM5_6	BM5_7	Ricci, 2000	Ricci, 2000	Ricci, 2000	GBM2A_5	GBM34-1	GBM34-2	GBM2A-3	GBM2A-4	Ricci, 2000	Ricci, 2000	Ricci, 2000	Ricci, 2000		GBM2-1	GBM2-2	GBM2-3
Rock type	Biotite granite					phlogopite-titanite granite							chlorite vein			Biotite granite		
Comment																core	rim	core
Mica type	Bt	Bt	Bt	Bt	Bt	Chl	Phl	Chl	Phl	Phl	Phl	Phl	Chl	Chl		Bt	Bt	Bt
SiO2	38.34	38.22	35.44	40.25	38.60	47.77	51.38	35.67	40.43	40.33	41.84	44.22	27.71	32.48		38.34	37.61	38.34
TiO2	3.70	3.59	3.99	3.44	4.15	0.04	1.52	0.00	0.56	0.58	2.08	0.97	0.08	0.07		3.70	5.09	3.70
Al2O3	15.49	15.58	15.48	12.71	14.61	33.69	6.27	18.18	14.91	14.48	13.28	12.36	20.94	20.26		15.49	17.13	15.49
FeO	17.80	17.24	15.45	16.79	18.74	1.85	1.29	8.55	5.05	4.94	6.24	5.03	22.73	7.04		17.80	22.06	17.80
Mno	0.28	0.27	0.11	0.10	0.08	< 0.01	< 0.01	0.27	0.09	0.04	0.04	0.05	0.08	0.18		0.28		0.28
MgO	9.57	8.92	9.82	13.28	11.74	0.46	23.81	26.11	22.14	22.11	20.66	19.79	16.39	23.08		9.57	8.49	9.57
CaO	0.11	0.05	0.04	< 0.01	0.12	0.04	0.01	0.58	< 0.01	< 0.01	0.03	< 0.01	0.13	0.06		0.11		0.11
Na2O	0.06	0.21	0.14	0.13	0.13	0.05	0.10	0.03	0.20	0.23	0.07	< 0.01	0.03	0.03		0.06		0.06
K2O	8.47	8.41	9.71	9.87	9.19	11.12	9.96	0.04	10.31	10.38	10.23	10.46	< 0.01	0.05		8.47	9.61	8.47
Cr2O3	< 0.01	< 0.01	0.05	0.01	0.02	0.02	< 0.01	< 0.01	0.02	0.02	0.02	0.02	0.06	0.05				
F	0.37	0.41	0.36	0.39	0.42	< 0.01	3.05	0.22	1.33	1.37	2.31	1.95	0.27	0.19		0.37		0.37
Tot	94.19	92.90	90.59	96.97	97.80	95.04	97.39	89.65	95.04	94.48	96.80	94.85	88.42	83.49		94.19	99.99	94.19
Structural formula, oxygen equivalents p.f.u. = 22																		
Si	5.80	5.86	5.61	5.94	5.69	6.38	6.89	6.62	5.77	5.79	5.88	6.27	5.67	6.41		5.81	5.50	5.81
Ti	0.42	0.41	0.48	0.38	0.46	0.01	0.15	0.01	0.06	0.06	0.22	0.10	0.01	0.01		0.42	0.56	0.42
Al	2.76	2.81	2.89	2.21	2.54	5.31	0.99	3.98	2.51	2.45	2.20	2.06	5.05	4.71		2.77	2.95	2.77
Cr	0.00	0.00	0.01	0.00	0.00	0.00	0.00	0.00	0.00	0.00	0.00	0.00	0.01	0.01		0.00	0.00	0.00
Fe	2.26	2.21	2.05	2.07	2.31	0.21	0.14	1.33	0.60	0.59	0.73	0.60	3.89	1.16		2.26	2.70	2.26
Mn	0.04	0.04	0.01	0.01	0.01	0.00	0.00	0.04	0.01	0.00	0.00	0.01	0.01	0.03		0.04	0.00	0.04
Mg	2.16	2.04	2.32	2.92	2.58	0.09	4.76	7.23	4.71	4.73	4.33	4.18	5.00	6.79		2.16	1.85	2.16
Ca	0.02	0.01	0.01	0.00	0.02	0.01	0.00	0.12	0.00	0.00	0.00	0.00	0.03	0.01		0.02	0.00	0.02
Na	0.02	0.06	0.04	0.04	0.04	0.01	0.03	0.01	0.06	0.06	0.02	0.00	0.01	0.01		0.02	0.00	0.02
K	1.64	1.64	1.96	1.86	1.73	1.90	1.70	0.01	1.88	1.90	1.83	1.89	0.00	0.01		1.64	1.79	1.64
F	0.04	0.20	0.18	0.18	0.20	0.00	1.29	0.13	0.60	0.62	1.03	0.87	0.17	0.12		0.18	0.00	0.18
Totale	15.16	15.28	15.56	15.61	15.56	13.91	15.97	19.46	16.19	16.22	16.24	15.98	19.88	19.29		15.30	15.36	15.30
Al IV	2.55	2.14	2.39	2.06	2.31	1.62	1.11	1.38	2.23	2.21	2.12	1.73	2.33	1.59		2.19	2.50	2.19
Al VI	0.53	0.67	0.50	0.15	0.22	3.69	-0.12	2.60	0.27	0.24	0.07	0.33	2.73	3.13		0.58	0.45	0.58
Sito O	5.31	5.36	5.36	5.54	5.58	4.00	4.94	11.20	5.65	5.63	5.36	5.22	11.66	11.13		5.45	5.57	5.45
Sito A	1.68	1.71	2.01	1.89	1.78	1.91	1.73	0.14	1.93	1.96	1.86	1.89	0.04	0.04		1.67	1.79	1.67
Mg#	0.49	0.48	0.53	0.59	0.53	0.31	0.97	0.84	0.89	0.89	0.86	0.88	0.56	0.85		0.49	0.41	0.49
Fe#	0.51	0.52	0.47	0.41	0.47	0.69	0.03	0.16	0.11	0.11	0.14	0.12	0.44	0.15		0.51	0.59	0.51

SEM-EDS	SEM-EDS	SEM-EDS	SEM-EDS	SEM-EDS	SEM-EDS	SEM-EDS	SEM-EDS	SEM-EDS	SEM-EDS	SEM-EDS	SEM-EDS	SEM-EDS	SEM-EDS	SEM-EDS	SEM-EDS	SEM-EDS	SEM-EDS	SEM-EDS
GBM2-4	GBM2-5	GBM2-6	GBM2-7	GBM2-8	GBM2-9	GBM2-10	GBM2-11	GBM2-12	GBM2b	GBM2b	GBM2b	GBM2b	GBM2b	GBM2b	GBM2b	GBM2b	GBM2b	GBM2b
									phlogopite-titanite granite									
rim									1	1chiaro	2scuro	2chiaro	3chiaro	3scuro	4	5	6	6bordo
Bt	Bt	Bt	Bt	Bt	Bt	Bt	Bt	Bt	Bt	Bt	Chl	Bt	Bt	chl	chl	Bt	Bt	Bt
36.07	44.62	40.47	39.77	36.20	39.18	36.83	38.39	36.17	40.30	39.48	31.55	36.33	39.37	32.42	30.27	38.52	39.64	62.04
4.22	1.21	2.95	4.36	2.36	4.51	4.11	3.65	4.16	3.69	3.57	0.67	4.60	3.65	2.07	0.29	4.08	2.71	0.60
17.27	12.47	13.90	13.57	18.18	14.39	16.47	14.75	17.39	20.01	20.20	15.12	16.59	15.09	20.89	24.13	14.15	13.92	20.21
24.21	11.18	18.42	20.64	22.29	22.20	23.08	23.48	24.52	15.12	15.31	31.07	21.64	21.58	29.54	30.74	23.20	21.82	0.54
8.59	19.91	14.12	11.53	10.83	10.55	9.94	9.81	8.19	6.93	6.93	13.56	10.12	10.87	13.68	14.14	10.09	11.68	2.15
									3.61	3.73	0.44	0.15	0.22	0.33	0.24	0.28	0.17	0.20
									1.35	2.06	0.43	2.09						
9.64	10.61	10.15	10.12	10.14	9.16	9.58	9.93	9.57	9.00	8.72	9.28	8.48	9.23	1.07	0.20	9.69	10.06	14.27
100.00	100.00	100.01	99.99	100.00	99.99	100.01	100.01	100.00	100.01	100.00	102.12	100.00	100.01	100.00	100.01	100.01	100.00	100.01
5.35	6.18	5.82	5.79	5.33	5.72	5.43	5.67	5.37	5.70	5.61	4.83	5.34	5.73	6.01	5.62	5.68	5.81	7.86
0.47	0.13	0.32	0.48	0.26	0.50	0.46	0.41	0.46	0.39	0.38	0.08	0.51	0.40	0.29	0.04	0.45	0.30	0.06
3.02	2.03	2.36	2.33	3.16	2.48	2.86	2.57	3.04	3.34	3.38	2.73	2.87	2.59	4.56	5.28	2.46	2.40	3.02
0.00	0.00	0.00	0.00	0.00	0.00	0.00	0.00	0.00	0.00	0.00	0.00	0.00	0.00	0.00	0.00	0.00	0.00	0.00
3.01	1.29	2.22	2.52	2.75	2.71	2.85	2.90	3.04	1.79	1.82	3.97	2.66	2.62	4.58	4.77	2.86	2.67	0.06
0.00	0.00	0.00	0.00	0.00	0.00	0.00	0.00	0.00	0.00	0.00	0.00	0.00	0.00	0.00	0.00	0.00	0.00	0.00
1.90	4.11	3.03	2.50	2.38	2.30	2.19	2.16	1.81	1.46	1.47	3.09	2.22	2.36	3.78	3.91	2.22	2.55	0.41
0.00	0.00	0.00	0.00	0.00	0.00	0.00	0.00	0.00	0.55	0.57	0.07	0.02	0.03	0.07	0.05	0.04	0.03	0.03
0.00	0.00	0.00	0.00	0.00	0.00	0.00	0.00	0.00	0.37	0.57	0.13	0.60	0.00	0.00	0.00	0.00	0.00	0.00
1.83	1.87	1.86	1.88	1.91	1.71	1.80	1.87	1.81	1.63	1.58	1.81	1.59	1.71	0.25	0.05	1.82	1.88	2.31
0.00	0.00	0.00	0.00	0.00	0.00	0.00	0.00	0.00	0.00	0.00	0.00	0.00	0.00	0.00	0.00	0.00	0.00	0.00
15.58	15.62	15.61	15.50	15.78	15.40	15.58	15.58	15.55	15.23	15.39	16.70	15.81	15.44	19.54	19.72	15.55	15.63	13.73
2.65	1.82	2.18	2.21	2.67	2.28	2.57	2.33	2.63	2.30	2.39	3.17	2.66	2.27	1.99	2.38	2.32	2.19	0.14
0.37	0.21	0.18	0.12	0.49	0.19	0.29	0.24	0.41	1.04	1.00	-0.45	0.21	0.31	2.58	2.90	0.14	0.21	2.88
5.75	5.74	5.75	5.62	5.87	5.70	5.78	5.70	5.74	4.69	4.67	6.69	5.60	5.69	11.23	11.63	5.68	5.73	3.40
1.83	1.87	1.86	1.88	1.91	1.71	1.80	1.87	1.81	2.54	2.72	2.01	2.21	1.75	0.32	0.10	1.87	1.91	2.33
0.39	0.76	0.58	0.50	0.46	0.46	0.43	0.43	0.37	0.45	0.45	0.44	0.45	0.47	0.45	0.45	0.44	0.49	0.88
0.61	0.24	0.42	0.50	0.54	0.54	0.57	0.57	0.63	0.55	0.55	0.56	0.55	0.53	0.55	0.55	0.56	0.51	0.12

SEM-EDS	SEM-EDS	SEM-EDS	SEM-EDS	SEM-EDS	SEM-EDS	SEM-EDS	SEM-EDS	SEM-EDS	SEM-EDS	SEM-EDS	SEM-EDS	SEM-EDS	SEM-EDS	SEM-EDS	SEM-EDS	SEM-EDS	SEM-EDS	SEM-EDS
GBM2b	GBM2b	GBM2b	GBM2b	GBM2b	GBM2b	GBM2b	GBM2b	GBM2b	GBM2b	GBM2b	GBM2b	GBM2b	GBM2b	GBM2b	GBM2b	GBM2b	GBM2b	GBM2b
6scuro	7	7' in Or	8 scuro	9 chiaro	9 scuro	10	11	12	13	14	15 chiaro	15 scuro	16 chiaro	16 scuro	17	18	19	20
chl	Bt	Bt	Bt	Bt	Bt	Bt	Bt	Bt	Bt	chl	Bt	Bt	Phl	Phl	Phl	Phl	Bt	Bt
31.64	36.54	38.97	29.38	39.77	30.61	36.97	38.94	39.09	39.65	34.12	37.22	30.48	44.84	44.84	45.78	46.11	39.45	38.98
0.38	4.86	3.54	0.25	3.61	0.68	4.89	3.46	1.31	1.03	0.40	5.21	0.14	2.93	2.93	3.00	1.15	3.96	4.12
24.06	16.94	13.78	25.03	14.32	22.69	15.72	14.73	15.22	15.27	22.37	15.19	21.86	14.14	14.14	15.12	13.78	14.80	14.43
28.94	23.63	21.98	33.60	21.53	30.89	23.13	23.09	21.87	19.44	26.55	24.26	32.73	4.27	4.27	3.50	2.77	21.99	23.37
14.70	8.13	11.11	11.35	11.07	14.34	9.15	10.02	12.49	14.05	15.55	8.37	14.61	22.71	22.71	22.09	25.67	10.08	9.38
0.14	0.23	0.38	0.23	0.23	0.40	0.47												
0.13	9.67	10.23	0.15	9.47	0.39	9.67	9.76	10.02	10.56	1.01	9.74	0.18	11.10	11.10	10.52	10.52	9.73	9.72
99.99	100.00	99.99	99.99	100.00	100.00	100.00	100.00	100.00	100.00	100.00	99.99	100.00	99.99	99.99	100.01	100.00	100.01	100.00
5.80	5.41	5.73	4.35	5.79	4.48	5.47	5.73	5.72	5.75	6.19	5.53	4.50	6.03	6.03	6.09	6.13	5.76	5.74
0.05	0.54	0.39	0.03	0.40	0.07	0.54	0.38	0.14	0.11	0.05	0.58	0.02	0.30	0.30	0.30	0.11	0.43	0.46
5.20	2.96	2.39	4.36	2.46	3.92	2.74	2.55	2.62	2.61	4.78	2.66	3.80	2.24	2.24	2.37	2.16	2.55	2.50
0.00	0.00	0.00	0.00	0.00	0.00	0.00	0.00	0.00	0.00	0.00	0.00	0.00	0.00	0.00	0.00	0.00	0.00	0.00
4.44	2.92	2.70	4.16	2.62	3.78	2.86	2.84	2.68	2.36	4.03	3.01	4.04	0.48	0.48	0.39	0.31	2.69	2.88
0.00	0.00	0.00	0.00	0.00	0.00	0.00	0.00	0.00	0.00	0.00	0.00	0.00	0.00	0.00	0.00	0.00	0.00	0.00
4.02	1.79	2.44	2.50	2.40	3.13	2.02	2.20	2.72	3.04	4.20	1.85	3.21	4.55	4.55	4.38	5.08	2.19	2.06
0.03	0.04	0.06	0.04	0.04	0.06	0.07	0.00	0.00	0.00	0.00	0.00	0.00	0.00	0.00	0.00	0.00	0.00	0.00
0.00	0.00	0.00	0.00	0.00	0.00	0.00	0.00	0.00	0.00	0.00	0.00	0.00	0.00	0.00	0.00	0.00	0.00	0.00
0.03	1.83	1.92	0.03	1.76	0.07	1.82	1.83	1.87	1.95	0.23	1.85	0.03	1.90	1.90	1.79	1.78	1.81	1.83
0.00	0.00	0.00	0.00	0.00	0.00	0.00	0.00	0.00	0.00	0.00	0.00	0.00	0.00	0.00	0.00	0.00	0.00	0.00
19.56	15.49	15.64	15.46	15.46	15.52	15.53	15.53	15.76	15.81	19.49	15.48	15.60	15.51	15.51	15.32	15.57	15.44	15.46
2.20	2.59	2.27	3.65	2.21	3.52	2.53	2.27	2.28	2.25	1.81	2.47	3.50	1.97	1.97	1.91	1.87	2.24	2.26
3.00	0.36	0.12	0.71	0.25	0.40	0.21	0.28	0.34	0.36	2.97	0.19	0.30	0.27	0.27	0.46	0.28	0.31	0.24
11.51	5.62	5.66	7.39	5.67	7.39	5.63	5.70	5.89	5.86	11.25	5.64	7.57	5.60	5.60	5.53	5.79	5.62	5.64
0.06	1.86	1.98	0.06	1.80	0.14	1.90	1.83	1.87	1.95	0.23	1.85	0.03	1.90	1.90	1.79	1.78	1.81	1.83
0.48	0.38	0.47	0.38	0.48	0.45	0.41	0.44	0.50	0.56	0.51	0.38	0.44	0.90	0.90	0.92	0.94	0.45	0.42
0.52	0.62	0.53	0.62	0.52	0.55	0.59	0.56	0.50	0.44	0.49	0.62	0.56	0.10	0.10	0.08	0.06	0.55	0.58

SEM-EDS	SEM-EDS	SEM-EDS	SEM-EDS	SEM-EDS	SEM-EDS	SEM-EDS	SEM-EDS	SEM-EDS	SEM-EDS	SEM-EDS	SEM-EDS	SEM-EDS	SEM-EDS	SEM-EDS	SEM-EDS	SEM-EDS	SEM-EDS
GBM2b	GBM7	GBM7	GBM18	GBM18	GBM18	GBM18	GBM18	GBM19A	GBM19A	GBM19A	GBM19A	GBM19A	GBM19A	GBM19A	GBM19A	GBM19A	GBM19A
	pyroxene exoskarn							Phl+Ttn granite								phlogopite-titanite granite	
21	1	2	1	2	3	4	5	1	1c	5	6	6rim	6s	7	7' in Or	8	9 c
Bt	Phl	Phl	chl	chl	chl	chl	chl	Bt	Bt	Phl	Phl	Bt	Phl	Phl	Phl	Bt	Phl
39.68	41.72	41.89	29.62	29.02	31.00	28.87	31.27	39.17	53.88	44.34	46.93	54.11	44.38	48.15	44.92	52.48	43.29
4.06		0.81	0.25	0.36	0.20	0.53	0.47	3.53	3.87	2.29	1.00			0.78	2.29		3.06
14.16	18.51	17.34	23.25	22.97	24.07	23.83	24.73	20.27	21.17	14.94	13.21	31.32	24.27	16.79	14.44	31.53	14.62
19.76	4.88	4.78	36.66	38.22	34.70	34.42	30.81	19.54	9.32	4.95	2.83		6.68	1.94	3.70		5.44
12.61	24.64	24.34	10.21	9.44	10.03	12.36	12.72	6.99	3.09	22.97	25.29	4.24	19.77	21.49	23.80	4.65	22.63
									4.79								
9.74	10.25	10.84	0.00	0.00	0.00	0.00	0.00	10.50	3.88	10.51	10.74	10.33	4.90	10.85	10.86	11.35	10.97
100.01	100.00	100.00	99.99	100.01	100.00	100.01	100.00	100.00	100.00	100.00	100.00	100.00	100.00	100.00	100.01	100.01	100.01
5.74	5.61	5.66	5.66	5.60	5.83	5.47	5.77	5.63	6.95	5.96	6.23	6.74	5.75	6.32	6.01	6.60	5.87
0.44	0.01	0.08	0.04	0.05	0.03	0.08	0.07	0.38	0.38	0.23	0.10	0.01	0.01	0.08	0.23	0.01	0.31
2.41	2.94	2.76	5.23	5.22	5.34	5.32	5.38	3.44	3.22	2.37	2.07	4.60	3.71	2.60	2.28	4.67	2.34
0.00	0.00	0.00	0.00	0.00	0.00	0.00	0.00	0.00	0.00	0.00	0.00	0.00	0.00	0.00	0.00	0.00	0.00
2.39	0.55	0.54	5.86	6.16	5.46	5.45	4.76	2.35	1.01	0.56	0.31	0.00	0.72	0.21	0.41	0.00	0.62
0.00	0.00	0.00	0.00	0.00	0.00	0.00	0.00	0.00	0.00	0.00	0.00	0.00	0.00	0.00	0.00	0.00	0.00
2.72	4.94	4.90	2.91	2.71	2.81	3.49	3.50	1.50	0.59	4.60	5.01	0.79	3.82	4.20	4.75	0.87	4.57
0.00	0.00	0.00	0.00	0.00	0.00	0.00	0.00	0.00	0.00	0.00	0.00	0.00	0.00	0.00	0.00	0.00	0.00
0.00	0.00	0.00	0.00	0.00	0.00	0.00	0.00	0.00	1.20	0.00	0.00	0.00	0.00	0.00	0.00	0.00	0.00
1.80	1.76	1.87	0.00	0.00	0.00	0.00	0.00	1.93	0.64	1.80	1.82	1.64	0.81	1.82	1.85	1.82	1.90
0.00	0.00	0.00	0.00	0.00	0.00	0.00	0.00	0.00	0.00	0.00	0.00	0.00	0.00	0.00	0.00	0.00	0.00
15.51	15.80	15.81	19.69	19.74	19.47	19.80	19.47	15.23	13.98	15.52	15.54	13.78	14.80	15.22	15.54	13.97	15.60
2.26	2.39	2.34	2.34	2.40	2.17	2.53	2.23	2.37	1.05	2.04	1.77	1.26	2.25	1.68	1.99	1.40	2.13
0.16	0.55	0.42	2.89	2.81	3.17	2.78	3.15	1.07	2.17	0.33	0.30	3.35	1.45	0.91	0.29	3.28	0.20
5.71	6.04	5.94	11.69	11.74	11.47	11.80	11.47	5.30	4.15	5.72	5.72	4.13	5.99	5.40	5.69	4.15	5.70
1.80	1.76	1.87	0.00	0.00	0.00	0.00	0.00	1.93	1.84	1.80	1.82	1.64	0.81	1.82	1.85	1.82	1.90
0.53	0.90	0.90	0.33	0.31	0.34	0.39	0.42	0.39	0.37	0.89	0.94	1.00	0.84	0.95	0.92	1.00	0.88
0.47	0.10	0.10	0.67	0.69	0.66	0.61	0.58	0.61	0.63	0.11	0.06	0.00	0.16	0.05	0.08	0.00	0.12

SEM-EDS	SEM-EDS	SEM-EDS	SEM-EDS	SEM-EDS	SEM-EDS	SEM-EDS	SEM-EDS	SEM-EDS	SEM-EDS	SEM-EDS	SEM-EDS	SEM-EDS	SEM-EDS	SEM-EDS	SEM-EDS	SEM-EDS	SEM-EDS
GBM19A	GBM19A	GBM19A	GBM19A	GBM19A	GBM19A	GBM19A	GBM22B	GBM22B	GBM22B	GBM22B	GBMX	GBMX	GBMX	GBMX	GBMX	GBMX	GBMX
							diopside-phlogopite exoskarn				chlorite vein vein						
9 sc	10	11	12	13	14	15 c	1	1c	2sc	2c	1	1c	2sc	2c	3c	3sc	
Phl	Bt	Ms	Ms	Phl	Ms	Phl	Phl	Phl	Phl	Phl	Chl	Chl	Chl	Chl	Chl	Chl	Chl
46.36	52.16	53.56	51.25	47.32	51.37	44.79	43.34	43.91	44.22	41.61	28.76	28.46	31.27	28.69	56.71	30.43	31.24
1.15	0.32	0.34	0.41	0.87	0.26	2.29											
12.74	31.52	30.71	33.09	12.69	32.25	15.06	16.98	16.41	16.25	15.08	22.74	23.73	23.35	23.01	30.32	21.06	22.90
5.57	0.80	0.78	0.75	2.44	0.47	3.34	0.51			7.87	37.52	36.93	27.19	38.71	1.25	38.91	29.54
											0.98	0.99	1.26		8.18		
23.15	4.18	4.30	3.89	25.29	4.41	23.99	28.40	28.68	28.02	32.72	10.00	9.90	16.93	9.59	3.54	9.60	16.33
11.04	11.02	10.32	10.61	11.39	11.23	10.52	10.77	11.00	11.51	2.72	< 0.1	< 0.1	< 0.1	< 0.1	< 0.1	< 0.1	< 0.1
100.01	100.00	100.01	100.00	100.00	99.99	99.99	100.00	100.00	100.00	100.00	100.00	100.01	100.00	100.00	100.00	100.00	100.01
6.25	6.58	6.71	6.45	6.29	6.48	5.97	5.73	5.80	5.85	5.48	5.56	5.48	5.73	5.55	8.81	5.88	5.75
0.12	0.03	0.03	0.04	0.09	0.02	0.23	0.01	0.01	0.01	0.01	0.01	0.01	0.01	0.01	0.01	0.01	0.01
2.02	4.68	4.54	4.91	1.99	4.80	2.37	2.65	2.55	2.53	2.34	5.18	5.39	5.04	5.25	5.55	4.79	4.97
0.00	0.00	0.00	0.00	0.00	0.00	0.00	0.00	0.00	0.00	0.00	0.00	0.00	0.00	0.00	0.00	0.00	0.00
0.63	0.08	0.08	0.08	0.27	0.05	0.37	0.06	0.00	0.00	0.87	6.07	5.95	4.17	6.26	0.16	6.29	4.55
0.00	0.00	0.00	0.00	0.00	0.00	0.00	0.00	0.00	0.00	0.00	0.16	0.16	0.20	0.00	1.08	0.00	0.00
4.65	0.79	0.80	0.73	5.01	0.83	4.77	5.60	5.65	5.53	6.43	2.88	2.84	4.62	2.77	0.82	2.76	4.48
0.00	0.00	0.00	0.00	0.00	0.00	0.00	0.00	0.00	0.00	0.00	0.00	0.00	0.00	0.00	0.00	0.00	0.00
0.00	0.00	0.00	0.00	0.00	0.00	0.00	0.00	0.00	0.00	0.00	0.00	0.00	0.00	0.00	0.00	0.00	0.00
1.90	1.77	1.65	1.70	1.93	1.81	1.79	1.82	1.85	1.94	0.46	0.00	0.00	0.00	0.00	0.00	0.00	0.00
0.00	0.00	0.00	0.00	0.00	0.00	0.00	0.00	0.00	0.00	0.00	0.00	0.00	0.00	0.00	0.00	0.00	0.00
15.57	13.94	13.81	13.91	15.59	14.00	15.51	15.85	15.85	15.85	15.58	19.85	19.82	19.75	19.83	16.42	19.72	19.76
1.75	1.42	1.29	1.55	1.71	1.52	2.02	2.27	2.20	2.15	2.52	2.44	2.52	2.27	2.45	-0.81	2.12	2.25
0.27	3.26	3.25	3.36	0.28	3.28	0.34	0.38	0.35	0.38	-0.18	2.74	2.87	2.77	2.80	6.36	2.67	2.73
5.67	4.16	4.16	4.21	5.66	4.19	5.72	6.04	6.00	5.91	7.12	11.85	11.82	11.75	11.83	8.42	11.72	11.76
1.90	1.77	1.65	1.70	1.93	1.81	1.79	1.82	1.85	1.94	0.46	0.00	0.00	0.00	0.00	0.00	0.00	0.00
0.88	0.90	0.91	0.90	0.95	0.94	0.93	0.99	1.00	1.00	0.88	0.32	0.32	0.53	0.31	0.83	0.31	0.50
0.12	0.10	0.09	0.10	0.05	0.06	0.07	0.01	0.00	0.00	0.12	0.68	0.68	0.47	0.69	0.17	0.69	0.50

																												bulk ID-ICP-MS		
Sample	**GBM34-1**	**GBM34-2**	**GBM34-3**	**GBM34-4**	**GBM34-5**	**GBM34-6**	**GBM34-7**	**GBM34-8**	**GBM34-9**	**GBM34-10**	**TITANIT1-2**	**TITANIT1-3**	**TITANIT1-4**	**TITANIT1-5**	**TITANIT1-6**	**TITANIT1-7**	**TITANIT1-8**	**TITANIT1-9**	**TITANIT1-10**	**TITANIT1-11**	**TITANIT1-12**	**TITANIT1-13**	**TITANIT1-13b**	**TITANIT1-14**	**TITANIT1-15**	**TITANIT1-16**	**TITANIT1-17**	**TITANIT1-18**	**TITANIT1-19**	**TITANIT1-20**	**TITANIT1-21**	**TITANIT1-22**	Ttn1	Ttn2	Ttn3
Rock type	**Titanite centimetric vein (GBM34)**																**biotite granite**			**Altered granite (GBM2A)**				**Altered granite (395m)**									**pyroxene endoskarn**		
Major elements (wt%)																																		
SiO2	30.79	30.88	31.07	31.81	30.76	30.98	31.38	31.44	31.04	31.18	30.74	30.69	31.45	30.87	31.04	31.03	31.28	30.53	30.90	30.71	30.54	30.47	30.83	30.67	30.61	31.03	31.33	31.02	30.41	30.93	30.47	30.45			
TiO2	33.42	33.12	33.13	31.15	34.36	31.58	34.21	33.54	34.35	34.05	33.60	33.47	32.59	33.77	33.19	33.66	33.57	33.91	31.97	32.19	33.95	35.01	33.61	33.88	34.16	33.50	32.95	33.19	34.37	32.61	33.75	33.06			
Al2O3	3.68	3.77	3.55	5.55	2.92	4.73	3.69	4.04	3.30	3.47	3.69	3.88	4.43	3.43	3.52	3.73	3.70	3.15	4.26	3.92	2.54	2.64	3.85	3.41	2.76	3.87	3.70	4.03	2.67	3.85	2.65	3.30			
FeO	0.27	0.23	0.22	0.11	0.25	0.27	0.25	0.50	0.32	0.26	0.25	0.28	0.22	0.24	0.22	0.31	0.20	0.16	0.25	0.43	0.45	0.33	0.21	0.33	0.22	0.18	0.27	0.20	0.23	0.21	0.28	0.33			
MnO	0.05	0.00	0.00	0.01	0.04	0.00	0.03	0.00	0.05	0.06	0.04	0.05	0.04	0.01	0.00	0.01	0.00	0.03	0.00	0.01	0.00	0.06	0.02	0.01	0.02	0.03	0.00	0.01	0.05	0.02	0.00	0.05			
MgO	0.17	0.16	0.14	0.07	0.19	0.27	0.08	0.03	0.06	0.06	0.14	0.16	0.09	0.14	0.11	0.12	0.08	0.16	0.20	0.21	0.11	0.07	0.16	0.25	0.10	0.14	0.12	0.13	0.09	0.13	0.14	0.23			
CaO	27.88	27.38	27.59	28.58	27.00	27.34	28.67	28.71	28.30	27.59	26.85	27.49	28.81	27.53	27.16	28.03	28.45	26.88	27.26	27.33	26.83	27.89	27.10	27.69	27.46	28.54	28.38	28.04	27.37	28.10	26.88	27.08			
Na2O	0.03	0.03	0.02	0.00	0.06	0.02	0.00	0.02	0.00	0.01	0.09	0.07	0.04	0.03	0.04	0.06	0.02	0.08	0.04	0.05	0.05	0.04	0.07	0.09	0.05	0.03	0.05	0.05	0.05	0.07	0.07	0.02			
Nb2O5	0.04	0.29	0.12	0.17	0.36	0.16	0.06	0.12	0.10	0.12	0.10	0.07	0.10	0.46	0.39	0.08	0.08	0.35	0.10	0.13	0.23	0.17	0.13	0.29	0.32	0.37	0.05	0.08	0.22	0.13	0.26	0.31			
La2O3	0.05	0.10	0.03	0.00	0.22	0.26	0.00	0.00	0.20	0.00	0.04	0.07	0.00	0.00	0.13	0.07	0.03	0.14	0.15	0.21	0.20	0.19	0.12	0.12	0.22	0.00	0.00	0.05	0.20	0.00	0.11	0.26			
Ce2O3	0.56	0.86	0.80	0.13	1.17	1.13	0.00	0.00	0.45	0.39	0.41	0.26	0.15	0.61	0.67	0.33	0.02	1.08	1.00	0.91	1.05	0.58	0.07	1.01	0.85	0.21	0.26	0.42	0.91	0.07	0.85	1.08			
Sm2O3	0.00	0.14	0.23	0.01	0.14	0.35	0.00	0.00	0.11	0.20	0.27	0.16	0.03	0.00	0.21	0.05	0.16	0.15	0.06	0.23	0.16	0.18	0.04	0.14	0.03	0.00	0.00	0.18	0.00	0.04	0.04	0.00			
Nd2O3	0.24	0.49	0.68	0.18	0.83	0.75	0.00	0.06	0.19	0.56	0.53	0.33	0.08	0.53	0.49	0.28	0.03	0.76	0.78	0.53	0.57	0.23	0.16	0.51	0.47	0.07	0.10	0.18	0.33	0.18	0.66	0.36			
F	0.48	0.50	0.43	0.79	0.31	0.59	0.52	0.63	0.44	0.40	0.45	0.50	0.59	0.35	0.44	0.44	0.55	0.35	0.49	0.46	0.26	0.41	0.46	0.45	0.25	0.49	0.58	0.53	0.31	0.56	0.29	0.38			
Totale	100.0	100.2	100.2	100.7	100.7	100.5	101.2	101.4	101.2	100.6	99.5	99.8	100.9	100.2	100.0	100.6	100.7	99.9	99.6	99.6	99.3	100.6	99.2	101.2	99.9	100.9	100.3	100.4	99.5	99.6	98.8	99.0			
Structural formula, oxygen equivalents p.f.u. = 5																																			
Si	1.02	1.03	1.04	1.04	1.03	1.03	1.03	1.03	1.02	1.03	1.03	1.02	1.03	1.03	1.04	1.02	1.03	1.02	1.03	1.03	1.03	1.01	1.03	1.02	1.03	1.02	1.04	1.03	1.02	1.03	1.03	1.03			
Ti	0.83	0.83	0.83	0.77	0.86	0.79	0.84	0.82	0.85	0.85	0.84	0.84	0.80	0.85	0.83	0.84	0.83	0.85	0.81	0.81	0.86	0.87	0.84	0.85	0.86	0.83	0.82	0.83	0.87	0.82	0.86	0.84			
Al	0.14	0.15	0.14	0.21	0.12	0.19	0.14	0.16	0.13	0.14	0.15	0.15	0.17	0.13	0.14	0.15	0.14	0.12	0.17	0.16	0.10	0.10	0.15	0.13	0.11	0.15	0.14	0.16	0.11	0.15	0.11	0.13			
Fe2+	0.01	0.01	0.01	0.00	0.01	0.01	0.01	0.01	0.01	0.01	0.01	0.01	0.01	0.01	0.01	0.01	0.01	0.00	0.01	0.01	0.01	0.01	0.01	0.01	0.01	0.00	0.01	0.01	0.01	0.01	0.01	0.01			
Mn	0.00	0.00	0.00	0.00	0.00	0.00	0.00	0.00	0.00	0.00	0.00	0.00	0.00	0.00	0.00	0.00	0.00	0.00	0.00	0.00	0.00	0.00	0.00	0.00	0.00	0.00	0.00	0.00	0.00	0.00	0.00	0.00			
Mg	0.01	0.01	0.01	0.00	0.01	0.01	0.00	0.00	0.00	0.00	0.01	0.01	0.00	0.01	0.01	0.01	0.00	0.01	0.01	0.01	0.01	0.00	0.01	0.01	0.01	0.01	0.01	0.01	0.00	0.01	0.01	0.01			
Ca	0.99	0.98	0.99	1.00	0.97	0.97	1.01	1.00	1.00	0.98	0.96	0.98	1.01	0.98	0.97	0.99	1.00	0.97	0.98	0.98	0.97	0.99	0.97	0.99	0.99	1.01	1.01	0.99	0.99	1.00	0.97	0.98			
Na	0.0019	0.0019	0.0013	0.0000	0.0039	0.0014	0.0000	0.0013	0.0000	0.0006	0.0058	0.0045	0.0025	0.0019	0.0026	0.0038	0.0013	0.0052	0.0026	0.0033	0.0033	0.0026	0.0045	0.0058	0.0033	0.0019	0.0032	0.0032	0.0033	0.0045	0.0046	0.0013			
Y	0.0003	0.0004	0.0001	0.0001	0.0002	0.0000	0.0000	0.0002	0.0002	0.0005	0.0011	0.0007	0.0001	0.0005	0.0004	0.0004	0.0001	0.0001	0.0001	0.0003	0.0003	0.0002	0.0001	0.0002	0.0002	0.0002	0.0001	0.0000	0.0000	0.0001	0.0001	0.0001			
Nb	0.0012	0.0024	0.0011	0.0011	0.0013	0.0024	0.0009	0.0015	0.0014	0.0012	0.0017	0.0009	0.0014	0.0022	0.0038	0.0010	0.0012	0.0037	0.0013	0.0008	0.0019	0.0021	0.0010	0.0029	0.0030	0.0026	0.0008	0.0007	0.0016	0.0015	0.0036	0.0014			
Ta	0.0001	0.0002	0.0001	0.0001	0.0001	0.0000	0.0000	0.0002	0.0002	0.0003	0.0006	0.0001	0.0002	0.0005	0.0004	0.0001	0.0002	0.0003	0.0001	0.0001	0.0002	0.0002	0.0001	0.0002	0.0002	0.0002	0.0000	0.0001	0.0003	0.0002	0.0004	0.0001			
La	0.0019	0.0029	0.0003	0.0002	0.0018	0.0032	0.0000	0.0008	0.0007	0.0009	0.0012	0.0010	0.0003	0.0014	0.0014	0.0010	0.0003	0.0032	0.0022	0.0022	0.0029	0.0028	0.0009	0.0005	0.0005	0.0005	0.0005	0.0017	0.0023	0.0016	0.0028	0.0017			
Ce	0.0067	0.0098	0.0014	0.0008	0.0074	0.0138	0.0000	0.0026	0.0023	0.0034	0.0055	0.0045	0.0011	0.0051	0.0050	0.0042	0.0013	0.0122	0.0094	0.0072	0.0091	0.0086	0.0030	0.0020	0.0021	0.0020	0.0020	0.0061	0.0077	0.0065	0.0098	0.0066			
Sm	0.0040	0.0055	0.0010	0.0007	0.0052	0.0040	0.0000	0.0015	0.0013	0.0027	0.0050	0.0037	0.0008	0.0036	0.0035	0.0032	0.0010	0.0074	0.0065	0.0046	0.0053	0.0050	0.0016	0.0014	0.0014	0.0013	0.0014	0.0025	0.0026	0.0038	0.0041	0.0036			
Nd	0.0009	0.0012	0.0003	0.0002	0.0011	0.0089	0.0000	0.0004	0.0004	0.0009	0.0018	0.0013	0.0003	0.0012	0.0011	0.0010	0.0003	0.0014	0.0012	0.0013	0.0014	0.0012	0.0003	0.0003	0.0003	0.0003	0.0003	0.0004	0.0003	0.0007	0.0006	0.0006			
F	0.0504	0.0526	0.0455	0.0818	0.0328	0.0626	0.0538	0.0650	0.0459	0.0419	0.0475	0.0526	0.0612	0.0369	0.0465	0.0460	0.0573	0.0371	0.0519	0.0489	0.0278	0.0430	0.0484	0.0473	0.0266	0.0510	0.0606	0.0554	0.0330	0.0589	0.0310	0.0406			
Tot	3.03	3.03	3.03	3.04	3.02	3.04	3.03	3.03	3.03	3.02	3.02	3.03	3.04	3.03	3.02	3.03	3.03	3.02	3.03	3.04	3.02	3.03	3.02	3.03	3.03	3.04	3.04	3.03	3.02	3.04	3.02	3.03			
Trace elements (ppm)																																			
Li	10.5	13.6	5.9	5.3	9.4			4.8	6.4	20.6	15.8	8.1	3.4	20.0	19.8	11.1	5.2	24.2	9.5	8.4	15.1	14.7	1.8	6.8	6.7	7.0	1.8	7.2	11.2	7.7	15.0	7.0	2.81	12.48	8.35
Be	0.2	0.3	bdl	0.1	0.2			bdl	bdl	0.0	0.2	bdl	0.1	bdl	0.2	bdl	0.0	1.1	0.2	0.3	0.3	1.7	bdl	bdl	bdl	bdl	bdl	bdl	bdl	bdl	bdl	bdl	0.1			
Sc	257	212	23	11	663			16	36	110	225	224	19	153	169	152	42	247	328	478	418	372	389	162	167	169	216	144	200	316	201	302			
V	1451	1122	358	476	1487			952	941	996	1096	1327	1003	1048	950	1221	920	1075	1476	1315	1116	1105	2398	1636	1661	1733	2030	1354	1306	1347	1132	1370	193	347	281
Cr	904	568	403	403	860			413	453	474	856	1112	217	520	554	976	636	603	964	1909	1457	1323	1422	786	803	852	1349	733	635	693	537	721	35	219	142
Mn	191	206	97	90	154			80	85	153	198	187	61	160	182	215	87	169	155	169	179	168	99	116	118	120	155	194	174	162	165	160			
Co	0.1	0.1	0.1	0.1	0.1			bdl	0.1	0.1	bdl	0.2	0.1	0.1	bdl	0.2	0.1	0.2	0.2	0.2	0.2	0.2	bdl	bdl	bdl	0.1	bdl	bdl	0.2	bdl	0.1	bdl	0.57	0.84	0.44
Ni	0.4	0.4	0.4	0.6	0.7			0.5	0.5	0.3	0.4	0.4	0.5	0.6	0.3	0.3	0.4	0.4	0.4	0.6	0.3	1.6	0.3	0.3	0.4	0.3	0.5	0.5	0.8	1.4	1.0	0.8	5.25	5.78	4.6
Cu	8.0	7.8	7.9	8.6	8.4			7.9	8.1	8.5	8.9	9.2	8.6	8.4	8.8	8.9	9.0	9.3	8.4	8.3	8.2	8.9	8.1	7.8	8.2	8.5	8.8	8.4	8.7	8.6	8.4	8.6	59	84	73
Zn	8.8	8.3	9.0	8.7	9.8			8.4	8.7	14.1	7.6	7.4	7.6	8.1	7.9	7.9	8.0	8.8	8.1	8.0	7.5	11.3	8.3	7.5	7.6	7.8	7.7	9.1	13.2	8.4	8.4	7.7	181	242	215
Ga	40.8	52.2	18.6	16.3	47.1			23.8	22.9	30.3	43.7	37.4	19.9	37.9	37.3	33.1	18.3	66.2	59.6	49.7	55.5	54.2	27.0	22.3	22.1	21.9	24.8	37.8	41.1	42.1	50.7	41.0	22.74	10.94	9.18
Rb	0.5	0.2	2.6	0.1	0.5			0.3	1.0	5.5	0.4	0.2	bdl	0.2	0.2	0.1	0.3	bdl	0.1	0.8	0.5	5.9	bdl	bdl	0.1	bdl	bdl	3.8	3.6	bdl	bdl	bdl	17.45	5.64	1.93
Sr	21.6	23.5	20.6	19.4	25.0			16.0	16.8	20.9	20.7	19.0	17.0	23.4	27.4	20.5	17.3	31.2	23.0	13.4	15.3	16.2	14.7	16.4	16.4	16.0	12.6	14.2	17.1	16.1	19.2	15.8	14.56	40.14	28.06
Y	1487	1903	465	540	777			1023	948	2800	5370	3460	647	2750	2240	2227	633	733	726	1624	1434	1239	482	797	818	788	479	230	206	384	276	345	443	594	498
Zr	444	764	487	405	1313			392	382	403	1489	453	590	431	681	299	433	757	516	571	1620	1710	1070	965	966	1180	344	286	2071	2270	6050	2037	211	1950	1348
Nb	828	1571	703	720	840			1025	922	823	1116	586	953	1448	2520	666	816	2440	843	521	1230	1388	639	1913	1952	1753	503	460	1063	989	2357	932	561	221	181
Sn	43.4	51.4	217.2	243.0	108.0			448.0	391.0	191.0	60.7	44.1	530.0	108.7	90.2	36.8	246.0	90.5	74.0	137.4	208.3	244.5	132.5	407.0	390.5	376.2	151.5	97.4	144.5	165.3	244.9	153.4	1988	1458	1266
Sb	0.1	0.1	0.1	0.1	0.1			0.1	0.1	0.1	bdl	bdl	0.1	bdl	bdl	bdl	bdl	bdl	0.2	0.2	0.1	0.6	bdl	0.1	bdl	bdl	0.1	bdl	0.1	0.1	0.1	bdl	2.88	0.89	0.68
Cs	0.3	0.0	0.4	0.1	0.1			0.2	0.7	4.0	bdl	bdl	bdl	bdl	bdl	bdl	0.2	bdl	bdl	0.3	0.3	0.6	0.0	bdl	bdl	bdl	bdl	5.4	3.8	0.1	bdl	0.0	2.1	1.57	0.76
Ba	0.1	0.0	3.8	0.2	0.4			0.1	0.1	0.7	bdl	bdl	0.0	bdl	bdl	bdl	0.0	0.0	0.0	0.1	0.1	0.6	bdl	bdl	0.0	bdl	bdl	1.1	0.7	bdl	bdl	0.0	9	5.72	1.41
La	1558	2338	275	168	1446			663	577	725	1000	836	244	1108	1107	823	282	2551	1816	1749	2320	2265	740	421	414	400	373	1384	1859	1344	2274	1340	96	132	104
Ce	5540	8050	1109	688	6020			2190	1900	2820	4521	3663	891	4170	4110	3479	1090	9910	7650	5850	7320	7110	2499	1679	1689	1655	1649	5030	6230	5330	7960	5316	530	497	406
Pr	771	1085	172	116	906			297	256	452	819	638	145	655	648	580	175	1432	1181	856	1026	994	336	268	269	259	277	617	695	773	993	744	107	94	81
Nd	3502	4820	877	628	4480			1340	1156	2340	4310	3250	715	3180	3060	2815	871	6420	5590	4000	4590	4410	1377	1212	1199	1151	1273	2200	2277	3320	3560	3052	527	460	396
Sm	788	1045	230	203	883			353	317	799	1527	1080	224	985	908	845	247	1157	1044	1054	1126	1044	275	275	275	256	267	301	284	595	475	521	176	123	106
Eu	5.6	7.1	4.8	5.7	3.9			9.5	8.4	6.6	5.5	4.7	7.8	5.9	5.6	4.2	6.2	3.8	3.6	9.7	9.6	10.9	9.6	12.9	13.0	12.7	9.0	5.7	5.7	6.1	7.5	5.9	13.3	11.3	8.9
Gd	582	755	168	166	533			287	260	743	1467	992	197	854	747	712	200	638	588	813	817	739	195	214	213	201	173	165	156	332	247	290	139	109	95
Tb	72.9	93.5	21.3	23.2	48.4			41.2	37.8	118.0	240.5	158.0	30.6	131.0	110.6	105.4	28.0	54.5	50.4	96.5	92.9	83.8	23.4	31.5	31.6	29.7	21.2	15.4	14.0	30.2	21.3	26.4	21.3	17.5	15.0
Dy	356.4	455.0	106.3	121.2	191.8			222.0	205.0	669.0	1303.0	839.0	156.5	689.0	571.0	546.0	142.3	193.4	182.0	420.0	392.1	346.0	106.1	167.7	169.7	161.1	100.1	58.2	52.7	109.4	76.6	96.9	113	111	93
Ho	56.0	72.0	17.2	19.8	27.8			36.7	33.9	109.0	227.1	144.0	26.6	114.0	94.4	92.7	23.9	27.3	27.1	65.9	58.9	51.3	18.1	29.7	30.4	29.2	17.6	9.0	8.2	15.3	10.8	13.7	17.4	22.47	19.07
Er	132.6	170.6	42.7	49.5	64.9			91.9	84.9	263.0	537.0	340.0	60.6	264.0	219.6	213.4	57.9	60.8	61.9	146.1	127.4	110.2	43.6	74.9	75.7	72.9	44.7	20.4	18.6	31.9	23.6	28.8	41	66	55
Tm	16.7	21.6	5.7	6.4	8.7			12.1	11.1	33.1	69.5	44.0	7.9	34.8	29.5	28.0	8.0	8.4	8.6	19.0	16.1	13.5	5.8	10.0	10.3	10.1	6.3	2.8	2.4	4.0	3.0	3.6	5.5	9.66	8.02
Yb	103.8	135.2	34.5	39.2	62.2			76.2	68.9	196.0	393.0	251.0	44.5	200.0	171.1	164.2	47.4	61.0	66.9	122.5	102.1	85.6	37.6	62.5	63.4	62.8	42.7	19.0	17.2	26.9	20.8	24.8	31.0	56	46
Lu	12.5	16.4	3.5	3.9	9.4			8.4	7.5	19.8	41.1	26.8	4.5	21.5	18.9	18.0	5.5	10.0	11.7	16.8	13.6	11.3	5.4	7.4	7.5	7.6	5.9	3.1	2.7	4.2	3.2	3.9	3.36	6.86	5.67
Hf	34	56	27	27	72			41	38	46	187	56	58	42	50	30	47	38	32	36	101	114	70	61	61	99	21	13	104	94	234	84	25.1	57	43
Ta	102	217	143	117	132			183	174	370	624	137	184	519	446	138	243	351	140	63	178	239	70	172	175	213	43	79	353	194	450	153	65	29	22
Pb	0.4	0.4	0.7	0.7	0.5			0.3	0.4	2.3	0.3	0.2	0.1	0.3	0.4	0.3	0.3	1.5	0.4	1.0	0.6	3.9	0.2	0.3	0.3	0.3	0.2	1.2	3.0	0.6	0.4	0.3	1.39	2.75	1.87
Bi	0.2	0.2	0.1	0.1	0.1			0.2	0.2	0.2	0.1	0.1	0.1	0.1	0.2	0.2	0.1	0.1	0.2	0.3	0.4	0.3	0.1	0.2	0.2	0.2	0.2	0.2	0.2	0.2	0.2	0.2	1.95	0.95	0.59
Th	258	506	122	123	170			61	64	111	177	110	77	189	270	114	83	374	349	321	384	335	161	225	221	211	99	152	168	140	220	138	10.7	388	300
U	394	696	180	196	177			120	124	197	296	209	134	309	420	211	151	276	313	279	280	244	267	395	392	381	220	229	200	222	281	219	40	148	113

EMP and LA-ICP-MS analysis for titanite

Rutile

Rt-13	Rt-14	Rt-15	Rt-16	Rt-17	Rt-18	Rt-19	Rt-20	Rt-21	Rt-22	Rt-23	Rt-24
Rut15 bright (core)	Rut27 dark (vein)	Rut27 bright (core)	Rut27 grey (vein)	Rut21 grey (rim)	Rut21 bright (core)	Rut31 bright (core)	Rut31 dark (core)	Rut31 grey (rim)	Rut32 dark (rim)	Rut32 (core)	Rut32 grey (core)
0.00	0.00	0.00	0.03	0.00	0.02	0.02	0.00	0.01	0.00	0.00	0.00
92.6	98.4	97.6	96.6	98.4	96.3	96.1	98.4	98.1	97.9	90.1	92.7
0.03	0.04	0.06	0.05	0.05	0.17	0.04	0.04	0.02	0.04	0.09	0.03
0.60	0.26	0.42	0.45	0.20	0.87	0.69	0.36	0.32	0.05	0.80	0.34
0.00	0.00	0.00	0.00	0.01	0.04	0.00	0.00	0.00	0.00	0.00	0.01
0.00	0.00	0.00	0.00	0.01	0.00	0.00	0.01	0.00	0.00	0.01	0.02
0.01	0.01	0.00	0.00	0.00	0.01	0.02	0.01	0.00	0.00	0.01	0.00
0.08	0.00	0.00	0.01	0.01	0.01	0.00	0.02	0.02	0.03	0.00	0.00
0.00	0.00	0.00	0.01	0.00	0.00	0.01	0.00	0.00	0.00	0.00	0.00
1.48	0.08	0.06	0.04	0.02	0.02	0.07	0.08	0.07	1.18	1.27	0.00
0.31	0.18	0.18	0.19	0.09	0.05	0.33	0.21	0.21	0.23	0.29	0.21
2.17	0.17	0.52	0.41	0.06	0.64	0.67	0.20	0.18	0.37	4.19	3.22
0.09	0.06	0.05	0.08	0.09	0.07	0.08	0.04	0.04	0.14	0.19	0.03
0.00	0.05	0.00	0.00	0.00	0.00	0.00	0.00	0.00	0.03	0.00	0.00
0.04	0.13	0.00	0.00	0.06	0.00	0.00	0.01	0.02	0.00	0.03	0.00
102.01	105.75	105.31	104.03	105.39	104.41	104.22	105.77	105.52	105.10	101.57	102.83
0.0000	0.0000	0.0000	0.0004	0.0000	0.0003	0.0003	0.0000	0.0001	0.0000	0.0000	0.0000
0.0005	0.0006	0.0010	0.0008	0.0008	0.0027	0.0006	0.0006	0.0003	0.0006	0.0015	0.0005
0.9621	0.9929	0.9900	0.9901	0.9958	0.9863	0.9849	0.9922	0.9928	0.9833	0.9458	0.9693
0.0069	0.0029	0.0047	0.0051	0.0023	0.0099	0.0079	0.0040	0.0036	0.0006	0.0093	0.0040
0.0000	0.0000	0.0000	0.0000	0.0001	0.0005	0.0000	0.0000	0.0000	0.0000	0.0000	0.0001
0.0000	0.0000	0.0000	0.0000	0.0002	0.0000	0.0000	0.0002	0.0000	0.0000	0.0002	0.0004
0.0001	0.0001	0.0000	0.0000	0.0000	0.0001	0.0003	0.0001	0.0000	0.0000	0.0001	0.0000
0.0021	0.0000	0.0000	0.0003	0.0003	0.0003	0.0000	0.0005	0.0005	0.0008	0.0000	0.0000
0.0000	0.0000	0.0000	0.0002	0.0000	0.0000	0.0002	0.0000	0.0000	0.0000	0.0000	0.0000
0.0161	0.0008	0.0006	0.0004	0.0002	0.0002	0.0007	0.0008	0.0007	0.0125	0.0140	0.0000
0.0028	0.0016	0.0016	0.0017	0.0008	0.0004	0.0030	0.0018	0.0019	0.0020	0.0027	0.0020
0.0136	0.0010	0.0032	0.0025	0.0004	0.0039	0.0041	0.0012	0.0011	0.0022	0.0264	0.0202
0.0003	0.0002	0.0002	0.0003	0.0003	0.0003	0.0003	0.0002	0.0001	0.0005	0.0007	0.0001
0.0004	0.0003	0.0003	0.0003	0.0001	0.0001	0.0004	0.0004	0.0003	0.0004	0.0004	0.0001
0.0002	0.0006	0.0000	0.0000	0.0003	0.0000	0.0000	0.0000	0.0001	0.0000	0.0001	0.0000
0.0000	0.0002	0.0000	0.0000	0.0000	0.0000	0.0000	0.0000	0.0000	0.0001	0.0000	0.0000
1.0052	1.0014	1.0015	1.0021	1.0014	1.0050	1.0027	1.0022	1.0017	1.0030	1.0013	0.9968
bdl	bdl	bdl	bdl	bdl	bdl	bdl	bdl	bdl	bdl	bdl	bdl
bdl	bdl	0.058	bdl	bdl	0.4	bdl	bdl	bdl	bdl	bdl	bdl
bdl	810	bdl	bdl	bdl	910	970	bdl	bdl	bdl	bdl	bdl
bdl	bdl	bdl	bdl	bdl	bdl	bdl	bdl	bdl	bdl	bdl	bdl
101.6	317.5	342	265.4	139.1	191	233.9	306.1	263	64.7	78.7	57.8
3051	1828	1800	1898	896	482	3318	2061	2147	2310	2880	2145
14780	760	590	403	165	185	662	764	660	11800	12720	1400
1.34	bdl	1.29	bdl	4.6	3.99	2.8	bdl	bdl	bdl	1.38	bdl
0.18	bdl	bdl	bdl	bdl	bdl	bdl	bdl	bdl	bdl	bdl	bdl
bdl	bdl	0.45	bdl	bdl	bdl	0.62	bdl	290	0.71	0.66	1.43
25.2	27.6	26.2	24	24.1	26.3	25	24.7	24.1	25	22.2	22
25.2	26.5	24.59	26.3	27.3	25.1	26.6	24.3	31.3	26	24.2	24
3.03	1.39	2.12	3.14	5.88	6.42	2.91	1.4	1.56	2.01	2.9	1.66
0.43	bdl	bdl	bdl	bdl	bdl	bdl	bdl	bdl	bdl	bdl	bdl
0.307	0.265	0.301	0.303	0.54	0.331	0.348	0.323	0.37	0.313	0.402	0.53
0.028	0.105	0.049	0.018	0.09	0.095	0.334	0.036	0.066	0.051	0.42	0.106
597	483	404	378.2	129.5	156	629	564	521	546	538	196
21310	2011	2350	3190	3960	3480	4310	1934	1890	20500	27250	3450
113.3	167.6	191.9	190.9	140.9	136	197	179.7	167.8	108.1	104.6	280
0.151	bdl	0.092	0.106	0.15	0.264	0.104	bdl	0.11	0.183	0.121	0.205
0.128	bdl	bdl	bdl	bdl	bdl	bdl	bdl	bdl	0.053	0.038	0.07
0.057	bdl	0.022	bdl	bdl	0.041	0.062	bdl	bdl	bdl	0.048	bdl
0.0041	0.066	0.0183	0.0064	0.067	0.18	0.46	bdl	0.082	0.013	0.52	0.085
0.004	0.114	0.063	0.0041	0.29	0.28	0.95	0.0031	0.28	0.059	0.71	0.11
bdl	bdl	0.0064	bdl	0.01	0.035	0.087	0.0049	0.13	0.0032	0.076	0.019
bdl	0.065	0.043	bdl	bdl	0.036	0.34	bdl	0.39	bdl	0.22	bdl
bdl	bdl	bdl	bdl	bdl	bdl	0.139	bdl	bdl	bdl	0.088	0.041
bdl	0.009	0.0012	bdl	bdl	bdl	0.011	bdl	bdl	bdl	0.056	0.013
bdl	0.029	0.029	bdl	bdl	0.055	0.052	bdl	bdl	bdl	0.084	0.044
bdl	bdl	0.0014	bdl	0.01	bdl	0.024	bdl	bdl	bdl	0.0155	bdl
bdl	0.027	0.014	bdl	0.019	bdl	0.045	bdl	0.014	bdl	0.077	0.039
bdl	0.013	0.004	bdl	0.0049	bdl	0.0128	bdl	bdl	0.0038	0.023	bdl
0.0054	bdl	0.0097	0.013	bdl	bdl	0.052	bdl	0.033	bdl	0.071	0.029
0.0008	bdl	0.0013	0.0029	bdl	bdl	bdl	bdl	0.0037	0.0017	0.0111	bdl
bdl	0.04	0.03	bdl	bdl	bdl	0.117	0.041	0.07	bdl	0.03	bdl
0.0048	0.0064	0.0077	0.0077	0.015	bdl	0.023	0.025	0.019	bdl	0.0049	0.0066
30.15	28.3	20.1	17.21	6.39	7.55	34.6	27.4	24.2	29.5	28.84	11.7
864	565	507	840	920	722	784	419	378	1360	1900	343
0.052	0.34	0.376	0.043	0.6	bdl	1.69	0.113	bdl	0.051	0.37	0.37
bdl	bdl	bdl	bdl	bdl	bdl	0.014	bdl	bdl	bdl	bdl	bdl
0.013	0.07	0.039	0.021	0.039	0.2	2.19	0.023	0.23	0.193	0.66	0.21
30.4	13.17	18.9	17.7	7.56	4.93	28.3	18.67	16.96	18.95	16.88	3.94

Sample	Rt-1	Rt-2	Rt-3	Rt-4	Rt-5	Rt-6	Rt-7	Rt-8	Rt-9	Rt-10	Rt-11	Rt-12
Comment	Rut8 bright (rim)	Rut8 medium (rim)	Rut8 dark (core)	Rut2 dark (core)	Rut2 bright (rim)	Rut1 bright (core)	Rut1 grey mid	Rut1 dark (rim)	Rut14 dark (rim)	Rut14 bright (core)	Rut15 dark (rim)	Rut15 grey (core)
Major elements (wt%)												
SiO2	0.02	0.00	0.00	0.03	0.01	0.00	0.02	0.02	0.02	0.00	0.00	0.00
TiO2	96.1	98.6	98.6	98.0	97.7	89.9	97.6	98.0	98.8	97.6	94.0	91.7
Al2O3	0.11	0.10	0.07	0.00	0.01	0.13	0.06	0.00	0.00	0.05	0.00	0.04
FeO	0.69	0.25	0.18	0.05	0.20	1.05	0.30	0.27	0.24	0.54	0.32	0.55
MnO	0.00	0.01	0.00	0.04	0.01	0.00	0.02	0.00	0.01	0.00	0.00	0.00
MgO	0.01	0.01	0.00	0.01	0.00	0.00	0.00	0.00	0.00	0.02	0.00	0.00
CaO	0.00	0.00	0.00	0.00	0.00	0.02	0.01	0.01	0.00	0.02	0.00	0.00
Na2O	0.02	0.04	0.00	0.04	0.01	0.00	0.00	0.00	0.00	0.02	0.02	0.00
K2O	0.00	0.00	0.01	0.00	0.01	0.01	0.00	0.00	0.00	0.01	0.00	0.00
Cr2O3	0.04	0.05	0.07	0.60	0.40	0.37	0.20	0.22	0.18	0.20	1.44	1.56
V2O3	0.25	0.18	0.23	0.15	0.19	0.18	0.22	0.20	0.20	0.21	0.31	0.34
Nb2O5	0.24	0.16	0.08	0.40	0.46	5.32	0.76	0.56	0.15	0.50	2.37	3.62
Ta2O5	0.01	0.01	0.01	0.08	0.06	0.07	0.07	0.05	0.04	0.05	0.12	0.14
Sm2O3	0.00	0.00	0.00	0.00	0.00	0.00	0.00	0.06	0.05	0.00	0.00	0.00
Nd2O3	0.00	0.00	0.00	0.05	0.14	0.05	0.00	0.04	0.05	0.09	0.05	0.00
Total	103.83	105.87	105.60	105.16	105.06	102.91	105.43	105.68	105.86	105.51	103.19	102.19
Structural formula, oxygen equivalents p.f.u. = 2												
Si	0.0003	0.0000	0.0000	0.0004	0.0001	0.0000	0.0003	0.0003	0.0003	0.0000	0.0000	0.0000
Al	0.0018	0.0016	0.0011	0.0000	0.0002	0.0021	0.0010	0.0000	0.0000	0.0008	0.0000	0.0006
Ti	0.9891	0.9933	0.9942	0.9884	0.9884	0.9441	0.9867	0.9890	0.9927	0.9873	0.9635	0.9505
Fe	0.0079	0.0028	0.0020	0.0006	0.0023	0.0123	0.0034	0.0030	0.0027	0.0061	0.0036	0.0063
Mn	0.0000	0.0001	0.0000	0.0005	0.0001	0.0000	0.0002	0.0000	0.0001	0.0000	0.0000	0.0000
Mg	0.0002	0.0002	0.0000	0.0002	0.0000	0.0000	0.0000	0.0000	0.0000	0.0004	0.0000	0.0000
Ca	0.0000	0.0000	0.0000	0.0000	0.0000	0.0003	0.0001	0.0001	0.0000	0.0003	0.0000	0.0000
Na	0.0005	0.0010	0.0000	0.0010	0.0003	0.0000	0.0000	0.0000	0.0000	0.0005	0.0005	0.0000
K	0.0000	0.0000	0.0002	0.0000	0.0002	0.0002	0.0000	0.0000	0.0000	0.0002	0.0000	0.0000
Cr	0.0004	0.0005	0.0008	0.0063	0.0043	0.0041	0.0021	0.0024	0.0019	0.0021	0.0155	0.0170
V	0.0023	0.0016	0.0021	0.0013	0.0017	0.0016	0.0019	0.0018	0.0017	0.0018	0.0028	0.0031
Nb	0.0015	0.0010	0.0005	0.0024	0.0028	0.0336	0.0046	0.0034	0.0009	0.0030	0.0146	0.0226
Ta	0.0000	0.0000	0.0000	0.0003	0.0002	0.0003	0.0003	0.0002	0.0002	0.0002	0.0004	0.0005
Zr	0.0001	0.0001	0.0001	0.0003	0.0005	0.0003	0.0003	0.0003	0.0003	0.0003	0.0004	0.0004
Nd	0.0000	0.0000	0.0000	0.0002	0.0007	0.0002	0.0000	0.0002	0.0002	0.0004	0.0002	0.0000
Sm	0.0000	0.0000	0.0000	0.0000	0.0000	0.0000	0.0000	0.0003	0.0002	0.0000	0.0000	0.0000
Total	1.0041	1.0022	1.0010	1.0020	1.0016	0.9992	1.0009	1.0010	1.0013	1.0035	1.0017	1.0010
Trace elements (ppm)												
Li	bdl	bdl	bdl	1.8	bdl	bdl	bdl	3.3	bdl	bdl	bdl	bdl
Be	0.057	bdl	0.14	bdl	bdl	bdl	0.075	bdl	bdl	0.36	0.17	bdl
Si	bdl	bdl	bdl	bdl	bdl	bdl	bdl	3100	bdl	bdl	bdl	bdl
Ca	bdl	bdl	bdl	1400	bdl	bdl	bdl	900	bdl	bdl	bdl	bdl
Sc	172.4	157.7	177.4	89.2	171.2	61.4	72.8	71.2	142	118.8	105.5	114.3
V	2490	1757	2330	1512	1890	1784	2190	2020	1959	2070	3110	3409
Cr	403	515	722	5950	4020	3710	1970	2230	1790	1994	14400	15590
Mn	3.16	bdl	2.8	7.9	bdl	bdl	bdl	bdl	bdl	bdl	2.1	bdl
Co	bdl	bdl	bdl	bdl	bdl	bdl	bdl	bdl	bdl	bdl	bdl	bdl
Ni	bdl	bdl	bdl	bdl	bdl	bdl	bdl	bdl	bdl	bdl	bdl	bdl
Cu	25.1	25.7	25.3	26.2	27.3	23.6	25.8	23.1	25.6	26.4	23.3	25.7
Zn	25.8	27.8	27	26.5	26.5	24.2	26.6	25.7	25.8	28.8	24.2	25.9
Ga	3.65	1.78	3.28	1.18	1.91	2.39	1.98	1.49	1.66	1.64	1.78	3.37
Rb	0.21	bdl	0.67	bdl	bdl	bdl	bdl	0.21	bdl	bdl	bdl	0.26
Sr	0.264	0.303	0.54	0.23	0.8	0.27	0.341	0.37	0.268	0.75	0.293	0.293
Y	0.179	0.052	0.8	0.137	0.145	0.026	0.029	0.03	0.018	0.042	0.049	0.025
Zr	77.5	92.8	157	476	705	497	490	416	490	495.6	615	594
Nb	1367	935	1447	6000	4120	6540	5600	4440	3860	3860	22600	28420
Sn	75.3	60.5	83	131.1	132	127.8	129.7	135	131.6	116.8	111	107.6
Sb	bdl	0.154	0.13	0.31	0.13	0.098	bdl	0.15	0.131	bdl	0.123	0.156
Cs	0.035	bdl	0.076	0.067	bdl	bdl	0.053	bdl	bdl	bdl	bdl	0.083
Ba	bdl	bdl	0.063	bdl	bdl	bdl	bdl	0.028	bdl	bdl	bdl	0.058
La	0.118	0.056	1.06	0.55	0.112	0.0012	bdl	bdl	bdl	0.011	bdl	bdl
Ce	0.22	0.099	2.61	0.185	0.28	0.0077	bdl	1	bdl	0.011	bdl	0.0074
Pr	0.0132	bdl	0.194	0.018	0.028	bdl	bdl	bdl	bdl	bdl	bdl	bdl
Nd	0.049	0.016	0.7	0.11	bdl	bdl	bdl	0.046	bdl	bdl	bdl	bdl
Sm	bdl	bdl	0.139	bdl	bdl	bdl	bdl	bdl	0.038	bdl	bdl	bdl
Eu	0.0141	bdl	0.055	bdl	bdl	bdl	bdl	bdl	bdl	bdl	bdl	bdl
Gd	0.013	0.017	0.148	bdl	0.026	bdl	bdl	0.016	bdl	bdl	bdl	bdl
Tb	0.0006	bdl	0.019	bdl	0.008	0.0018	bdl	bdl	bdl	bdl	bdl	bdl
Dy	0.038	0.021	0.189	0.016	0.031	bdl	bdl	bdl	bdl	bdl	bdl	bdl
Ho	0.0131	0.0027	0.034	0.014	bdl	bdl	bdl	bdl	bdl	bdl	0.0027	bdl
Er	0.039	bdl	0.154	0.075	0.024	bdl	bdl	bdl	bdl	bdl	bdl	bdl
Tm	0.0049	bdl	0.016	0.004	0.007	bdl	bdl	bdl	bdl	bdl	bdl	bdl
Yb	0.066	0.042	0.172	bdl	0.08	bdl	bdl	bdl	bdl	bdl	bdl	bdl
Lu	0.0272	0.0076	0.036	0.008	0.008	bdl	0.0009	0.006	bdl	bdl	bdl	bdl
Hf	4.94	4.74	9.23	22.3	31.1	24.1	23.86	20.88	23	23.4	33.5	32
Ta	125.1	89.2	126.2	830	591	682	720	485	441	511	1199	1373
Pb	0.064	bdl	0.75	0.39	bdl	bdl	0.14	0.35	bdl	bdl	bdl	0.05
Bi	0.068	bdl	bdl	0.47	bdl	bdl	0.0083	0.059	bdl	bdl	bdl	bdl
Th	0.068	0.029	0.49	0.89	0.97	0.0025	bdl	0.011	0.0063	bdl	bdl	0.0041
U	46.6	22.3	44.1	23.9	26.63	14.31	10.4	8.99	12.6	15	27.2	25.58

Pyroxene

Sample	GBM46-13	GBM46-13b	GBM46-12	GBM46-12b	Cpx-26	Cpx-28	Cpx-29	Cpx-30	Cpx-31	Cpx-32	Cpx-33
Rock type	exoskarn Di+Ep+Ttn+Vs+Cal					endoskarn vein					
Comment	Cpx dark (core)	Cpx dark2 (core)	Cpx e bright (rim)	Cpx bright2 (rim)	Px27 bright	Px27 grey mid	Px27 bright (rim)	Px29 dark (core)	Px29 bright (rim)	Px34 dark (core)	Px34 bright (rim)
Major elements (wt%)											
SiO2	51.21	51.82	50.72	51.02	54.57	55.06	53.71	55.24	53.79	55.45	54.29
TiO2	0.00	0.00	0.03	0.06	0.03	0.00	0.00	0.09	0.00	0.05	0.00
Al2O3	0.15	0.13	0.36	0.28	0.20	0.18	0.22	0.05	0.25	0.26	0.39
FeO	19.86	18.93	23.29	22.86	5.82	2.98	8.18	2.28	8.54	2.29	8.53
MnO	0.49	0.48	0.55	0.56	0.16	0.07	0.22	0.04	0.24	0.06	0.15
MgO	5.59	6.01	3.58	3.18	14.49	16.34	13.14	16.87	12.49	16.67	12.73
CaO	23.63	22.93	23.24	23.11	25.26	25.16	24.97	25.51	24.61	25.66	24.57
Na2O	0.12	0.12	0.09	0.10	0.03	0.00	0.11	0.00	0.11	0.00	0.13
K2O	0.00	0.00	0.00	0.00	0.00	0.01	0.00	0.00	0.00	0.00	0.01
V2O3	0.03	0.04	0.00	0.00	0.00	0.03	0.01	0.00	0.02	0.01	0.00
Ce2O3	0.16	0.18	0.00	0.00	0.04	0.13	0.01	0.00	0.11	0.13	0.00
La2O3	0.00	0.00	0.03	0.06	0.15	0.00	0.04	0.06	0.00	0.00	0.00
Total	101.23	100.64	101.90	101.23	100.74	100.00	100.68	100.17	100.26	100.60	100.80
Structural formula, oxygen equivalents p.f.u. = 6											
Si	2.00	2.02	2.00	2.02	2.00	2.01	2.00	2.01	2.01	2.01	2.01
Ti	0.00	0.00	0.00	0.00	0.00	0.00	0.00	0.00	0.00	0.00	0.00
Al	0.01	0.01	0.02	0.01	0.01	0.01	0.01	0.00	0.01	0.01	0.02
Fe^{2+}	0.65	0.62	0.77	0.76	0.18	0.09	0.25	0.07	0.27	0.07	0.26
Mn	0.02	0.02	0.02	0.02	0.00	0.00	0.01	0.00	0.01	0.00	0.00
Mg	0.33	0.35	0.21	0.19	0.79	0.89	0.73	0.91	0.70	0.90	0.70
Ca	0.99	0.96	0.98	0.98	0.99	0.98	0.99	0.99	0.99	1.00	0.98
Na	0.01	0.01	0.01	0.01	0.00	0.00	0.01	0.00	0.01	0.00	0.01
K	0.0000	0.0000	0.0000	0.0000	0.0000	0.0000	0.0000	0.0000	0.0000	0.0000	0.0000
V	0.0009	0.0013	0.0000	0.0000	0.0000	0.0009	0.0003	0.0000	0.0006	0.0003	0.0000
Ce	0.0000	0.0000	0.0000	0.0000	0.0000	0.0000	0.0000	0.0000	0.0000	0.0000	0.0000
La	0.0000	0.0000	0.0004	0.0009	0.0020	0.0000	0.0005	0.0008	0.0000	0.0000	0.0000
Totale	4.00	3.98	4.00	3.98	3.99	3.99	4.00	3.99	3.99	3.99	3.98
Trace elements (ppm)											
Li	71.7	89.7	55.3	56.4	50.4	34.0	106.4	9.8	49.7	16.5	87.0
Be	2.7	3.3	1.9	1.5	2.0	18.6	4.3	16.6	6.5	19.8	4.2
Sc	5.6	5.6	5.5	5.5	5.3	5.4	5.4	5.8	5.0	6.1	5.2
Ti	41	42	104	105	111	212	90	133	72	203	115
V	24.8	26.8	16.4	16.7	11.3	15.7	17.6	10.4	7.4	13.6	18.3
Cr	7.9	7.7	6.8	9.3	1.6	1.4	2.6	3.1	1.6	3.7	3.4
Mn	5215	5113	4831	4740	1041	612	1532	468	1291	584	1710
Co	12.9	12.1	20.4	20.7	5.9	2.3	10.8	1.9	6.3	2.3	4.4
Ni	5.6	5.3	3.3	5.7	3.5	1.7	24.1	0.4	11.8	0.7	7.5
Cu	bdl	0.2	bdl	bdl	0.2	0.4	0.3	0.3	0.7	0.2	0.2
Zn	411	397	421	410	108	44	116	35	99	45	91
Ga	6.1	5.7	7.1	6.2	2.8	4.7	4.2	2.7	4.0	4.1	5.1
Rb	0.4	bdl	bdl	bdl	0.9	1.0	1.8	0.1	5.0	0.5	1.4
Sr	20.0	20.3	25.4	22.3	13.4	12.1	15.1	11.3	23.2	11.9	13.6
Y	0.7	0.5	0.8	0.8	1.2	9.0	1.6	6.1	1.8	6.6	1.5
Zr	2.2	2.4	8.4	5.9	2.8	11.0	4.1	3.4	2.5	9.5	2.5
Nb	bdl	bdl	0.0	0.0	0.0	0.3	0.0	0.0	0.0	0.2	0.0
Sn	4.2	5.4	8.7	6.2	4.2	7.8	6.3	2.1	5.4	5.9	5.5
Sb	0.1	0.1	0.1	0.0	0.1	0.2	0.4	0.0	0.3	0.1	0.2
Cs	0.5	0.0	bdl	bdl	1.1	1.4	3.9	0.1	2.0	0.3	2.4
Ba	0.1	0.0	0.0	0.0	0.4	0.8	1.6	0.0	2.5	0.2	1.1
La	0.5	0.3	1.3	1.3	1.2	2.7	1.0	1.8	1.3	2.8	1.0
Ce	1.5	1.0	2.6	2.5	2.8	8.4	2.5	5.9	3.4	8.5	2.6
Pr	0.2	0.2	0.3	0.3	0.4	1.3	0.3	0.9	0.5	1.3	0.4
Nd	1.0	0.6	1.1	1.2	1.6	6.3	1.7	4.5	2.2	6.2	1.9
Sm	0.2	0.1	0.2	0.3	0.4	2.1	0.5	1.5	0.6	1.9	0.6
Eu	0.0	0.0	0.0	0.0	0.0	0.1	0.0	0.1	0.0	0.1	0.1
Gd	0.1	0.1	0.1	0.2	0.4	2.0	0.4	1.4	0.5	1.7	0.5
Tb	0.0	0.0	0.0	0.0	0.1	0.3	0.1	0.2	0.1	0.3	0.1
Dy	0.2	0.1	0.1	0.1	0.2	1.7	0.3	1.3	0.4	1.4	0.4
Ho	0.0	0.0	0.0	0.0	0.0	0.3	0.1	0.2	0.1	0.2	0.1
Er	0.1	0.1	0.1	0.1	0.1	0.8	0.2	0.6	0.2	0.6	0.2
Tm	0.0	0.0	0.0	0.0	0.0	0.1	0.0	0.1	0.0	0.1	0.0
Yb	0.6	0.5	0.4	0.5	0.1	0.8	0.3	0.5	0.2	0.5	0.3
Lu	0.2	0.1	0.1	0.1	0.0	0.1	0.1	0.1	0.0	0.1	0.1
Hf	0.2	0.2	0.4	0.3	0.2	0.3	0.3	0.1	0.1	0.4	0.2
Ta	bdl	0.0	0.0	bdl	0.0	0.3	0.0	0.0	0.0	0.3	0.0
Pb	0.3	0.1	0.2	0.2	0.5	0.8	0.4	0.1	2.2	0.4	0.5
Bi	0.0	0.0	0.0	0.0	0.1	0.0	0.0	0.0	0.3	0.1	0.1
Th	0.0	0.0	0.0	0.0	0.0	0.1	0.1	0.0	0.1	0.1	0.1
U	0.0	0.0	0.0	0.0	0.0	0.1	0.1	0.0	0.1	0.0	0.1

EMP and LA-ICP-MS analysis for pyroxene

Sample	GBM46-9	GBM46-10	GBM46-10b	GBM46-11	GBM46-11b	STAB1-1	STAB1-2	STAB1-3	STAB1-2	STAB1-3	STAB1-3	STAB1-4	STAB1-4	STAB1-4	GBM45-1	GBM45-2	GBM45-3	GBM45-4	GBM45-5	GBM45-6	GBM45-7	GBM45-8	GBM45-9	GBM45-10
Rock type	exoskarn Di+Ep+Ttn+Vs+Cal					Di+Qtz+Cal±Ep±Vs±Grt exoskarn									Vs exoskarn									
Comment	Vs 7b dark core	Vs 7b bright core	Vs 7b bright core 2	Vs 7b dark rim	Vs 7b dark rim	Vs1.1 homogeneous	Vs1.1 homogeneous2	Vs1.1 homogeneous3	Vs1.2 homogeneous	Vs1.2 homogeneous2	Vs1.3 homogeneous	Vs1.3 homogeneous2	Vs1.4 homogeneous	Vs1.4 homogeneous2	Vs 2.1 (rim) dark	Vs 2.1 bright	Vs 2.1 mid	Vs 2.1 dark	Vs 2.1 bright	Vs 2.2 (core) dark	Vs 2.2 mid	Vs 2.2 (rim) bright	Vs 3 - (rim) bright	Vs 3 - (core) dark
Major elements (wt%)																								
SiO2	36.61	36.18	36.42	36.03	36.03	37.00	37.00	37.00	36.87	36.87	37.19	37.19	37.15	37.15	36.84	36.22	35.84	36.39	36.27	36.58	37.07	37.28	36.77	36.68
TiO2	1.52	1.52	1.49	2.06	2.06	0.29	0.29	0.29	1.85	1.85	0.17	0.17	0.16	0.16	1.58	1.64	1.44	0.51	1.12	0.63	0.95	0.13	1.17	0.62
Al2O3	16.06	15.06	15.17	14.94	14.94	16.86	16.86	16.86	15.08	15.08	16.67	16.67	16.78	16.78	15.63	15.13	14.94	15.94	15.36	15.37	15.36	15.72	15.44	15.41
FeO	5.68	6.80	6.34	6.22	6.22	5.34	5.34	5.34	6.82	6.82	5.44	5.44	5.05	5.05	6.07	7.04	6.73	6.46	6.67	6.24	6.43	6.32	6.63	6.39
MnO	0.55	0.55	0.43	0.11	0.11	0.07	0.07	0.07	0.09	0.09	0.14	0.14	0.12	0.12	0.07	0.10	0.19	0.14	0.18	0.10	0.15	0.16	0.21	0.17
MgO	1.00	1.01	0.99	0.91	0.91	1.33	1.33	1.33	1.03	1.03	1.27	1.27	1.43	1.43	1.07	0.72	1.11	1.24	1.05	2.03	1.67	1.99	1.34	1.72
CaO	34.27	33.62	33.75	33.80	33.80	35.31	35.31	35.31	34.22	34.22	35.50	35.50	35.64	35.64	34.74	32.40	33.01	34.69	34.44	34.16	34.16	34.59	34.72	34.67
Na2O	0.03	0.04	0.04	0.06	0.06	0.03	0.03	0.03	0.06	0.06	0.00	0.00	0.02	0.02	0.08	0.09	0.06	0.07	0.02	0.00	0.07	0.02	0.03	0.02
La2O3	0.30	0.57	0.57	0.47	0.47	0.06	0.06	0.06	0.60	0.60	0.10	0.10	0.09	0.09	0.36	0.59	0.59	0.50	0.55	0.28	0.41	0.30	0.26	0.17
Ce2O3	0.61	1.01	1.01	0.86	0.86	0.16	0.16	0.16	0.79	0.79	0.18	0.18	0.16	0.16	0.54	1.52	1.43	0.46	0.58	0.52	0.59	0.21	0.24	0.24
Sm2O3	0.00	0.12	0.12	0.02	0.02	0.00	0.00	0.00	0.05	0.05	0.00	0.00	0.08	0.08	0.00	0.14	0.00	0.04	0.06	0.00	0.00	0.00	0.10	0.01
Nd2O3	0.15	0.32	0.32	0.28	0.28	0.17	0.17	0.17	0.10	0.10	0.00	0.00	0.00	0.00	0.04	0.68	0.36	0.00	0.00	0.10	0.13	0.04	0.00	0.02
F	0.88	0.68	0.72	0.84	0.84	0.88	0.88	0.88	0.73	0.73	0.80	0.80	0.85	0.85	0.81	0.73	0.73	0.72	0.74	0.75	0.77	0.73	0.71	0.74
Total	97.19	97.06	97.37	96.60	96.60	97.53	97.53	97.53	98.30	98.30	97.47	97.47	97.54	97.54	97.93	97.00	96.43	97.16	97.04	96.76	97.77	97.50	97.63	96.88
Structural formula, oxygen equivalents p.f.u. = 50																								
Si	17.93	18.05	18.11	17.95	17.93	17.99	17.98	17.99	18.09	18.09	18.06	18.06	18.04	18.04	18.02	18.16	18.13	17.97	18.04	18.11	18.21	18.24	18.04	18.08
Ti	0.56	0.57	0.56	0.77	0.77	0.11	0.11	0.11	0.68	0.68	0.06	0.06	0.06	0.06	0.58	0.62	0.55	0.19	0.42	0.23	0.35	0.05	0.43	0.23
Al	9.27	8.86	8.89	8.77	8.76	9.66	9.66	9.66	8.72	8.72	9.54	9.54	9.61	9.60	9.01	8.94	8.91	9.28	9.00	8.97	8.89	9.07	8.93	8.95
Fe^{3+}	2.33	2.84	2.64	2.59	2.59	2.17	2.17	2.17	2.80	2.80	2.21	2.21	2.05	2.05	2.48	2.95	2.85	2.67	2.77	2.58	2.64	2.59	2.72	2.63
Mn	0.04	0.05	0.04	0.05	0.05	0.04	0.04	0.04	0.04	0.05	0.05	0.04	0.04	0.05	0.04	0.05	0.05	0.05	0.05	0.04	0.04	0.04	0.04	0.05
Mg	0.73	0.75	0.73	0.68	0.68	0.96	0.96	0.96	0.75	0.75	0.92	0.92	1.04	1.04	0.78	0.54	0.84	0.91	0.78	1.50	1.22	1.45	0.98	1.26
Ca	17.98	17.97	17.98	18.04	18.02	18.39	18.39	18.39	17.99	17.99	18.47	18.47	18.55	18.55	18.20	17.41	17.89	18.36	18.35	18.12	17.97	18.14	18.25	18.31
Na	0.03	0.04	0.04	0.06	0.06	0.03	0.03	0.03	0.06	0.06	0.00	0.00	0.02	0.02	0.08	0.09	0.06	0.07	0.02	0.00	0.07	0.02	0.03	0.02
La	0.08	0.09	0.06	0.10	0.10	0.03	0.03	0.02	0.10	0.09	0.09	0.09	0.01	0.02	0.04	0.11	0.02	0.08	0.01	0.01	0.02	0.01	0.04	0.03
Ce	0.00	0.00	0.00	0.00	0.00	0.00	0.00	0.00	0.00	0.00	0.00	0.00	0.00	0.00	0.00	0.00	0.00	0.00	0.00	0.00	0.00	0.00	0.00	0.00
Sm	0.01	0.01	0.01	0.01	0.01	0.00	0.00	0.00	0.00	0.00	0.00	0.00	0.00	0.00	0.00	0.01	0.00	0.00	0.00	0.00	0.00	0.00	0.00	0.00
Nd	0.00	0.00	0.00	0.00	0.00	0.00	0.00	0.00	0.00	0.00	0.00	0.00	0.00	0.00	0.00	0.00	0.00	0.00	0.00	0.00	0.00	0.00	0.00	0.00
Yb	0.05	0.05	0.04	0.06	0.07	0.00	0.00	0.00	0.02	0.01	0.01	0.01	0.00	0.00	0.00	0.07	0.00	0.01	0.00	0.00	0.00	0.00	0.01	0.01
Th	0.00	0.00	0.03	0.00	0.00	0.00	0.00	0.00	0.00	0.00	0.00	0.00	0.00	0.00	0.00	0.00	0.00	0.00	0.00	0.00	0.00	0.00	0.00	0.01
U	0.03	0.02	0.02	0.03	0.04	0.00	0.00	0.00	0.00	0.00	0.00	0.00	0.00	0.00	0.00	0.05	0.00	0.00	0.00	0.00	0.00	0.00	0.00	0.01
F	1.36	1.07	1.13	1.32	1.32	1.35	1.35	1.35	1.13	1.13	1.23	1.23	1.31	1.31	1.25	1.16	1.17	1.12	1.16	1.17	1.20	1.13	1.10	1.15
Totale	49.07	49.31	49.20	49.13	49.12	49.39	49.39	49.39	49.26	49.26	49.43	49.43	49.43	49.44	49.28	49.03	49.30	49.61	49.46	49.57	49.42	49.61	49.49	49.60
Trace elements (ppm)																								
Li	214.9	179.4	272.2	193.7	184.0	110.3	112.4	113.5	156.6	152.3	207.3	168.0	106.8	107.6	193.8	206.4	170.6	148.6	116.5	147.3	151.7	141.1	161.9	142.5
Be	180.1	179.7	147.2	172.6	187.8	82.8	95.1	81.7	57.2	59.4	57.1	53.6	42.7	77.9	114.0	275.1	162.4	198.7	166.1	57.2	87.4	80.3	212.5	299.0
Sc	3.7	3.5	3.3	3.6	3.5	7.0	7.2	6.8	5.6	5.0	4.9	4.8	7.0	6.3	4.6	4.7	3.7	4.0	4.0	3.9	3.9	4.2	4.4	4.0
V	88.6	82.4	95.0	83.5	72.1	11.9	13.5	11.6	140.2	133.0	174.8	172.5	5.9	8.0	97.7	73.1	14.1	53.9	31.2	15.5	13.7	19.6	62.5	37.4
Cr	21.9	24.0	35.0	29.3	33.0	36.3	36.0	29.4	17.6	15.4	20.2	25.5	1.1	3.1	bdl	2.1	3.5	2.3	2.5	bdl	bdl	bdl	12.8	15.9
Mn	1036.0	1072.0	998.0	1106.0	1096.0	1033.0	1061.0	1080.0	1066.0	1128.0	1135.0	1077.0	1031.0	1149.0	1001.0	1144.0	1092.0	1220.0	1195.0	1020.0	1050.0	1060.0	1011.0	1134.0
Co	5.1	4.8	5.1	5.1	5.1	2.7	2.8	2.6	4.3	4.3	4.5	4.4	2.6	2.9	3.1	5.4	3.3	3.6	2.7	2.9	3.0	3.1	3.9	1.8
Ni	3.8	0.4	10.9	0.6	0.5	0.8	0.7	0.9	0.8	0.8	0.7	0.5	0.7	0.8	0.6	6.7	1.0	1.7	2.2	1.1	1.2	1.5	2.1	1.3
Cu	0.7	0.5	0.5	0.5	0.6	bdl	bdl	bdl	0.6	0.5	0.6	0.6	bdl	bdl	bdl	0.3	bdl	0.4	bdl	bdl	bdl	0.4	0.3	0.4
Zn	136.9	130.9	135.0	142.1	137.3	96.8	96.5	98.3	118.0	116.7	114.0	111.7	96.1	99.6	115.9	117.3	109.2	103.9	115.6	117.2	110.6	111.9	104.4	107.9
Ga	93.4	93.5	84.5	99.3	103.3	48.9	49.2	50.0	77.2	74.7	76.3	75.7	43.0	45.0	70.4	115.4	48.8	77.5	54.6	46.5	48.6	46.5	66.3	64.7
Rb	0.1	0.1	bdl	2.3	0.1	bdl	bdl	bdl	0.1	0.2	0.1	0.3	bdl	bdl	bdl	0.1	bdl	7.6	0.4	1.7	2.3	bdl	0.8	bdl
Sr	50.6	51.5	44.5	55.6	52.2	57.1	59.6	55.5	53.3	49.2	57.7	58.5	60.8	59.9	55.8	49.1	55.2	54.1	70.6	58.0	55.8	57.5	58.0	55.4
Y	864.0	679.0	587.0	769.0	1145.0	29.6	31.9	26.6	170.4	164.1	129.6	121.3	4.6	11.4	57.7	1474.0	58.8	154.9	13.2	9.1	9.8	8.0	186.0	119.0
Zr	22.2	30.0	13.1	28.5	23.7	408.8	331.0	344.1	119.5	57.0	38.7	36.2	201.9	48.0	23.9	38.0	24.8	35.2	32.4	130.9	110.3	87.2	42.4	152.0
Nb	1.3	1.6	0.7	2.1	1.6	10.8	9.4	9.4	3.6	3.1	3.0	2.7	2.3	3.3	3.6	1.9	1.3	3.6	2.9	5.6	4.4	8.0	9.1	9.1
Sn	59.2	63.8	42.4	71.0	66.0	44.6	43.7	45.3	79.3	70.9	66.1	66.8	41.7	43.7	37.4	42.3	37.2	35.6	49.9	43.4	43.0	41.5	40.8	30.4
Sb	62.2	63.7	69.0	70.7	65.0	49.5	49.9	49.4	61.4	56.7	65.0	67.7	42.7	49.2	59.8	60.5	58.0	76.8	54.6	45.7	46.9	48.4	59.1	56.9
Cs	bdl	bdl	bdl	2.1	bdl	bdl	bdl	bdl	bdl	bdl	0.1	0.1	0.1	bdl	bdl	0.0	0.0	bdl	0.9	0.2	1.3	2.6	0.0	0.5	bdl
Ba	0.2	0.0	0.0	0.2	bdl	bdl	bdl	bdl	0.0	0.0	0.1	0.2	0.2	bdl	bdl	0.0	0.0	bdl	0.5	0.3	0.5	0.6	0.0	0.6	bdl
La	4504.0	4985.0	3268.0	5480.0	5250.0	1435.0	1588.0	1364.0	5400.0	5160.0	4970.0	4915.0	798.0	1075.0	2143.0	5720.0	1038.0	4480.0	728.0	503.0	882.0	564.0	2098.0	1630.0
Ce	8560.0	9020.0	6120.0	9830.0	10340.0	1590.0	1777.0	1523.0	6340.0	6180.0	5490.0	5454.0	677.0	1151.0	1916.0	12310.0	1308.0	5890.0	766.0	289.8	651.0	333.0	2761.0	1690.0
Pr	895.0	914.0	625.0	995.0	1128.0	94.1	105.9	91.5	393.0	395.5	337.9	330.3	33.7	65.2	108.9	1296.0	99.0	384.0	49.4	13.1	28.5	14.8	218.2	138.0
Nd	3561.0	3405.0	2435.0	3780.0	4630.0	205.5	231.1	197.1	1003.0	966.0	817.0	788.0	58.7	130.7	245.0	4770.0	301.1	851.0	134.7	26.4	46.8	29.5	683.0	549.0
Sm	607.0	516.0	443.0	577.0	803.0	18.4	20.8	17.4	102.5	101.2	78.7	74.3	3.9	9.7	24.8	754.0	46.5	93.4	16.2	3.8	4.4	4.0	105.0	111.0
Eu	60.0	62.2	44.0	66.2	68.1	9.2	9.8	9.3	53.0	49.2	29.3	29.7	5.2	8.1	29.3	95.5	10.8	57.1	10.4	7.0	10.7	9.1	13.9	21.5
Gd	409.6	321.0	306.0	364.9	548.0	10.6	11.9	9.7	64.5	63.4	48.8	46.7	2.5	5.4	15.8	495.0	30.2	56.7	8.2	2.6	3.5	2.8	67.6	73.1
Tb	45.3	34.6	33.8	39.9	61.1	1.1	1.2	1.0	6.6	6.7	5.2	4.8	0.2	0.4	1.8	61.3	3.3	6.2	0.7	0.3	0.4	0.3	8.1	7.6
Dy	212.7	163.4	157.0	187.5	287.7	5.4	5.9	4.7	32.6	33.4	25.6	23.6	0.8	2.1	9.9	317.6	14.8	31.4	3.1	1.7	2.0	1.6	41.4	33.4
Ho	33.2	25.1	24.2	29.1	45.0	0.9	1.0	0.8	5.8	5.9	4.5	4.3	0.1	0.3	1.8	53.9	2.1	5.2	0.5	0.3	0.3	0.3	6.9	4.8
Er	75.7	58.7	55.2	67.3	103.9	2.5	2.7	2.2	18.2	17.7	14.8	13.7	0.4	1.0	5.7	140.0	4.8	13.7	1.3	0.9	0.9	0.7	18.6	11.0
Tm	8.2	6.6	6.0	7.5	11.3	0.4	0.4	0.3	3.5	3.1	2.8	2.7	0.1	0.1	0.9	16.8	0.5	2.0	0.2	0.1	0.1	0.1	2.5	1.3
Yb	43.1	36.8	31.6	40.4	56.9	2.7	3.0	2.4	35.4	28.4	29.1	27.2	0.5	1.1	8.0	88.8	2.8	13.8	1.6	1.0	1.0	0.9	17.1	7.8
Lu	3.8	3.5	3.0	3.6	4.7	0.4	0.4	0.3	6.0	4.6	5.2	4.7	0.1	0.2	1.1	7.4	0.3	1.7	0.2	0.2	0.1	0.1	2.2	1.0
Hf	0.9	1.0	0.5	1.0	0.9	5.3	4.4	4.3	2.7	1.7	1.4	1.3	3.2	1.0	1.3	1.5	0.5	0.9	0.9	2.6	1.9	1.9	1.7	2.8
Ta	0.1	0.1	0.0	0.2	0.1	1.4	1.3	1.2	0.6	0.5	0.4	0.4	0.2	0.2	1.2	0.4	0.3	0.5	0.8	3.3	2.7	6.3	2.2	3.7
Pb	1.3	1.1	2.1	2.0	1.3	0.6	0.7	0.7	1.0	1.0	1.2	1.3	0.7	0.7	0.7	1.0	0.9	1.1	1.4	1.4	1.6	0.8	1.4	1.3
Bi	41.0	42.2	49.3	46.5	43.0	29.3	30.6	30.7	62.6	64.5	77.6	81.2	27.0	28.7	47.6	44.2	37.5	61.9	31.8	28.5	29.9	29.3	48.6	23.4
Th	252.0	8.7	2521.0	94.0	272.9	2.7	3.6	1.9	47.9	45.4	18.4	16.0	0.0	0.1	0.6	12.8	34.6	39.2	2.2	0.2	0.0	0.4	148.9	570.0
U	2588.0	1980.0	2016.0	2442.0	3875.0	17.9	19.8	16.6	203.3	181.5	111.2	112.4	3.5	7.8	45.3	4119.0	155.9	358.0	59.3	3.4	1.5	2.6	190.0	583.0
ΣREE	19018.6	19551.9	13551.8	21468.5	23337.7	3376.0	3759.0	3223.8	13464.0	13015.0	11859.0	11719.0	1581.1	2450.4	4512.1	26126.3	2862.2	11886.0	1720.5	850.2	1631.7	961.3	6043.5	4279.5

EMP and LA-ICP-MS analysis for vesuvianite

Sample	GBM47_1	GBM47_2	GBM47_3	GBM47_4	GBM47_5	GBM47_6	GBM47_7	GBM47_8	GBM46-9	GBM46-10	GBM46-11	GBM45_1	GBM45_1	GBM45_2	GBM45_3	GBM45_4	GBM45_1	GBM45_2	GBM45_3	GBM45_4	GBM45_5	GBM45_6	GBM45_7	GBM45_8	GBM45_9
Rock type	Vs+Grt exoskarn											Vs exoskarn													
Major elements (wt%)																									
SiO2	39.41	38.16	38.70	40.12	39.09	38.99	37.48	38.83	36.60	36.20	36.00	36.50	36.65	36.96	39.78	36.84	36.22	35.84	36.39	36.27	36.58	37.07	37.28	36.77	36.68
TiO2	0.00	0.37	0.00	0.00	0.00	0.00	0.00	0.00	1.52	1.52	2.06	0.00	0.47	0.00	0.00	1.58	1.64	1.44	0.51	1.12	0.63	0.95	0.13	1.17	0.62
Al2O3	20.39	19.57	20.61	22.89	20.42	20.69	21.94	20.22	16.10	15.10	14.90	1.03	7.01	0.00	2.14	15.63	15.13	14.94	15.94	15.36	15.37	15.36	15.72	15.44	15.41
FeO	4.42	2.53	3.37	7.52	3.35	4.97	1.19	3.84	0.00	0.00	0.00	0.00	0.00	0.00	6.95	0.00	1.89	0.00	0.00	0.00	0.00	0.00	0.00	0.00	0.00
MnO	0.00	0.62	0.00	0.47	0.00	0.00	0.00	0.84	0.07	0.14	0.11	0.00	0.00	0.00	0.00	0.07	0.10	0.19	0.14	0.18	0.10	0.15	0.16	0.21	0.17
MgO	0.00	0.00	0.00	0.00	0.00	0.00	0.00	0.00	1.00	1.01	0.91	0.00	0.00	0.00	0.00	1.07	0.72	1.11	1.24	1.05	2.03	1.67	1.99	1.34	1.72
CaO	33.33	33.41	33.49	31.20	33.87	32.51	34.05	32.58	34.30	33.60	33.80	34.14	34.96	34.81	31.70	34.74	32.40	33.01	34.69	34.44	34.16	34.16	34.59	34.72	34.67
Total	100.28	100.58	100.43	99.75	100.35	100.30	100.61	100.41	95.90	95.13	94.69	103.16	102.40	103.19	102.16	96.80	93.82	94.04	96.41	96.03	96.16	96.71	97.26	97.25	96.37
Structural formula, oxygen equivalents p.f.u. = 24																									
Si	3.01	2.92	2.95	3.05	2.98	2.98	2.85	2.97	2.93	2.94	2.94	2.98	2.93	3.02	3.24	2.94	2.99	2.95	2.91	2.92	2.92	2.95	2.94	2.92	2.92
Ti	0.00	0.02	0.00	0.00	0.00	0.00	0.00	0.00	0.09	0.09	0.13	0.00	0.03	0.00	0.00	0.09	0.10	0.09	0.03	0.07	0.04	0.06	0.01	0.07	0.04
Al	1.83	1.77	1.85	2.05	1.83	1.86	1.96	1.82	1.52	1.45	1.43	0.10	0.66	0.00	0.21	1.47	1.47	1.45	1.50	1.46	1.45	1.44	1.46	1.44	1.45
Fe3+	0.16	0.34	0.24	-0.14	0.21	0.18	0.34	0.24	0.43	0.48	0.43	1.94	1.43	1.96	1.32	0.47	0.35	0.48	0.62	0.57	0.63	0.54	0.64	0.58	0.64
Fe2+	0.28	0.16	0.21	0.48	0.21	0.32	0.08	0.25	0.00	0.00	0.00	0.00	0.00	0.00	0.47	0.01	0.13	0.01	0.00	0.00	0.00	0.00	0.00	0.00	0.00
Mn	0.00	0.04	0.00	0.03	0.00	0.00	0.00	0.05	0.00	0.01	0.01	0.00	0.00	0.00	0.00	0.01	0.01	0.01	0.01	0.01	0.01	0.01	0.01	0.01	0.01
Mg	0.00	0.00	0.00	0.00	0.00	0.00	0.00	0.00	0.12	0.12	0.11	0.00	0.00	0.00	0.00	0.13	0.09	0.14	0.15	0.13	0.24	0.20	0.23	0.16	0.20
Ca	2.72	2.74	2.74	2.54	2.77	2.66	2.77	2.67	2.95	2.93	2.96	2.99	2.99	3.05	2.76	2.97	2.86	2.91	2.97	2.97	2.93	2.91	2.93	2.95	2.96
Total	8.0	8.0	8.0	8.0	8.0	8.0	8.0	8.0	8.0	8.0	8.0	8.0	8.0	8.0	8.0	8.0	8.0	8.0	8.0	8.0	8.0	8.0	8.0	8.0	8.2
Almandine	9.4	5.5	7.3	11.7	7.2	10.7	2.7	8.3	0.0	0.0	0.0	0.0	0.0	0.0	14.6	0.0	4.2	0.0	0.0	0.0	0.0	0.0	0.0	0.0	0.0
Spessartine	0.0	1.4	0.0	1.0	0.0	0.0	0.0	1.8	0.2	0.3	0.2	0.0	0.0	0.0	0.0	0.2	0.2	0.4	0.3	0.4	0.2	0.3	0.4	0.5	0.4
Pyrope	0.0	0.0	0.0	0.0	0.0	0.0	0.0	0.0	3.9	4.0	3.6	0.0	0.0	0.0	0.0	4.2	2.9	4.5	5.0	4.2	8.2	6.6	7.9	5.3	6.4
Grossular	83.5	78.0	81.9	89.4	83.4	81.4	83.0	79.6	75.0	71.7	73.8	4.9	31.9	0.0	11.5	74.0	74.7	71.8	71.5	71.5	68.8	70.4	69.1	70.6	64.6
Andradite	7.1	15.1	10.8	0.0	9.5	7.9	14.4	10.3	21.0	24.0	22.3	95.3	69.3	100.9	73.9	23.8	18.0	24.0	29.5	28.0	29.9	26.5	30.1	28.2	28.6
Uvarovite	0.0	0.0	0.0	0.0	0.0	0.0	0.0	0.0	0.0	0.0	0.0	0.0	0.0	0.0	0.0	0.0	0.0	0.0	0.0	0.0	0.0	0.0	0.0	0.0	0.0

EMP and LA-ICP-MS analysis for garnet

EMP and LA-ICP-MS analysis for epidote

Rock-type	Exoskarn diopsdie+titanite+quartz+calcite±epidote (GBM46)							Pyroxene exoskarn (STAB1)									Phlogopite-titanite granite (STAB1)			
Sample	**Ep1 dark (core)**	**Ep4 scuro**	**Ep4 scuro2**	**Ep4 rim chiaro**	**Ep4 dark (mid)**	**Ep2 dark**	**Ep2 brigtht**	**All3.5 dark core**	**All3.5 bright (rim)**	**All3.5 mid**	**All3.1 bright (core)**	**All3.1 dark (rim)**	**All3.1 mid**	**All3.2 bright (rim)**	**All3.2 dark (core)**	**All3.2 mid**	**All4.2 bright (rim)**	**All4.2 dark (core)**	**All4.4 dark (core-rim)**	**All4.4 bright (rim)**
Major elements (wt%)																				
SiO2	36.59	38.00	38.00	37.49	36.98	34.42	33.88	33.96	33.57	33.51	33.32	34.32	33.20	33.51	34.37	33.75	33.68	34.76	34.69	33.72
TiO2	0.01	0.00	0.00	0.29	0.05	0.23	0.37	0.28	0.21	0.36	0.21	0.16	0.34	0.27	0.26	0.46	0.19	0.30	0.23	0.28
Al2O3	19.57	19.63	19.63	19.59	18.22	20.31	18.45	20.73	18.36	19.98	18.36	20.15	17.88	18.43	21.09	19.20	18.73	21.32	21.45	18.19
FeO	15.45	16.33	16.33	16.36	16.55	11.48	12.70	8.24	8.86	8.88	8.74	8.01	9.29	9.07	8.01	8.59	8.44	7.77	7.48	8.85
MnO	0.29	0.10	0.10	0.08	0.04	0.10	0.08	0.10	0.07	0.12	0.10	0.09	0.17	0.14	0.09	0.10	0.13	0.12	0.07	0.13
MgO	0.00	0.00	0.00	0.00	0.02	0.12	0.23	1.21	2.11	1.25	2.16	1.87	2.15	2.36	1.28	1.76	2.49	1.25	1.15	2.56
CaO	19.50	22.70	22.70	21.30	22.60	14.00	12.40	13.20	11.10	12.60	11.60	12.20	11.00	11.30	13.20	12.30	11.30	13.40	13.60	11.50
La2O3	4.05	0.25	0.25	2.25	0.29	7.24	6.96	7.95	10.62	8.34	10.16	9.35	10.43	10.05	8.47	8.56	9.63	7.84	7.94	10.50
Ce2O3	2.04	0.17	0.17	1.28	0.24	9.35	11.08	10.37	12.07	11.42	11.85	11.71	12.23	12.24	10.70	11.59	12.29	10.38	10.09	12.33
Pr2O3	0.12	0.08	0.09	0.01	0.09	0.00	0.46	0.67	0.60	0.60	0.66	0.61	0.59	0.79	0.63	0.68	0.68	0.67	0.67	0.62
Sm2O3	0.00	0.00	0.00	0.06	0.08	0.10	0.17	0.05	0.05	0.03	0.03	0.00	0.07	0.22	0.10	0.17	0.04	0.11	0.00	0.05
Nd2O3	0.06	0.00	0.00	0.13	0.18	1.80	2.48	1.73	1.79	1.88	1.53	1.39	1.40	1.66	1.44	1.78	1.60	1.73	1.33	1.50
F	0.03	0.00	0.00	0.00	0.05	0.07	0.14	0.13	0.35	0.19	0.40	0.16	0.36	0.38	0.16	0.25	0.37	0.15	0.15	0.37
Totale	97.72	97.29	97.29	98.82	95.36	99.12	99.27	98.46	99.42	99.04	98.72	99.82	98.76	100.06	99.61	98.97	99.18	99.69	98.74	100.20
Structural formula, oxygen equivalents p.f.u. = 16 and anions p.f.u. = 25																				
Si	6.29	6.37	6.37	6.31	6.38	6.14	6.19	6.10	6.16	6.07	6.14	6.14	6.15	6.11	6.10	6.13	6.14	6.12	6.14	6.14
Ti	0.00	0.00	0.00	0.04	0.01	0.03	0.05	0.04	0.03	0.05	0.03	0.02	0.05	0.04	0.03	0.06	0.03	0.04	0.03	0.04
Al	3.97	3.88	3.88	3.88	3.71	4.27	3.97	4.38	3.97	4.26	3.98	4.25	3.90	3.96	4.41	4.11	4.03	4.43	4.47	3.90
Fe2+	2.22	2.29	2.29	2.30	2.39	1.71	1.94	1.24	1.36	1.34	1.35	1.20	1.44	1.38	1.19	1.30	1.29	1.14	1.11	1.35
Mn	0.04	0.01	0.01	0.01	0.01	0.02	0.01	0.02	0.01	0.02	0.02	0.01	0.03	0.02	0.01	0.02	0.02	0.02	0.01	0.02
Mg	0.00	0.00	0.00	0.00	0.01	0.03	0.06	0.32	0.58	0.34	0.59	0.50	0.59	0.64	0.34	0.48	0.68	0.33	0.30	0.69
Ca	3.60	4.08	4.08	3.83	4.18	2.67	2.42	2.53	2.18	2.45	2.29	2.33	2.18	2.21	2.50	2.40	2.20	2.53	2.58	2.23
La	0.26	0.02	0.02	0.14	0.02	0.48	0.47	0.53	0.72	0.56	0.69	0.62	0.71	0.68	0.55	0.57	0.65	0.51	0.52	0.70
Ce	0.13	0.01	0.01	0.08	0.02	0.61	0.74	0.68	0.81	0.76	0.80	0.77	0.83	0.82	0.69	0.77	0.82	0.67	0.65	0.82
Pr	0.01	0.00	0.01	0.00	0.01	0.00	0.03	0.04	0.04	0.04	0.04	0.04	0.04	0.05	0.04	0.04	0.05	0.04	0.04	0.04
Sm	0.00	0.00	0.00	0.00	0.00	0.01	0.01	0.00	0.00	0.00	0.00	0.00	0.00	0.01	0.01	0.01	0.00	0.01	0.00	0.00
Nd	0.00	0.00	0.00	0.01	0.01	0.11	0.16	0.11	0.12	0.12	0.10	0.09	0.09	0.11	0.09	0.12	0.10	0.11	0.08	0.10
Tot	16.52	16.67	16.67	16.60	16.73	16.09	16.06	15.99	15.98	16.01	16.02	15.96	16.01	16.04	15.97	16.00	16.00	15.95	15.94	16.04
Trace elements (ppm)																				
Li	4.0	4.2	4.7	7.4	3.1	26.0	9.3	244	254	125	248	235	242	357	182	150	337	157	154	234
Be	0.4	0.4	0.9	2.8	0.3	4.0	0.8	0.2	0.2	0.4	0.3	0.2	0.3	0.4	0.4	0.3	0.4	0.6	0.6	
Sc	5.6	5.2	5.7	7.1	4.8	5.0	4.8	6.5	6.2	6.2	7.0	5.8	5.7	5.9	6.2	5.4	14.5	19.0	18.8	15.5
Ti	275	627	681	67	692	38	1093	1305	1265	2360	1393	1546	1450	1623	2649	2092	1833	2800	3116	1181
V	12	81	94	13	25	19	123	120	106	98	158	82	73	169	237	201	489	712	634	569
Cr	bdl	6.2	10.0	3.2	3.5	5.1	48.0	6.6	4.9	3.6	15.0	5.9	5.9	20.0	4.8	23	77	201	102	273
Mn	1455	1322	1950	19200	1353	4610	1371	914	921	837	984	1052	1036	1174	942	895	1158	800	805	912
Co	bdl	bdl	0.3	5.4	0.2	5.7	2.6	2.2	2.4	2.3	2.2	2.5	2.3	2.4	2.0	2.0	1.0	1.1	1.3	1.0
Ni	2.1	0.8	1.2	5.0	2.0	2.5	1.6	bdl	bdl	bdl	bdl	bdl	0.4	bdl	bdl	bdl	bdl	bdl	bdl	bdl
Cu	bdl	bdl	1.1	2.9	bdl	0.4	0.7	bdl	bdl	bdl	bdl	bdl	bdl	bdl	bdl	bdl	bdl	bdl	bdl	bdl
Zn	26	34	48	99	27	195	99	78	77	65	76	77	68	84	73	77	80	69	68	78
Ga	117	85	98	10	85	9	434	683	642	683	640	647	612	683	670	718	641	710	712	654
Rb	bdl	bdl	0.30	1.80	bdl	0.10	0.40		1.10	0.20	0.30	2.30	bdl	bdl	bdl	2.10	bdl	bdl	bdl	bdl
Sr	1051	1098	900	152	822	154	620	221	197	210	186	194	178	162	188	180	192	230	236	234
Y	250	211	141	16	151	5	264	168	150	123	87	79	71	85	116	77	92	102	108	136
Zr	12.00	26.00	36.00	2.40	24.00	1.00	5.00	2.40	3.20	2.90	10.00	14.00	17.00	50.00	3.50	2.00	89.00	3.00	6.90	2.30
Nb	0.06	0.03	bdl	0.01	0.05	bdl	bdl	0.02	0.03	0.02	0.05		0.03	0.06	0.06	0.02	0.08	0.05	0.09	0.03
Sn	1753	1900	473	190	3360	98	461	22	24	85	30	34	32	27	85	57	39	66	81	23
Sb	453	28	55	10	291	5.60	2.10	bdl	bdl	bdl	0	0	bdl	0	bdl	0	bdl	bdl	bdl	bdl
Cs	0.04	bdl	0.14	1.12	0.07	0.12	0.12	bdl	0.54	0.07	0.16	0.98	bdl	bdl	bdl	0.51	bdl	bdl	bdl	bdl
Ba	1.30	0.47	0.68	3.90	0.78	0.25	0.76	0.13	1.30	0.20	0.46	0.54	0.07	0.05	0.03	0.88	0.08	0.08	0.09	0.12
La	56600	47400	52900	2270	29000	488	46200	100300	92900	71900	98300	95200	90700	112100	73500	82600	93200	79400	79500	93600
Ce	30300	19700	23400	1370	17240	352	57400	105800	97100	88300	106900	100300	97100	125300	93300	102900	106700	100000	99720	99000
Pr	1248	753	905	53	858	18	4570	6677	6030	6000	6610	6120	5940	7870	6290	6780	6830	6650	6660	6190
Nd	2140	1430	1578	81	1843	38	13250	15690	14090	14590	14790	13660	13290	17900	15020	15630	15560	15500	15580	13920
Sm	162	133	100	8.8	163	4.15	1191	1092	977	1063	877	808	795	973	984	925	951	1016	1023	890
Eu	12.9	17.7	6.76	1.39	16	0.69	74	23	21	24	18	17	17	17	18	17	21	23	23	20
Gd	146	136	101	10	113	2.70	552	557	508	488	437	404	396	493	462	438	461	474	478	460
Tb	11.85	13.10	7.72	0.72	9.21	0.26	36.00	30.42	27.80	26.20	19.58	17.85	17.34	20.30	23.27	19.26	20.80	23.80	24.00	24.70
Dy	50.00	53.00	32.00	3.00	37.00	1.00	104.00	76.00	67.00	61.00	40.00	36.00	33.00	39.00	52.00	37.00	42.00	51.00	54.00	60.00
Ho	9.20	8.10	5.30	0.50	6.00	0.19	12.00	7.90	7.10	6.00	4.00	3.60	3.40	4.10	5.30	3.60	4.40	5.00	5.20	6.40
Er	25.00	17.00	12.00	1.20	14.00	0.60	20.00	14.00	13.00	10.00	8.70	7.80	7.30	9.10	10.00	7.40	10.00	9.10	9.50	12.00
Tm	4.20	2.00	1.60	0.24	1.80	0.07	1.80	1.20	1.10	0.91	0.77	0.73	0.71	1.00	0.83	0.58	1.00	0.72	0.83	1.10
Yb	31.00	11.00	10.00	3.00	11.00	0.74	8.30	6.90	6.00	5.20	4.80	5.40	5.20	8.30	5.90	3.80	8.90	4.20	4.60	5.40
Lu	4.60	1.50	1.60	0.60	1.50	0.13	0.84	0.85	0.74	0.65	0.76	0.80	0.77	1.30	0.77	0.52	1.50	0.53	0.64	0.76
Hf	0.39	1.50	2.50	0.22	1.20	0.10	0.63	0.25	0.30	0.29	0.88	1.20	1.30	6.70	0.75	0.30	12.00	0.74	1.20	0.36
Ta	0.03	0.01	0.01	0.03	0.01	0.00	0.01	0.01	0.01	0.02	0.00	0.01	0.01	0.04	0.02	0.01	0.02	0.04	0.09	0.00
Pb	1.70	0.49	1.10	4.10	1.10	0.60	3.00	0.41	1.10	0.25	0.40	2.70	0.16	0.46	0.57	0.68	0.27	0.37	0.29	0.86
Bi	17.00	1.70	2.40	0.38	8.40	0.17	0.32	0.05	0.07	0.09	0.05	0.24	0.05	0.05	0.05	0.11	0.06	0.07	0.08	0.03
Th	0.64	2.70	4.80	0.41	52	2.60	1931	585	393	53	227	86	63	792	708	659	339	502	313	1556
U	66	129	93	11	104	5	130	194	182	55	45	32	32	29	40	26	46	56	56	158
Th/U	0.0	0.0	0.1	0.0	0.5	0.6	14.9	3.0	2.2	1.0	5.0	2.7	2.0	27.3	17.7	25.4	7.4	9.0	5.6	9.9

EMP and LA-ICP-MS analysis for fluorite and tourmaline

Sample	Fl-1	Fl-2	Fl-3	Fl-4	Fl-5	Fl-6	Fl-7	Fl-8	Fl-9	Fl-10	Fl-11	Fl-12
Comment	GBM1 white-pink	GBM1 white-pink	Pale violet	violet	dark violet	white-colourless	GBM1 green	GBM1 pale green	Monte Valerio green	GBM1 Pink	Giglio allume1	Giglio allume2
Major elements (wt%)												
SiO2	0.02	0.02	0.05	0.03	0.01	0.02	0.04	0.05	0.03	0.01	0.01	0.03
TiO2	0.00	0.00	0.00	0.00	0.00	0.00	0.00	0.00	0.00	0.00	0.00	0.00
Al2O3	0.01	0.01	0.00	0.04	0.03	0.00	0.01	0.00	0.04	0.03	0.01	0.00
FeO	0.00	0.00	0.00	0.01	0.00	0.00	0.00	0.00	0.01	0.00	0.00	0.00
MnO	0.00	0.00	0.00	0.02	0.00	0.01	0.00	0.00	0.02	0.00	0.00	0.00
MgO	0.02	0.02	0.01	0.00	0.00	0.04	0.02	0.01	0.00	0.00	0.01	0.01
CaO	68.33	68.33	71.12	69.95	68.75	71.16	71.60	71.32	69.22	66.06	74.83	72.66
F	33.94	33.94	28.91	30.97	32.40	33.11	33.66	33.95	35.04	37.20	30.43	32.60
Total	102.31	102.31	100.09	101.03	101.20	104.35	105.39	105.40	104.39	103.30	105.29	105.31
Trace elements (ppm)												
Li	0.00	0.00	0.00	0.18	0.08	0.00	0.00	0.14	25.60	0.00	0.00	0.00
Be	0.00	0.00	0.00	0.10	0.02	0.00	0.05	0.00	0.00	0.00	0.00	0.00
Si	0.00	250.00	0.00	470.00	206.00	0.00	211.00	231.00	248.00	280.00	0.00	0.00
Ca	-	-	-	-	-	-	-	-	-	-	-	-
Sc	0.00	0.00	0.00	0.00	0.00	0.00	0.00	0.13	0.00	0.00	0.00	0.00
Ti	0.00	0.00	1.10	0.00	0.67	0.00	0.00	0.00	0.00	0.00	0.00	0.00
Ti	0.00	2.70	1.00	0.75	1.80	0.71	0.74	1.20	0.66	1.00	0.00	0.77
V	0.00	0.10	0.00	0.32	0.00	0.00	0.00	0.00	0.00	0.12	0.00	0.00
Cr	0.00	0.00	0.00	0.00	0.00	0.00	0.00	0.00	0.00	0.00	0.00	0.55
Mn	0.00	0.00	0.47	85.00	0.48	0.00	0.45	0.42	10.63	0.45	0.00	0.00
Co	0.40	0.61	0.14	0.37	0.64	1.10	0.19	0.28	0.32	0.17	0.18	0.30
Ni	1.80	0.79	4.30	0.74	0.73	0.68	0.87	4.50	2.90	0.69	0.75	3.60
Cu	0.00	0.25	0.25	0.23	0.00	0.25	0.00	0.00	0.33	0.19	0.00	0.18
Zn	0.00	0.23	0.18	2.46	0.25	0.00	0.00	0.22	6.14	0.00	0.00	0.24
Ga	0.00	0.04	0.04	0.02	0.05	0.00	0.47	0.08	0.34	0.05	0.02	0.02
Rb	0.00	0.12	0.06	0.05	0.07	0.00	0.06	0.07	7.08	0.00	0.00	0.00
Sr	155.40	153.20	112.20	113.90	107.80	85.70	56.20	53.30	37.60	44.40	63.30	83.90
Y	8.84	8.79	37.90	36.80	22.14	82.20	36.01	38.01	24.62	78.30	6.92	40.54
Zr	0.00	0.02	0.02	0.00	0.00	0.00	0.02	0.01	0.00	0.00	0.02	0.00
Nb	0.00	0.01	0.00	0.00	0.08	0.00	0.00	0.01	0.00	0.02	0.00	0.00
Sn	0.05	0.09	0.07	0.04	0.05	0.04	0.07	0.07	0.70	0.07	0.04	0.07
Sb	0.00	0.00	0.00	0.00	0.00	0.00	0.00	0.00	0.23	0.00	0.00	0.00
Cs	0.00	0.00	0.00	0.01	0.00	0.00	0.01	0.02	4.98	0.00	0.00	0.00
Ba	0.01	0.00	0.03	0.05	0.00	0.00	0.00	0.00	1.09	0.01	0.00	0.00
La	1.14	1.10	2.33	1.22	1.03	0.42	15.63	0.95	54.20	0.08	1.54	0.17
Ce	2.80	2.88	5.83	3.35	3.29	1.38	47.20	4.47	62.90	0.30	2.25	0.48
Pr	0.44	0.47	0.96	0.57	0.58	0.31	10.98	1.28	6.87	0.12	0.26	0.10
Nd	2.54	3.17	6.24	3.84	3.68	2.53	92.00	12.74	28.30	1.37	1.13	0.87
Sm	0.65	0.69	1.71	1.50	1.27	1.41	44.90	6.67	3.22	1.52	0.15	0.36
Eu	0.06	0.04	0.08	0.12	0.05	0.06	2.16	0.30	0.37	0.41	0.06	0.31
Gd	0.71	0.73	2.44	2.41	1.53	3.23	36.00	8.17	2.25	4.53	0.17	1.04
Tb	0.07	0.08	0.29	0.29	0.19	0.43	3.22	0.77	0.15	0.87	0.03	0.22
Dy	0.50	0.40	1.68	1.72	1.04	2.71	10.87	3.36	0.69	6.34	0.22	2.17
Ho	0.09	0.08	0.32	0.32	0.21	0.60	1.01	0.47	0.13	1.31	0.05	0.68
Er	0.23	0.19	0.75	0.78	0.50	1.61	1.43	0.91	0.35	3.50	0.18	2.60
Tm	0.02	0.02	0.09	0.08	0.05	0.17	0.12	0.09	0.03	0.40	0.02	0.36
Yb	0.14	0.15	0.50	0.47	0.33	0.95	0.55	0.45	0.19	2.46	0.13	2.81
Lu	0.02	0.02	0.06	0.05	0.04	0.11	0.05	0.05	0.03	0.30	0.01	0.48
Hf	0.00	0.00	0.00	0.00	0.00	0.00	0.01	0.01	0.00	0.00	0.00	0.01
Ta	0.00	0.00	0.00	0.00	0.00	0.00	0.00	0.01	0.00	0.00	0.00	0.00
Pb	0.00	0.00	0.02	0.04	0.07	0.00	0.01	0.03	2.18	0.01	0.00	0.04
Bi	0.00	0.01	0.00	0.01	0.00	0.00	0.00	0.01	0.02	0.00	0.00	0.02
Th	0.00	0.04	0.00	0.07	0.00	0.00	0.11	0.03	0.08	0.01	0.00	0.30
U	0.04	0.03	0.12	0.08	0.02	0.00	0.31	0.02	0.00	0.03	0.00	0.03

Sample	Tur-1	Tur-2	Tur-3	Tur-4
Major elements (wt%)				
SiO2	36.49	35.67	35.70	35.98
TiO2	0.40	1.83	0.97	1.27
Al2O3	32.82	30.76	34.08	33.45
FeO	11.36	10.64	8.58	9.76
MnO	0.06	0.07	0.05	0.04
MgO	3.50	4.50	4.05	3.89
CaO	0.22	0.92	0.41	0.48
Na2O	2.02	2.09	1.87	2.06
K2O	0.06	0.06	0.03	0.04
F	0.09	0.20	0.16	0.15
V2O3	0.06	0.14	0.09	0.13
Nb2O5	0.00	0.00	0.00	0.02
Ce2O3	0.00	0.11	0.16	0.00
La2O3	0.00	0.00	0.01	0.00
Sm2O3	0.12	0.00	0.04	0.00
Nd2O3	0.00	0.00	0.14	0.00
Total	87.21	86.98	86.33	87.29
Trace elements (ppm)				
Li	127.10	114.90	85.80	72.80
Be	8.94	12.74	5.88	3.74
Ca	3490.00	3100.00	3930.00	3930.00
Sc	45.40	36.66	40.00	50.60
Ti	5390.00	4210.00	6940.00	6160.00
V	199.80	180.40	238.10	290.10
Cr	409.00	418.80	350.00	435.60
Mn	440.00	434.10	454.10	470.40
Co	26.35	25.98	30.05	30.32
Ni	80.30	74.50	151.50	157.20
Cu	bdl	bdl	bdl	bdl
Zn	296.40	295.80	328.00	324.70
Ga	111.90	107.90	117.30	127.00
Rb	bdl	bdl	bdl	bdl
Sr	34.80	28.30	25.80	25.16
Y	0.19	0.13	0.12	0.05
Zr	3.19	2.54	0.94	0.44
Nb	9.68	7.10	4.80	0.82
Sn	49.50	39.70	28.01	33.49
Sb	bdl	bdl	bdl	bdl
Cs	bdl	bdl	0.22	bdl
Ba	0.22	0.35	0.14	0.14
La	4.70	4.25	4.73	3.92
Ce	7.83	6.53	7.86	6.58
Pr	0.64	0.60	0.73	0.60
Nd	2.16	1.76	2.13	1.83
Sm	0.24	0.24	0.26	0.13
Eu	0.15	0.14	0.10	0.13
Gd	0.20	0.09	0.11	0.07
Tb	0.02	0.01	0.01	0.01
Dy	0.04	0.04	0.04	0.01
Ho	0.00	0.00	0.00	bdl
Er	0.02	bdl	bdl	bdl
Tm	0.00	bdl	bdl	bdl
Yb	0.01	bdl	bdl	bdl
Lu	0.01	bdl	0.00	bdl
Hf	0.85	0.61	0.09	0.03
Ta	8.29	7.05	1.02	0.45
Pb	5.46	5.13	5.52	6.27
Bi	bdl	bdl	bdl	bdl
Th	0.13	0.11	0.07	0.01
U	0.03	0.02	0.06	0.00

7. The plutonic-subvolcanic-volcanic connection in the long-lived Campiglia Marittima igneous system (Tuscany, Italy): a zircon CA-ID-TIMS dating study

Gabriele Paoli[1], Sergio Rocchi[1], Andrea Dini[2], Urs Schaltegger[3], Maria Ovtcharova[3]

[1]*Dipartimento di Scienze della Terra, Università di Pisa, Via Santa Maria 53, 56126 Pisa, Italy*

[2]*CNR, Istituto di Geoscienze e Georisorse, Via Moruzzi 1, 56124 Pisa, Italy*

[3]*Section des Sciences de la Terre et de l'environnement, Université de Genève, 1205 Genève, Switzerland*

Keywords

Crustal magmas, CA-ID-TIMS, U-Pb dating, time-transgressive crystallization

Abstract

The knowledge deriving from high precision U-Pb zircon geochronological methods is pivotal in estimating the duration of processes at different levels of the plumbing system. Several igneous bodies (either plutonic or volcanic) could show time intervals of zircon crystallization that are significantly larger than the time required for the complete solidification of a single pulse of magma, suggesting a multistage, pulsed, growth history. The melting of multiple crustal anatectic sources, the formation of peraluminous magmas, and their sequential transfer and emplacement at shallow level, is a common occurrence in the Tuscan Magmatic Province (Elba Island, Larderello, Castel di Pietra magmatic complexes). In these contexts, mantle-derived magmas are supposed to play a pivotal role in the activation of such crustal sources. The Campiglia system offers exposures of the full range of emplacement types for magmas and related fluids, including plutonic, subvolcanic, volcanic and hydrothermal units. New U-Pb CA-ID-TIMS geochronology from these realms allows to hypothesise the existence of a bimodal deep reservoir that remains in a magmatic condition (melt-present) for about 1000 ka. The magma extraction from a crustal felsic reservoir fed a pluton and its hydrothermal system during a short time interval at 5.4 Ma. At ca. 4.9 Ma the extraction of magma from a mafic reservoir supplied the Temperino mafic porphyry. Finally, the late extraction of magma from the felsic reservoir (probably the same of the Botro ai Marmi granite) fed the San Vincenzo rhyolites, where early-crystallised zircons were transported/recycled within portions of melts extracted from the reservoir.

7.1. Introduction

The knowledge deriving from high precision U-Pb zircon geochronological methods is pivotal in estimating magma fluxes, time intervals over which magmas are emplaced, the lifespan of a magma reservoir, and the thermal history of such complex systems (e.g. Leuthold et al., 2012; Caricchi et al., 2016; Schaltegger et al., 2009). Moreover, assuming that zircons are mobile within a magmatic systems (Caricchi et al., 2014), their ages could provide key informations on otherwise inaccessible portions of a magmatic system (Caricchi et al., 2016). Thus, combining timescales of events, defined by U-Pb and Ar-Ar geochronology, with petrochemical and isotopic data could help to resolve the duration of processes at different levels of the plumbing system.

Several intrusive bodies show time intervals of zircon crystallization that are significantly larger than the time required for the complete solidification of a single pulse of magma, suggesting a multistage, pulsed, growth history (Annen, 2009; de Saint Blanquat et al., 2011). Significant spread in ages supports time-transgressive crystallization and mobility of zircon grains, both in plutonic and volcanic realms (Caricchi et al., 2016). For subvolcanic and volcanic realms, zircons grains can be withdrawn from partially crystallised magma mushes before or during an eruption, either as isolated crystals (Cooper and Wilson, 2014) or crystals carried by mobilised residual melt pockets (Cashman and Giordano, 2014).

The melting of multiple crustal anatectic sources, the formation of peraluminous magmas, and their sequential transfer and emplacement at shallow level represent a common occurrence in the Tuscan Magmatic Province, as testified by the Elba Island magmatic complex (Dini et al., 2002; Rocchi et al., 2002). At Elba Island mantle-derived magmas played a pivotal role in the activation of crustal sources, providing heat and mass able to generate large volumes of hybrid, slightly peraluminous, magmas (Dini et al., 2005). Moreover, evidence of significant contribution from mantle-derived magmas has been proved by the occurrence of hybrid granites in the nearby Castel di Pietra well (Franceschini et al., 2000), and suppose for the Larderello granite (Dini et al., 2005).

The Campiglia Marittima area offers a suitable scenario to study the duration of processes at different levels of the plumbing system and the connection existing between felsic and mafic sources at such a shallow anatectic level. Here, uplift and erosional processes have exposed plutonic, subvolcanic, and volcanic rocks (both from mantle and crust), as well as hydrothermal products (Fig. 7.1). High-precision U-Pb thermal ionization mass spectrometry (TIMS) geochronology on zircons from all these igneous units provides the opportunity to resolve time-transgressive crystallization of crustal igneous processes. To set these data in a larger framework, the obtained ages are compared with other well-documented examples of time-transgressive construction of volcanic (Fish Canyon Tuff) and plutonic (Tuolumne, Mount Stuart, Tenpeak, Torres del Paine) magmatic systems. Moreover, the timing for the Botro ai Marmi pluton emplacement was compared with the Monte Capanne pluton of Elba Island, for which the time frame of multiple magma injection in the upper continental crust has been reconstructed (Farina et al., 2010; Barboni et al., 2014, 2015).

This thesis examines in detail a system linking plutonic, subvolcanic, volcanic and hydrothermal realms aiming to determine (i) the timescale of processes at different levels of the plumbing system and the genetic relationships between exposed rocks and their hidden sources, (ii) the link between igneous and hydrothermal deposits, (iii) the connection between magmatic activity produced by crustal and mantle derived magmas at such a shallow anatectic level.

7.2. Geological background

The Tuscan Magmatic Province is characterised by Miocene-Quaternary bimodal magmatism, dominated by crustal peraluminous granites, with minor mantle-derived lamproites, shoshonites, K-andesites and latites. A sequence of magmatic centres are triggered by post-collisional extension, as the Northern Apennine chain was progressively thinned and heated by asthenosphere upwelling, during the eastward roll-back of the subducting Adriatic Plate. Most of the

igneous centres were short-lived, resulting in the emplacement of a single, small magmatic body. In contrast, multiple batches of felsic and mafic magmas sequentially emplaced in Elba Island (8.5-6.0 Ma), Campiglia Marittima (5.7-4.3 Ma) and Larderello (3.8-1.3 Ma). In most cases mantle-derived mafic magmas emplaced after major peraluminous intrusions, built at relatively shallow crustal depth (4-6 km; Dini et al., 2008).

The Campiglia Marittima area (Fig. 7.1) is characterised by the coexistence of (i) the Botro ai Marmi peraluminous monzogranite pluton, provoking the intense metamorphism of the host carbonate, (ii) a subvolcanic dyke complex (mafic latite porphyry and felsic rhyolitic porphyry), crosscutting the contact aureole produced by the pluton, and (iii) the rhyolitic extrusive complex of San Vincenzo. Skarn and ore concentrations, linked to these intrusive rocks, occur as minor metasomatic bodies at the pluton-carbonate contact, as veins in the host rock and into the monzogranite body, and as distal ore and skarn body (Vezzoni et al., 2016). Geologic observation allow to define a chronologic sequence from the emplacement of the Botro ai marmi pluton, through the mafic and felsic dikes to the final San Vincenzo rhyolite event.

Magmatic units

The Botro ai Marmi monzogranitic pluton represent the first magmatic event occurred in the Campiglia Marittima area (Borsi et al., 1967). The magma intruded below a limestone sequence at a depth corresponding to ~0.1 GPa, producing an N-S elongated thermal aureole (Vezzoni et al., 2016; and reference therein). The top of the granitic body crops out for as little as ~500 m^2, with a buried volume of 30-45 km^3, reconstructed by geophysical data and exploratory wells (length of 15 km^2; Vezzoni et al., submitted). The granite stock thickness (2-3 km) is estimated by comparison with other peraluminous magmatic bodies from the Tuscan Magmatic Province (i.e. Monte Capanne pluton, 2-3 km; Farina et al., 2010; Dini et al., 2008). The pluton has a syenogranitic to monzogranitic composition (SiO_2 between 68 and 72 wt%) and a peraluminous character (ASI=1.1-1.3). Its primary paragenesis consists of quartz, K-feldspar, plagioclase, biotite, and cordierite along with accessory apatite, zircon and late-magmatic tourmaline. The magmatic assemblage is rarely preserved in the biotite monzogranite, due to pervasive hydrothermal alteration. However the Botro ai Marmi system is affected by a metal-poor potassic alteration, while a metalliferous mineralization occurs in a later skarn to vein stage, and is mostly localised away from the intrusion (Lattanzi et al., 2001; Vezzoni et al., 2016).

The Temperino mafic porphyry occurs as isolated sub-vertical dykelets (0.3–2 m thick and up to 30 m long) and it is found only spatially associated with distal skarn bodies. The contact zones between skarn and porphyry reveal that the Temperino porphyry was emplaced after skarn formation. The primary paragenesis of this deeply altered porphyritic igneous rock consists of phenocrysts of plagioclase, biotite, clinopyroxene, orthopyroxene, and olivine, along with abundant coarse-grained sanidine and quartz xenocrysts, all set in a fine-grained groundmass. The groundmass is completely recrystallised into a fine-grained aggregate of K-feldspar, quartz and chlorite, with mafic phenocrysts replaced by actinolite, epidote, chlorites and carbonates. The only relicts are biotite and rare clinopyroxene, as well as accessory minerals as chromite, apatite, zircon, monazite, and ilmenite.

The felsic porphyry consists of two dykes (10s m thick) cropping out discontinuously, crosscutting both the skarn and the Temperino porphyry. The felsic porphyritic dykes show similar mineralogy, with phenocrysts of quartz, centimetric sanidine, plagioclase, biotite and cordierite set in a fine-grained groundmass completely re-crystallised in K-feldspar, quartz and minor chlorite. Rare mafic enclaves up to 10 cm in size are also present (Vezzoni et al., 2016).

The San Vincenzo rhyolite has been emplaced less than 1 km to the west of the Botro ai Marmi intrusion as a viscous lava flows or domes, covering a surface area of about 10 km^2. The rhyolite has a porphyritic texture dominated by phenocrysts of quartz, K-feldspar, plagioclase, biotite, cordierite, as well as accessory apatite, monazite, zircon, ilmenite (Ferrara et al., 1989; Ridolfi et al., 2016). Rare small mafic enclaves and clinopyroxene xenocrysts are also present.

Existing geochronological constraints

The Botro ai Marmi granite has been previously dated by Borsi et al. (1967) by K-Ar on K-feldspar, giving an age of ~5.7 Ma. More recently, Vezzoni et al. (in prep.) obtained a biotite ^{40}Ar-^{39}Ar age of 5.41 ± 0.06 Ma, indistinguishable within the analytical uncertainty from the ^{40}Ar-^{39}Ar age of 5.36±0.05 Ma obtained for phlogopite from the exoskarn body bordering the magmatic intrusion.

Vezzoni et al. (in prep.) reported two ^{40}Ar-^{39}Ar ages on biotite of 5.07±0.04 Ma and 5.12±0.05 Ma for the subvolcanic mafic Temperino porphyry as well. Moreover, ^{40}Ar-^{39}Ar ages of sanidine from the same samples yielded two identical younger ages of 4.87±0.05 Ma and 4.88±0.05 (Fig. 7.2), that has been interpreted to record the emplacement event (Vezzoni et al., in prep.). On contrary, the emplacement age of the felsic porphyry is of 4.30±0.13 Ma (whole rock K-Ar age; Borsi et al., 1967).

The eruption age of the San Vincenzo rhyolite has been constrained at 4.38±0.04 Ma (average ^{40}Ar-^{39}Ar date on sanidine; Feldstein et al., 1994). The Ar-Ar ages recalculated using new intercalibration factors (ArAR; Mercer and Hodges, 2016) give an age of 4.412±0.019 Ma (MSWD=0.80; n=9), not differing significantly from the literature data.

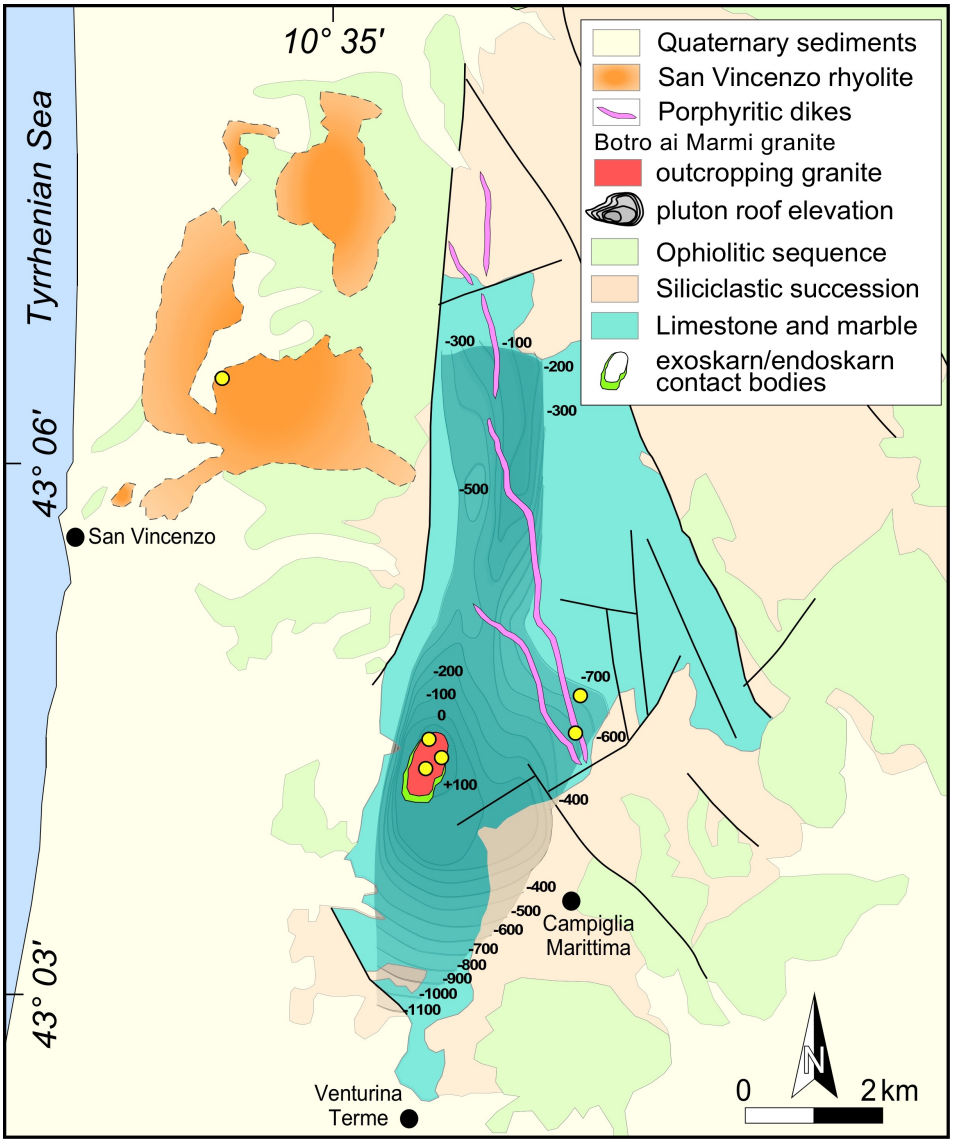

Fig. 7.1 - Geological map of the Campiglia Marittima area (modified after Vezzoni et al., 2016). The pluton roof elevation is also shown (Vezzoni et al., submitted). Yellow circles indicate sampling localities.

7.3. Methods

Three samples have been collected from the Botro ai Marmi monzogranitic pluton. The samples have been selected according to the granite metasomatic alteration degree to observe possible difference in zircon ages. Two samples (BM5 and GBM4) are from the unaltered or slightly altered biotite granite, while one sample (GBM2A) is from the altered phlogopite-titanite granite. Moreover, two samples were collected from Temperino porphyry (MGC, PV-319) and one from the San Vincenzo rhyolite (GZT4). These last three samples were collected looking for as much as possible unaltered rocks. U-Pb age determinations on zircon have been carried out using high-precision bulk dating techniques (chemical abrasion-isotope dilution-thermal ionization mass spectrometry; CA-ID-TIMS), and by spatially resolved spot analysis using a laser ablation inductively coupled plasma mass spectrometer (LA-ICP-MS). These techniques differ largely in terms of sampled volumes and precisions. Accuracy depends on a well-calibrated tracer solution for CA-ID-TIMS (Condon et al., 2015) and on external reference materials for the in-situ technique. CA-ID-TIMS utilises whole grains or parts of grains (inevitably mixing zones of different age) with precision and accuracy in $^{206}Pb/^{238}U$ age of 0.1% to 0.3% (2σ) for an age of 5 Ma, contrasting to the ca. 1–2% typical uncertainties for LA-ICP- MS (Schaltegger et al., 2015). CA-ID-TIMS high-precision $^{206}Pb/^{238}U$ ages are capable of resolving timescales of magmatic crystallization, which are commonly in the range of 10^4 to few 10^5 years for crustal plutons (e.g., Leuthold et al., 2012; Barboni et al., 2015; Samperton et al., 2015). Any age will provide time-averaged information, weighted for volume of the different zircon sectors and their U-content.

LA-ICP-MS U-Pb analysis were performed on zircon collected from the San Vincenzo rhyolite, using a Thermo-Finnigan Element 2 sector field ICP-MS coupled with a 193 nm ArF Excimer Resonetics RESOlution M-50 LR laser, at the University of Bergen. The results of U–Pb isotope analysis are reported in Supplementary Material (S.1).

CA-ID-TIMS U–Pb analysis were performed on zircon from all samples. Prior to zircon dating by U-Pb chemical abrasion-isotope dilution-thermal ionisation mass spectrometry analysis (U-Pb CA-ID-TIMS), bulk separated zircon grains were mounted in epoxy resin, polished, imaged by cathodoluminescence (CL) and backscattered electrons (BSE). The CA-ID-TIMS U–Pb analysis were performed at the University of Geneva, Switzerland, following procedures described in Wotzlaw et al. (2015). The detailed analytical methods are reported in *Supplementary Table 5.1*.

7.4. Results from CA-ID-TIMS U-Pb geochronology

The igneous units selected for U-Pb dating have significantly variable petrochemical affinities and origin (felsic and mafic; Ferrara et a., 1989; Ridolfi et al., 2016; Vezzoni et al., in prep.). The volumetrically minor Temperino porphyry has a geochemical-isotopic signature typical of mantle-derived magmas ($^{87}Sr/^{86}Sr$=0.7085-0.7099 and $^{143}Nd/^{144}Nd$=0.51221-0.51224; Vezzoni et al., in prep.). Oddly, the Temperino porphyry displays more pronounced geochemical similarities with K-andesites from Capraia Island (far in space -60 km- and time -7.4 Ma-) than with mafic microgranular enclaves from the San Vincenzo rhyolites (temporally and spatially overlapping). The Botro ai Marmi granite and the San Vincenzo rhyolite, display trace element and isotopic signatures ($^{87}Sr/^{86}Sr$=0.7180-0.7190 and $^{143}Nd/^{144}Nd$=0.51214-0.51216; Vezzoni et al., in prep.) akin to dominantly crustal anatectic products of the Tuscan Magmatic Province (Dini et al., 2002, 2005; Poli and Peccerillo, 2016; Ridolfi et al., 2015). Preliminary LA-HR-ICP-MS U-Pb datings of zircon from the San Vincenzo rhyolite, show that (i) despite this origin, only less than 10% of zircon cores show inherited ages comparable with the detrital zircons signature of the Tuscan basement (Sirevaag et al., 2016; Paoli et al., 2016), and (ii) most of the zircon ages range from 4.74±0.12 to 5.52±0.22 Ma. This range, although based on dates affected by high errors, suggests a prolonged interval of zircon crystallization in the order of several hundreds ka. This preliminary data encouraged to perform more precise CA-ID-TIMS U-Pb analysis on the crustal

igneous products from the Campiglia system (Fig. 7.2), in order to resolve the timescale of each magmatic crystallization event.

U-Pb age determinations on a total of 30 zircon grains were performed using high-precision bulk, single-grain CA-ID-TIMS technique, which allows to resolve the crystallization timescale intrinsic to each magmatic events. Among these zircons, three grains are distinctly older (7.369±0.068 and 9.758±0.034 Ma), with one grain from the Temperino porphyry, showing a clearly inherited core (294.72±0.46 Ma). Thus, twenty-seven ages have been used for timescale interpretations. Each single $^{206}Pb/^{238}U$ ratios were corrected for initial disequilibrium in $^{230}Th/^{238}U$, using a fixed Th/U (melt) calculated from the lattice strain model for zircon-melt partitioning of Th and U. Sample locations are shown in Fig. 7.1 and representative CL images are given in Supplementary Materials.

Thirteen zircons were analyzed from the Botro ai Marmi monzogranite, four from both samples of biotite granite (BM5 and GBM4), and five from the altered phlogopite-titanite granite (GBM2A). Considering that the weighted mean $^{206}Pb/^{238}U$ age calculated for each single sample is indistinguishable from the others within the analytical uncertainty (GBM4: 5.4402±0.0089 Ma; BM5: 5.444±0.016 Ma; GBM2A: 5.4266±0.0089 Ma), it is acceptable to calculate a cumulative weighted means age, that result to be 5.442±0.012 Ma (n=13, MSWD=1.5). The ages range between 5.502±0.027 and 5.404±0.085 Ma inferring a period of zircon crystallization of 98±21 ka. For the mafic Temperino porphyry, five zircons for sample PV-319 yielded a range of $^{206}Pb/^{238}U$ ages between 5.52±0.11 and 5.263±0.068, and four zircons from sample MGC yielded ages ranging between 5.261±0.0.034 and 5.068±0.060 Ma. The two samples are petrochemically identical (Vezzoni et al., in prep.), thus an overall range of 452±66 ka is envisaged as the crystallization time interval for the Temperino magmatic unit (Fig. 7.2). Six zircons from the San Vincenzo rhyolite show ages between 5.129±0.027 and 5.428±0.044 Ma suggesting an extended period of zircon crystallization of 299±28 ka (Fig. 7.2).

7.5. Discussion

Understanding processes of protracted magma crystallization is pivotal to resolve the dynamics of complex magma reservoirs. The construction interval of a magmatic system (plutonic or volcanic) can vary by orders of magnitude and is correlated with the magma chamber volume and magma flux (Fig. 7.3; e.g., Caricchi et al., 2014; Deering et al. 2016; Lipmann and Bachmann, 2015; Saint Blanquat et al., 2011). A well-documented example of time-transgressive construction of a magmatic system is the Fish Canyon Tuff (FCT), one of the largest described volcanic eruption on Earth (5000 km^3), that show an incremental assembly and consolidation of magma chambers that lasted at least 300 ka (e.g. Bachmann et al., 2007; Coble et al., 2013; Wotzlaw et al. 2013). On the other side, intrusive examples are the intrusions of Tuolumne suite (2500 km^3 in 8 Ma), the Mount Stuart (1200 km^3 in 5.5 Ma) and the Tenpeak (400 km^3 in 2.6 Ma), as well as the Torres del Paine felsic pluton (100-200 km^3 in 90 ka) (Saint Blanquat et al., 2011, and reference therein). Moreover, it is interesting to note that the magma volume resulting from thermal modelling of zircons dates (e.g. Monte Capanne pluton: Δt=~200–400 ka, Barboni and Schoene, 2014; V=500-1000 km^3, Caricchi et al., 2016) is significantly larger than that estimated from fieldwork (~135 km^3, Farina et al., 2010). This suggests that most of the zircons may be crystallised within a deeper larger reservoir and record conditions of the magmatic system at that level.

Timescales in Campiglia

The timescales of magma storage and those of magma extraction-transfer-emplacement are difficult to disentangle. In this respect, a case study like Campiglia is promising, in its offering exposures of an igneous complex including plutonic, subvolcanic, volcanic and hydrothermal units, that is the full range of emplacement types for magmas and related fluids. The new zircon U-Pb CA-ID-TIMS dates obtained for plutonic, subvolcanic, volcanic and hydrothermal products from Campiglia show a distribution which is at odd with what could be expected. Indeed, the extent of the full

crystallization period is shortest for the Botro ai marmi granitic pluton (~100 ka), intermediate for the subvolcanic mafic Temperino porphyry (up to 650 ka), and longest for the volcanic San Vincenzo rhyolite (up to 1000 ka).

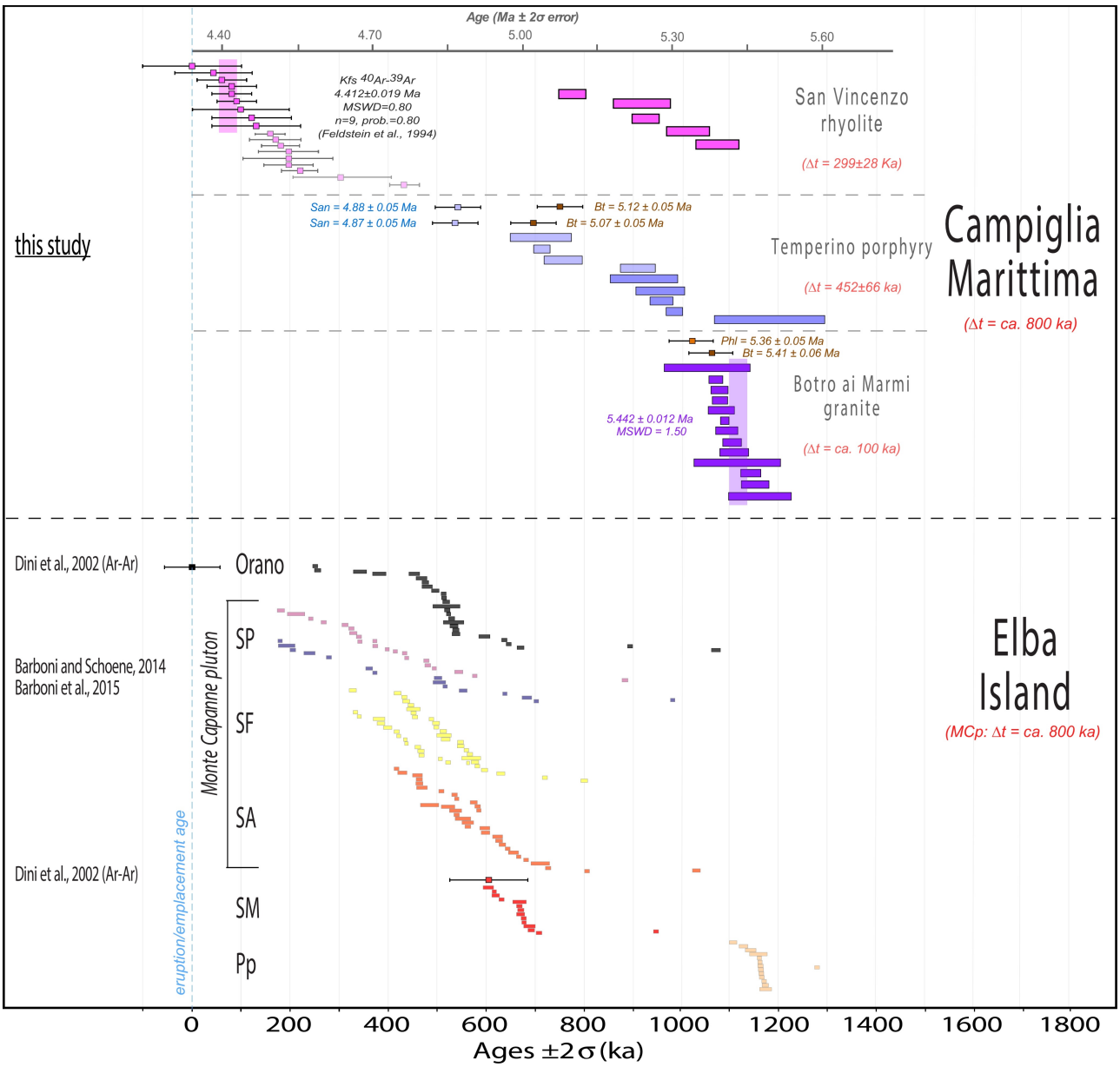

Fig. 7.2 - U-Pb geochronology, showing $^{206}Pb/^{238}U$ ages for individual zircons from the Botro ai Marmi granite, the San Vincenzo rhyolite and the Temperino porphyry. LA-ICP-MS ages from the San Vincenzo rhyolite are represented by a grey shaded area. Eruption/emplacement Ar-Ar ages are also shown. Each bar is an individual analysis with vertical size indicating ±2σ uncertainty. The x-axes indicate the spread in age observed between the eruption/emplacement age and the age of the different event. For comparison are shown multiple CA-ID-TIMS ages on zircons from the crustal magmatic system of the Elba Island (Δt = ~800 ka; modified from Barboni et al. 2015). Monte Capanne pluton: SP=San Pietro facies; SF=San Francesco facies; SA=Sant'Andrea facies. SM=San Martino porphyry; Pp=Portoferraio porphyry.

The zircon dates for the Botro ai Marmi granite define a short crystallization interval of ~100 ka. Moreover, the youngest U-Pb zircon age (5.404±0.085 Ma) overlaps with the ^{40}Ar-^{39}Ar age of biotites from the granite (5.41±0.06 Ma) and age of phlogopite from the contact metasomatic products (5.36±0.05 Ma). These data record a relatively short period of crystallization for different minerals (zircon, biotite, and phlogopite) in the different sub-units (granite and skarn). This time interval could be compatible with complete crystallization at the emplacement site, closely followed by a skarn/metasomatic event. However, the magma flux of $10^{-2.7}$-10^{-2} km^3a^{-1} pointed out by means of thermal modelling of zircon dates for the similar pluton of Monte Capanne, Elba Island (Caricchi et al., 2016), would suggest that in a 100 ka time interval, at least 200 km^3 of magma should have been transferred within the crust (Fig.3). Therefore, the 30-45 km^3 estimate for the Botro ai Marmi pluton could represent only a fraction of the total amount of felsic magma produced by crustal melting. Moreover, the mechanism of metasomatic alteration of both the monzogranite and the host limestone/marbles has been recently revised (Paoli et al., in prep. - see chapter 5), showing the requirement of heat and components (i.e., Mg, Ba, Sr) input from a mafic source. ^{40}Ar-^{39}Ar date of phlogopite from the metasomatic body highlight the activity of metasomatic fluid released from a mafic source almost contemporaneously with the emplacement of the Botro ai Marmi granite.

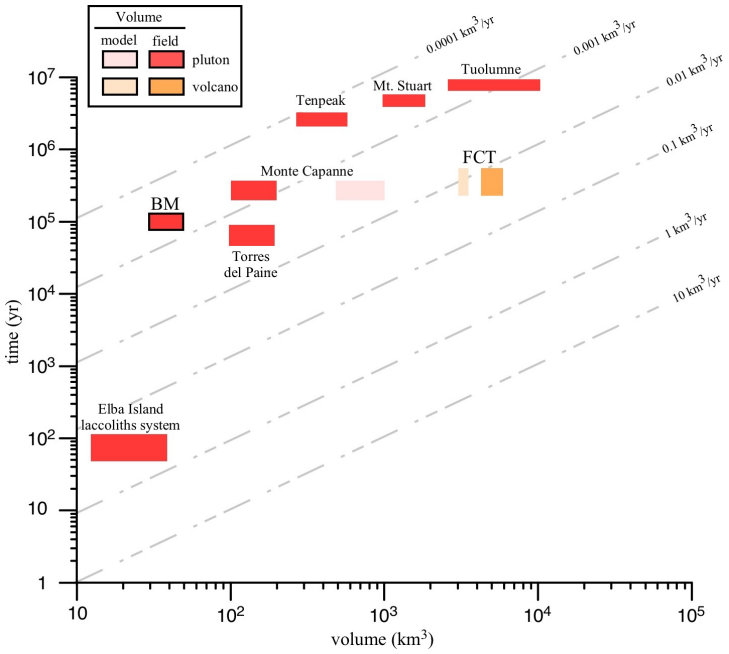

Fig. 7.3 - Comparison of estimated average magma supply and assembly rates for overall construction of plutons and volcanic bodies. Volume values obtained from field observations (field) are compared with values of volume estimated by zircon geochronology (model). BM=Botro ai Marmi pluton; FCT=Fish Canyon Tuff. Literature data are from de Saint Blanquat et al. (2011) and Caricchi et al. (2016).

The two samples of mafic Temperino porphyry, even showing a clear quench texture, record quite extended period of zircon crystallization distributed over 193 and 257 ka, respectively. The end of crystallization is marked by the sanidine ^{40}Ar-^{39}Ar age, some 200 ka younger than the youngest zircon. This zircon age distribution can be interpreted as the result of extended magma residence time and/or multiple magma batches emplacement within the same magmatic chamber/reservoir. The oldest zircons dates from the mafic Temperino porphyry correspond to the emplacement age of the Botro ai Marmi pluton, suggesting the contemporaneous activity of both mafic and felsic reservoir with sequential extraction of magma at emplacement ages.

Even more puzzling is the distribution of ages observed for the San Vincenzo rhyolite. Indeed, despite the glassy texture, the period of zircon crystallization is quite extended (~300 ka) and becomes much longer if final eruption age is considered (~1000 ka). The oldest zircons dates correspond to the same age of the Botro ai Marmi magma, suggesting that zircons crystallised at the same time in the same magma system with subsequent extraction of magma (suspended zircon in a melt), provoking the emplacement of the San Vincenzo rhyolite.

Common oldest age for zircons from the intrusive Botro ai Marmi pluton, the subvolcanic Temperino porphyry, and the effusive San Vincenzo rhyolite can be interpreted as the result of the activation of a crustal melting system coeval with a mafic magma reservoir. The interval of zircon crystallization for the subvolcanic and volcanic units is likely related to mobility/extraction of zircons from partially crystallised magmatic mushes before or during an eruption either

as isolated crystals (Cooper and Wilson, 2014) or crystals carried by mobilised residual melt pockets (Cashman and Giordano, 2014). On the other hand, the gap between U-Pb and ^{40}Ar-^{39}Ar ages could be linked to the time elapsed between the period of deep crystallization and the geologically instantaneous episode of final shallow emplacement (Temperino porphyry) or eruption (San Vincenzo rhyolite).

The complex age distribution resulting from the San Vincenzo rhyolite and the Temperino porphyry mirror their tangled isotopic and geochemical composition. Indeed, $^{87}Sr/^{87}Sr$ data on individual minerals from both rhyolites and mafic microgranular enclaves (found as blobs in the San Vincenzo rhyolite) reveal marked isotopic disequilibria with the host glass as well as within-grain zonation (Ferrara et al., 1989; Feldstein et al., 1994; Ridolfi et al., 2016). This disequilibria has been attributed to the interaction (mingling/mixing) of rhyolites with a mantle-derived magma and to the presence of both restitic (e.i., Px, Ol, Bt) and newly crystallized phases (Ferrara et al., 1989; Feldstein et al., 1994). Comparably diverse Sr and Pb isotopic values have been obtained from the Temperino porphyry (Vezzoni et al., submitted), supporting the evolution from a complex magma reservoir(s). In this respect, multiple episodic batches of mafic magma could be responsible for triggering the subvolcanic and volcanic activity at Campiglia.

Timescales compared

The U-Pb and ^{40}Ar-^{39}Ar ages for the San Vincenzo rhyolite and the Temperino porphyry are distributed over a time interval from oldest zircons, through biotite, to younger sanidine (recording the eruption/emplacement age). Similar age distribution for zircon, hornblende, biotite and sanidine has been observed for large volcanic systems such as the Fish Canyon Tuff (Bachmann et al., 2007). The age difference between biotite and sanidine has been interpreted to result from the different ability of these minerals to preserve small fractions of inherited argon in structural traps over much longer time periods than 10^4 years (Bachmann et al., 2007). On the other hand, the difference between U-Pb and ^{40}Ar-^{39}Ar ages has been interpreted as evidence for an extended period of magma crystallization (Bachmann et al., 2007).

The new documentation of an extended period of crystallization for the Campiglia igneous system match with the long-lived magmatic systems of Larderello (Dini et al., 2005, 2008) and western Elba Island (Dini et al., 2002, 2008). These data allow to speculate on the existence of multiple crustal reservoirs that are far larger than outcropping igneous products. Moreover, the observed mantle signature of metasomatic fluids (Paoli et al., in prep. - chapter 5, 6), as well as the need for an extra-heat source to produce a such extend metamorphism and later metasomatism of the Botro ai Marmi carbonatic host, suggest the presence of hidden mantle-derived reservoir into the crust (between 10 and 23 km). At such level conditions for crustal melting were episodically reached, and low fractions of crustal melts were locally produced and sequentially transferred to shallow levels. This behaviour could be controlled by multiple, small batches of mafic magma. Time-transgressive magmatic activity (both from mantle and crust), as well as rapid crystallization and cooling of magma, probably prevented the formation of a single, homogeneous, hybrid pluton at the emplacement level (Dini et al., 2008).

7.6. Conclusions

The Campiglia system offers exposures of the full range of emplacement types for magmas and related fluids, thus represents a prime case study to investigate the timescales of mechanism of magma deep storage, extraction, transfer, and shallow emplacement/eruption. New U-Pb CA-ID-TIMS geochronology from the Campiglia igneous system allow to reconstruct the evolution of crustal-derived and mantle-derived magmas that fed plutonic, subvolcanic and volcanic units over ~1 Ma.

Distribution of zircon ages is at odds with what can be expected for the crystallization interval of an igneous body. Indeed, that interval is shortest for the Botro ai Marmi pluton (~100 ka), intermediate for the subvolcanic mafic

Temperino porphyry (~650 ka), and longest for the volcanic San Vincenzo rhyolite (~1000 ka). Moreover, also the increasing extent of the gap between zircon U-Pb and sanidine Ar-Ar ages with decreasing emplacement depth, contrast with the usual cooling rate for the different igneous realms.

Geochronological data for the Campiglia igneous system lend support to a scenario (Fig. 7.4) where a bimodal deep reservoir remains in a magmatic condition (melt-present) for ~1 Ma. The magma extraction from a crustal felsic reservoir fed a pluton and its hydrothermal system during a short time interval at 5.4 Ma. At ~4.9 Ma the extraction of magma from a mafic reservoir fed the Temperino mafic porphyry. Finally, the late extraction of magma from the felsic reservoir (probably the same of the Botro ai Marmi granite) fed the San Vincenzo rhyolites, where early-crystallised zircons were transported/recycled within portions of melts extracted from the reservoir.

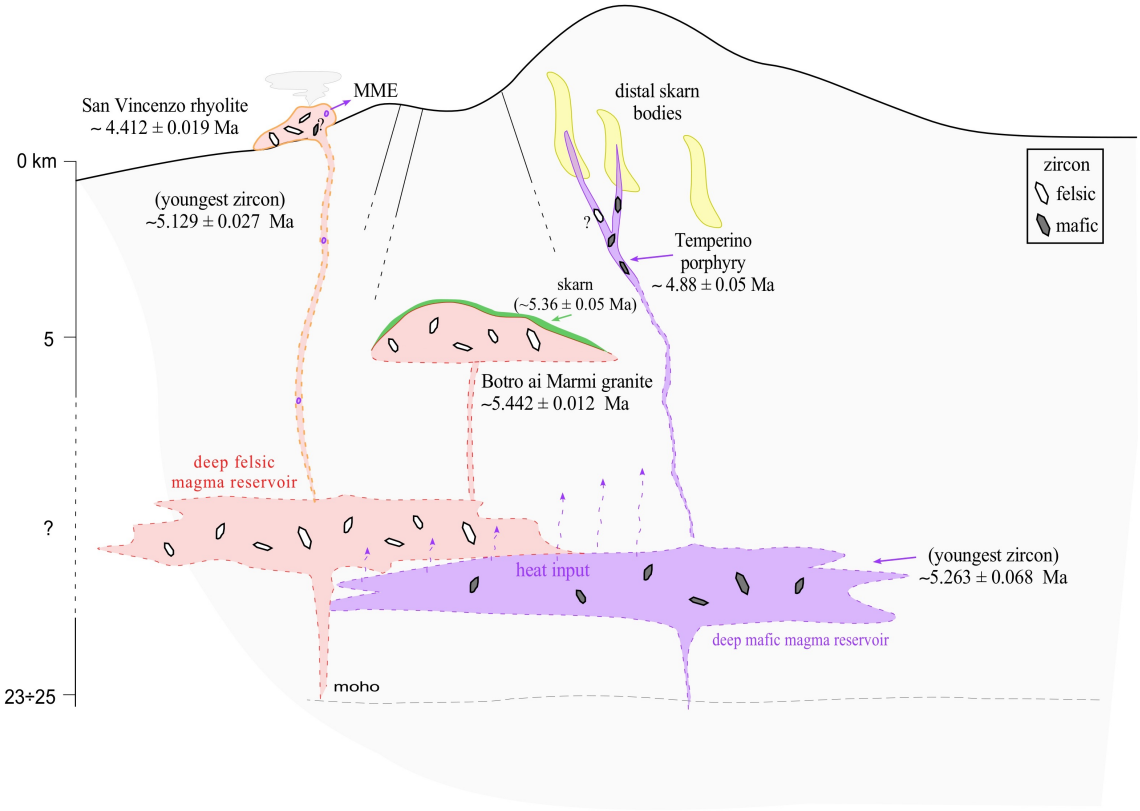

Fig. 7.4 - Schematic model for the evolution of the Campiglia Marittima magmatic-hydrothermal system, not to scale. Between bracket is indicated the emplacement/eruption age by Ar-Ar dating of sanidine. MME: mafic microgranular enclaves.

Acknowledgements

This project was partly funded by the Progetto di Ricerca di Ateneo PRA_2016_33. Thanks to G. Di Vincenzo and S. Vezzoni for fruitful discussion of unpublished ^{40}Ar-^{39}Ar data.

References

Annen, C., 2009. From plutons to magma chambers: thermal constraints on the accumulation of eruptible silicic magma in the upper crust. Earth Planet. Sci. Lett. 284, 409–416.

Bachmann, O., Oberli, F., Dungan, M. A., Meier, M., Mundil, R., Fischer, H., 2007. $^{40}Ar/^{39}Ar$ and U–Pb dating of the Fish Canyon magmatic system, San Juan Volcanic field, Colorado: Evidence for an extended crystallization history. Chemical Geology 236(1–2):,134-166.

Barboni, M., and Schoene, B., 2014. Short eruption window revealed by absolute crystal growth rates in a granitic magma. Nat. Geosci. 7, 524–528.

Barboni, M., Annen, C., and Schoene, B., 2015. Evaluating the construction and evolution of upper crustal magma reservoirs with coupled U/Pb zircon geochronology and thermal modeling: a case study from the Mt. Capanne pluton (Elba, Italy). Earth Planet. Sci. Lett. 432, 436–448.

Borsi, S., Ferrara, G., Tongiorgi, E., 1967. Determinazione con il metodo K/Ar delle età delle rocce magmatiche della Toscana. Boll. Soc. Geol. Ital. 86, 403–411.

Caricchi, L., Simpson, G., Schaltegger, U., 2014. Zircons reveal magma fluxes in the Earth's crust. Nature 511, 457-461

Caricchi, L., and Blundy, J. 2015. The temporal evolution of chemical and physical properties of magmatic systems, in Chemical, Physical and Temporal Evolution of Magmatic Systems. Geological Society of London, 1–15.

Caricchi, L., Simpson, G., Schaltegger, U., 2016. Estimates of Volume and Magma Input in Crustal Magmatic Systems from Zircon Geochronology: The Effect of Modeling Assumptions and System Variables. Frontiers in Earth Science 4.

Cashman, K.V., and Giordano, G., 2014. Calderas and magma reservois. Journal of Volcanology and Geothermal Research 288, 28–45.

Coble, M.A., 2013. New ion microprobe U-Pb analysis on unpolished zircon surfaces and polished grain interiors from the 28 Ma Fish Canyon Tuff reveal a protracted crystallization history. AGU fall meeting, San Francisco 2013.

Coleman, D.S., Gray, W., Glazner, A.F., 2004. Rethinking the emplacement and evolution of zoned plutons: geochronologic evidence for incremental assembly of the Tuolumne Intrusive Suite, California. Geology 32, 433. doi: 10.1130/g20220.1

Cooper, G.F., and Wilson, C.J.N., 2014. Development, mobilisation and eruption of a large crystal-rich rhyolite: the ongatiti ignimbrite, New Zealand. Lithos 198, 38–57.

de Saint Blanquat, M., Horsman, E., Habert, G., Morgan, S., Vanderhaeghe, O., Law, R., Tikoff, B., 2011. Multiscale magmatic cyclicity, duration of pluton construction, and the paradoxical relationship between tectonism and plutonism in continental arcs. Tectonophysics 500, 20-33.

Deering, C.D., Keller, B., Schoene, B., Bachmann, O., Beane, R., Ovtcharova, M., 2016. Zircon record of the plutonic-volcanic connection and protracted rhyolite melt evolution. Geology 44(4), 267-270.

Dini, A., Innocenti, F., Rocchi, S., Tonarini, S., Westerman, D.S., 2002. The magmatic evolution of the late Miocene laccolith–pluton–dyke granitic complex of Elba Island, Italy. Geological Magazine 139, 257-279.

Dini, A., Gianelli, G., Puxeddu, M., Ruggieri, C., 2005. Origin and evolution of Pliocene–Pleistocene granites from the Larderello geothermal field (Tuscan Magmatic Province, Italy). Lithos 81, 1–31.

Dini, A., Westerman, D.S., Innocenti, F., Rocchi, S., 2008. Magma emplacement in a transfer zone: the Miocene mafic Orano dyke swarm of Elba Island, Tuscany, Italy. Geol. Soc. (Lond.) Spec. Publ. 302, 131–148.

Farina, F., Dini, A., Innocenti, F., Rocchi, S., and Westerman, D.S., 2010. Rapid incremental assembly of the Monte Capanne pluton (Elba Island, Tuscany) by downward stacking of magma sheets. Geol. Soc. Am. Bull. 122, 1463–1479.

Feldstein, S.N., Halliday, A.N., Davies, G.R. and Hall, C.M., 1994. Isotope and chemical microsampling: Constraints on the history of an S-type rhyolite, San Vincenzo, Tuscany, Italy. Geochimica et Cosmochimica Acta 58, 943-958.

Ferrara, G., Petrini, R., Serri, G. and Tonarini, S., 1989. Petrology and isotope- geochemistry of San Vincenzo rhyolites (Tuscany, Italy). Bulletin Volcanologique 51, 379-388.

Franceschini, F., Innocenti, F., Marsi, A., Tamponi, M., Serri, G., 2000. Petrography and chemistry of the buried Pliocene Castel di Pietra pluton (Southern Tuscany, Italy). Neues Jahrb. Geol. Paleontol. Abh. 215, 17–46.

Kuiper, K.F., Deino, A., Hilgen, F.J., Krijgsman, W., Renne, P.R., and Wijbrans, J.R., 2008, Synchronizing rock clocks of earth history. Science 320, 500–504

Lattanzi, P., Benvenuti, M., Costagliola, P., Maineri, C., Mascaro, I., Tanelli, G., Dini, A. and Ruggieri, G.,2001. Magmatic versus hydrothermal processes in the formation of raw ceramic material deposits in southern Tuscany. Water-Rock interaction, 725-728.

Leuthold, J., Muntener, O., Baumgartner, L.P., Putlitz, B., Ovtcharova, M., Schaltegger, U., 2012. Time resolved construction of a bimodal laccolith (Torres del Paine, Patagonia). Earth and Planetary Science Letters 325, 85-92.

Lipman, P.W., and Bachmann, O., 2015. Ignimbrites to batholiths: Integrating perspectives from geological, geophysical, and geochronological data. Geosphere 11, 705-743.

Mercer, C.M. and Hodges, K.V., 2016. ArAR – A software tool to promote the robust comparison of K-Ar and $^{40}Ar/^{39}Ar$ dates published using different decay, isotopic, and monitor-age parameters. Chemical Geology 440, 148-163.

Michaut, C.and Jaupart, C., 2006. Ultra-rapid formation of large volumes of evolved magma. Earth Planet. Sci. Lett. 250, 38–52.

Paoli, G., Stokke, H.H., Rocchi, S., Sirevaag, H., Ksienzyk, A., Jacobs, J., Košler, J., 2016. Basement provenance revealed by U-Pb detrital zircon ages: a tale of African and European heritage in Tuscany, Italy. Lithos, in pres.

Renne, P.R., Mundil, R., Balco, G., Min, K., Ludwig, K.R., 2010. Joint determination of ^{40}K decay constants and $^{40}Ar^*/^{40}K$ for the Fish Canyon sanidine standard, and improved accuracy for $^{40}Ar/^{39}Ar$ geochronology. Geochim. Cosmochim. Acta 74 (18), 5349–5367.

Ridolfi, F., Renzulli, A., Perugini, D., Cesare, B., Braga, R., Del Moro, S. 2016. Unravelling the complex interaction between mantle and crustal magmas encoded in the lavas of San Vincenzo (Tuscany, Italy). Part II: Geochemical overview and modelling. Lithos 244, 233-249.

Rocchi, S., Dini, A., Mazzarini, F., Poli, G., 2003. Campiglia Marittima and Gavorrano intrusive magmatism. Periodico di Mineralogia 72, 127-132.

Samperton, K.M., Schoene, B., Cottle, J.M., Brenhin Keller, C., Crowley, J.L., Schmitz, M.D., 2015. Magma emplacement, differentiation and cooling in the middle crust: Integrated zircon geochronological–geochemical constraints from the Bergell Intrusion, Central Alps. Chemical Geology 417, 322–340.

Samson., D., and Alexandere., C., 1987. Calibration of the inter-laboratory $^{40}Ar/^{39}Ar$ dating standard, MMhb-1. Chem. Geol. 66, 27-34.

Sirevaag, H., Jacobs, J., Ksienzyk, A.K., Rocchi, S., Paoli, G., Jørgensen, H., Košler, J., 2016. From Gondwana to Europe: The journey of Elba Island (Italy) as recorded by U–Pb detrital zircon ages of Paleozoic metasedimentary rocks. Gondwana Research 38, 273–288.

Schaltegger, U., Brack, P., Ovtcharova, M., Peytcheva, I., Schoene, B., Stracke, A., Marocchi, M., Bargossi, G.M., 2009. Zircon and titanite recording 1.5million years of magma accretion, crystallization and initial cooling in a composite pluton (southern Adamello batholith, northern Italy). Earth and Planetary Science Letters 286, 208-218.

Vezzoni, S., Dini, A., Rocchi, S., 2016. Reverse telescoping in a distal skarn system (Campiglia Marittima, Italy). Ore Geology Reviews 77, 176-193.

Wotzlaw, J.F., Bindeman, I.N., Stern, R.A., D'Abzac, F.X., Schaltegger, U., 2015. Rapid heterogeneous assembly of multiple magma reservoirs prior to Yellowstone supereruptions. Scientific Reports 5.

Supplementary material

Ar-Ar methodology

In Vezzoni et al., in prep. - The San Vincenzo rhyolite event has been previously dated to 4.38±0.04 Ma (average Ar-Ar date on sanidine; Feldstein et al., 1994), using the MMhb-1 hornblende standard. Because $^{40}Ar/^{39}Ar$ ages are based on independent age determinations for standard minerals, it is critical that these standards be well characterised. This includes constraints both on the age of the standards themselves and the ages of the standards relative to one another. Spell and McDougall (2003) stated that results obtained inter-calibrating the MMhb-1 hornblende standard indicate homogeneity using subsamples of tens of milligrams, indicating that total fusion analysis of such large aliquots will yield reproducible results. However the MMhb-1 hornblende do not meet the criteria for acceptable standards at the single crystal sampling level, which compromises their usefulness especially on a small sample basis. Thus, the absolute uncertainty of $^{40}Ar/^{39}Ar$ dates are particularly sensitive to decay constant uncertainties. Uncertainties reflecting these systematic errors should be reported routinely, whenever $^{40}Ar/^{39}Ar$ dates are likely to be compared with dates obtained by independent methods (Renne et al., 1998).

The San Vincenzo age has been calculated prior to the development of the community consensus values for basic decay constants, isotopic abundances, and the ages of common monitor minerals. Thus, the whole age dataset has been recalculated using the Argon Age Recalculator (ArAR; Mercer and Hodges, 2016) allowing for more robust comparisons. The recalculated ages are usually ~1% older respect to the original data, nevertheless, these values are accurate enough for the aim of this study. In particular, the previous ages obtained for the San Vincenzo rhyolite using the MMhb-1 standard age (Samson and Alexander, 1987) has been recalculated using an intercalibration factor (R) based on new decay constants (Renne et al., 2011) and the up-to-date MMhb-1 standard age (Renne et al., 1998). Moreover, the correction allows for an increase related to the potential bias in the decay parameters of ^{40}K (Renne et al., 2011). The resulting "corrected" eruption age of 4.412±0.019 Ma (MSWD=0.80; n=9) do not varied significantly from the literature data. Therefore, we may define an eruption age of ~4.4 Ma, that is considerably younger than the youngest zircon age obtained from the San Vincenzo rhyolite (5.129±0.027 Ma).

U-Pb CA-ID-TIMS zircon ages

						Isotopic Ratios								Dates (Ma)						
Fraction	Th/U a	Pb* (pg) b	Pbc (pg) c	Pb*/Pbc d	206Pb/204Pb f	207Pb/206Pb g	±2σ %	207Pb/235U g	±2σ %	206Pb/238U g	±2σ %	Corr.coef.	207Pb/206Pb h	±2σabs	207Pb/235U h	±2σabs	206Pb/238U h	±2σabs	206Pb/238U<Th> i	±2σabs	% disc j
CA-ID-TIMS Zrn bulk																					
GBM4 unaltered granite																					
GBM4_z5	0.23	0.707	1.09	1	58	0.0532	40.8	0.0061	42	0.000826	1.8	0.751	338	920	6.1	2.6	5.323	0.098	**5.404**	**0.085**	98.43
GBM4_z2	0.18	2.20	0.59	4	253	0.04677	8.02	0.00535	8.3	0.0008300	0.33	0.742	36	190	5.42	0.45	5.348	0.018	**5.429**	**0.015**	85.22
GBM4_z4	0.24	4.81	0.44	11	694	0.04657	2.83	0.00534	2.9	0.0008315	0.15	0.641	26	68	5.40	0.16	5.3578	0.0081	**5.4403**	**0.0075**	79.70
GBM4_z6	0.17	1.36	0.41	3	228	0.04889	8.67	0.00562	9.0	0.0008340	0.38	0.743	141	200	5.69	0.51	5.374	0.021	**5.456**	**0.017**	96.20
GBM5 unaltered granite																					
GBM5_z1	0.19	1.73	0.81	2	150	0.04891	13.5	0.00560	14	0.0008308	0.56	0.747	143	320	5.67	0.79	5.353	0.030	**5.433**	**0.025**	96.24
GBM5_z4	0.19	1.07	0.44	2	172	0.04832	12.0	0.00554	12	0.0008326	0.50	0.755	114	280	5.61	0.69	5.365	0.027	**5.444**	**0.022**	95.28
GBM5_z2	0.36	0.843	0.40	2	146	0.04956	13.9	0.00572	14	0.0008369	0.59	0.749	173	320	5.79	0.83	5.393	0.032	**5.459**	**0.028**	96.89
GBM5_z3	0.13	0.796	0.39	2	149	0.04756	14.4	0.00551	15	0.0008401	0.60	0.751	76	340	5.58	0.82	5.413	0.032	5.502	0.027	92.89
GBM2A altered granite																					
GBM2A_z1	0.40	3.46	0.59	6	366	0.04826	5.25	0.00551	5.4	0.0008291	0.22	0.726	111	120	5.58	0.30	5.342	0.012	**5.424**	**0.011**	95.18
GBM2A_z4	0.29	2.08	0.49	4	281	0.04841	7.02	0.00554	7.3	0.0008299	0.31	0.730	118	170	5.61	0.41	5.348	0.017	**5.430**	**0.015**	95.48
GBM2A_z5	0.09	1.12	0.45	2	179	0.04718	11.6	0.00545	12	0.0008388	0.48	0.748	57	280	5.52	0.66	5.405	0.026	**5.491**	**0.019**	90.57
GBM2A_z6	0.33	0.394	0.40	1	77	0.0514	28.7	0.0060	30	0.000842	1.3	0.752	256	660	6.0	1.8	5.426	0.068	5.511	0.063	97.88
GBM2A_z2	0.42	0.747	0.72	1	78	0.0589	29.4	0.0068	31	0.000836	1.7	0.817	561	640	6.9	2.1	5.387	0.093	5.465	0.086	99.04
PV319 mafic dyke																					
PV319_z1	0.25	5.61	1.16	5	319	0.04640	6.49	0.00521	6.7	0.0008145	0.29	0.670	17	160	5.28	0.35	5.249	0.015	**5.331**	**0.014**	69.92
PV319_z9	0.25	2.87	1.06	3	186	0.04572	11.5	0.00511	12	0.0008112	0.46	0.726	-18	280	5.18	0.61	5.227	0.024	**5.309**	**0.021**	128.49
PV319_z19	0.38	0.938	0.74	1	93	0.0488	23.9	0.0055	25	0.0008105	0.99	0.751	137	560	5.5	1.4	5.222	0.052	**5.304**	**0.047**	96.19
PV319_z51	0.36	0.557	0.55	1	79	0.0487	29.6	0.0054	30	0.0008039	1.2	0.751	132	700	5.5	1.7	5.180	0.063	**5.263**	**0.068**	96.07
PV319_z48	0.70	0.848	0.74	1	80	0.0534	26.4	0.0083	27	0.001131	1.2	0.749	345	600	8.4	2.3	7.287	0.088	7.369	0.088	97.89
PV319_z42	0.60	0.391	0.63	1	53	0.0520	48.3	0.0061	50	0.000844	2.1	0.752	285	1100	6.1	3.0	5.44	0.12	5.52	0.11	98.09
MGC_P mafic dyke																					
MGC_P_z15	0.45	3.31	0.88	4	238	0.04761	8.40	0.00508	8.7	0.0007741	0.35	0.740	79	200	5.14	0.44	4.988	0.018	**5.070**	**0.016**	93.69
MGC_P_z13	0.56	1.09	0.56	2	127	0.04981	16.1	0.00552	17	0.0008037	0.69	0.748	185	370	5.59	0.93	5.179	0.036	**5.261**	**0.034**	97.20
MGC_P_z7	0.32	1.56	1.05	1	108	0.04973	19.5	0.0054	20	0.0007807	0.82	0.749	181	460	5.4	1.1	5.031	0.041	**5.113**	**0.037**	97.22
MGC_P_z21	0.25	0.593	0.65	1	74	0.0448	34.7	0.0048	36	0.000772	1.3	0.751	-68	850	4.8	1.7	4.977	0.066	5.068	0.060	107.32
GZT4 San Vincenzo rhyolite																					
GZT4_z2	0.20	3.54	1.84	2	138	0.04901	14.9	0.00529	15	0.0007833	0.63	0.746	147	350	5.36	0.82	5.047	0.032	**5.129**	**0.027**	96.57
GZT4_z7	0.19	1.05	0.52	2	146	0.05094	13.7	0.00566	14	0.0008065	0.62	0.748	237	310	5.73	0.81	5.197	0.032	5.279	0.027	97.81
GZT4_z6	0.52	3.03	0.73	4	255	0.04789	7.79	0.00990	8.0	0.0015005	0.35	0.710	93	180	10.01	0.80	9.665	0.034	9.758	0.034	89.58
GZT4_z5	0.29	0.605	0.46	1	98	0.0474	23.3	0.0054	24	0.0008219	0.95	0.751	70	550	5.4	1.3	5.296	0.051	5.366	0.043	92.45
GZT4_z4	0.22	0.811	0.65	1	95	0.0496	22.9	0.0057	24	0.0008301	0.96	0.751	173	530	5.7	1.3	5.349	0.051	5.428	0.044	96.91
GZT4_z3	0.55	0.448	0.40	1	81	0.0514	27.0	0.0057	28	0.0008054	1.2	0.751	260	620	5.8	1.6	5.190	0.062	5.272	0.058	98.00

a Th contents calculated from radiogenic 208Pb and the 207Pb/206Pb date of the sample, assuming concordance between U-Th and Pb systems.
b Total mass of radiogenic Pb.
c Total mass of common Pb.
d Ratio of radiogenic Pb (including 208Pb) to common Pb.
e Th/U ratio of magma from which mineral crystallized.
f Measured ratio corrected for fractionation and spike contribution only.
g Measured ratios corrected for fractionation, tracer and blank.
h Isotopic dates calculated using the decay constants λ238 = 1.55125E-10 and λ235 = 9.8485E-10 (Jaffey et al. 1971).
i Corrected for initial Th/U disequilibrium using radiogenic 208Pb and Th/U[magma] specified.
j % discordance = 100 - (100 * (206Pb/238U date) / (207Pb/206Pb date))

U-Pb LA-ICP-MS zircon ages from San Vincenzo rhyolite

	Isotopic Ratios								Dates (Ma)						
Fraction	*206Pb/204Pb f*	*207Pb/206Pb g*	*±2σ %*	*207Pb/235U g*	*±2σ %*	*206Pb/238U g*	*±2σ %*	*Corr.coef.*	*207Pb/206Pb h*	*±2σabs*	*207Pb/235U h*	*±2σabs*	*206Pb/238U h*	*±2σabs*	*% disc j*
GZT4-01	1156	0.164	0.9	3.258	35	0.153	26	0.37	2414	21	1471	508	915	233	62
GZT4-02	50	0.053	4.8	0.005	16	0.001	13	0.26	37	117	5.0	0.8	4.9	0.4	87
GZT4-03	175	0.047	5.5	0.006	28	0.001	22	0.37	24	133	5.9	1.6	5.9	1.2	75
GZT4-04	24	0.052	7.4	0.007	31	0.001	13	0.23	776	156	7.2	2.2	5.2	0.7	99
GZT4-06	112	0.052	5.4	0.005	18	0.001	13	0.21	-37	132	5.0	0.9	5.1	0.4	114
GZT4-07	7508	0.073	4.1	0.007	52	0.001	13	0.08	793	87	7.0	3.6	5.0	0.4	99
GZT4-09	-14	0.049	7.3	0.005	20	0.001	29	0.62	375	166	5.4	1.1	4.7	1.2	99
GZT4-11	48	0.054	5.1	0.005	22	0.001	14	0.26	55	125	4.6	1.0	4.6	0.5	92
GZT4-12	-28945	0.061	6.7	0.006	16	0.001	13	0.34	498	149	6.3	1.1	5.2	0.6	99
GZT4-13	244	0.050	5.2	0.007	15	0.001	11	0.23	320	120	6.6	1.0	5.8	0.4	98
GZT4-15	920	0.059	1.7	0.316	37	0.038	42	0.57	645	42	279	103	239	101	63
GZT4-16	312	0.044	4.1	0.004	15	0.001	13	0.24	-600	113	4.1	0.6	5.2	0.4	101
GZT4-17	-56	0.111	6.1	0.012	12	0.001	13	0.41	1883	112	12	1.5	5.0	0.5	100
GZT4-20	16355	0.062	1.9	0.480	8	0.059	10	0.59	601	44	398	32	367	35	39
GZT4-21	68	0.126	7.6	0.017	15	0.001	11	0.25	2117	134	17	2.7	6.0	0.5	100
GZT4-28	-23	0.072	6.5	0.006	46	0.001	13	0.15	261	153	5.8	2.6	5.2	0.7	98
GZT4-29	9696	0.057	2.8	0.006	15	0.001	11	0.28	159	69	6.2	0.9	5.8	0.5	96
GZT4-30	3491	0.069	1.6	0.772	7	0.082	7	0.45	891	36	581	43	508	34	43
GZT4-33	-99	0.256	4.5	0.037	11	0.001	8	0.29	3071	72	37	4	8	0	100
GZT4-34	4	0.118	5.7	0.018	11	0.001	11	0.31	2328	98	18	2.0	5.8	0.4	100
GZT4-37	287	0.033	5.8	0.002	26	0.001	13	0.16	-2295	243	2.3	0.6	4.9	0.4	100
GZT4-38	-40	0.057	4.6	0.007	10	0.001	13	0.34	624	101	6.9	0.7	5.3	0.4	99
GZT4-39	3983	0.065	0.8	0.762	16	0.090	13	0.40	663	25	575	91	557	71	16
GZT4-40	-68	0.065	4.8	0.008	9	0.001	13	0.41	853	100	7.8	0.7	5.4	0.4	99
GZT4-41	1830	0.097	6.2	0.009	20	0.001	13	0.21	1126	125	8.8	1.7	5.3	0.4	100
GZT4-41	430	0.051	3.9	0.005	13	0.001	13	0.26	-72	100	4.7	0.6	4.9	0.4	107
GZT4-42	112	0.053	5.1	0.005	21	0.001	13	0.23	24	125	4.9	1.0	4.9	0.5	80
GZT4-43	369	0.060	5.1	0.007	10	0.001	11	0.31	526	114	7.0	0.7	5.6	0.4	99
GZT4-44	139	0.106	9.0	0.011	109	0.001	30	0.16	1190	178	11	12	6.3	2.2	99
GZT4-46	82	0.382	5.7	0.005	624	0.001	38	0.03	-152	142	4.6	29	5.0	1.7	103
GZT4-48	92	0.059	5.2	0.007	15	0.001	13	0.32	552	116	6.9	1.0	5.5	0.5	99
GZT4-50	-202	0.062	5.4	0.007	12	0.001	13	0.30	482	123	6.7	0.8	5.5	0.4	99
GZT4-53	-185	0.176	1.2	0.946	11	0.040	11	0.53	2576	25	676	71	254	28	90
GZT4-54	1678	0.056	1.8	0.007	123	0.001	91	0.36	-126	48	6.9	8.6	7.4	6.5	106
GZT4-56	-3	0.045	4.9	0.005	10	0.001	14	0.66	130	116	5.0	0.5	4.8	0.6	96
GZT4-57	7151	0.073	2.6	0.480	36	0.037	91	1.25	1501	52	398	145	237	216	84
GZT4-58	-13	0.074	4.5	0.007	20	0.001	13	0.27	714	97	6.7	1.3	4.9	0.5	99
GZT4-59	504	0.060	3.7	0.007	13	0.001	11	0.29	438	83	6.8	0.9	5.7	0.4	99
GZT4-61	-18	0.047	8.2	0.006	25	0.001	25	0.61	554	180	6.5	1.6	5.1	1.5	99
GZT4-63	-11	0.081	7.6	0.006	54	0.001	33	0.24	776	160	5.6	3.0	4.0	1.0	99
GZT4-64	16	0.050	5.2	0.005	39	0.001	25	0.28	7	126	5.2	2.0	5.2	1.1	23
GZT4-66	1801	0.054	5.9	0.005	19	0.001	13	0.18	123	142	5.5	1.0	5.3	0.3	96
GZT4-68	13	0.131	5.5	0.019	16	0.001	20	0.78	2295	95	19	3.0	6.2	1.5	100

GZT4-72	229	0.055	5.4	0.008	16	0.001	11	0.19	734	116	8.0	1.3	5.8	0.4	99
GZT4-73	34	0.058	5.7	0.005	24	0.001	14	0.25	335	129	5.5	1.3	4.8	0.6	99
GZT4-74	11	0.076	6.2	0.012	13	0.001	8	0.45	1034	127	12	1.5	7.6	0.9	99
GZT4-75	-6805	0.058	5.0	0.006	16	0.001	13	0.34	395	113	5.8	1.0	5.0	0.6	99
GZT4-76	-34	0.096	4.5	0.009	20	0.001	11	0.19	1023	92	8.8	1.7	5.6	0.4	99
GZT4-78	-77	0.067	3.4	0.007	12	0.001	11	0.28	496	77	6.9	0.9	5.6	0.4	99
GZT4-79	112	0.043	5.5	0.004	17	0.001	14	0.32	-239	142	4.3	0.7	4.8	0.5	102
GZT4-80	31	0.051	3.5	0.006	13	0.001	13	0.40	149	84	5.7	0.7	5.4	0.5	96
GZT4-81	-55	0.065	13.0	0.006	167	0.001	25	0.09	292	299	5.9	10	5	2	98
GZT4-82	-82	0.059	5.1	0.005	18	0.001	0	0.18	48	123	5.1	0.9	5.1	0.3	89
GZT4-83	206	0.055	8.7	0.006	38	0.001	14	0.17	711	187	6.5	2.4	4.8	0.6	99
GZT4-84	-176	0.058	5.7	0.006	22	0.001	0	0.14	385	128	6.0	1.3	5.1	0.3	99
GZT4-85	-391	0.067	2.7	0.010	7	0.001	10	0.42	909	59	10	0.7	6.6	0.4	99
GZT4-86	70	0.118	4.3	0.018	27	0.001	9	0.23	2052	78	18	5.0	6.8	0.9	100
GZT4-89	133	0.101	5.6	0.012	16	0.001	11	0.40	1622	107	12	2.0	5.7	0.7	100
GZT4-90	257	0.052	7.5	0.008	11	0.001	10	0.36	609	161	7.9	0.9	6.1	0.5	99
GZT4-91	99	0.064	4.2	0.004	27	0.001	13	0.14	-320	109	4.5	1.2	5.2	0.4	102
GZT4-92	46	0.427	3.5	0.078	46	0.001	46	0.48	4016	54	76	35	8.5	3.7	100
GZT4-93	294	0.053	4.5	0.005	14	0.001	13	0.29	75	108	5.0	0.7	4.9	0.4	93
GZT4-94	-72	0.078	6.1	0.007	40	0.001	13	0.19	760	130	6.9	2.7	5.0	0.7	99
GZT4-95	26	0.069	5.5	0.007	11	0.001	11	0.28	494	122	7.0	0.8	5.7	0.4	99
GZT4-96	121	0.070	6.0	0.006	16	0.001	13	0.25	579	131	6.2	1.1	4.8	0.4	99
GZT4-97	646	0.055	4.2	0.005	19	0.001	13	0.21	-187	107	4.8	0.9	5.2	0.4	103
GZT4-98	11	0.060	5.1	0.006	33	0.001	43	0.72	766	110	6.4	2.1	4.6	2.1	99
GZT4-99	18100	0.054	1.1	0.330	6	0.045	6	0.51	338	30	289	18	286	18	15
GZT4-103	2	0.139	5.2	0.015	76	0.001	44	0.28	1945	95	15	11	5.7	2.5	100
GZT4-105	26	0.111	9.4	0.011	94	0.001	38	0.20	1592	177	11	10	5.2	1.9	100
GZT4-107	-623	0.056	5.4	0.005	22	0.001	13	0.23	51	128	5.1	1.1	5.0	0.5	90
GZT4-108	-61	0.114	8.0	0.015	17	0.001	10	0.21	1762	147	15	2.6	6.6	0.5	100
GZT4-109	-155	0.056	8.1	0.005	74	0.001	11	0.05	-525	216	4.8	3.5	6.0	0.4	101
GZT4-110	-13255	0.048	4.4	0.005	17	0.001	11	0.22	-365	118	4.7	0.8	5.5	0.4	102
GZT4-111	-125	0.060	7.3	0.006	73	0.001	25	0.15	386	163	6.1	4.4	5.2	1.1	99
GZT4-112	42	0.042	8.7	0.006	15	0.001	60	1.99	-185	217	6.3	0.9	6.4	3.8	103
GZT4-113	77	0.049	9.5	0.005	76	0.001	25	0.16	141	224	4.7	3.5	5.1	1.2	96
GZT4-114	83	0.158	11.4	0.020	20	0.001	22	0.43	2441	192	20	4.0	5.6	1.0	100
GZT4-115	24	0.050	6.4	0.005	87	0.001	11	0.04	225	145	4.6	3.9	5.7	0.4	97
GZT4-115	1661	0.048	6.3	0.005	10	0.001	13	0.44	90	150	5.1	0.6	5.0	0.5	94
GZT4-116	52	0.040	4.7	0.004	7	0.001	0	0.19	-315	121	4.3	0.4	5.0	0.2	102
GZT4-117	43	0.357	15.5	0.023	1659	0.001	389	0.12	3749	236	23	380	5.5	23	100
GZT4-118	1793	0.083	5.2	0.011	9	0.001	0	0.21	1292	100	11	1.0	6.1	0.2	100
GZT4-118	3	0.082	6.7	0.010	14	0.001	0	0.17	1269	130	10	1.4	5.8	0.3	100
GZT4-119	179	0.080	6.5	0.010	12	0.001	0	0.18	1221	127	10	1.2	5.5	0.2	100
GZT4-120	-45	0.054	4.1	0.005	15	0.001	14	0.24	399	92	4.8	0.7	4.8	0.4	99
GZT4-121	1380	0.048	3.9	0.005	8	0.001	0	0.30	125	95	5.1	0.4	4.7	0.2	96

Supplementary Table 7.2. - Cathodoluminescence images of selected zircons from the Botro ai marmi granite.. Sample name and facies labeled in each panel. See Supplementary Table 7.1. for full ID-TIMS $^{206}Pb/^{238}U$ dates.

Phlogopite-titanite granite - GBM2A

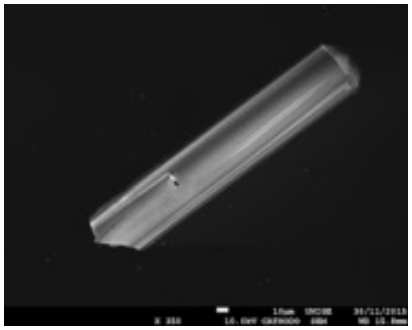

GBM2A-01 #85

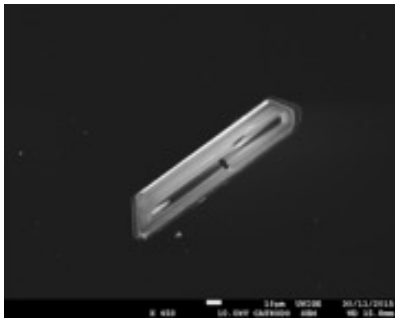

GBM2A-03 #2

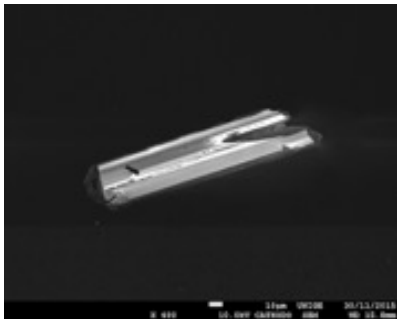

GBM2A-05 #73

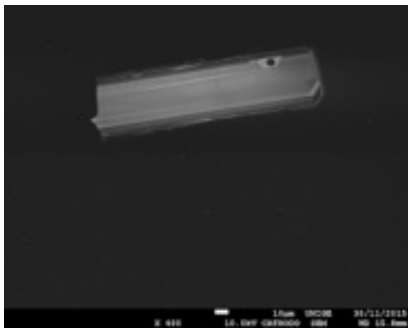

GBM2A-15 #77

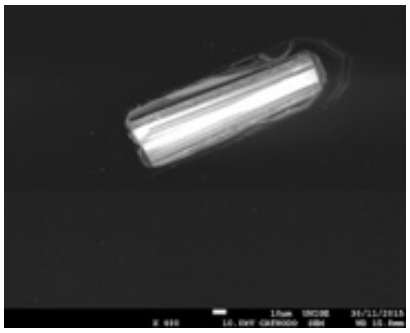

GBM2A-16 #53

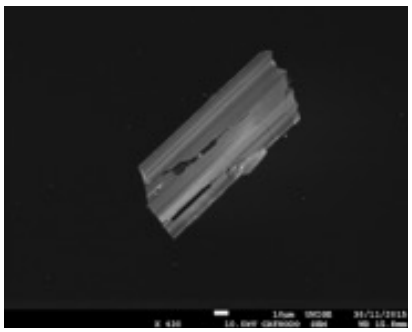

GBM2A-09 #15

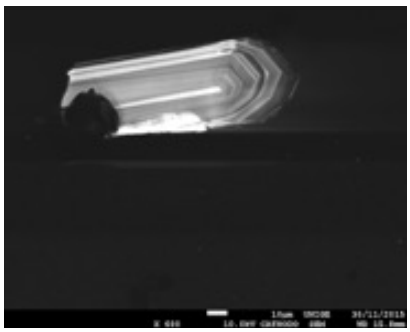

GBM2A-13 #70

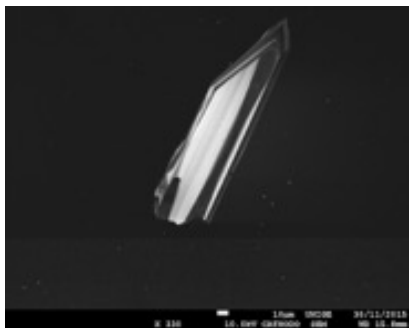

GBM2A-06 #16

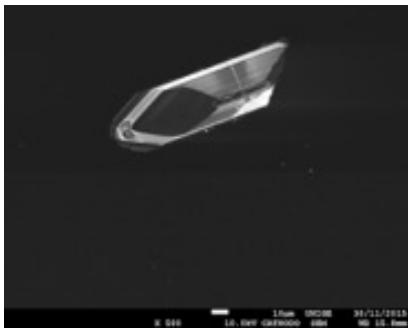

GBM2A-14 #66

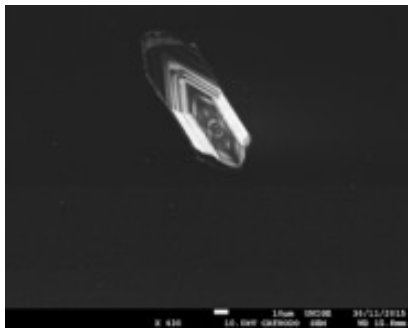

GBM2A-21 #69

Temperino porphyry - MGC, PV-319

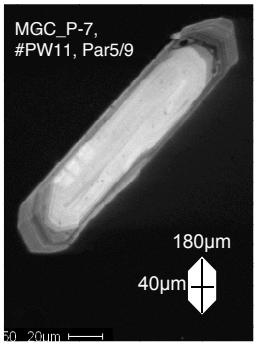

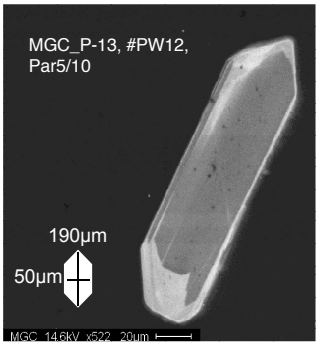

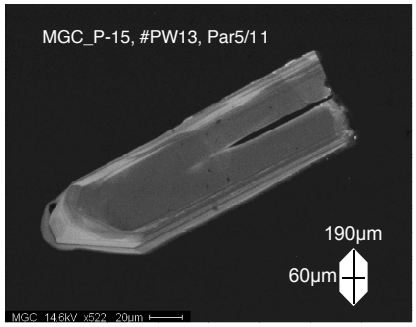

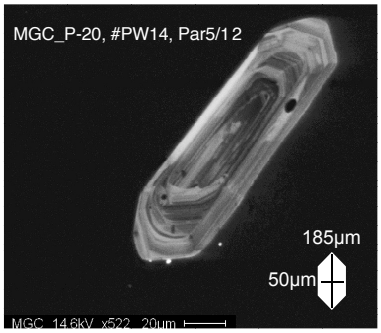

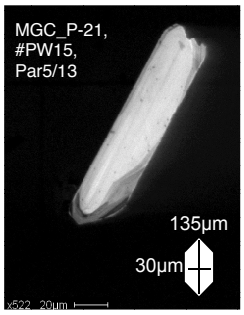

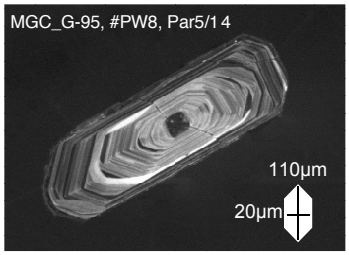

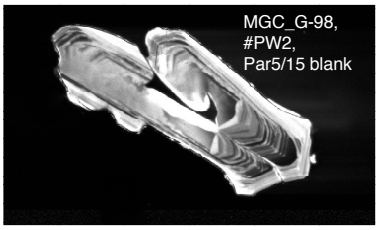

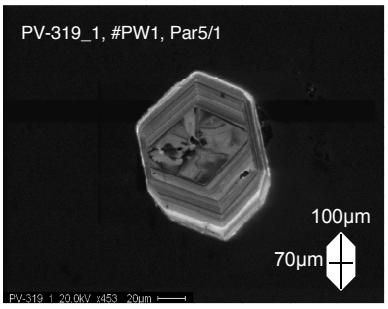

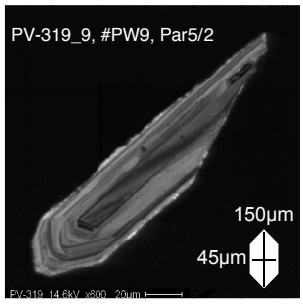

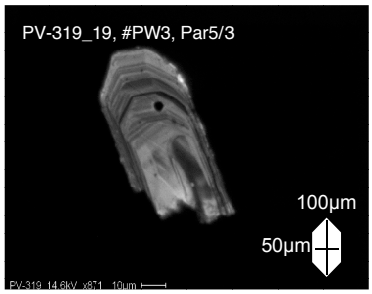

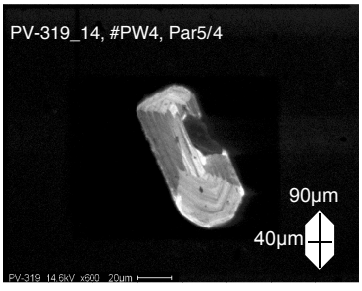

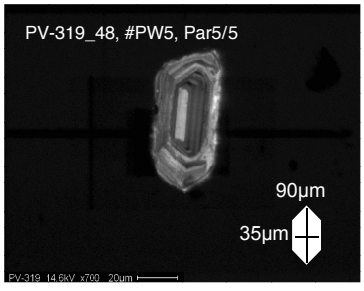

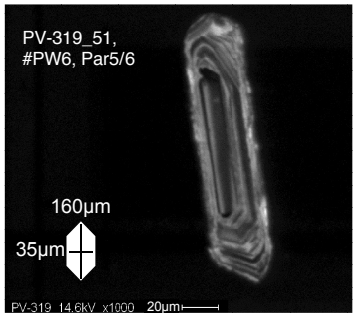

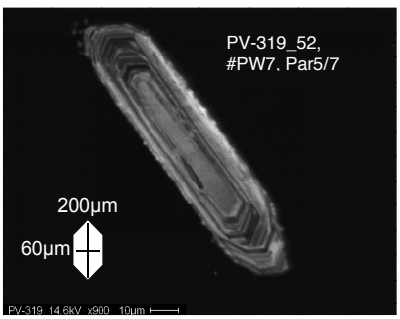

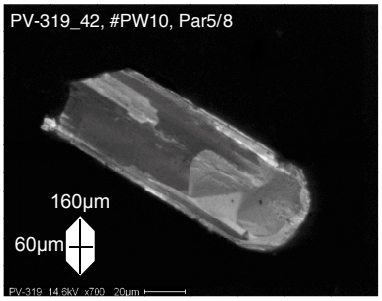

Biotite granite - GBM4, BM5

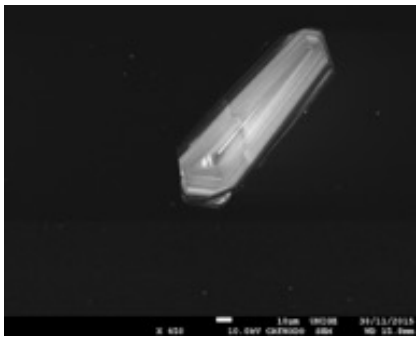

GBM5-23 #127

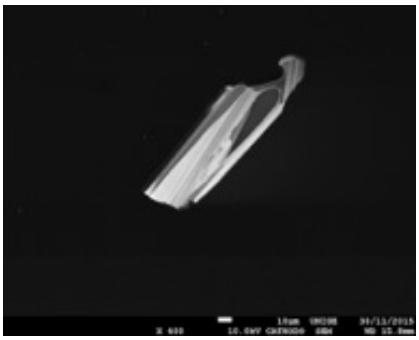

GBM5-26 #132

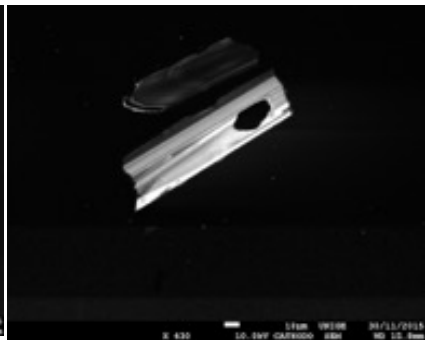

GBM5-37 #14

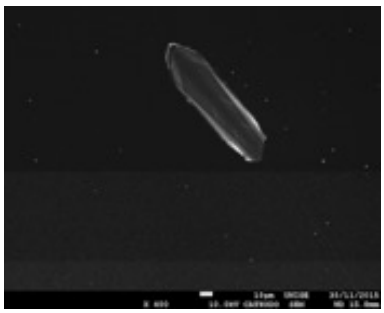

GBM5-49 #121

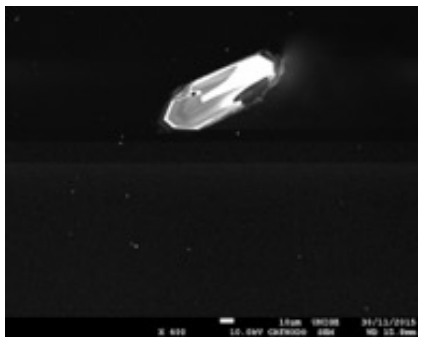

GBM5-48 #121

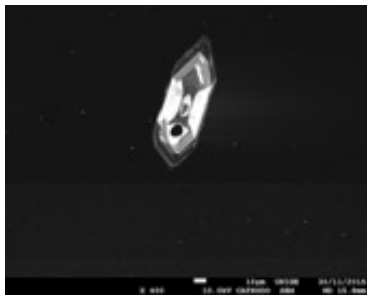

GBM5-32 #121

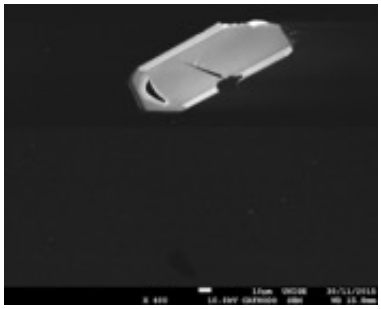

GBM4-56 #71

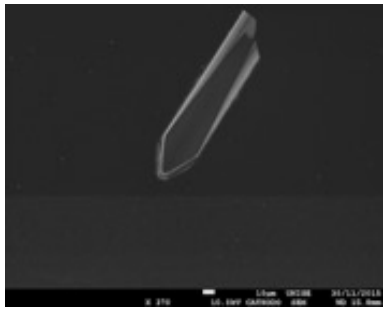

GBM4-57 #125

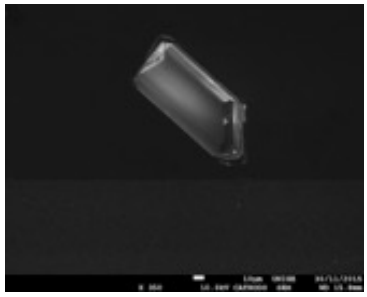

GBM4-65 #119

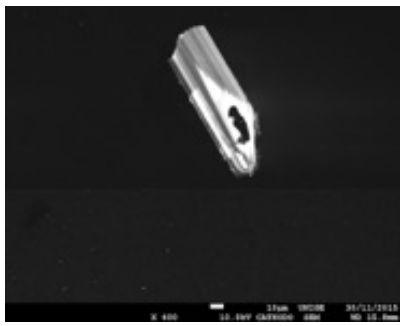

GBM4-61 #103

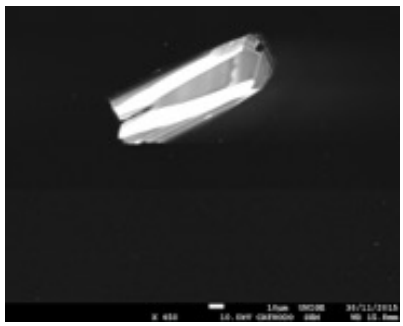

GBM4-58 #130

8. Summary and conclusions

At Campiglia the occurrence of multiple magmatic events over about 1000 ka generated an intense metasomatic fluid circulation. These magmatic processes began with the emplacement of the Botro ai Marmi monzogranitic pluton (~5.4 Ma), that was followed by mafic and later felsic porphyritic bodies (from 4.9 to 4.5 Ma) crosscutting the contact aureole generated by the monzogranite intrusion in the carbonate host rock. The closing event is represented by the early Pliocene (~4.4 Ma) rhyolitic extrusive complex of San Vincenzo. The hydrothermal metasomatic activity related to the whole igneous cycle generated proximal endo- and exoskarn as well as distal mineralised skarn bodies, exploited for Cu-Pb-Zn-Ag for over twenty-seven centuries and which are considered as a classic example of contact exoskarn generated by the interaction between a magmatic body and a marble host rock.

The Campiglia system offers exposures of the full range of emplacement types for magmas and related fluids, thus represents a prime case study to investigate the timescales of mechanism of magma deep storage, extraction, transfer, and shallow emplacement/eruption. New U-Pb CA-ID-TIMS geochronology from the Campiglia igneous system allows to reconstruct the evolution of crustal-derived and mantle-derived magmas that fed plutonic, subvolcanic and volcanic units over 1000 ka. Distribution of zircon ages is at odds with what can be expected for the crystallization interval of an igneous body. Indeed, that interval is short for the Botro ai Marmi pluton (100 ka), intermediate for the subvolcanic mafic Temperino porphyry (450 ka), and long for the volcanic San Vincenzo rhyolite (700 ka). The youngest zircons from the Botro ai Marmi granite have ages identical to ^{40}Ar-^{39}Ar ages of biotite from the granite and metasomatic phlogopite from skarn crosscutting the granite. The Temperino mafic porphyry and the San Vincenzo rhyolite show younger sanidine ages (emplacement/eruption age). The youngest zircon age from the pluton is therefore assumed to approximate the age of emplacement and final crystallization of the melt, whereas the zircons from the Temperino mafic porphyry and the San Vincenzo rhyolite are considered antecrystic, derived from re-mobilised earlier magma extracted from a deeper reservoir at the emplacement age. The new documentation of an extended period of crystallization for the Campiglia igneous system (about 1000 ka) matches with observations for the long-lived magmatic systems of Larderello and Elba Island. These data support the existence of multiple crustal reservoirs far larger than outcropping igneous products. The observed mantle signature of metasomatic fluids suggests the presence of hidden mantle-derived reservoir able to activate episodically crustal melting and magma transfer to shallow levels. This sequential magmatic activity (both from mantle and crust) could be controlled by multiple, small batches of mafic magma, that did not lead to the formation of a single, homogeneous, hybrid pluton at the emplacement level.

The Botro ai Marmi granitic pluton underwent intense metasomatic alteration and post-magmatic fluid-rock interaction processes. The complicated patterns of alteration resulted from the superimposition of alteration and mineralisation patterns associated with multiple metasomatic events. Potassic and calcic metasomatism are associated with fluids released by a deep mafic source. Indeed, metasomatic alteration produced the significant gain of Mg, Fe, Ca, as well as gain of metals. Potassic alteration interested the whole exposed monzogranite, while calcic and more acidic metasomatism is confined along the magmatic jointing (endoskarn veins) and adjacent to de contact between the pluton and the host marble (exoskarn). Fluid flow away from the intrusion generated Mg-rich skarn in the folded marble. Moreover, Ca-rich bodies are affected by secondary dissolution/replacement textures, suggesting the increasing acidity of hydrothermal fluids. Reciprocal reactions involving replacement of (i) plagioclase by K-feldspar, (ii) biotite by phlogopite+chlorite+titanite, (iii) biotite by diopside+titanite+phlogopite±allanite, and (iv) calcite+dolomite±micas by garnet±vesuvianite±diopside±phlogopite±epidote reflect the exchange of mass between fluid and wall rock. Moreover, hydrothermal circulation of HFSE, REE, Th, U, P, Zr, Ti resulted in the local crystallisation of HFSE-REE and Th-U accessory minerals. Fluid(s) circulation is enhanced by the diffuse jointing at the top of the pluton, probably generated by the continuous release of volatiles from the magmatic reservoir. Shortly after emplacement or during a late-magmatic stage, circulation of B-rich fluid formed disseminated tourmaline-quartz orbicules, which tend to be

particularly abundant in zones of fracturing forming veinlets systems. The intrusion generates a widespread contact aureole and an almost pure marble. Successively, a high-temperature, mafic fluid generated a pervasive potassic metasomatism. During this process plagioclase has been intensively replaced by K-feldspar, while biotite has been replaced by phlogopite-chlorite-titanite aggregates. Almost simultaneously, the circulation of Ca-Mg-rich fluids resulted in the crystallization of a variety of calc-silicates (e.g., diopside, vesuvianite, garnet, epidote), particularly abundant at the carbonate-granite contact, and along veins into the granite. During this stage, the monzogranite experienced loss of Fe and Na and gain of Mg, K, Rb, Ba, Sr. Trace elements, REE, Ti and P show only a local mobilisation/ recrystallisation effect. Upon cooling, fluids became more acidic, with the increasing fluorine activity. The increasing acidity is testified by the widespread crystallisation of fluorite frequently related to the occurrence of textural disequilibrium (fluorite-Ca-silicates pseudomorphs, patchy zoning of calc-silicates, dissolution/precipitation textures). The metasomatic alteration of earlier calc-silicates increased the mobilisation of REE and HFSE. During this process, low-temperature and low pH as well as availability of F and Cl to complex with HFSE and REE support the destabilisation of accessory minerals, such as zircons, apatite, monazite. Once the fluid mixed with the Ca-bearing fluid a new generation of metasomatic accessory minerals precipitated on a large scale, both in the granite and metasomatic bodies (e.g., zircon, apatite, allanite, thorite, uraninite as well another HFSE-REE-bearing minerals).

Thus, the present study allows to reconstruct a model able to explain the main mechanisms responsible for the metasomatic alteration of a shallow level, peraluminous monzogranite. High fluid pressure (input from a mafic reservoir) would be responsible for the bulge structure of the monzogranite pluton. Magmatic joints, marble bedding, and carbonate folding probably have been promoted the fluid circulation, also at long distance (up to 3 km). The diffusive alteration outward from endoskarn veins testify pervasive fluid-rock reactions. The character of the metasomatic alteration, typical of porphyry copper systems (Ca-Mg-Ba-Sr gains), supports the hypothesis of fluid released by a mafic reservoir. Concluding, this study emphasises the importance of relating field studies to petrographic observation and detailed geochemical analysis. Moreover, it shows how such linkage can lead to the construction of a litho-geochemical model for the element mobilities in a crustal magmatic-hydrothermal setting.

References (referring to chapter 1 to 4)

Acocella, V. and Rossetti F., 2002. The role of extensional tectonics at different crustal levels on granite ascent and emplacement: an example from Tuscany (Italy). Tectonophysics 354, 71-83.

Acocella, V., Rossetti, F., Facenna, C., Funiciello, R., Lazzarotto, A., 2000. Strike-slip faulting and pluton emplacement in Southern Tuscany: the Campiglia Marittima case. Bollettino della Società Geologica italiana 119(10): 22.

Aleksandrov, S.M. and Troneva, M.A., 2000. Isomorphism in Borates of the Ludwigite–Vonsenite Series from Magnesian Skarns of North America. Geochem. Int. 38, 144–158.

Andersen, T., 2005. Detrital zircons as tracers of sedimentary provenance: limiting conditions from statistics and numerical simulation: Chemical Geology, 216, 249-270.

Baldi, P., Bellani, S., Ceccarelli, A., Fiordalisi, A., Squarci, P., Taffi, L., 1994. Correlazioni tra le anomaile termiche ed altri elementi geofisici e strutturali della Toscana meridionale. Studi Geologici Camerti 1, 139- 149.

Barberi, F., Innocenti, F., Mazzuoli, R., 1967. Contributo alla conoscenza chimico-petrografica e magmatologica delle rocce intrusive, vulcaniche e filoniane del Campigliese (Toscana). Memorie Società Geologica Italiana 6, 643-681.

Barberi, F., Innocenti, F., Ricci, C. A., 1971. Il magmatismo nell'Appennino centro-settentrionale. Rendiconti Società Italiana di Mineralogia e Petrologia 27, 3-46.

Borsi, S., Ferrara, G., Tongiorgi, E., 1967. Determinazione con il metodo K/Ar delle età delle rocce magmatiche della Toscana. Boll. Soc. Geol. Ital. 86, 403–411.

Bossio, A., Costantini, A., Foresi, L., Lazzarotto, A., Liotta, D., Mazzanti, R., Mazzei, R., Salvatorini, G., Sandrelli, F. (1995). Studi preliminari sul sollevamento della Toscana meridionale dopo il Pliocene medio. Studi Geologici Camerti 1, 87-91.

Bowden, P., 1985. The geochemistry and mineralization of alkaline ring complexes in Africa (a review). Journal of African Earth Sciences 3, 17-40.

Bowden, P., Kinnard, J.A., Abaa, S.I., Ike, E.C., Turaki, U. M., 1984. Geology and mineralization of the Nigerian anorogenic ring complexes. Geologisches Jahrbuch Reihe B 56, 1-65.

Bowring, J.F., McLean, N.M., Bowring, S.A., 2011. Engineering cyber infrastructure for U-Pb geochronology: Tripoli and U-Pb Redux. Geochemistry Geophysics Geosystems, 12.

Brogi, A. and Cerboneschi, A., 2007. Upper crust "boudinage" during post-collisional Miocene extension in Tuscany: insights from the southern part of the Larderello geothermal area (Northern Apennines, Italy). Geodinamica Acta 20, 327-351.

Brogi, A., 2008. The Triassic and Paleozoic successions drilled in the Bagnore Geothermal field and Poggio Nibbio area (Monte Amiata, Northern Apennines, Italy). Bollettino della Società Geologica Italiana 3, 599-613.

Burt, D.M., 1981. Acidity-salinity diagrams- application to greisen and porphyry deposits. Economic Geology 76(4), 832-843.

Caricchi, L., Simpson, G., Schaltegger, U., 2014. Zircons reveal magma fluxes in the Earth's crust. Nature 511, 457-461.

Caricchi, L., Simpson, G., Schaltegger, U., 2016. Estimates of Volume and Magma Input in Crustal Magmatic Systems from Zircon Geochronology: The Effect of Modelling Assumptions and System Variables. Frontiers in Earth Science, http://dx.doi.org/10.3389/feart.2016.00048

Carmignani, L., Decandia, F.A., Fantozzi, P. L., Lazzarotto, A., Liotta, D., Meccheri, M., 1994. Tertiary extensional tectonics in Tuscany (Northern Apennines, Italy). Tectonophysics 238 (1- 4), 295-315.

Carmignani, L., Decandia, F. A., Disperati, L., Fantozzi, P.L., Lazzarotto, A., Liotta, D., Oggiano, G., 1995. Relationships between the Tertiary structural evolution of the Sardinia-Corsica-Provencal domain and the northern Apennines. Terra Nova 7, 128-137.

Carmignani, L., Oggiano, G., Barca, S., Conti, P., Salvadori, I., eltrudis A., Funedda A., Pasci, S., 2001. Geologia della Sardegna; Note descrittive della Carta Geologica della Sardegna in scala 1:200.000. Memorie descrittive della Carta Geologica d'Italia 60, Servizio Geologico d'Italia, Roma, 283.

Carminati, E., Lustrino, M., Doglioni, C., 2012. Geodynamic evolution of the central and western Mediterranean: Tectonics vs. igneous petrology constraints. Tectonophysics 579, 173-192.

Chelle-Michou, C., Chiaradia, M., Ovtcharova, M., Ulianov, A., Wotzlaw, J.F., 2014. Zircon petrochronology reveals the temporal link between porphyry systems and the magmatic evolution of their hidden plutonic roots (the Eocene Coroccohuayco deposit, Peru). Lithos 198-199, 129-140.

Connolly, J.A.D., 1997. Devolatilization-generated fluid pressure and deformation-propagated fluid flow during prograde regional metamorphism. Journal of Geophysical Research 102, 18149-18173.

Decandia, F.A., Lazzarotto, A., Liotta, D., 2001. Structural feature of Southern Tuscany, Italy. Ofioliti 26, 14.

Dini, A., Innocenti, F., Rocchi, S., Tonarini, S., Westerman, D. S., 2002. The magmatic evolution of the late Miocene laccolith-pluton-dyke granitic complex of Elba Island, Italy. Geological Magazine (decade III) 139, 257-279.

Dini, A., Gianelli, G., Puxeddu, M., Ruggieri, C., 2005. Origin and evolution of Pliocene-Pleistocene granites from the Larderello geothermal field (Tuscan Magmatic Province, Italy). Lithos 81, 1-31.

Dini, A., Vezzoni, S., Rocchi, S., 2013. Geologia e minerogenesi. Evoluzione del pensiero scientifico nel Campigliese. Rivista Mineralogica Italiana Campigliese. Min. Miner. 1, 21-27.

Ennis, D.J., Dunbar, N.W., Campbell, A.R., Chapin, C.E., 2000. The effects of K-metasomatism on the mineralogy and geochemistry of silicic ignimbrites near Socorro, New Mexico. Chemical Geology 167, 285-312.

Ersoy, E.Y., 2013. PETROMODELER (Petrological Modeler): a Microsoft® Excel© spreadsheet program for modelling melting, mixing, crystallization and assimilation processes in magmatic systems. Turkish Journal of Earth Sciences 22, 115-125.

Feldstein, S.N., Halliday, A.N., Davies, G.R., Hall, C.M., 1994. Isotope and chemical microsampling: Constrains on the history of an S-type rhyolite, San Vincenzo, Tuscany, Italy. Geochimica et Cosmochimica Acta 58, 943-958.

Ferrara, G., Petrini, R., Serri, G., Tonarini, S., 1989. Petrology and isotope-geochemistry of San Vincenzo rhyolites (Tuscany, Italy). Bulletin Volcanologique 51, 379-388.

Franceschini, F., Innocenti, F., Marsi, A., Tamponi, M., Serri, G., 2000. Petrography and Chemistry of the buried Pliocene Castel di Pietra pluton (Southern Tuscany, Italy). Neues Jahrbuch fur Geologie und Palaontologie-Abhandlungen 21, 17-46.

Franceschelli, M., Gianelli G., Pandeli E., Puxeddu, M., 2004. Varisican and Alpine metamorphic events in the northern Apennines (Italy): a review. Periodico di Mineralogia 73, 23-42.

Franzini M., Leoni L., Saitta M., 1976. Enhancement effects in X-ray analysis of rocks. X-Ray Spectrometry 5, 208-211.

Gerstenberger, H., and Haase, G., 1997. A highly effective emitter substance for mass spectrometric Pb isotope ratio determinations. Chem. Geol. 136, 309–312.

Gianelli, G., Manzella, A., Puxeddu, M., 1997. Crustal models of the geothermal areas of southern Tuscany (Italy). Tectonophysics 281, 221-239.

Gianelli, G., Ruggieri, G., 2002. Evidence of a contact metamorphic aureole with high- temperature metasomatism in the deepest part of the active geothermal field of Larderello, Italy. Geothermics 31, 443-474.

Gysi, A.P., and Williams-Jones, A.E., 2013. Hydrothermal mobilization of pegmatite-hosted REE and Zr at Strange Lake, Canada: A reaction path model. Geochimica et Cosmochimica Acta 122, 324-352.

Gysi, A.P., Williams-Jones, A.E., Harlow, D., 2015. The solubility of Xenotime-(Y) and other HREE phosphates (DyPO4, ErPO4 and YbPO4) in aqueous solutions from 100 to 250°C and psat. Chemical Geology 401, 83- 95.

Gysi, A.P., William-Jones, A.E., Collins, P., 2016. Lithogeochemical Vectors for Hydrothermal Processes in the Strange Lake Peralkaline Granitic REE-Zr-Nb Deposit. Society of Economic Geologists, Inc. Economy Geology 111, 1241-1276.

Harlov, D. E., and Austrheim, H., 2013. Metasomatism and Chemical transformation of Rock: Rock-Mineral-fluid Interaction in Terrestrial and Extraterrestrial Environments. Lecture Notes in Earth System Sciences, 1-16.

Hemley, J.J, and Jones, W. R., 1964. Chemical aspects of hydrothermal alteration with emphasis on hydrogen metasomatism. Economic Geology 59(4), 538-567.

Hiess J1, Condon DJ, McLean N, Noble SR., 2012. 238U/235U Systematics in terrestrial uranium-bearing minerals. Science. 335, 1610-4.

Innocenti, F., Serri, G., Ferrara, G., Manetti, P., Tonarini, S., 1992. Genesis and classification of the rocks of the Tuscan Magmatic Province: thirty years after Marinelli's model. Acta Vulcanologica 2, 247-265.

Jackson, S.E., Pearson, N.J., Grin, W.L., and Belousova, E.A., 2004. The application of laser ablation-inductively coupled plasma-mass spectrometry to in situ U-Pb zircon geochronology: Chemical Geology, 211, 47-69,

Jolivet, L., Dubois, R., Goffé, B., Michard, A., Jourdan, C., 1990. Ductile extension in Alpine Corsica. Geology 18, 1007-1010.

Jolivet, L., Facenna, C., Goffé, B., Mattei, M., Rossetti, F., Brunet, C., Storti, F., Funiciello, R., Cadet, J.P., D'Agostino, N., Parra, T., 1998. Midcrustal shear zones in postorogenic extesion: example from the northern Tyrrhenian Sea. Journal of Geophysical Research 103, 12123-12160.

Korzhinskii, D.S., 1953. Outline of metasomatic processes. Main problems on the science of magmatogenic ore deposits. Acad. Sci. Publishing, Moscow, 334-456.

Krogh T. E., 1973. A low contamination method for hydrothermal decomposition of zircon and extraction of U and Pb for isotopic age determination. Geochimica and Cosmochimica Acta 37, 485– 494.

Lattanzi, P., Benvenuti, M., Costagliola, P., Maineri, C., Mascaro, I., Tanelli, G., Dini, A., Ruggieri, G., 2001. Magmatic versus hydrothermal processes in the formation of raw ceramic material deposits in southern Tuscany. Water-rock interaction, 725-728.

Leoni, L., Tamponi, M., 1991. Thermometamorphism in the Campiglia Marittima aureole (Tuscany, Italy). N. Jb. Miner. Mh. 4, 145–157.

Lindegren, W., 1925. Metasomatism. Geological Society of America Bulletin 36, 1-114.

Longerich, H.P., Jackson, S.E., Günther, D., 1996. Laser ablation inductively coupled plasma mass spectrometric transient signal data acquisition and analyte concentration calculation. Journal of Analytical Atomic Spectrometry, 11, 899–904.

Ludwig, K.R., 2012. User's Manual for Isoplot 3.75, A Geochronological Toolkit for Microsoft Excel, Berkeley Geochronology Center Special Publication 5.

Marinelli, G., Barberi, F., Cioni, R., 1993. Sollevamenti neogenici e intrusioni acide della Toscana e del Lazio settentrionale. Mem. Società Geologica Italiana 49, 279-288.

Marinelli, G.,1967. Genèse des magmas du volcanisme Plio-Quaternaire des Apennines. Geol. Rundsch 57, 127-141.

Mazzarini, F., Ruggieri, G., Isola, I., Boschi, C., Dini, A., Musumeci A., Rocchi, S., 2014. Fluid transfer and vein thickness distribution in high and low temperature hydrothermal systems at shallow crustal level in southern Tuscany (Italy). Annals of Geophysics, 57, 3.

Migdisov, A.A., William-Jones, A.E., Wagner, T., 2009. An experimental study of the solubility and speciation of the rare earth elements (III) in flouride-and chloride-bearing aqueous solutions at temperatures up to 300°C. Geochimica et Cosmochimica Acta 73, 7087-7109.

Migdisov, A.A., Williams-Jones, A.E., Van Hinsberg, V., Salvi, S., 2011. An experimental study of the solubility of baddelite (ZrO2) in flouride-bearing solutions at elevated temperature. Geochimica et Cosmochimica Acta 75, 7426-7434.

Mongelli, F., Palumbo, F., Puxeddu, M., Villa, I.M., Zito, G., 1998. Interpretation of the geothermal anomaly of Larderello, Italy. Memorie Società geologica Italiana 52, 305-318.

Moss, R.L., Tzimas, E., Kara, H., Willis, P. Kooroshy, J., 2011. Critical Metals in Strategic Energy Technologies. European Commission Joint Research Centre Institute for Energy and Transport.

Naumann, C.F., 1826. Grundriss der Kristallographie. Verlag von Johann Ambrosius Barth, Leipzig.

Pasquaré, G., Chiesa, S., Vezzoli, L., Zanchi, A. 1983. Evoluzione paleogeografica e strutturale di parte della Toscana Meridionale a partire dal Miocene superiore. Mem. Società Geologica Italiana 25, 145-157.

Pearce, N.J.G., Perkins, W.T., Westgate, J.A., Wade, S.C., 2011. Trace-element microanalysis by LA-ICP-MS: the quest for comprehensive chemical characterisation of single, sub-10 μm glass shards. Quaternary International 298, 276–277.

Peccerillo, A., 1999. Relationships between ultrapotassic and carbonate-rich volcanic rocks in central Italy: petrogenetic implications and geodynamic significance. Lithos 43, 267-279.

Peccerillo, A., Conticelli, S., Manetti P., 1987. Petrological characteristics and the genesis of Recent magmatism of Southern Tuscany and Northern Latium. Periodico di Mineralogia 56, 157-172.

Peccerillo, A., and Donati, C., 2003. Miocene-Quaternary magmatism in central-southern Italy. Periodico di Mineralogia 72 (Special Issue), 11-23.

Peccerillo, A., 2005. Plio-Quaternary magmatism in Central-Southern Italy: a new classification scheme for volcanic provinces and its geodynamic implications. Bollettino Società Geologica Italiana, volume speciale 1, 113-127.

Perugini, D., Poli, G., 2003. Chaotic mixing of magmas in the Tuscan Magmatic Province. Periodico di Mineralogia 72 (Special Issue), 53-61.

Petrelli, M., Caricchi, L., and Ulmer, P., 2007. Application of high spatial resolution laser ablation ICP-MS to crystal-melt trace element partition coefficient determination. Geostandards and Geoanalytical Research 31, 13–25.

Petrelli, M., Laeger, K., Perugini, D. 2016. High spatial resolution trace element determination of geological samples by laser ablation quadrupole plasma mass spectrometry: implications for glass analysis in volcanic products, Geosciences Journal, in press.

Piana Agostinetti, N., Amato A., 2009. Moho depht and Vp/Vs ratio in peninsular Italy from teleseismic receiver functions. Journal of Geophysical Research 114, 1-17.

Pirajno, F., 2009. Hydrothermal processes and mineral systems. Springer, Berlin.

Pirajno, F., 2013. Effects of Metasomatism on Mineral Systems and Their Host Rocks: Alkali Metasomatism, Skarns, Greisens, Tourmalinites, Rodingites, Black-Wall Alteration and Listvenites. Metasomatism and the Chemical Transformation of Rock: The Role of Fluids in Terrestrial and Extraterrestrial Processes. Berlin, Heidelberg, Springer Berlin Heidelberg, 203-251.

Platt, J.P., 2007. From orogenic hinterlands to Mediterranean-style back-arc basins: a comparative analysis. Journal of the Geological Society 164(2), 297-311.

Poli, G., Manetti, P., Tommasini S.,1989. A petrological review on Miocene-Pliocene intrusive rocks from Southern Tuscany and Tyrrenhian Sea (Italy). Periodico di Mineralogia LVIII, 109- 126.

Poli, G., Peccerillo, A., Donati, C., 2002. Genesis of Miocene-Pliocene intrusive rocks from Tuscan Magmatic Province: implication on the structure of Apeninic litosphere. Bollettino Società Geologica Italiana 1, 129- 139.

Poli, G., 2004. Genesis and evolution of Miocene-Quaternary intermediate-acid rocks from the Tuscan Magmatic Province. Periodico di Mineralogia LXXIII,187-214.

Poli, G., and Peccerillo, A., 2016. The Upper Miocene magmatism of the Island of Elba (Central Italy): compositional characteristics, petrogenesis and implications for the origin of the Tuscany Magmatic Province. Mineralogy and Petrology, 109(6).

Pollard, P. J., 1983. Magmatic and postmagmatic processes in the formation of rocks associated with rare element deposits. Transaction of the Institution of Mining and Metallurgy 92, 1-9.

Ridolfi, F., Renzulli, A., Perugini, D., Cesare, B., Braga, R., Del Moro, S. 2016. Unravelling the complex interaction between mantle and crustal magmas encoded in the lavas of San Vincenzo (Tuscany, Italy). Part II: Geochemical overview and modelling. Lithos 244, 233-249.

Rocchi, S., Dini, A., Innocenti F., Tonarini, S., Westerman, D. S., 2003. Elba Island: intrusive magmatism. Periodico di Mineralogia 72 (Special Issue), 73-104.

Rodolico, F., 1945. Ragguagli sul granito del Campigliese. Atti Società Toscana Scienze Naturali Mem., serie A 73, 62-74.

Rossetti, F., Facenna, C., Acocella, V., Funiciello, R., Jolivet, L., Salvini, F., 2000. Pluton emplacement in the Northern Tyrrenian area, Italy. Geological Society of America Special Papers 174, 55-77.

Rossetti, F., Facenna, C. Funiciello, Pascucci, R., Pietrini, V., Sandrelli, F., 2001. Strike slip faulting and pluton emplacement in the Colline Metallifere region: the Gavorrano- Capanne Vecchie area. Boll. Società Geologica Italiana 120, 15-30.

Salvi, S., Williams-Jones, A.E., 1997. The role of Hydrothermal preocesses in the granite-hosted Zr, Y, REE deposit at Strange Lake, Quebec/Labrador: Evidence from fluid inclusions. Geochimica et Cosmochimica Acta 54, 2403-2418.

Schoene B., Crowley J.L., Condon D.C., Schmitz M.D., Bowring S.A., 2006. Reassessing the uranium decay constants for geochronology using ID-TIMS U-Pb data. Geochim. Cosmochim. Acta 70, 426–445.

Schoene, B., Latkoczy, C. Schaltegger, U. Günther, D., 2010. A new method integrating high-precision U–Pb geochronology with zircon trace element analysis (U–Pb TIMS-TEA). Geochimica et Cosmochimica Acta 74, 7144-7159.

Seedorff, E., Dilles, J.H., Proffett, J.M., Einaudi, M.T., Zurcher, L., Stavast ,W.J.A., Johnson, D.A., Barton, M.D., 2005. Porphyry deposits: characteristics and origin of hypogene features. Economic Geology 100, 251-298.

Serri, G., Innocenti, F., Manetti, P., 1993. Geochemical and petrological evidence of the subduction of delaminatesd Adriatic continental lithosphere in the genesis of the Neogene-Quaternary magmatism of central Italy. Tectonophysics 223, 117-147.

Sláma, J., KoÇler, J., Condon, D.J., Crowley, J.L., Gerdes, A., Hanchar, J.M., Horstwood, M.S.A., Morris, G.A., Nasdala, L., Norberg, N., Schaltegger, U., Schoene, B., Tubrett, M.N., and Whitehouse, M.J., 2008. Plesovice zircon - A new natural reference material for U-Pb and Hf isotopic microanalysis: Chemical Geology 249, 135.

Tamponi M., Bertoli M., Innocenti F., Leoni L., 2003. X-ray fluorescence analysis of major elements in silicate rocks using fused glass discs. Atti della Società Toscana di Scienze Naturali Memorie 108, 1-8.

Tiepolo, M., Bottazzi, P., Palenzona, M., and Vannucci, R., 2003. A laser probe couplet with ICP-double focusing sector-field mass spectrometer for in situ analysis of geological samples and U-Pb dating of zircon. The Canadian Mineralogist 41, 259–272.

Tropper, P., and Manning, C., 2007. The solubility of flourite in H2O and H2O-NaCl at high pressure and temperature. Geochimica et Cosmochimica Acta 172, 205- 224.

Venerandi-Pirri, I. and Zuffardi, P., 1982. The Tin Deposit of Monte Valerio (Tuscany, Italy): Pneumatolytic-Hydrothermal or Sedimentary-Remobilization Processes? Ore Genesis. G. C. Amstutz, G. Frenzel, C. Kluthet al, Springer Berlin Heidelberg. 2: 57-65.

Vermeesch, P., 2004. How many grains are needed for a provenance study?: Earth and Planetary Science Letters 224, 441-451.

Vezzoni, S., Dini, A., Rocchi, S., 2016. Reverse telescoping in a distal skarn system (Campiglia Marittima, Italy). Ore Geology Reviews 77, 176-193.

Wendt, I., and C. Carl, 1991, The statistical distribution of the mean squared weighted deviation, Chem. Geol. 86, 275–285.

Wiedenbeck, M., Allé, P., Corfu, F., Griffin, W.L., Meier, M., Oberli, F., von Quadt, A., Roddick, J.C. and Spiegel, W., 1995. Three natural zircon standards for U-Th-Pb, Lu-Hf, trace element and REE analysis. Geostandards Newsletter 19, 1-23.

Wotzlaw, J.-F., Bindeman, I.N., Schaltegger, U., Brooks, C.K., Naslund, H.R., 2012. High-resolution insights into episodes of crystallization, hydrothermal alteration and remelting in the Skaergaard intrusive complex. Earth and Planetary Science Letters 355-356,

Zaraisky, G.P., 1994. The influence of acidic flouride and chloride solutions on the geochemical behaviour of Al, Si, and W. Fluids in the Crust: Equilibrium and transport properties, In: Shmulovich, K.I., Yardley, B.V.D., Gonchar, G.G., London, Chapman and Hall, 142-165.

Zharikov, V., Pertsev, N., Rusinov, V., Callegari, E., Fettes, D., 2007. Metasomatism and metasomatic rocks, In: Fettes, D., Desmons, J. (eds) Metamorphic rocks – a classification and glossary of terms. Cambridge University Press, Cambridge, 58–68.

Final Report - Gabriele Paoli, Pegasus PhD Program, Università di Firenze

Petrogeochemical and geochronological framework of element mobilities during magmatic-metasomatic processes (Campiglia Marittima, Tuscany)

This PhD thesis is part of a larger project focusing on the magmatic-hydrothermal system of Campiglia Marittima. The project involves the collaboration between the University of Pisa and the CNR, as well as the University of Geneva (UNIGE), aiming to investigate the processes of element mobilities resulting from the magmatic-hydrothermal activity characterising the Campiglia Marittima area. Indeed, at Campiglia, multiple magmatic events over an interval of about 1000 ka generated an intense metasomatic fluid circulation. The hydrothermal activity related to this igneous cycle generated minor endo- and exoskarn, as well as major distal mineralised exoskarn bodies, that have been exploited for Cu-Pb-Zn-Ag for over twenty-seven centuries, and that are considered in the literature as a classic example of contact exoskarn generated by interaction between a magmatic body and a carbonate host rock.

In this context, the aims of this PhD thesis were (i) to characterise the products of the metasomatic activity localised at the pluton-marble contact, testifying prolonged period of fluid-rock interaction, (ii) to reconstruct the metasomatic processes and the nature of fluid(s) that have been promoted the chemical transformation and replacement of the original granite and the host carbonate, (iii) to define the litho-geochemical vectors responsible for the significative element mobilisation, including the local mobilisation of usually poorly mobile elements. Thus, this study carried out detailed textural and geochemical investigations of the monzogranite, its carbonate host, and the products of their hydrothermal-metasomatic alteration, in the field, under the optical and electron microscope, and by QEMSCAN (at University of Geneva), EPMA (at University of Milan) and (LA)-ICP-MS (at Universities of Perugia and Pisa).

The obtained results allowed to discriminate between metasomatic processes occurred at different temperature, fluid(s) composition and pH. Moreover, the determination of a mineral paragenetic sequence coupled with precise chemical analysis allowed to reconstruct the sequence of these metasomatic events. To define the chronological framework of the multiple igneous episodes occurred at Campiglia and to constrain the multiple hydrothermal episodes, a precise CA-ID-TIMS U-Pb dating has been carried out at the University of Geneva, on carefully selected zircon grains from the Botro ai Marmi monzogranite, the mafic Temperino porphyry crosscutting the metasomatic aureole, and the San Vincenzo rhyolite.

These new CA-ID-TIMS U-Pb zircon ages (combined with available ^{40}Ar-^{39}Ar emplacement ages) suggest the existence of a long-lived magmatic-hydrothermal system in the Campiglia Marittima area. The magmatic-hydrothermal activity in this area is triggered by a deeper crustal level felsic reservoir, that gave way to the ascent of magma that emplaced as the Botro ai Marmi granitic pluton (~5.4 Ma). These events generated a widespread contact aureole in the intruded carbonatic sequence. The fluids exsolved from the pluton caused the occurrence of metasomatic bodies at the pluton-carbonate contact, or as veins in the host rock and into the monzogranitic body. The protracted exsolution of fluids possibly enhanced by successive magmatic emplacement events generated distal ore and skarn bodies. These bodies are crosscutted by mafic and felsic porphyry postdating the main hydrothermal event (~4.9 to ~4.5 Ma). Finally, the San Vincenzo rhyolite emplacement (~4.4 Ma) closed the magmatic cycle in the area.

Concluding, the geochronological data support the existence of a prolonged magmatic activity. The zircon age distribution, too large to be explained with *in situ* crystallisation of rather small igneous bodies, suggests that the zircons crystallised within a larger reservoir at a deeper crustal level. This evidence supports an extended period of magma assemblage, cooling, and rejuvenation protracted for approximatively 1000 ka, from the intrusion of the Botro ai Marmi pluton to the closing eruption of the San Vincenzo rhyolite.

Conference abstracts

Paoli G., Rocchi S., Jacobs J., Ksienzyk A., Zircon beyond geochronology: inherited and antecrystic zircons as igneous petrogenesis tools. SIMP, Milano 2014.

Paoli G., Sirevaag H., Stokke H.H., Jorgensen H., Ksienzyk A., Jacobs J., Rocchi S., The journey of Tuscany basement blocks from Gondwana to Europe as recorded by U-Pb dating of detrital zircons. 8th Hutton Symposium, Florianopolis-Brasile 2015.

Rocchi S., Paoli G., Jacobs J. & Ksienzyk A., Inherited and antecrystic zircons as time markers for magma ascent/ storage. SIMP-AIV-SoGeI-SGI, Firenze 2015.

Joachim Jacobs, Hallgeir Sirevaag, Anna K. Ksienzyk, Sergio Rocchi, Gabriele Paoli, From Gondwana to Europe: the journey of Elba Island (Italy) as recorded by U-Pb detrital zircon ages of Paleozoic metasedimentary rocks. EGU General Assembly, Vienna 2016.

Paoli G., Rocchi S. and Dini A., Element mobility between granite, fluids and skarn (Campiglia Marittima, Tuscany). EMC Conference, Rimini 2016.

Publications

Paoli, G., Stokke, H.H., Rocchi, S., Sirevaag, H., Ksienzyk, A., Jacobs, J., Košler, J., 2017. Basement provenance revealed by U-Pb detrital zircon ages: a tale of African and European heritage in Tuscany, Italy. Lithos 277, 376–387.

Sirevaag, H., Jacobs, J., Ksienzyk, A.K., Rocchi, S., Paoli, G., Jørgensen, H., Košler, J., 2016. From Gondwana to Europe: The journey of Elba Island (Italy) as recorded by U–Pb detrital zircon ages of Paleozoic metasedimentary rocks. Gondwana Research 38, 273–288.